

INVESTIGATION OF THE CHARMLESS  
DECAY  $B^\pm \rightarrow K^\pm \pi^\pm \pi^\mp$  USING A  
DALITZ PLOT ANALYSIS AT *BABAR*

**Sian Ellen Morgan**

*A thesis submitted for the degree of  
Doctor of Philosophy*



Particle Physics Group,  
School of Physics and Astronomy,  
University of Birmingham.

March 2005.

# Abstract

The *BABAR* experiment operating at the PEP-II  $e^+e^-$  collider is designed to study  $CP$  violation effects in the  $B$ -meson system. The data sample collected between May 1999 and July 2004 consists of 231.8 million  $B\bar{B}$  pairs. This data is used to study the decays  $B^- \rightarrow K^- \pi^- \pi^+$  and  $B^+ \rightarrow K^+ \pi^+ \pi^-$ . A Dalitz-plot analysis is used to examine the resonant and non-resonant contributions to these three-body decays. A discussion of the fitting technique used and the alternative genetic algorithm procedure is given. Measurements, including full statistical and systematic errors, for the fit fractions and phases are provided for the following components:

- $K^{*0}(892)\pi^\pm$
- $K_0^{*0}(1430)\pi^\pm$
- $\rho^0(770)K^\pm$
- $f_0(980)K^\pm$
- $\chi_{c0} K^\pm$
- non-resonant  $K^\pm \pi^\pm \pi^\mp$

Upper limits are set for the fit fractions of additional higher resonances that are found to have small contributions to the Dalitz plots. The inclusive branching fractions are measured as  $(64.1 \pm 3.5 \pm 4.5) \times 10^{-6}$  for  $B^- \rightarrow K^- \pi^- \pi^+$  and  $(64.7 \pm 3.5 \pm 4.6) \times 10^{-6}$  for  $B^+ \rightarrow K^+ \pi^+ \pi^-$ .

# Dedication

This thesis is dedicated to my dad

I wish you were here to see the finished article. Thank you for always believing in me and your unconditional support.

I miss you so much.

# Acknowledgements

For Patrick, Emma, James, Clare, Julia, Kate, Sugi and Emma for being the best friends I could ever ask for. Thanks for helping me through the bad times and celebrating with me in the good times. Thanks to Jo and Jason for always being willing to chat even from foreign lands. Thanks to the rest of the Maggiedog group of New College graduates and also to my New College tutors who convinced me I could be a physicist and helped to set me on this road.

For Kelly, for our mutual love of football, introducing me to the world of shoes, and a thousand other things that have made these last three years so much fun. Thank you so much for keeping me sane.

For Tom for being a gentlemen and an amazing person to work with. Thanks for being my computer administrator and introducing me to the world of fine wine.

Thanks to my supervisor Chris Hawkes for his guidance, support and valuable input. Thanks also to Alan Watson and the rest of the staff in the Birmingham Particle Physics Group. Thanks to Bruce for cinema trips and listening to me rant when things were going badly, and the other students in Birmingham for fun lunchtimes and distractions from work. Thanks to Fiona and Saher for memorable nights out and helping me to make it through my first year.

Thanks to Paul and Theresa Harrison for their wisdom and support. Thanks to John Back for being an incredibly nice guy and always answering my questions.

Thanks to the rest of the Charmless Group for providing advice and being great people to collaborate with and learn from.

Thanks to Marc, Jack and the rest of the UK physicists who spent time at SLAC for making my time in California so enjoyable. Thanks to Jamie for sharing my love of rugby and watching the games with me in the middle of the night.

Thanks to PPARC for funding my studies and allowing me to spend time living in California.

And finally special thanks to Mum and Rhys, my family, I couldn't have done this without you. Thanks for everything, but mostly for providing a much needed non-academic sense of reality and always being there to go home to.

# Declaration

I declare that no part of the work in this thesis has been previously presented to this, or any other, university as part of the requirements of a higher degree.

The data used in this analysis was collected at the *BABAR* experiment by the *BABAR* collaboration. The author contributed to the running of the detector through the taking of general shifts and being a member of the team responsible for the maintenance of the electromagnetic trigger.

The event selection described in Chapter 3 uses code available to all *BABAR* members, and specific pre-selection code developed by the charmless three-body analysis working group. The cut optimisation described in Section 3.6.3 was performed by John Back. The *Laura++* code used for the Dalitz-plot analysis was developed by the author, Paul Harrison, John Back and Tom Latham. The  $B^\pm \rightarrow K^\pm \pi^\pm \pi^\mp$  analysis described in Chapters 4, 5 and 6 was undertaken jointly with Tom Latham. The background normalisation fit (Section 4.6) and the optimisation of the  $K_0^{*0}(1430)$  lineshape (Section 6.3.2) is the sole work of Tom Latham. The work on the analytical continuum model (Section 4.5.1), the optimisation of the  $f_0(980)$  lineshape (Section 6.3.1), the work on the seven component model (Section 6.7) and the calculation of the upper limits (Section 6.10) are the sole work of the author. The description and analysis of fitting routines and genetic algorithms (Chapter 5) is also the work of the author.

# Contents

<b>Introduction</b>	<b>1</b>
<b>1 <i>CP</i> Violation in the <i>B</i>-meson system</b>	<b>3</b>
1.1 Introduction . . . . .	3
1.2 <i>CP</i> Violation in the Standard Model and the CKM Matrix . . . . .	4
1.3 The Unitarity Triangle . . . . .	6
1.4 Different Types of <i>CP</i> Violation . . . . .	7
1.4.1 <i>CP</i> Violation in Decay . . . . .	8
1.4.2 <i>CP</i> Violation in Mixing . . . . .	9
1.4.3 <i>CP</i> Violation in the Interference Between Decay and Mixing .	10
1.5 Experimental Measurements of <i>CP</i> Violation . . . . .	11
1.5.1 Constraints on the CKM Matrix . . . . .	11
1.5.2 Angles of the Unitarity Triangle . . . . .	12
1.5.3 Direct <i>CP</i> Violation in <i>B</i> Meson Decay . . . . .	15
1.6 $B^\pm \rightarrow K^\pm \pi^\pm \pi^\mp$ Decay . . . . .	15

1.6.1	Charmless Hadronic Three-Body $B$ Decays . . . . .	15
1.6.2	Intermediate Resonances . . . . .	16
1.6.3	Decay Diagrams . . . . .	16
1.6.4	Theoretical Predictions . . . . .	18
1.6.5	Previous Experimental Measurements . . . . .	19
1.7	Dalitz Plot Theory . . . . .	21
1.7.1	Dalitz Kinematics . . . . .	21
<b>2</b>	<b>The <i>BABAR</i> Experiment</b>	<b>26</b>
2.1	Introduction . . . . .	26
2.2	PEP-II $B$ Factory . . . . .	27
2.2.1	The Injection System and Interaction Region . . . . .	27
2.2.2	Machine Backgrounds . . . . .	28
2.2.3	PEP-II Performance . . . . .	29
2.3	The <i>BABAR</i> Detector . . . . .	29
2.4	Silicon Vertex Tracker . . . . .	31
2.5	Drift Chamber . . . . .	33
2.6	Detector of Internally Reflected Cerenkov Light . . . . .	36
2.7	Electromagnetic Calorimeter . . . . .	38
2.8	Instrumented Flux Return . . . . .	41

2.9	Trigger . . . . .	43
2.9.1	L1 Trigger . . . . .	43
2.9.2	L3 Trigger . . . . .	44
2.10	Data Acquisition . . . . .	44
2.11	Online Prompt Reconstruction . . . . .	45
2.12	Monte Carlo Simulation . . . . .	45
<b>3</b>	<b>Data Reconstruction and Event Selection</b>	<b>48</b>
3.1	Analysis Method . . . . .	48
3.2	Data Sample . . . . .	49
3.3	Discriminating Variables . . . . .	49
3.3.1	Kinematic Variables . . . . .	49
3.3.2	Event Shape Variables . . . . .	52
3.4	Tracking . . . . .	55
3.4.1	Tracking Efficiency Corrections . . . . .	57
3.5	Particle Identification . . . . .	57
3.5.1	Kaon Identification . . . . .	57
3.5.2	Particle Identification Efficiency Corrections . . . . .	60
3.5.3	Electron Identification . . . . .	60
3.6	Event Selection . . . . .	61

3.6.1	Event Pre-Selection . . . . .	61
3.6.2	Batch Level Pre-Analysis . . . . .	61
3.6.3	Final Selection . . . . .	62
<b>4</b>	<b>Dalitz-Plot Analysis</b>	<b>65</b>
4.1	Introduction . . . . .	65
4.2	Dalitz Fitting . . . . .	66
4.2.1	Per Event Likelihood . . . . .	66
4.2.2	Normalisation . . . . .	67
4.2.3	Fit Fractions . . . . .	68
4.3	Signal Resonance Modelling . . . . .	68
4.3.1	$f_0(980)$ modelling . . . . .	71
4.3.2	The $K\pi$ S-wave . . . . .	71
4.3.3	Excited $\pi\pi$ resonances . . . . .	72
4.4	$B\bar{B}$ Background Modelling . . . . .	73
4.4.1	Charm Vetoes . . . . .	80
4.4.2	$\chi_{c0}$ . . . . .	81
4.5	Continuum Background Modelling . . . . .	81
4.5.1	Analytical Model . . . . .	81
4.5.2	Histogram Model . . . . .	83

4.6	Background Normalisations . . . . .	88
4.7	Efficiency Modelling . . . . .	91
4.7.1	Self Cross Feed Decays . . . . .	93
<b>5</b>	<b>Fitting Procedures</b>	<b>95</b>
5.1	Introduction . . . . .	95
5.2	Multiple Solutions . . . . .	95
5.3	Minuit . . . . .	98
5.4	Toy MC Tests . . . . .	99
5.5	Full MC Tests . . . . .	103
5.6	Genetic Algorithms . . . . .	105
5.6.1	Default Genetic Algorithm Setup . . . . .	107
5.6.2	Initial Optimisation . . . . .	108
5.6.3	Steady State Reproduction . . . . .	109
5.6.4	Mutation Rate . . . . .	111
5.6.5	Final Optimisation . . . . .	112
5.6.6	Results . . . . .	113
5.6.7	Conclusion . . . . .	114
<b>6</b>	<b><math>B^\pm \rightarrow K^\pm \pi^\pm \pi^\mp</math> Dalitz Analysis - Final Results</b>	<b>118</b>
6.1	Introduction . . . . .	118

6.2	Data Projection Plots . . . . .	119
6.2.1	Nominal Model . . . . .	121
6.3	Lineshapes . . . . .	122
6.3.1	$f_0(980)$ . . . . .	124
6.3.2	$K\pi$ S Wave . . . . .	130
6.4	Results - Six Component Nominal Model . . . . .	133
6.5	Omission Tests . . . . .	137
6.6	Addition Tests . . . . .	140
6.7	Results - Seven Component Model . . . . .	143
6.7.1	Projection Plots . . . . .	143
6.7.2	Addition Tests . . . . .	144
6.8	Systematic Errors on Fit Fractions and Phases . . . . .	149
6.8.1	Histogram Fluctuations . . . . .	149
6.8.2	Background Fraction Fluctuations . . . . .	149
6.8.3	Fit Bias Tests . . . . .	155
6.8.4	Conclusions . . . . .	159
6.9	Model Dependence . . . . .	162
6.10	Final Results for the Six Component Nominal Model . . . . .	163
6.11	Upper Limits . . . . .	164
6.12	Total Rate Measurement . . . . .	166

6.12.1 Systematics on Total Rate Measurement . . . . .	167
<b>7 Conclusion and Discussion</b>	<b>170</b>
<b>A GA Evolution Histograms</b>	<b>174</b>
<b>B Pull Plots</b>	<b>178</b>

# List of Tables

1.1	Theoretical Predictions for the $B^+ \rightarrow \rho^0(770)K^+$ mode . . . . .	20
1.2	Theoretical Predictions for the $B^+ \rightarrow K^{*0}(892)\pi^+$ mode . . . . .	20
3.1	Definitions of fitting regions. . . . .	52
3.2	Summary of average efficiencies in the analysis of $B^\pm \rightarrow K^\pm\pi^\pm\pi^\mp$ . .	64
4.1	Possible resonances in the $\pi\pi$ spectrum . . . . .	73
4.2	Charm $B^+B^-$ background modes . . . . .	75
4.3	Charmless $B^+B^-$ background modes . . . . .	76
4.4	Charm $B^0\bar{B}^0$ background modes. . . . .	77
4.5	Charmless $B^0\bar{B}^0$ background modes . . . . .	78
4.6	The invariant mass veto ranges . . . . .	80
4.7	The event yields from the fit to $m_{ES}$ . . . . .	90
5.1	Fitted parameters of the two solutions in the negative log-likelihood distribution. . . . .	97
5.2	Magnitude and phase pulls in fit with 6 components . . . . .	102

5.3	Magnitude and phase results of fit to reweighted MC dataset with six signal components . . . . .	104
5.4	Fitted parameters of the solutions found by five GA fits with the default setup. . . . .	108
5.5	Fitted parameters of the solutions found by five GA fits after initial optimisation. . . . .	109
5.6	Fitted parameters of the solutions found by five GA fits using different reproduction plans. . . . .	110
5.7	Fitted parameters of the solutions found by five GA fits with the new reproduction plan and subsequent settings. . . . .	111
5.8	Fitted parameters of the solutions found by five GA fits with a new mutation plan and three different mutation rates. . . . .	112
5.9	Fitted parameters of the solutions found by five GA fits with different numbers of individuals. . . . .	116
5.10	Fitted parameters of the solutions found by five GA fits with different numbers of digits encoding the phenotypes. . . . .	117
6.1	Results of fits to $B^-$ and $B^+$ data with nominal 6 component model .	134
6.2	Results of fit to $B^-$ data with 5 components. . . . .	138
6.3	Results of fit to $B^+$ data with 5 components. . . . .	139
6.4	Results of fit to $B^-$ data with 7 components . . . . .	141
6.5	Results of fit to $B^+$ data with 7 components . . . . .	142
6.6	Results of fit to $B^-$ data with 8 components . . . . .	147

6.7	Results of fit to $B^+$ data with 8 components . . . . .	148
6.8	Absolute systematic errors on the fit fractions and phases due to the efficiency histogram fluctuation . . . . .	150
6.9	Absolute systematic errors on the fit fractions and phases due to the $q\bar{q}$ background histogram fluctuation . . . . .	151
6.10	Absolute systematic errors on the fit fractions and phases due to the $B\bar{B}$ background histogram fluctuation . . . . .	152
6.11	Absolute systematic errors on the fit fractions and phases due to the $q\bar{q}$ background fraction fluctuation . . . . .	153
6.12	Absolute systematic errors on the fit fractions and phases due to the $B\bar{B}$ background fraction fluctuation . . . . .	154
6.13	Magnitude, fit fraction and phase pulls in toy MC tests using the nominal fit results . . . . .	156
6.14	Fit fraction distribution means and widths from toy MC samples using the nominal fit results . . . . .	158
6.15	Phase distribution means from toy MC samples using the nominal fit results . . . . .	159
6.16	Percentage systematic errors on the fit fractions of the nominal six component model . . . . .	160
6.17	Absolute systematic errors on the phases of the nominal six component model . . . . .	161
6.18	Results of fits to $B^-$ and $B^+$ data with different lineshape models . .	163

6.19	Final results of fits with statistical, systematic and model dependent errors, to $B^-$ and $B^+$ data with 6 component model. . . . .	164
6.20	Upper limits for the $\chi_{c0}$ and non-resonant components . . . . .	165
6.21	Upper limits for the components used in the addition tests . . . . .	165
6.22	Efficiency correction factors . . . . .	167
7.1	Final branching fraction results with statistical and systematic errors.	171
7.2	Final upper limits . . . . .	172

# List of Figures

1.1	Unitarity Triangle . . . . .	7
1.2	$B^0 - \bar{B}^0$ mixing . . . . .	10
1.3	The $(\bar{\rho}, \bar{\eta})$ plane . . . . .	13
1.4	Decay diagrams for $B^- \rightarrow \rho^0(770)K^-$ . . . . .	17
1.5	Simulated Dalitz plots for the $B^\pm \rightarrow K^\pm \pi^\pm \pi^\mp$ decay . . . . .	24
2.1	The SLAC linac and PEP-II storage rings . . . . .	27
2.2	The PEP-II interaction region . . . . .	28
2.3	The <i>BABAR</i> detector . . . . .	30
2.4	The SVT detector: end view . . . . .	32
2.5	The SVT detector: longitudinal view . . . . .	32
2.6	The DCH detector: longitudinal view . . . . .	34
2.7	The DCH detector: first four superlayers . . . . .	35
2.8	The DIRC detector . . . . .	37
2.9	The EMC detector: longitudinal view . . . . .	39

2.10	The energy resolution of the EMC . . . . .	40
2.11	The IFR detector . . . . .	42
2.12	The IFR detector: Cross section of an RPC . . . . .	42
2.13	Schematic diagram of the data acquisition . . . . .	45
3.1	$\Delta E$ - $m_{\text{ES}}$ plane, showing signal strip, sideband and signal box. . . . .	51
3.2	$ \cos \theta_T $ distributions for non-resonant $B^\pm \rightarrow K^\pm \pi^\pm \pi^\mp$ MC events and off-resonance events . . . . .	53
3.3	$\mathcal{F}$ distributions for non-resonant $B^\pm \rightarrow K^\pm \pi^\pm \pi^\mp$ MC events and off-resonance events. . . . .	54
3.4	Track reconstruction efficiency . . . . .	56
3.5	DCH $dE/dx$ distributions for data . . . . .	58
4.1	Simulated Dalitz plot for $B^+ \rightarrow K^+ \pi^+ \pi^-$ . . . . .	70
4.2	$B\bar{B}$ background invariant mass squared distributions for $B^-$ and $B^+$ . . . . .	79
4.3	$B\bar{B}$ background histograms . . . . .	80
4.4	Invariant mass distributions for on-resonance events in different sideband $m_{\text{ES}}$ regions . . . . .	82
4.5	Results of fit to on-resonance sideband data . . . . .	84
4.6	$q\bar{q}$ background invariant mass squared distributions for off-resonance and on-resonance sideband events . . . . .	85
4.7	$q\bar{q}$ background invariant mass squared distributions for $B^-$ and $B^+$ . . . . .	86

4.8	$q\bar{q}$ background Dalitz-plot distribution . . . . .	87
4.9	The $m_{\text{ES}}$ fit to $B^-$ data events . . . . .	89
4.10	The $m_{\text{ES}}$ fit to $B^+$ data events . . . . .	89
4.11	Reconstruction efficiency Dalitz plot histograms . . . . .	92
4.12	Efficiency variation across the Dalitz plot . . . . .	92
4.13	SCF variation across the Dalitz plot . . . . .	94
5.1	Negative log-likelihood distributions for the toy MC experiment . . .	97
5.2	Negative log-likelihood distributions for different toy MC samples. . .	98
5.3	Negative log-likelihood distributions for the toy MC experiment using different initial step sizes . . . . .	99
5.4	Negative log-likelihood distributions for the toy MC experiment using different <code>Minuit</code> strategies . . . . .	100
5.5	Magnitude pull distributions for the 500 toy MC samples . . . . .	101
5.6	Phase pull distributions for the 500 toy MC samples . . . . .	101
5.7	Evolution of the GA for the $\rho^0(770)$ component . . . . .	113
5.8	Negative log-likelihood distributions for different toy MC samples fit- ted with the GA. . . . .	115
6.1	Data Dalitz plots . . . . .	119
6.2	Invariant mass projections for the $B^-$ data . . . . .	120
6.3	Invariant mass projections for the $B^+$ data . . . . .	121

6.4	Background subtracted data Dalitz plots . . . . .	122
6.5	Background subtracted invariant mass projections for data . . . . .	122
6.6	Background subtracted invariant mass projections for data with a 2 GeV/ $c^2$ cut on the other mass pair applied . . . . .	123
6.7	The Flatté lineshape for the $f_0(980)$ resonance with different values for the parameters $g_\pi$ and $g_K$ . . . . .	124
6.8	The Flatté lineshape for the $f_0(980)$ resonance with different values for the mass . . . . .	125
6.9	Invariant mass projection for the $B^-$ data in the $f_0(980)$ region . . .	126
6.10	Negative log-likelihood results for fits using different Flatté lineshapes	127
6.11	Negative log-likelihood results for fits using different values for the $f_0(980)$ mass . . . . .	128
6.12	Invariant mass projections for the $B^-$ and $B^+$ data in the $f_0(980)$ region with an improved Flatté lineshape . . . . .	129
6.13	Invariant mass projection for the $B^-$ data in the $K_0^{*0}(1430)$ region . .	130
6.14	Invariant mass projection for the $B^-$ and $B^+$ data in the $K_0^{*0}(1430)$ region with an improved LASS lineshape . . . . .	132
6.15	Invariant mass projections for the data and fit results . . . . .	135
6.16	Invariant mass projections for the data and fit results with a 2 GeV/ $c^2$ cut on the other mass pair applied . . . . .	136
6.17	Signal data and fit results in the 1.2 - 1.8 GeV/ $c^2$ region of the $m_{\pi\pi}$ spectrum for $B^-$ . . . . .	144

6.18	Signal data and fit results in the 1.2 - 1.8 GeV/ $c^2$ region of the $m_{\pi\pi}$ spectrum for $B^+$ . . . . .	145
6.19	Invariant mass projections for the data and fit results using a seven component model . . . . .	146
6.20	Fit fraction distributions for the 500 $B^-$ toy MC samples . . . . .	157
6.21	Fit fraction distributions for the 500 $B^+$ toy MC samples . . . . .	157
6.22	Average efficiency distributions for the 500 toy MC samples . . . . .	168
A.1	Evolution of the GA for the $K_0^{*0}(1430)$ component . . . . .	174
A.2	Evolution of the GA for the $f_0(980)$ component . . . . .	175
A.3	Evolution of the GA for the $\chi_{c0}$ component . . . . .	176
A.4	Evolution of the GA for the NR component . . . . .	177
B.1	Magnitude pull distributions for the 500 $B^-$ toy MC samples . . . . .	178
B.2	Fit fraction pull distributions for the 500 $B^-$ toy MC samples . . . . .	179
B.3	Phase pull distributions for the 500 $B^-$ toy MC samples . . . . .	179
B.4	Magnitude pull distributions for the 500 $B^+$ toy MC samples . . . . .	180
B.5	Fit fraction pull distributions for the 500 $B^+$ toy MC samples . . . . .	180
B.6	Phase pull distributions for the 500 $B^+$ toy MC samples . . . . .	181

# Introduction

Natural curiosity leads to a wish to explain the universe that surrounds us and its origin. The Big Bang theory has been widely accepted as a description of the birth of the universe. The theory tells us that initially the universe consisted solely of energy which can be transformed into pairs of matter and antimatter particles. However this cannot be a complete description of events as the universe is known to consist of matter, which leads to the question “*what happened to the anti-matter?*”. Antimatter can be destroyed by annihilation, but this process also requires the mutual destruction of matter. The logical explanation for this puzzle is that there must be some inherent asymmetry in the physical universe that treats matter differently from antimatter.

The study of physics has led to the discovery of a wide range of particles. The Standard Model (SM) of particle physics provides an order and a framework for describing these particles, and is successful at describing all current measurements. The SM is not completely satisfactory however, and one of its failings is that it has yet to provide an explanation for the matter-antimatter asymmetry observed in the universe. Violation of the combined charge-conjugation parity ( $CP$ ) transformation symmetry is one of a set of conditions that could account for the matter-antimatter asymmetry.  $CP$  violation can be incorporated into the Standard Model via the quark mixing matrix. It is unclear however whether this source of  $CP$  violation could create an effect that is large enough to explain the universe and it is therefore necessary to study this topic in great detail. If  $CP$  violation is found to be small in

the SM then this leads to the search for new physics beyond the SM.

$CP$  violation was first studied in the 1960's using kaon decays. After the discovery of the third quark generation, the  $B$ -meson sector offered unexplored potential for studying  $CP$  violation. The PEP-II  $B$  Factory and  $BABAR$  detector were constructed in the 1990's, with the large number of  $B\bar{B}$  pairs produced and the excellent efficiency of the  $BABAR$  detector combining to provide the right conditions to make precision measurements of  $CP$  asymmetries using decays of  $B$  mesons.

# Chapter 1

## *CP* Violation in the *B*-meson system

### 1.1 Introduction

The action of the charge conjugation operator ( $C$ ) is to change the sign of all the quantum numbers of a particle, and hence change the particle into its antiparticle without modifying its momentum or spin. The parity transformation ( $P$ ) changes the space vector  $\vec{r}$  into  $-\vec{r}$  and therefore reverses the sign of the momentum of a particle while leaving its spin unchanged. The strong and electromagnetic forces are invariant under the separate  $C$  and  $P$  transformations whereas the weak interaction is not, as was discovered in 1957 in studies of  $\beta$  decay [1]. It was further discovered in 1964 in studies of  $K_L^0$  decays to pions [2] that the weak interaction is not invariant under the combined  $CP$  transformation.

$CP$  violation fits naturally into the Standard Model (SM) with three generations of quarks and has been investigated in both the kaon and more recently the  $B$ -meson sectors. In 2001 *BABAR* observed  $CP$  violation in  $B$ -meson decays to final states such as  $J/\psi K_S^0$  [3] and these results were confirmed by the Belle experiment [4].

In this chapter a description of how  $CP$  violation fits into the SM is given, followed by a discussion of the CKM quark mixing matrix and the Unitarity Triangle. A description of the three possible types of  $CP$  violation is then given. The  $B^\pm \rightarrow K^\pm \pi^\pm \pi^\mp$  mode is introduced with a description of the possible processes contributing to this decay. This is followed by a brief introduction to the theoretical techniques used to make predictions for this decay mode and a discussion of previous experimental measurements. The chapter concludes by describing the Dalitz-plot technique.

## 1.2 $CP$ Violation in the Standard Model and the CKM Matrix

The SM Lagrangian is a Lorentz scalar which depends on terms that are bilinear in fermion fields multiplied by coefficients that represent coupling constants or masses. Under a  $CP$  transformation, the field terms transform into their Hermitian conjugates whereas the coefficients are unchanged. A non  $CP$ -symmetric Lagrangian can result if the coefficients in front of  $CP$ -related terms are complex, in which case  $CP$ -violating effects may be visible as rate differences between pairs of  $CP$ -conjugate decays in physical processes that depend on these terms. If these complex coefficients can be made real through a phase redefinition then no  $CP$  violation will be observed.

The weak charged current Lagrangian can be written as:

$$\mathcal{L} = -\frac{g}{\sqrt{2}} \left( \bar{u}'_L, \bar{c}'_L, \bar{t}'_L \right) \gamma^\mu \begin{pmatrix} d'_L \\ s'_L \\ b'_L \end{pmatrix} W_\mu^\dagger + h.c. \quad (1.1)$$

where  $q'_L$  are the left handed projections of the weak eigenstates of the quark fields,  $g$  is the weak coupling constant,  $\gamma^\mu$  are the Dirac matrices,  $W_\mu$  are the weak charged

bosons and  $h.c.$  denotes the Hermitian conjugate. The Lagrangian shown in Equation 1.1 can be rewritten as:

$$\mathcal{L} = -\frac{g}{\sqrt{2}} (\bar{u}_L, \bar{c}_L, \bar{t}_L) \gamma^\mu V_{CKM} \begin{pmatrix} d_L \\ s_L \\ b_L \end{pmatrix} W_\mu^\dagger + h.c. \quad (1.2)$$

where  $q_L$  are now the quark mass eigenstates and  $V_{CKM}$  is the mixing matrix introduced to relate the weak eigenstates to the mass eigenstates:

$$V_{CKM} = \begin{pmatrix} V_{ud} & V_{us} & V_{ub} \\ V_{cd} & V_{cs} & V_{cb} \\ V_{td} & V_{ts} & V_{tb} \end{pmatrix} \quad (1.3)$$

The Cabibbo matrix [5] describes the mixing in the SM with only two quark generations present. This matrix has only one parameter, the Cabibbo mixing angle  $\theta_{cabibbo}$ , which is real so there is no possibility of  $CP$  violation. Kobayashi and Maskawa [6] suggested that a third quark generation may exist as the resulting quark mixing matrix could then accommodate  $CP$  violation. The existence of this third generation of quarks was confirmed in 1977 with the discovery of the  $\Upsilon$  resonance, a bound  $b\bar{b}$  state [7]. With three generations of quarks the mixing matrix  $V_{CKM}$  (known as the CKM matrix) can contain three angles and six phases. It is possible to remove five of these phases with suitable redefinitions, but one phase remains. It is this phase which is responsible for  $CP$ -violating effects in the SM.

The charged current Lagrangian shown in Equation 1.2 can be expanded to give terms such as:

$$\mathcal{L} = -\frac{g}{2\sqrt{2}} \left[ \bar{u}_i \gamma^\mu W_\mu^+ (1 - \gamma_5) V_{ij} d_j + \bar{d}_j \gamma^\mu W_\mu^- (1 - \gamma_5) V_{ij}^* u_i \right] \quad (1.4)$$

where  $\frac{1}{2}(1 - \gamma_5)$  is the left-handed projection operator. The  $CP$  operator transforms the field terms in Equation 1.4 as:

$$\bar{u}_i \gamma^\mu W_\mu^+ (1 - \gamma_5) d_j \rightarrow \bar{d}_j \gamma^\mu W_\mu^- (1 - \gamma_5) u_i . \quad (1.5)$$

Therefore the field terms in Equation 1.4 would be interchanged but the  $V_{CKM}$  couplings  $V_{ij}$  and  $V_{ij}^*$  would remain the same. The complex element present in the CKM matrix allows these couplings  $V_{ij}$  and  $V_{ij}^*$  to be different and hence  $CP$  violation is possible.

The standard Particle Data Group (PDG) [8] parameterisation of the CKM matrix is:

$$V_{CKM} = \begin{pmatrix} c_{12}c_{13} & s_{12}c_{13} & s_{13}e^{-i\delta} \\ -s_{12}c_{23} - c_{12}s_{23}s_{13}e^{+i\delta} & c_{12}c_{23} - s_{12}s_{23}s_{13}e^{+i\delta} & s_{23}c_{13} \\ s_{12}s_{23} - c_{12}c_{23}s_{13}e^{+i\delta} & -c_{12}s_{23} - s_{12}c_{23}s_{13}e^{+i\delta} & c_{23}c_{13} \end{pmatrix} \quad (1.6)$$

where  $\theta_{ij}$  is the mixing angle between the  $i$ th and  $j$ th generations,  $c_{ij} = \cos\theta_{ij}$ ,  $s_{ij} = \sin\theta_{ij}$  and  $\delta$  represents the phase. Experimental results indicate a hierarchy in the magnitudes of the matrix elements  $|V_{ii}|$  ( $|V_{ud}|, |V_{cs}|, |V_{tb}|$ )  $\approx 1$ ,  $|V_{12}| = |V_{21}|$  ( $|V_{us}|, |V_{cd}|$ )  $\approx \lambda$ ,  $|V_{23}| = |V_{32}|$  ( $|V_{cb}|, |V_{ts}|$ )  $\approx \lambda^2$  and  $|V_{13}| = |V_{31}|$  ( $|V_{ub}|, |V_{td}|$ )  $\approx \lambda^3$  where  $\lambda \approx 0.22$ . The Wolfenstein parameterisation [9] of the CKM matrix expresses the elements as a power series in  $\lambda$ :

$$V_{CKM} = \begin{pmatrix} 1 - \lambda^2/2 & \lambda & A\lambda^3(\rho - i\eta) \\ -\lambda & 1 - \lambda^2/2 & A\lambda^2 \\ A\lambda^3(1 - \rho - i\eta) & -A\lambda^2 & 1 \end{pmatrix} + \mathcal{O}(\lambda^4) \quad (1.7)$$

where  $A$  and  $\rho$  are real numbers and the complex component is described by  $\eta$ .

### 1.3 The Unitarity Triangle

The unitarity of the CKM matrix leads to nine orthonormal relations between its elements. The most interesting of these relations for current experimental physics involves the  $B$ -meson sector:

$$V_{ud}V_{ub}^* + V_{cd}V_{cb}^* + V_{td}V_{tb}^* = 0 \quad (1.8)$$

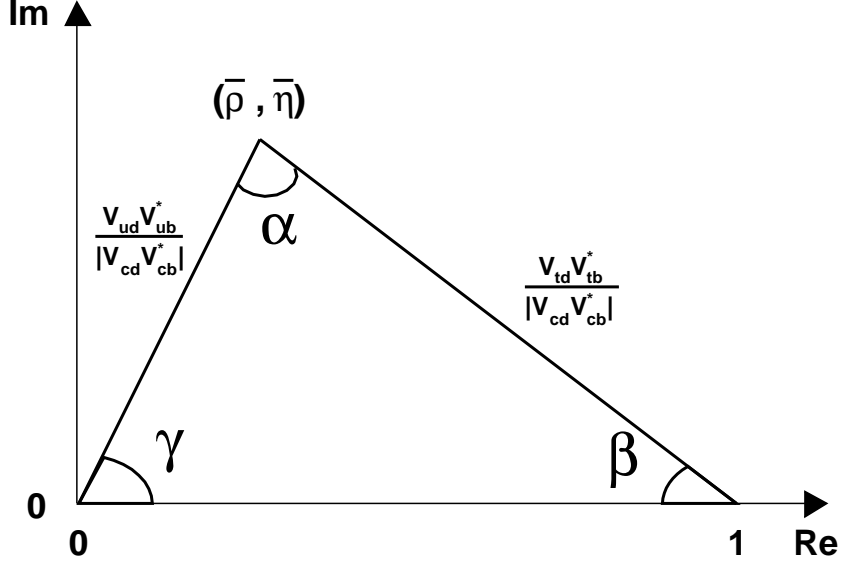


Figure 1.1: Unitarity Triangle

Each of the three terms in Equation 1.8 is of order  $\lambda^3$ . In a complex plane this relation corresponds to a triangle which has sides of approximately the same length. This triangle is known as the Unitarity Triangle and can be seen in Figure 1.1.  $V_{cd}V_{cb}^*$  is chosen to be real and the sides of the Unitarity Triangle are divided by  $|V_{cd}V_{cb}^*|$  to give one with unit length and the apex of the triangle at co-ordinates  $(\bar{\rho}, \bar{\eta})$  where  $\bar{\rho} = (1 - \frac{\lambda^2}{2})\rho$  and  $\bar{\eta} = (1 - \frac{\lambda^2}{2})\eta$ .

The angles of the triangle  $\alpha$ ,  $\beta$  and  $\gamma$  are given by:

$$\alpha = \arg \left[ -\frac{V_{td}V_{tb}^*}{V_{ud}V_{ub}^*} \right], \beta = \arg \left[ -\frac{V_{cd}V_{cb}^*}{V_{td}V_{tb}^*} \right], \gamma = \arg \left[ -\frac{V_{ud}V_{ub}^*}{V_{cd}V_{cb}^*} \right] \quad (1.9)$$

## 1.4 Different Types of $CP$ Violation

There are three possible types of  $CP$  violation in  $B$  meson decays. They are:

- ***CP* violation in decay.** This is also commonly known as direct *CP* violation. It is the only form of *CP* violation observable in charged *B*-meson decays but can also occur in neutral *B*-meson decays. In this case the amplitudes for a decay  $B \rightarrow f$  and its *CP* conjugate process  $\bar{B} \rightarrow \bar{f}$  have different magnitudes.
- ***CP* violation in mixing.** This is also known as indirect *CP* violation and can only occur in neutral *B*-meson decays. This asymmetry is solely due to  $B^0 - \bar{B}^0$  mixing. It reveals that  $B^0 \rightarrow \bar{B}^0 \neq \bar{B}^0 \rightarrow B^0$
- ***CP* violation in the interference between decays with and without mixing.** This process only occurs for neutral *B*-meson decays to final states that are accessible to both  $B^0$  and  $\bar{B}^0$ .

### 1.4.1 *CP* Violation in Decay

Consider a decay process  $B \rightarrow f$  which has an amplitude  $A_f$  and its *CP* conjugate process  $\bar{B} \rightarrow \bar{f}$  which has an amplitude  $\bar{A}_{\bar{f}}$ . *CP* violation in decay occurs if:

$$\left| \frac{\bar{A}_{\bar{f}}}{A_f} \right| \neq 1 \quad (1.10)$$

Each contribution to the decay amplitude can be written in terms of a magnitude, a strong phase and a weak phase. Weak phases are so called because they occur in the CKM matrix which forms part of the electroweak sector of the SM. These phases appear as complex parameters in the Lagrangian and hence have different signs for the amplitude  $B \rightarrow f$  and its *CP* conjugate  $\bar{B} \rightarrow \bar{f}$ . Strong phases are so called because the dominant rescattering effect is due to the strong interaction. These phases can appear in scattering or decay amplitudes even when the Lagrangian is real and hence these phases have the same sign for the amplitude  $A_f$  and its *CP* conjugate  $\bar{A}_{\bar{f}}$ .

If the amplitude  $A_f$  has a single contribution then it can be written as:

$$A_f = |A| e^{i\phi_W} e^{i\delta_S} \quad (1.11)$$

where  $\phi_W$  is the weak phase and  $\delta_S$  is the strong phase. The  $CP$  conjugate amplitude is:

$$\bar{A}_{\bar{f}} = |A| e^{-i\phi_W} e^{i\delta_S} \quad (1.12)$$

In this case  $|\bar{A}_{\bar{f}}/A_f| = 1$ . This illustrates that  $CP$  violation cannot be seen as a difference in rates between  $CP$  conjugate processes when there is a single decay amplitude.

Now consider the case when there are two amplitudes contributing to  $A_f$  and  $\bar{A}_{\bar{f}}$

$$A_f = |A_1| e^{i\phi_1} e^{i\delta_1} + |A_2| e^{i\phi_2} e^{i\delta_2} \quad (1.13)$$

$$\bar{A}_{\bar{f}} = |A_1| e^{-i\phi_1} e^{i\delta_1} + |A_2| e^{-i\phi_2} e^{i\delta_2} \quad (1.14)$$

Defining  $\phi = \phi_1 - \phi_2$  and  $\delta = \delta_1 - \delta_2$  gives:

$$\Gamma(B \rightarrow f) = |A_1|^2 + |A_2|^2 + 2|A_1||A_2| \cos(\phi + \delta) \quad (1.15)$$

$$\Gamma(\bar{B} \rightarrow \bar{f}) = |A_1|^2 + |A_2|^2 + 2|A_1||A_2| \cos(\phi - \delta) \quad (1.16)$$

So considering the rate difference  $\Gamma(B \rightarrow f) - \Gamma(\bar{B} \rightarrow \bar{f})$  gives the result:

$$\Gamma(B \rightarrow f) - \Gamma(\bar{B} \rightarrow \bar{f}) = -4|A_1||A_2| \sin \phi \sin \delta \quad (1.17)$$

$$= -4|A_1||A_2| \sin(\phi_1 - \phi_2) \sin(\delta_1 - \delta_2) \quad (1.18)$$

This shows that  $CP$  violation can be observed as a difference in rates between  $CP$  conjugate processes when there are two contributing decay amplitudes but only if these amplitudes have *different weak and different strong phases*.

## 1.4.2 $CP$ Violation in Mixing

$B^0$  and  $\bar{B}^0$  mixing proceeds via a second order weak interaction as shown in Figure 1.2.

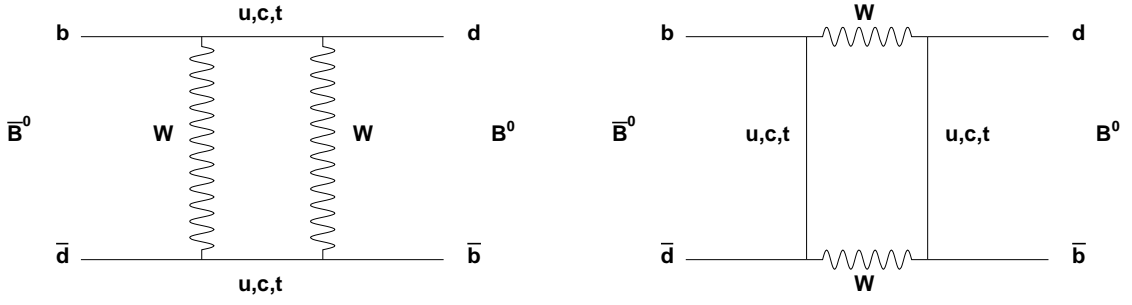


Figure 1.2:  $B^0 - \bar{B}^0$  mixing

This type of  $CP$  violation occurs when the two neutral mass eigenstates of the  $B$  meson cannot be chosen to be  $CP$  eigenstates. The flavour eigenstates of definite quark content are  $B^0 = \bar{b}d$  and  $\bar{B}^0 = \bar{d}b$ . The light  $B_L$  and heavy  $B_H$  mass eigenstates are linear combinations of the flavour eigenstates:

$$|B_L\rangle = p|B^0\rangle + q|\bar{B}^0\rangle \quad (1.19)$$

$$|B_H\rangle = p|B^0\rangle - q|\bar{B}^0\rangle \quad (1.20)$$

where  $p$  and  $q$  are complex coefficients. When  $CP$  is conserved the mass eigenstates must be  $CP$  eigenstates and for  $CP$  violation in mixing to occur it is required that:

$$\left| \frac{q}{p} \right| \neq 1 \quad (1.21)$$

### 1.4.3 $CP$ Violation in the Interference Between Decay and Mixing

Consider neutral  $B$ -meson decays to a  $CP$  eigenstate  $f_{CP}$  that is accessible to both  $B^0$  and  $\bar{B}^0$ . A phase independent quantity is:

$$\lambda \equiv \frac{q}{p} \frac{\bar{A}_{f_{CP}}}{A_{f_{CP}}} = \eta_{f_{CP}} \frac{q}{p} \frac{\bar{A}_{f_{CP}}}{A_{f_{CP}}} \quad (1.22)$$

where  $\eta_{f_{CP}}$  is the  $CP$  eigenvalue of  $f_{CP}$  which has possible values of  $\pm 1$ . If  $CP$  violation occurs then:

$$\lambda \neq \pm 1 \quad (1.23)$$

If  $CP$  is conserved then  $|q/p| = 1$  (no  $CP$  violation in mixing),  $|\bar{A}_{f_{CP}}/A_{f_{CP}}| = 1$  (no  $CP$  violation in decay) and there must also be no relative phase between  $q/p$  and  $\bar{A}_{f_{CP}}/A_{f_{CP}}$ . It is this possibility of a relative phase between  $q/p$  and  $\bar{A}_{f_{CP}}/A_{f_{CP}}$  that leads to a third type of  $CP$  violation in the absence of the other two types ( $CP$  violation in mixing and decay). In this case:

$$|\lambda| = 1, \quad \text{Im } \lambda \neq 0 \quad (1.24)$$

The two necessary contributions to the decay amplitude come from the direct decay  $B^0 \rightarrow f_{CP}$  and the mixing of  $B^0 \rightarrow \bar{B}^0$  followed by the decay  $\bar{B}^0 \rightarrow f_{CP}$ . Consider the time dependent rate asymmetry [10]:

$$a_{f_{CP}}(t) = \frac{\Gamma(B^0 \rightarrow f_{CP}) - \Gamma(\bar{B}^0 \rightarrow f_{CP})}{\Gamma(B^0 \rightarrow f_{CP}) + \Gamma(\bar{B}^0 \rightarrow f_{CP})} \quad (1.25)$$

$$= \frac{(1 - |\lambda|^2) \cos(\Delta m_B t) - 2 \text{Im} \lambda \sin(\Delta m_B t)}{1 + |\lambda|^2} \quad (1.26)$$

where  $\Delta m_B$  is the difference in mass of the neutral  $B$ -meson mass eigenstates. This asymmetry will be non-vanishing if any of the three types of  $CP$  violation are present. However if the only source of  $CP$  violation is from the interference between decay and mixing, then  $|\lambda| = 1$  and the asymmetry simplifies to become:

$$a_{f_{CP}}(t) = -\text{Im } \lambda \sin(\Delta m_B t) \quad (1.27)$$

## 1.5 Experimental Measurements of $CP$ Violation

### 1.5.1 Constraints on the CKM Matrix

There are many constraints on the CKM description of  $CP$  violation both from direct measurements of the individual CKM elements and relations from indirect sources.

All measurements and diagrams in this Section are taken from [11, 12]. The apex of the Unitarity Triangle in the  $(\bar{\rho}, \bar{\eta})$  plane can be constrained by  $\epsilon_K$  which is the measure of  $CP$  violation in the  $K$  sector and also by the  $\Delta m$  values measured in  $B_d$  mixing and  $B_s$  mixing. The latest measurements for these quantities are:

- $|\epsilon_K| = (2.282 \pm 0.017) \times 10^{-3}$ .
- $\Delta m_d = (0.502 \pm 0.006) \text{ ps}^{-1}$ .
- A 95% confidence level (CL) lower limit is calculated for  $\Delta m_s$  and is found to be  $14.4 \text{ ps}^{-1}$ .

This is illustrated in Figure 1.3. Further constraints are provided by measurements of the CKM matrix elements  $|V_{ud}|$ ,  $|V_{ub}|$ ,  $|V_{us}|$  and  $|V_{cb}|$ :

- $|V_{ud}|$  can be measured in a variety of different  $\beta$  decays. The most precise measurement comes from superallowed nuclear  $\beta$ -decays which gives a value  $|V_{ud}| = 0.9740 \pm 0.0001 \pm 0.0008$ .
- $|V_{ub}|$  can be measured in exclusive and inclusive  $b \rightarrow ul^{-}\bar{\nu}$  decays. The average of these measurements yields a value  $|V_{ub}| = (3.90 \pm 0.08 \pm 0.68) \times 10^{-3}$ .
- $|V_{us}|$  can be measured in kaon semi-leptonic decays. The average value is found to be  $|V_{us}| = 0.2228 \pm 0.0039 \pm 0.0018$ .
- $|V_{cb}|$  can be measured in exclusive and inclusive  $b \rightarrow cl^{-}\bar{\nu}$  decays. The results from the inclusive measurements yield  $|V_{cb}| = (42.0 \pm 0.6 \pm 0.8) \times 10^{-3}$ .

## 1.5.2 Angles of the Unitarity Triangle

The angle  $\beta$  was the first of the Unitarity Triangle angles to be measured experimentally. In 2001 both the *BABAR* and Belle collaborations measured  $\sin 2\beta$  from

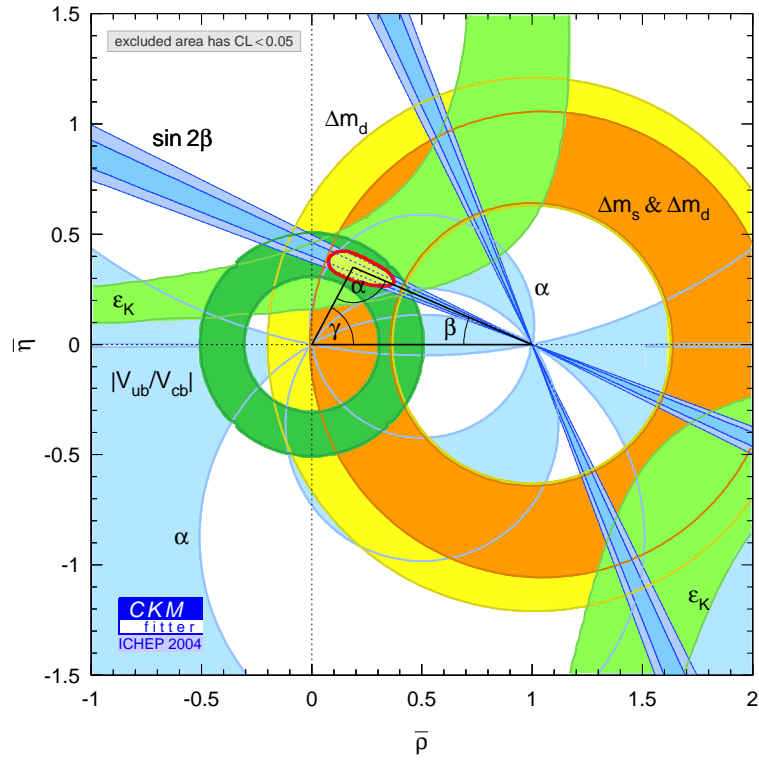


Figure 1.3: The  $(\bar{\rho}, \bar{\eta})$  plane showing the allowed region for the apex of the Unitarity Triangle.

time dependent asymmetries in neutral  $B$  decays to final states containing charmium mesons, such as  $J/\psi K_s^0$  [3, 4]. These decays are chosen as their direct  $CP$  asymmetries are expected to be negligible. The time dependent asymmetry is then related to the imaginary part of  $\lambda$  as shown in Equation 1.27 and for these decays  $Im\lambda$  is equal to  $\sin 2\beta$ . The latest results for  $\sin 2\beta$ , reported in summer 2004 using significantly larger datasets, are  $\sin 2\beta = 0.722 \pm 0.040 \pm 0.023$  [13] from the *BABAR* collaboration and  $\sin 2\beta = 0.728 \pm 0.056 \pm 0.023$  [14] from the Belle collaboration.

There has been some progress made in measuring the angle  $\alpha$  [15]. Any decay with a  $b \rightarrow u\bar{u}d$  quark transition is a possible source of information on  $\alpha$ . However these modes suffer from theoretical uncertainties arising from possible penguin contributions to the decay amplitude. A penguin diagram has an internal quark loop that radiates a gluon, photon or  $Z^0$  boson. Typically the presence of additional vertices in the penguin diagram results in their contribution being smaller than the standard tree diagram. However the CKM matrix terms involved in the decays can enhance or further suppress these penguin contributions. If the penguin contributions to these decays are significant then the imaginary part of  $\lambda$  cannot be simply related to  $\sin 2\alpha$  and direct  $CP$  violation may be present. These problems mean that no useful  $\alpha$  measurements can currently be extracted from the  $B \rightarrow \pi\pi$  and  $B \rightarrow \rho\pi$  modes, although these are still of interest for  $CP$  violation measurements. Greater success has been found in the  $B \rightarrow \rho^+\rho^-$  decay where a powerful constraint on  $\alpha$  is obtained. Choosing the solution closest to the standard CKM fit [12], *BABAR* quotes  $\alpha = (96 \pm 10_{stat} \pm 4_{syst} \pm 13_{theory})^\circ$ .

The angle  $\gamma$  is the most difficult to measure experimentally. Work is currently in progress using the modes  $B^+ \rightarrow D_{CP}^0 K^+$  where the  $D$  meson decays to a  $CP$  eigenstate and  $B^- \rightarrow [K^+\pi^-]_D K^-$  where the  $K$  and  $\pi$  are from the decay of a neutral  $D$  meson. The most promising mode in the study of  $\gamma$  is neutral  $B$ -meson decay to final states  $D^{*\mp}\pi^\pm$  [16]. This yields the constraint  $|\sin(2\beta + \gamma)| > 0.58$  at 90% confidence level.

### 1.5.3 Direct $CP$ Violation in $B$ Meson Decay

The first measurement<sup>1</sup> of direct  $CP$  violation in  $B$  decays was presented by the *BABAR* collaboration in 2004 [17]. An asymmetry is found in yields for  $B^0 \rightarrow K^+\pi^-$  and  $\bar{B}^0 \rightarrow K^-\pi^+$  decays, where the flavour of the neutral  $B$  meson can be determined from the charge of the  $K$  meson. The measured asymmetry is  $\mathcal{A}_{K\pi} = -0.133 \pm 0.030 \pm 0.009$ . Further evidence for this asymmetry was subsequently reported by the Belle collaboration [18] who find  $\mathcal{A}_{K\pi} = -0.101 \pm 0.025 \pm 0.005$ . The possibility of the non-zero value of  $\mathcal{A}_{K\pi}$  arising purely from  $CP$  violation in mixing is discounted as this effect is found experimentally to be small [19].

## 1.6 $B^\pm \rightarrow K^\pm \pi^\pm \pi^\mp$ Decay

### 1.6.1 Charmless Hadronic Three-Body $B$ Decays

Charmless hadronic  $B$  decays are suppressed in the Standard Model due to the  $b \rightarrow u$  quark transition. As such they have low branching fractions of order  $10^{-5}$  -  $10^{-7}$ , and many of these decays have yet to be observed experimentally. The tree diagrams of charmless decays may be of similar magnitude to the penguin loop diagrams. This gives hope for large direct  $CP$  asymmetries in these decays and also a chance to study these penguin amplitudes. In the SM, the interference between  $B$  mixing,  $K$  mixing and  $b \rightarrow s\bar{s}s$  or  $b \rightarrow s\bar{d}d$  penguin processes yields the angle  $\beta$ . Penguin dominated channels such as  $B^0 \rightarrow f_0(980)K_s^0$  and  $B^0 \rightarrow \phi K^0$  [20] can be used to further test the SM as new physics may enter in the penguin loop. A large departure of  $\sin 2\beta$  measured in these charmless channels compared to that measured in the charmonium decays (which are  $b \rightarrow c\bar{c}s$  tree dominated processes) would indicate the contribution of new physics such as supersymmetry (SUSY).

---

<sup>1</sup>In all measurements the first error is statistical and the second error is systematic unless otherwise stated

## 1.6.2 Intermediate Resonances

The  $B$ -meson decay to the three-body final state  $K^\pm\pi^\pm\pi^\mp$  can proceed via intermediate resonances formed from two of the particles. The  $\pi^+$  and  $\pi^-$  can combine to form resonances such as  $\rho^0(770)$ ,  $f_0(980)$ ,  $\rho^0(1450)$ ,  $f_2(1270)$ ,  $f_0(1370)$  and other higher excitations. The  $K$  and  $\pi$  can combine to form resonances such as  $K^{*0}(892)$ ,  $K_0^{*0}(1430)$ ,  $K_2^{*0}(1430)$  and  $K^{*0}(1680)$ . These two-body states can interfere with each other and with the non-resonant three-body decay.

## 1.6.3 Decay Diagrams

There are many amplitudes that can contribute to the overall decay amplitude. For  $B^- \rightarrow \rho^0(770)K^-$  there are eight processes which are thought to contribute to this decay. They are illustrated in Figure 1.4.

Diagram (a) shows the standard tree diagram with Diagram (b) showing the corresponding colour suppressed tree diagram (the quarks emitted by the gauge boson must be of the correct colour to join with the quarks from the  $B$  meson to form a colour neutral hadron which has the effect of suppressing the amplitude by a factor of three). Diagrams (c) and (d) are gluonic penguin diagrams involving a loop and the presence of two gauge bosons. There are three possibilities for the flavour of the quark in the loop; u, c or t. Usually the t quark loop is taken to be the dominant process due to the large value of  $|V_{tb}|$ . Diagrams (e) and (f) are electroweak penguin diagrams involving a  $Z^0$  boson or photon instead of a gluon. Electroweak penguins have smaller amplitudes than the gluonic penguins due to the relative sizes of the electroweak and QCD couplings. Diagrams (g) and (h) show annihilation diagrams which are suppressed compared to the tree diagram.

The presence of both tree and penguin amplitudes in decays where a resonance is formed from the  $\pi^+$  and  $\pi^-$  such as  $B^- \rightarrow \rho^0(770)K^-$  fulfils the requirements for a

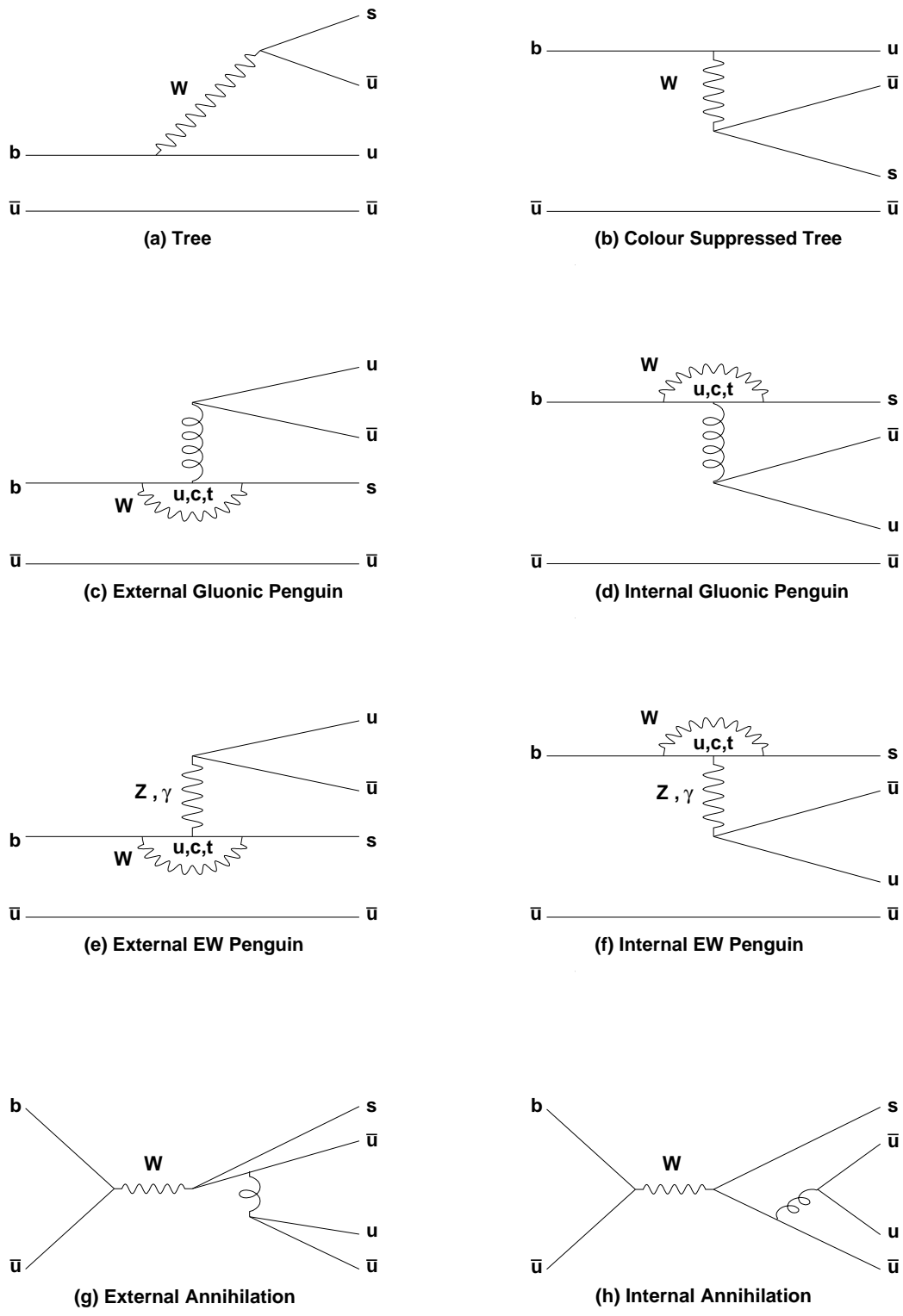


Figure 1.4: Decay diagrams for  $B^- \rightarrow \rho^0(770)K^-$ .

direct  $CP$  asymmetry to be possible in these modes.

Decays where the resonance forms from the  $K$  and  $\pi$ , such as  $B^- \rightarrow \bar{K}^{*0}(892)\pi^-$ , have fewer contributions to the overall amplitude. Only the internal gluonic penguin (d), internal electroweak penguin (f) and internal annihilation (h) diagrams are possible. As the last two of these are expected to be small there is only a single amplitude that has a significant contribution to this decay and as such direct  $CP$  asymmetries in these modes are expected to be small.

### 1.6.4 Theoretical Predictions

An operator product expansion [21] can be used to write the effective Hamiltonian for the  $B$ -meson decay as:

$$\mathcal{H}_{eff} = \frac{G_F}{\sqrt{2}} \sum_{q=u,c} V_q \left\{ C_1(\mu) O_1^q(\mu) + C_2(\mu) O_2^q(\mu) + \sum_{k=3}^{10} C_k(\mu) O_k(\mu) \right\} + h.c. \quad (1.28)$$

where the calculable short distance contributions are in the Wilson coefficients  $C_i(\mu)$  and the long distance parts are in the operators  $O_i(\mu)$ .  $V_q$  are the appropriate CKM matrix elements for a given quark transition and  $G_F$  is the Fermi constant.  $O_{1,2}^q$  are the left handed tree current-current operators arising from  $W$  boson exchange,  $O_{3,4,5,6}$  are QCD penguin operators and  $O_{7,8,9,10}$  are electroweak penguin operators. These operators summarise the effects of interactions below the scale  $\mu$  and the Wilson coefficients absorb the effects above  $\mu$ . This scale is arbitrary and chosen to be  $\mathcal{O}(m_b)$ .

The matrix elements are of the form:

$$\langle h_1 h_2 | O_i | B \rangle \quad (1.29)$$

where  $h_1$  and  $h_2$  are the final state mesons (for  $B^\pm \rightarrow K^\pm \pi^\pm \pi^\mp$  one of these mesons is a resonant state and the decay is  $B \rightarrow PV$  with  $P$  denoting a pseudoscalar particle and  $V$  a vector particle). Provided that the decay meson containing the spectator

quark is not heavy then factorisation can be used to evaluate these matrix elements. Under factorisation the matrix element shown in Equation 1.29 can be written as a product of a form factor and a decay constant as shown in Equation 1.30:

$$\langle h_1 | J_{1i} | B \rangle \times \langle h_2 | J_{2i} | 0 \rangle \quad (1.30)$$

where  $J_{1i}$  and  $J_{2i}$  are currents that can be expressed in terms of known quantities. The decay constants  $\langle h_2 | J_{2i} | 0 \rangle$  can be calculated from leptonic decays and the form factors  $\langle h_1 | J_{1i} | B \rangle$  can be calculated using Lattice QCD. These decay constants and form factors are however scale ( $\mu$ ) independent and so there is now an overall scale dependency contained in the Wilson coefficients  $C_i(\mu)$ . Beneke *et al.* [22, 23] proposed an extension to factorisation based on QCD, known as QCD factorisation (QCDF) which solves this problem of scale dependency. In the limit that  $m_b \gg \Lambda_{QCD}$  the matrix element now becomes:

$$\langle h_1 | J_{1i} | B \rangle \langle h_2 | J_{2i} | 0 \rangle \left[ 1 + \sum r_n \alpha_s^n + \mathcal{O}(\Lambda_{QCD}/m_b) \right] \quad (1.31)$$

Neglecting the radiative corrections in  $\alpha_s$  and the power corrections in  $\Lambda_{QCD}$  recovers the conventional factorisation approach.

The theoretical techniques described here can be used to make predictions for the branching fractions (BFs) of some of the quasi-two-body modes that contribute to the  $B^\pm \rightarrow K^\pm \pi^\pm \pi^\mp$  decay. Theoretical predictions for the  $B^+ \rightarrow \rho^0(770)K^+$  mode<sup>2</sup> can be seen in Table 1.1 and for the  $B^+ \rightarrow K^{*0}(892)\pi^+$  mode in Table 1.2.

### 1.6.5 Previous Experimental Measurements

The CLEO collaboration, using a sample of 9.7 million  $B\bar{B}$  pairs, has placed upper limits on the  $B^+ \rightarrow K^{*0}(892)\pi^+$  and  $B^+ \rightarrow \rho^0(770)K^+$  branching fractions [30]. The BELLE collaboration has presented the first observations of  $B^+ \rightarrow K^{*0}(892)\pi^+$  and  $B^+ \rightarrow f_0(980)K^+$  [31] using a sample of 31.3 million  $B\bar{B}$  pairs. They use a ‘quasi

---

<sup>2</sup>Charge conjugate states are implied throughout this and the following section

Table 1.1: Theoretical Predictions for the  $B^+ \rightarrow \rho^0(770)K^+$  mode

Authors	Model	BF Prediction $\times 10^{-6}$
Aleksan <i>et al.</i> 2003 [24]	QCDF	1.9
Aleksan <i>et al.</i> 2003 [24]	QCDF + Charming Penguins [25]	5.7
Beneke and Neubert 2003 [26]	QCDF	2.6
Cottingham <i>et al.</i> 2003 [28]	QCDF	2.0
Cottingham <i>et al.</i> 2003 [28]	QCDF + Charming Penguins [25]	4.6
Du <i>et al.</i> 2002 [29]	Conventional Factorisation	0.45
Du <i>et al.</i> 2002 [29]	QCDF	0.43
Du <i>et al.</i> 2002 [29]	QCDF + Annihilation	0.53

Table 1.2: Theoretical Predictions for the  $B^+ \rightarrow K^{*0}(892)\pi^+$  mode

Authors	Model	BF Prediction $\times 10^{-6}$
Aleksan <i>et al.</i> 2003 [24]	QCDF	7.9
Aleksan <i>et al.</i> 2003 [24]	QCDF + Charming Penguins [25]	11.1
Beneke and Neubert 2003 [26]	QCDF	3.3
Cottingham <i>et al.</i> 2002 [27]	QCDF	5.0
Cottingham <i>et al.</i> 2003 [28]	QCDF	4.4
Cottingham <i>et al.</i> 2003 [28]	QCDF + Charming Penguins [25]	9.1
Du <i>et al.</i> 2002 [29]	Conventional Factorisation	2.6
Du <i>et al.</i> 2002 [29]	QCDF	3.5
Du <i>et al.</i> 2002 [29]	QCDF + Annihilation	3.8

2-body' approach in which invariant mass selection criteria are applied to treat these decays in isolation from the other contributions to the  $B^+ \rightarrow K^+\pi^+\pi^-$  decay. They

measure  $(19_{-3.9}^{+4.2+2.1+3.5}) \times 10^{-6}$  for  $B^+ \rightarrow K^{*0}(892)\pi^+$  and  $(9.6_{-2.3}^{+2.5+1.5+3.4}) \times 10^{-6}$  for  $B^+ \rightarrow f_0(980)K^+ (f_0(980) \rightarrow \pi^+\pi^-)$  where the first error is statistical, the second error is systematic and the third error is the model dependent error which represents the uncertainty due to possible interference between different intermediate states. They also provide an inclusive BF measurement for  $B^\pm \rightarrow K^\pm\pi^\pm\pi^\mp$  of  $(55.6 \pm 5.8 \pm 7.7) \times 10^{-6}$ . *BABAR* has made an inclusive measurement, using a sample of 88.8 million  $B\bar{B}$  pairs, of  $(59.1 \pm 3.8 \pm 3.2) \times 10^{-6}$  [32, 33]. *BABAR* has also presented a ‘quasi 2-body’ study of the resonant contributions to this mode [34], using a sample of 61.6 million  $B\bar{B}$  pairs, measuring  $(15.5 \pm 1.8_{-4.0}^{+1.5}) \times 10^{-6}$  for  $B^+ \rightarrow K^{*0}(892)\pi^+$ ,  $(9.2 \pm 1.2_{-2.6}^{+2.1}) \times 10^{-6}$  for  $B^+ \rightarrow f_0(980)K^+ (f_0(980) \rightarrow \pi^+\pi^-)$  and placing upper limits on the contributions of the non-resonant and  $\rho^0(770)K$  components. The analysis does not allow for interference between the contributions but accounts for the possibility of interference effects in the systematic error. A first attempt at a Dalitz-plot analysis of the  $B^\pm \rightarrow K^\pm\pi^\pm\pi^\mp$  decay, using a data set of 152 million  $B\bar{B}$  pairs, has been reported by the BELLE collaboration in [35]. A preliminary version of the analysis described in this thesis, based on a smaller data sample of 182 million  $B\bar{B}$  pairs, is documented in [36].

The discrepancy between the theoretical predictions of the  $B^+ \rightarrow K^{*0}(892)\pi^+$  BF and the experimentally measured values has been noted by many theorists [24, 28]. However the models that include Charming Penguins have higher predicted BFs that are in closer agreement with experimental measurements.

## 1.7 Dalitz Plot Theory

### 1.7.1 Dalitz Kinematics

Consider the decay of a spin-zero  $B$ -meson with mass  $m_B$  to three daughter particles labelled 1,2,3 with masses  $m_{1,2,3}$ , momenta  $p_{1,2,3}$  and energy  $E_{1,2,3}$  respectively. The

Lorentz invariant phase space is given by:

$$dN \propto \frac{d^3p_1 d^3p_2 d^3p_3}{E_1 E_2 E_3} \delta(p_B - p_1 - p_2 - p_3) \delta(E_B - E_1 - E_2 - E_3) \quad (1.32)$$

$$= \frac{p_1^2 dp_1 p_2^2 dp_2 d\Omega_1 d\Omega_2}{E_1 E_2 E_3} \delta(E_B - E_1 - E_2 - E_3) \quad (1.33)$$

where the momentum  $\delta$ -function has been used to remove the integration of particle 3 and spherical polar coordinates are used. The  $B$  decay is isotropic so choosing to fix the direction of particle 1 gives  $\int d\Omega_1 = 4\pi$  and  $\int d\Omega_2 = 2\pi \int d\cos\theta_{12}$  where  $\theta_{12}$  is the angle between particles 1 and 2, so:

$$dN \propto 8\pi^2 \frac{p_1^2 dp_1 p_2^2 dp_2 d\cos\theta_{12}}{E_1 E_2 E_3} \delta(E_B - E_1 - E_2 - E_3) \quad (1.34)$$

Using conservation of momentum:

$$E_3^2 = p_3^2 + m_3^2 = p_1^2 + p_2^2 + 2p_1 p_2 \cos\theta_{12} + m_3^2 \quad (1.35)$$

It can be shown that  $E_3 dE_3 = p_1 p_2 d\cos\theta_{12}$ , so:

$$dN \propto \frac{p_1 dp_1 p_2 dp_2 dE_3}{E_1 E_2} \delta(E_B - E_1 - E_2 - E_3) \quad (1.36)$$

Also  $E_i dE_i = p_i dp_i$  so:

$$dN \propto dE_1 dE_2 dE_3 \delta(E_B - E_1 - E_2 - E_3) \quad (1.37)$$

$$\propto dE_1 dE_2 \quad (1.38)$$

The invariant mass combinations of the daughter particles  $i$  and  $j$  can be written as:

$$m_{ij}^2 = m_B^2 - 2m_B E_k + m_k^2 \quad (k \neq i, j) \quad (1.39)$$

So:

$$dN \propto dm_{23}^2 dm_{13}^2 \quad (1.40)$$

A plot of  $m_{23}^2$  vs  $m_{13}^2$  is known as a Dalitz plot [37]. The decay rate  $\Gamma$  is proportional to this Lorentz invariant phase space multiplied by the modulus squared of the

appropriate matrix element. Decays that have unity for the matrix element (i.e. non-resonant decay which proceeds through phase space alone) will have a uniform population across the Dalitz plot. Any non-uniformities in the Dalitz plot indicate a matrix element that differs from unity and the presence of resonances. Only two of the possible invariant mass combinations are independent as the third can be constructed using energy and momentum conservation:

$$m_{12}^2 + m_{23}^2 + m_{13}^2 = m_B^2 + m_1^2 + m_2^2 + m_3^2 \quad (1.41)$$

This describes the boundary of the kinematically allowed region of the Dalitz plot.

The helicity angle,  $\theta_{H_{ij}}$ , is defined as the angle between particles  $j$  and  $k$  in the  $ij$  rest frame, so  $\theta_{H_{13}}$  is the angle between particles 2 and 3 in the 13 rest frame. The  $m_{23}^2$  variable can be written as:

$$m_{23}^2 = m_2^2 + m_3^2 + 2E_2^*E_3^* - 2|p_2^*||p_3^*|\cos\theta_{H_{13}} \quad (1.42)$$

where  $E_{2,3}^*$  and  $p_{2,3}^*$  are calculated in the  $m_{13}$  rest frame and  $\cos\theta_{H_{13}}$  is the angle between particles 2 and 3 in the 13 rest frame. Rearranging gives:

$$\cos\theta_{H_{13}} = -\frac{m_{23}^2 - m_2^2 - m_3^2 - 2E_2^*E_3^*}{2|p_2^*||p_3^*|} \quad (1.43)$$

For a given value of  $m_{13}^2$  then the maximum and minimum possible values of  $m_{23}^2$  occur when  $\vec{p}_2$  and  $\vec{p}_3$  are anti-parallel and parallel respectively.

$$(m_{23}^2)_{max} = (E_2^* + E_3^*)^2 - (p_2^* - p_3^*)^2 \quad (1.44)$$

$$(m_{23}^2)_{min} = (E_2^* + E_3^*)^2 - (p_2^* + p_3^*)^2 \quad (1.45)$$

The  $\cos\theta_{H_{13}}$  helicity angle can also be written as:

$$\cos\theta_{H_{13}} = 1 - 2\left(\frac{m_{23}^2 - (m_{23}^2)_{min}}{(m_{23}^2)_{max} - (m_{23}^2)_{min}}\right) \quad (1.46)$$

This equation shows that the  $\cos\theta_{H_{13}}$  helicity angle can be written in terms of the  $m_{23}^2$  invariant mass pair. The  $\cos\theta_{H_{13}}$  helicity angle distribution depends on the spin of the resonance and hence the  $m_{23}^2$  distribution will be different for spin 0, spin 1 and

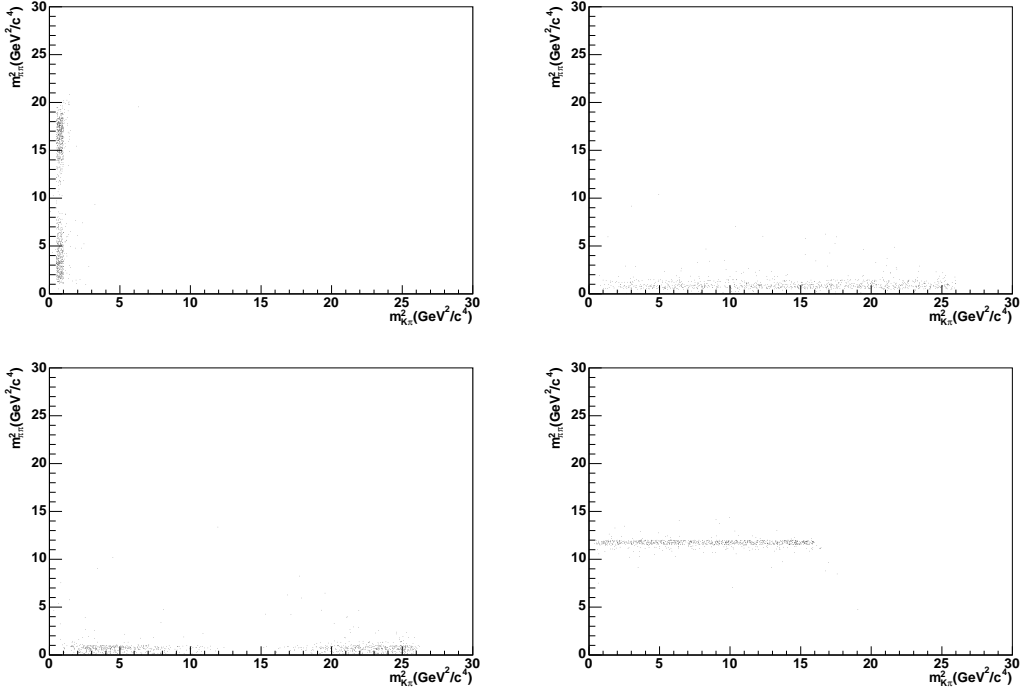


Figure 1.5: Simulated Dalitz plots for the  $B^\pm \rightarrow K^\pm \pi^\pm \pi^\mp$  decay. The top left plot shows the vector  $K^{*0}(892)$  resonance, the top right plot shows the scalar  $f_0(980)$  resonance, the bottom left plot shows the vector  $\rho^0(770)$  resonance and the bottom right plot shows the scalar  $\chi_{c0}$  resonance.

spin 2 resonances. Simulated Dalitz plots for four possible resonant contributions to the  $B^+ \rightarrow K^+ \pi^+ \pi^-$  decay are shown in Figure 1.5.

The resonant and non-resonant amplitudes in the Dalitz plot will undergo quantum mechanical interference as they all result in the same final state  $K^\pm \pi^\pm \pi^\mp$ . Consider the case of two amplitudes  $\mathcal{M}_A$  and  $\mathcal{M}_B$  with relative phase  $\psi$ . The total matrix element can be written as:

$$|\mathcal{M}|^2 = |\mathcal{M}_A + \mathcal{M}_B e^{i\psi}|^2 \quad (1.47)$$

$$= |\mathcal{M}_A|^2 + |\mathcal{M}_B|^2 + 2\text{Re}(\mathcal{M}_A \mathcal{M}_B^* e^{i\psi}) \quad (1.48)$$

The resonant matrix elements are the product of two parts, a dynamical amplitude and an angular amplitude. The angular distribution is modelled by a Legendre

polynomial,  $\mathcal{P}_S$  where S is the spin of the resonance. The orthogonality of the Legendre polynomials:

$$\int_{-1}^{+1} \mathcal{P}_l(x)\mathcal{P}_m(x)dx = 0 \quad (1.49)$$

for  $l \neq m$  shows that there will be no overall interference between two neighbouring resonances of different spins when the whole helicity region is considered. This highlights the deficiency of the ‘quasi 2-body method’. *A full Dalitz-plot analysis is necessary to correctly model the interference between the different amplitudes contributing to the  $B^\pm \rightarrow K^\pm \pi^\pm \pi^\mp$  decay.*

The Dalitz-plot analysis described in this thesis will measure the magnitudes and phases of the different amplitudes that contribute to the  $B^- \rightarrow K^- \pi^- \pi^+$  and  $B^+ \rightarrow K^+ \pi^+ \pi^-$  decays. As can be seen from Equations 1.11 and 1.12 a difference in the overall phases measured for a given resonance, say  $B^- \rightarrow \rho^0(770)K^-$  and  $B^+ \rightarrow \rho^0(770)K^+$ , is to be expected as the amplitudes have opposite weak phases ( $\phi_W$ ), however any difference in magnitude ( $|A|$ ) is an indication for the presence of direct  $CP$  violation.

# Chapter 2

## The *BABAR* Experiment

### 2.1 Introduction

The PEP-II *B* Factory and *BABAR* detector were built to study *CP* violating asymmetries in the decays of *B* mesons.

In this chapter a description of the PEP-II *B* Factory is given with a discussion of accelerator backgrounds that affect the *BABAR* detector and subsequent physics analysis. A summary of the current performance of PEP-II is provided. A general introduction to the *BABAR* detector is followed by a detailed discussion of the five main sub-detectors and trigger. A more in-depth discussion of the *BABAR* detector can be found in [38] which is the principal source of information for this chapter.

The coordinate system used to describe the *BABAR* detector is oriented such that  $z$  is the direction of the Lorentz boost (which coincides with the direction of the high energy electron beam), the  $x$  axis points toward the centre of the rings and the  $y$  axis points vertically upward. The azimuthal angle about the  $z$  axis is labelled  $\phi$  and the polar angle is labelled  $\theta$ . This coordinate system can be seen in Figure 2.3.

## 2.2 PEP-II $B$ Factory

### 2.2.1 The Injection System and Interaction Region

The PEP-II  $B$  Factory is an asymmetric energy  $e^+e^-$  collider operating at a centre of mass energy of 10.58 GeV which corresponds to the mass of the  $\Upsilon(4S)$  resonance. The cross-section for production of the  $\Upsilon(4S)$  is 1.05 nb while that for  $q\bar{q}$  production (where  $q$  corresponds to a  $u, d, s$  or  $c$  quark) is 3.39 nb. The  $\Upsilon(4S)$  resonance lies just above the production threshold for  $B\bar{B}$  pairs and so decays to a pair of  $B$  mesons (charged or neutral) almost 100% of the time. The resultant  $B\bar{B}$  pairs are produced almost at rest in the centre-of-mass (CM) frame but have significant momenta in the laboratory frame as the asymmetric energies of the beams result in a Lorentz boost of  $\beta\gamma = 0.56$ . This allows measurements of the  $B$ -meson decay vertices which are needed for studies of time dependent  $CP$  asymmetries.

The layout of the  $B$  Factory showing the SLAC linac and PEP-II storage rings can be seen in Figure 2.1.

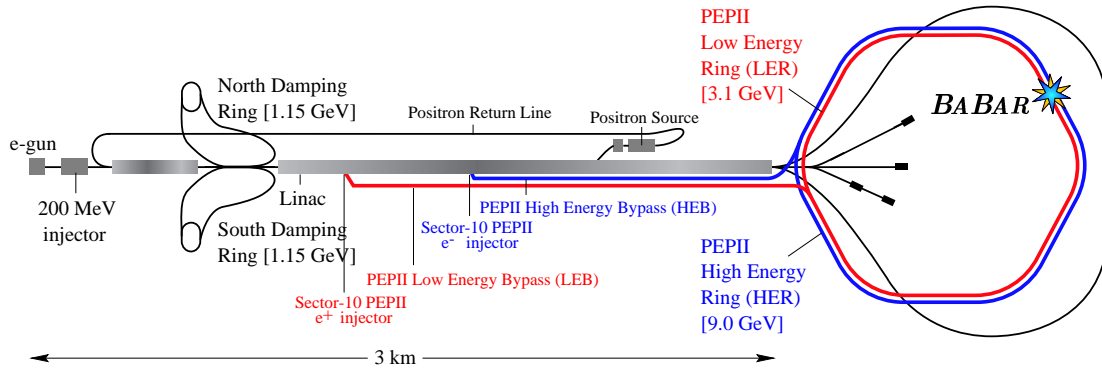


Figure 2.1: The SLAC linac and PEP-II storage rings

Electron bunches are produced by the electron gun and accelerated by the linac. They are then stored in the high energy ring (HER) at an energy of 9 GeV. The electron gun produces a second set of electrons which are accelerated to high energy

and fired onto a tungsten-rhenium target to produce positrons. These positrons are accelerated by the linac and injected into the low energy ring (LER) with an energy of 3.1 GeV.

The electrons and positrons are collided head on. Dipole magnets (B1) are used to bring the HER and LER beams to collision and separate them again in a short distance in order to avoid secondary interactions of the bunches. A series of quadrupole magnets (Q1, Q2, Q4 and Q5) are used to focus the beams. The interaction region (IR) and surrounding area is shown in Figure 2.2. The IR has typical dimensions of  $120\ \mu\text{m}$  in the  $x$  direction,  $5.6\ \mu\text{m}$  in the  $y$  direction and 9 mm in the  $z$  direction.

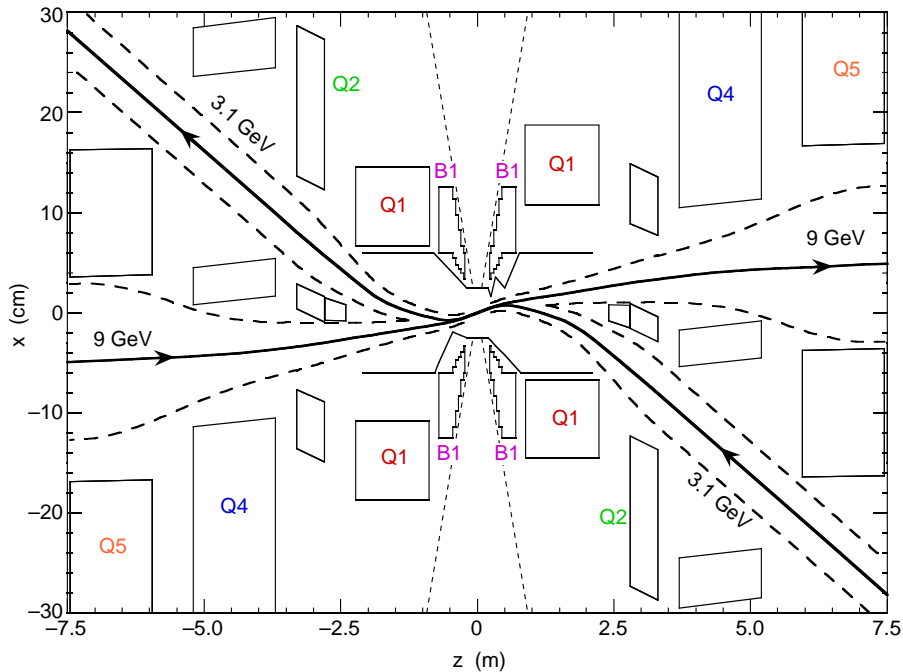


Figure 2.2: The PEP-II interaction region

## 2.2.2 Machine Backgrounds

There are three main sources of backgrounds coming from the beams which are collectively known as machine backgrounds. They are synchrotron radiation, beam

gas interactions and luminosity backgrounds. Machine backgrounds must be minimised as they lead to high occupancies in the detector which adversely affect physics measurements and can result in radiation damage to the detector.

The main sources of synchrotron radiation are the focusing quadrupole and separating dipole magnets. The interaction region is designed so that most of this radiation is diverted away from the detector. The dominant source of machine background arises from bremsstrahlung or coulombic interactions of beam particles with residual gas molecules. This results in the beam particles being lost from the acceptance of the storage ring. This background is reduced by maintaining a tight vacuum around the IR. The final source of machine background is from radiative Bhabha scattering which results in energy-degraded electrons and positrons hitting the beam pipe which surrounds the IR or other PEP-II components and consequently spraying the *BABAR* detector with electromagnetic shower debris. This background is directly proportional to the instantaneous luminosity, hence its designation as luminosity background.

### 2.2.3 PEP-II Performance

PEP-II has performed exceptionally well with a peak luminosity of  $9.213 \times 10^{33} \text{ cm}^{-2} \text{ s}^{-1}$  achieved in May 2004 with 1588 bunches, and a current of 2450 mA in the HER and 1550 mA in the LER.

## 2.3 The *BABAR* Detector

The *BABAR* detector is an asymmetric detector, offset in  $z$  from the beam-beam interaction point by 0.37m in order to provide the best coverage of the boosted  $\Upsilon(4S)$  decays. The detector, shown in Figure 2.3, consists of five sub-detectors and a magnet. The silicon vertex tracker (SVT) is closest to the beam pipe and is designed to

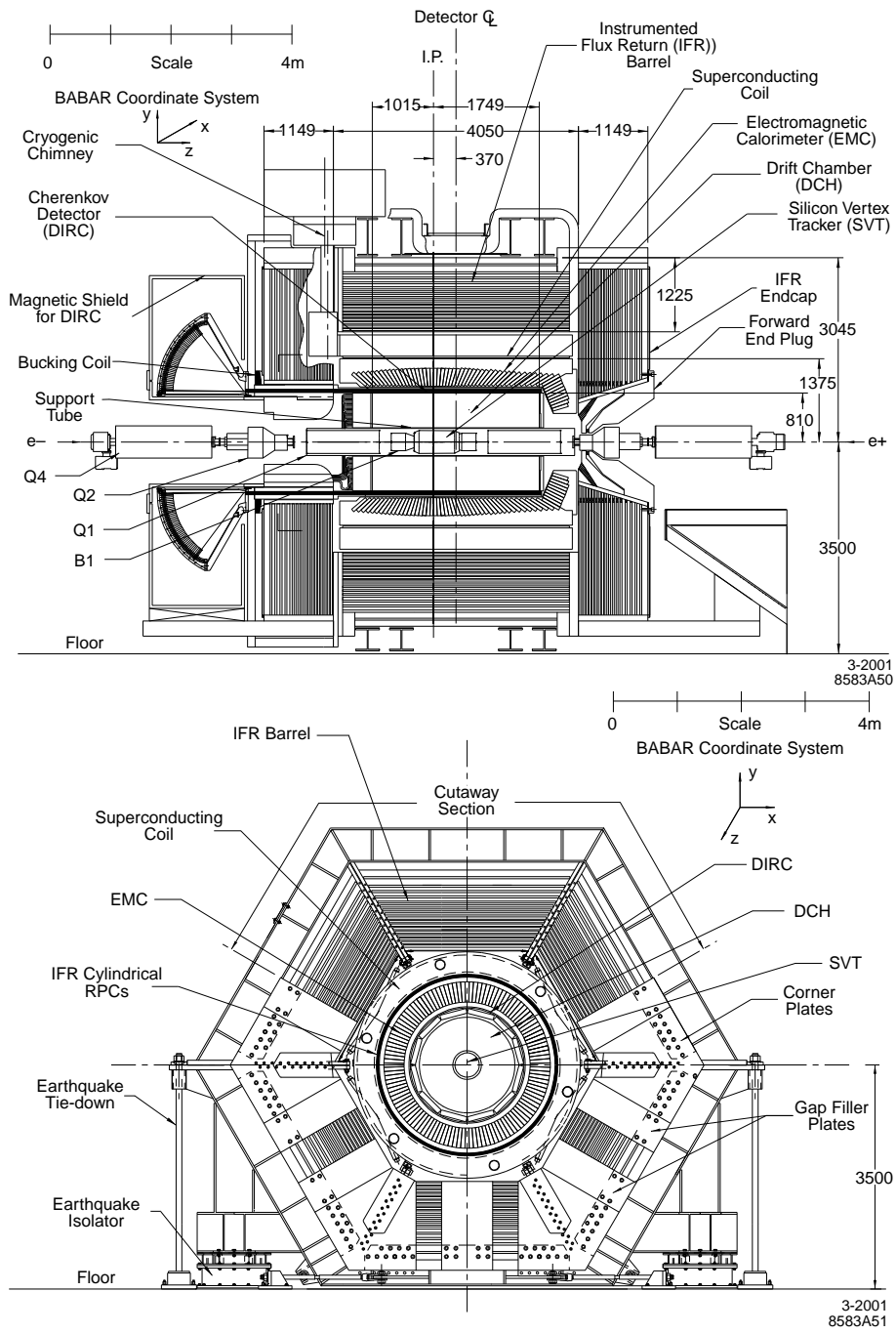


Figure 2.3: The *BABAR* detector: longitudinal and end view

measure positions of charged particles accurately, which allows precise determination of decay vertices. The drift chamber (DCH) provides momentum measurements for charged particles as well as a measurement of the energy loss  $dE/dx$  which aids in particle identification. The detector of internally reflected Cerenkov light (DIRC) surrounds the DCH and is a particle identification device designed to distinguish charged hadrons such as kaons, pions and protons. The electromagnetic calorimeter (EMC) is designed to detect and measure electromagnetic showers which aid in electron identification and also identify photons from decays of neutral particles such as  $\pi^0$ . These four sub-detectors are surrounded by a superconducting solenoid providing a field of 1.5T. The steel flux return of the magnet is segmented into layers and is instrumented for muon and neutral hadron detection. This system is known as the instrumented flux return (IFR) sub-detector.

## 2.4 Silicon Vertex Tracker

The silicon vertex tracker (SVT) measures the angles and positions of charged particles just outside the beam pipe. Tracks that have a sufficiently low momentum will not reach the DCH and hence the SVT must provide standalone tracking for particles with transverse momentum,  $p_t$ , less than 120 MeV/ $c$ . The SVT is solely responsible for measuring decay vertices near the interaction region, with a required resolution of less than 80  $\mu\text{m}$  in the  $z$  direction and around 100  $\mu\text{m}$  in the plane perpendicular to the beam line. The SVT must cover as much of the solid angle as possible (the presence of the PEP-II magnets prevents total coverage) and also contain as little material as possible to minimise multiple scatterings (that will affect subsequent measurements by the other subdetectors).

The SVT is designed with five layers of double sided silicon strip sensors. The three inner layers perform the impact parameter measurements while the outer layers perform low  $p_T$  tracking and form the link between the SVT and DCH information.

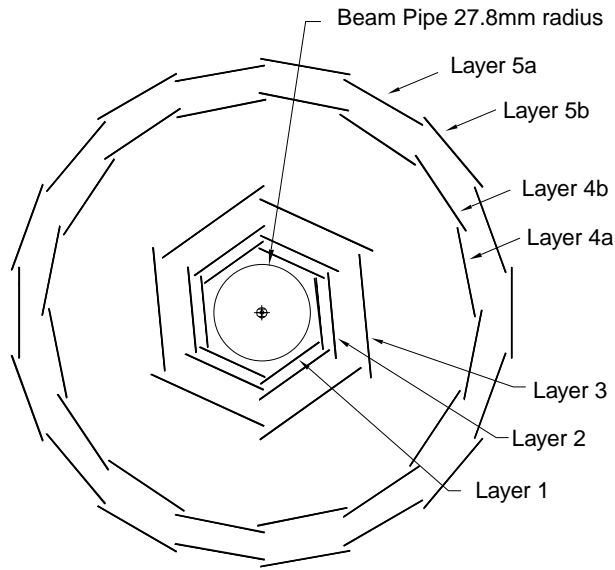


Figure 2.4: The SVT detector: end view showing the layer structure

The SVT design can be seen in Figures 2.4 and 2.5. Layers 4 and 5 are arch shaped, as seen in Figure 2.5, in order to minimize the amount of silicon required to cover the solid angle. The five layers are organized in 6, 6, 6, 16 and 18 modules respectively, with the inner layers' modules tilted slightly to give overlap between adjacent modules. The outer modules cannot be tilted due to the arch geometry and as such the outer two layers are divided into two sublayers as can be seen in Figure 2.4. The strips on each side of the sensor are oriented orthogonally with the

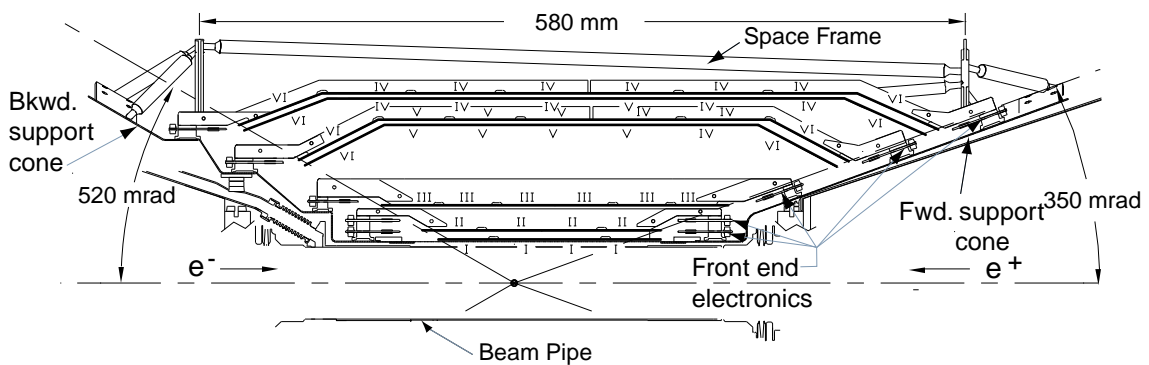


Figure 2.5: The SVT detector: longitudinal view showing the arch structure

$\phi$  measuring strips running parallel to the beam and the  $z$  measuring strips oriented transversely to the beam axis. There are a total of 340 silicon detectors present in the SVT and the material traversed by particles is about 4% of a radiation length. The signals from the strips are amplified, shaped and compared to a threshold that has been predetermined. The time interval (TOT) during which they exceed the threshold is approximately logarithmically related to the charge induced on the strips. These TOT measurements are converted to pulse height measurements and hence ionization measurements,  $dE/dx$ , are obtained.

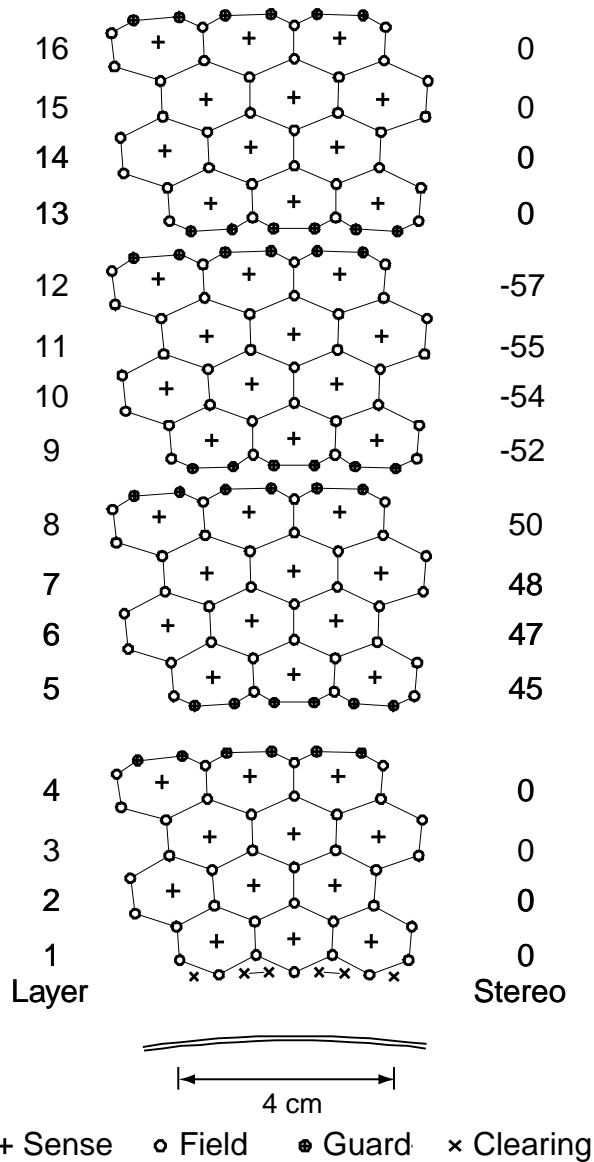
Local alignment determines the relative positions of the 340 silicon sensors and is achieved using di-muon and cosmic ray events. Global alignment is needed to align the SVT as a complete system within the detector coordinate system defined by the DCH. This is achieved using tracks that leave a sufficient number of hits in both the SVT and DCH. Two fits are performed using first DCH and then SVT information only and then the difference between these two fits is minimised.

The achieved spatial resolution of the SVT is about 10-15  $\mu\text{m}$  for the inner layers and around 40  $\mu\text{m}$  for the two outer layers. The SVT efficiency can be calculated for each half module by comparing the number of associated hits to the number of tracks crossing the active area of the module. A combined hardware and software efficiency of 97% is measured. Generally defects that have occurred during running (rather than installation) do not contribute to the inefficiency as most tracks deposit charge in two or more strips due to the track crossing angle and charge distribution.

## 2.5 Drift Chamber

The drift chamber (DCH) is designed for the detection of charged particles with measurement of their momenta and angles with high precision. It is solely responsible for the reconstruction of decay vertices such as  $K_s^0$  decays that occur outside the SVT volume and hence needs to measure longitudinal positions with a resolution of





1-2001  
8583A14

Figure 2.7: The first four superlayers of the DCH detector with the stereo angles of the wires in mrad shown

The field wires are maintained at ground potential and a positive high voltage is applied to the sense wires with a resultant electric field that is almost circularly symmetric over a large portion of the cell. Charged particles ionize the gas and the electrons created are accelerated in the field towards the sense wire creating an

avalanche of charge which is detected. The typical gain is  $5 \times 10^4$  for an operating voltage of 1960V. The drift time is extracted from the leading edge of the amplified signal produced from these drifting electrons arriving at the sense wire.

The precise relation between the measured drift time and drift distance is determined from  $e^+e^-$  and  $\mu^+\mu^-$  events. Values of  $dE/dx$  for the charged tracks are derived from measurements obtained from the sum of pulse heights for each drift cell after calibration corrections have been applied.

The measured  $dE/dx$  resolution for Bhabha events is typically 7.5%. The resolution on the drift time is about 1ns and the average single cell resolution in the DCH is  $125 \mu\text{m}$ .

## 2.6 Detector of Internally Reflected Cerenkov Light

Charged hadron identification in the *BABAR* detector is primarily provided by the Detector of Internally Reflected Cerenkov Light (DIRC). The DIRC is designed to give a  $4\sigma$  separation of pions and kaons over the wide momentum range 0.7-4.2 GeV/c. The DIRC should have a small, uniform radiation length to provide the best conditions for the calorimeter.

Cerenkov light is produced when particles with velocity  $\beta > 1/n$  traverse a material of refractive index  $n$ . The radiation produced has a characteristic Cerenkov angle given by  $\cos\theta_c = 1/n\beta$ . A portion of this radiation is trapped in the DIRC due to total internal reflection. The radiator material of the DIRC is synthetic fused silica. This material was chosen for many reasons including its long attenuation length and large index of refraction. This silica is in the form of bars that have dimensions 17mm by 35mm by 4.9m long. These bars are grouped into sets of 12 and are contained in bar boxes. An air gap is maintained between the bars in these boxes to ensure optical isolation. There are 12 bar boxes giving a total of 144

silica bars. A mirror is placed at the forward end of the bars to reflect the forward travelling photons to the backwards end of the bars where the instrumentation is situated. A fused silica wedge is placed at the end of the bars to reflect photons at large angles to reduce the size of the detection system needed. The DIRC detection system consists of a standoff box (SOB) filled with 6000 litres of purified water and instrumented with photomultiplier tubes (PMTs). Purified water is chosen as it is inexpensive and has a refractive index almost equal to that of the silica and hence reduces the internal reflection at the bar/box interface. A diagram of the DIRC is shown in Figure 2.8.

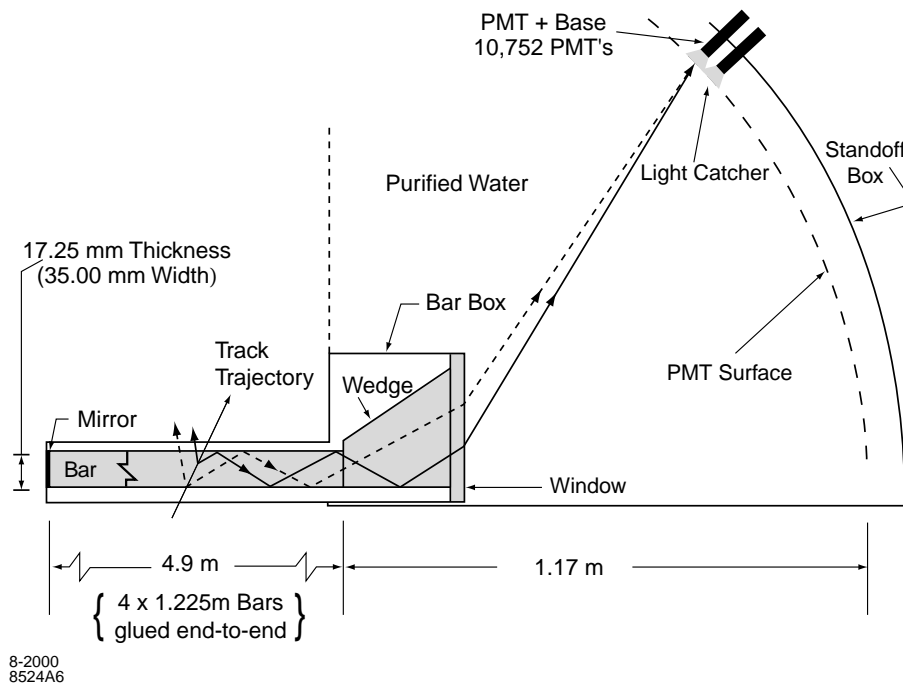


Figure 2.8: The DIRC detector: Schematic of a silica bar and the photon detection equipment

There are in total 10752 PMTs in the detection system. Each PMT has a diameter of 28.2mm and is surrounded by a light catcher which detects photons that would otherwise miss the active area of the PMTs. The PMTs are situated 1.2m from the silica bars and the light pattern at the PMTs is a conic section with the cone angle related to the Cerenkov angle. The DIRC detector comprises 17% of a radiation

length and covers 83% of the CM polar angle.

The propagation angle is calculated from a vector which points from the centre of the PMT to the centre of the bar. This information is combined with information from the tracking system to determine the Cerenkov angle. About 80% of the light is maintained after multiple bounces along the bars. The dominant contributor to the overall detection efficiency is the quantum efficiency of the PMT which is about 25%. The number of Cerenkov photons detected varies between 20 for small polar angles at the centre of the barrel and 65 at large polar angles. Timing information is used to suppress background hits from the beam or other tracks in the same event. The time resolution is about 1.7ns (which is close to the 1.5ns spread of the PMT's) and the Cerenkov angle resolution is 2.5mrad.

## 2.7 Electromagnetic Calorimeter

The electromagnetic calorimeter (EMC) is designed to measure showers with excellent efficiency, energy resolution and angular resolution over a wide energy range from 20 MeV to 9 GeV. The lower limit is set by beam and event related backgrounds. The upper limit derives from the need to measure accurately high energy photons from QED processes.

The EMC is a total-absorption calorimeter consisting of a finely segmented array of thallium doped caesium iodide (CsI(Tl)) crystals. This material is chosen for its high light yield, small Molière radius and short radiation length. This provides the necessary energy and angular resolution while allowing shower containment in a short distance. The EMC is arranged into a cylindrical barrel containing 5760 crystals and a conical forward endcap which contains 820 crystals. There is full coverage in azimuth and 90% solid angle coverage in the CM frame. A schematic view of the EMC can be seen in Figure 2.9.

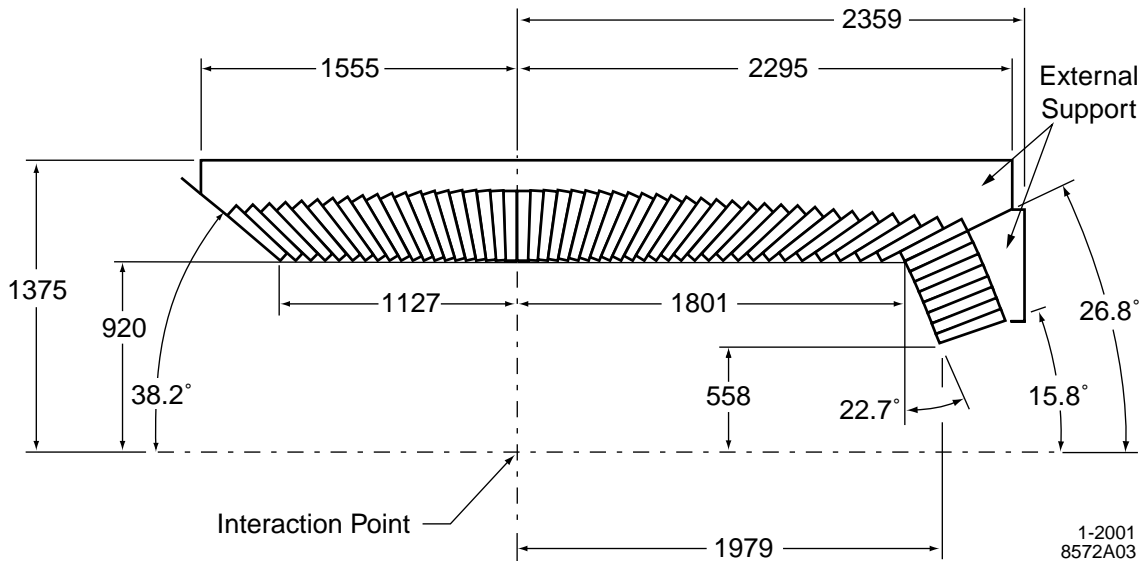


Figure 2.9: The EMC detector: longitudinal view - top half only. All distances shown are in mm.

The crystals are trapezoidal with their axes pointing towards the IR. In order to minimise the amount of CsI(Tl) needed the crystals vary in radiation length from  $16.0 X_0$  to  $17.5 X_0$ . The crystals are read out with silicon photodiodes. Feature extraction algorithms are run to determine the energy and time of the signal peak in the crystal. In order to reduce the stored data volume only crystals with energy greater than 1 MeV are included. Typical electromagnetic showers spread over many adjacent crystals forming a cluster of energy deposits. If it is not possible to associate a cluster with a track projected to the EMC from the DCH then the cluster is assumed to originate from a neutral particle. Electrons are separated from charged hadrons on the basis of shower energy, lateral shower moments and track momentum.

There are two important calibrations needed for the EMC. The first relates the measured pulse height to the actual energy deposited. The light yield is non-uniform in energy, can vary between the individual crystals and may change over time. At low energies this calibration is done using a 6.13 MeV radioactive source. At high energies Bhabha scattering events are used as their energies can be predicted from

polar angles. The second calibration infers the energy of the incoming particle from the energy in the cluster.  $\pi^0$  decays are used to provide a correction for absorption and shower leakage. This correction is applied as a function of cluster energy and polar angle.

The energy resolution is measured at low energies using the 6.13 MeV radioactive source and at high energies is derived from Bhabha events. Figure 2.10 shows the energy resolution extracted from a variety of processes as a function of energy, from which the empirical parameterisation is found to be:

$$\frac{\sigma_E}{E} = \frac{(2.32 \pm 0.30)\%}{\sqrt[4]{E(\text{GeV})}} \oplus (1.85 \pm 0.12)\% \quad (2.1)$$

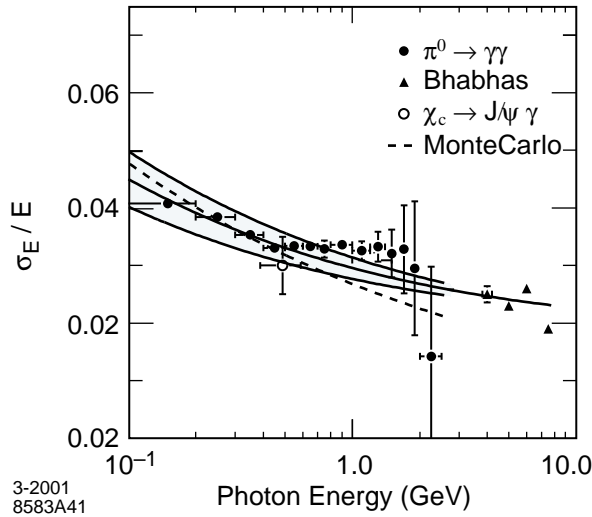


Figure 2.10: The energy resolution of the EMC. The points are data taken from various physical processes. The solid line is a fit to the data points of the expected resolution function  $\frac{\sigma_E}{E} = \frac{a}{\sqrt[4]{E(\text{GeV})}} \oplus b$  and the shaded area denotes the RMS error of the fit.

The energy dependent term primarily arises from fluctuations in photon statistics but has contributions from electronics noise and beam backgrounds. This term dominates at low energies. The constant term arises from non-uniformity in light

collection, leakage or absorption in the material between and in front of the crystals, and uncertainties in the calibrations. Angular resolution is determined empirically to be:

$$\sigma_{\theta} = \sigma_{\phi} = \left( \frac{3.87 \pm 0.07}{\sqrt{E(\text{GeV})}} + 0.00 \pm 0.04 \right) \text{mrad} \quad (2.2)$$

The parameterisation is based on the analysis of  $\pi^0$  and  $\eta$  decays to two photons.

## 2.8 Instrumented Flux Return

The instrumented flux return (IFR) is designed to detect muons with high efficiency and purity and also to detect neutral hadrons such as  $K_L^0$  over a wide range of angles and momenta.

The steel flux return for the magnet is segmented into layers which vary in thickness from 2cm at the inner side to 10cm at the outer side. Resistive plate chambers (RPC) of different geometries are installed between these layers to detect streamers from ionizing particles. There are 19 RPC layers in the barrel, 18 layers in the endcap and 2 additional layers of cylindrical RPCs placed between the EMC and the magnet to provide the necessary information to link tracks from the EMC to the IFR. A schematic view of the IFR can be seen in Figure 2.11. The RPCs consist of two bakelite sheets 2mm thick separated by a gap of 2mm which is filled with a gas mixture. This gas mixture is 57% argon, 39% freon and 4% isobutane and is chosen for its non flammable and environmentally safe properties. The bakelite sheets are coated in graphite with one side at a potential of 8kV and the other side maintained at ground potential. Orthogonal aluminium readout strips are placed on the modules to measure both  $z$  and  $\phi$  for the barrel modules and  $x$  and  $y$  for the endcap modules. A diagram of an RPC can be seen in Figure 2.12. A number of factors are used to determine the particle type such as the number of interaction lengths passed through by the particle, the matching of tracks to RPC clusters and the distribution of RPCs hit in the IFR layers.

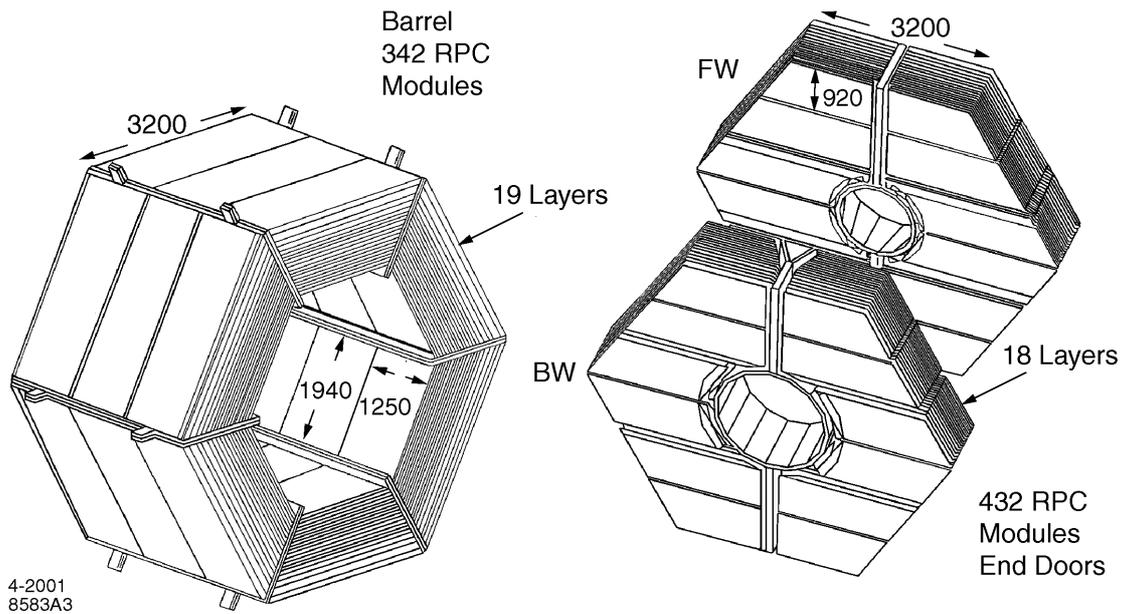


Figure 2.11: The IFR detector: Diagram showing the barrel and forward and backward endcaps. All dimensions shown are in mm

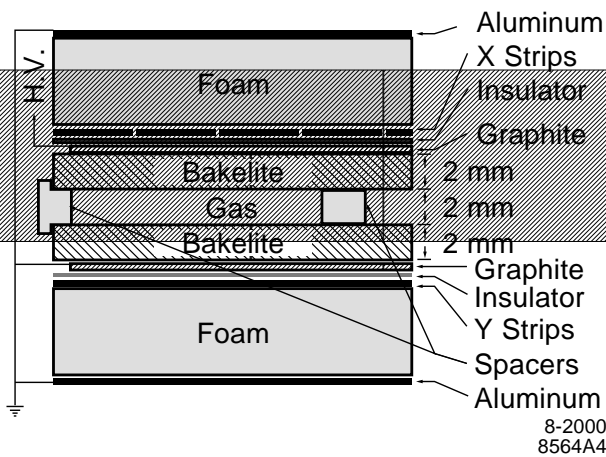


Figure 2.12: The IFR detector: Cross section of an RPC

An RPC is considered efficient if a signal is detected within 10cm of a track that has been extrapolated into the IFR. This efficiency can be calculated using collision data and cosmic ray events. The time resolution is of order 1ns.

## 2.9 Trigger

The trigger system is designed to select interesting physics events, with a high and well-understood efficiency, while rejecting background events. The basic backgrounds are Bhabha events (which have a huge rate compared to other physics rates), radiative Bhabha events (which have a smaller rate but look like interesting physics), beam backgrounds (such as those described in Section 2.2.2) and low mass two-photon events.

The *BABAR* trigger system is implemented in two stages. The Level-1 (L1) trigger is hardware based and is followed by the Level-3 (L3) trigger which is software based. The PEP-II bunch crossing rate is around 238MHz (4.2ns bunch spacing). The L1 trigger reduces the event rate to less than 2kHz which is the maximum rate allowed by the data acquisition system (DAQ). The L3 trigger further reduces the rate to around 100Hz which is the upper limit set by storage and reconstruction considerations.

### 2.9.1 L1 Trigger

The L1 trigger decision is based on a drift chamber trigger (DCT) and an electromagnetic trigger (EMT).

The DCT and EMT form trigger primitives which are summaries of the position and energy of particles present. There are 3 DCT primitives which correspond to short tracks, long tracks and high  $p_t$  tracks. The EMT primitives consist of towers, which are the summed energy of groups of calorimeter crystals. Different energy thresholds are applied to these towers to form 5 EMT primitives. These trigger primitives are sent to the Global trigger (GLT) where the information is combined into trigger lines. If trigger criteria are satisfied then a Level 1 accept is issued and event readout is initiated. The typical L1 rate is about 1kHz. The DCT and EMT

provide orthogonal triggers with an individual efficiency for  $B\bar{B}$  events greater than 99% and a combined efficiency greater than 99.9%. L1 is effective at reducing beam backgrounds by looking at tracks which come from the IP in  $r$  and  $\phi$  and also looking at EMT towers. Future improvements to the L1 DCT trigger will make greater use of the  $z$  information, which will then enable the trigger to reject a substantial amount of beam background which originates from beam optics at  $\pm 20$  cm in  $z$ .

### 2.9.2 L3 Trigger

The L3 trigger receives the L1 trigger output and has access to the complete event data including timing information. It further reduces the rate while flagging interesting categories of events for physics analysis or alternatively diagnostic and calibration purposes. L3 implements improved tracking and clustering procedures which allow for greater rejection of backgrounds. Certain physics processes, such as Bhabha scattering, have high cross-sections. In order to keep the recorded data at a manageable level prescaling factors are applied to such processes. If the L3 trigger is passed then the event is stored for full reconstruction and processing.

For a luminosity of  $2.6 \times 10^{33} \text{ cm}^{-2}\text{s}^{-1}$ , desired physics events (hadrons,  $\tau\tau$  and  $\mu\mu$ ) contribute about 16Hz which is approximately 13% of the L3 output. QED and two-photon events contribute around 11% while calibration and diagnostic samples contribute around 40%.

## 2.10 Data Acquisition

The *BABAR* data acquisition system (DAQ) is responsible for the transport of event data from the detector to mass storage with a minimum of dead time. A schematic of the DAQ system is shown in Figure 2.13.

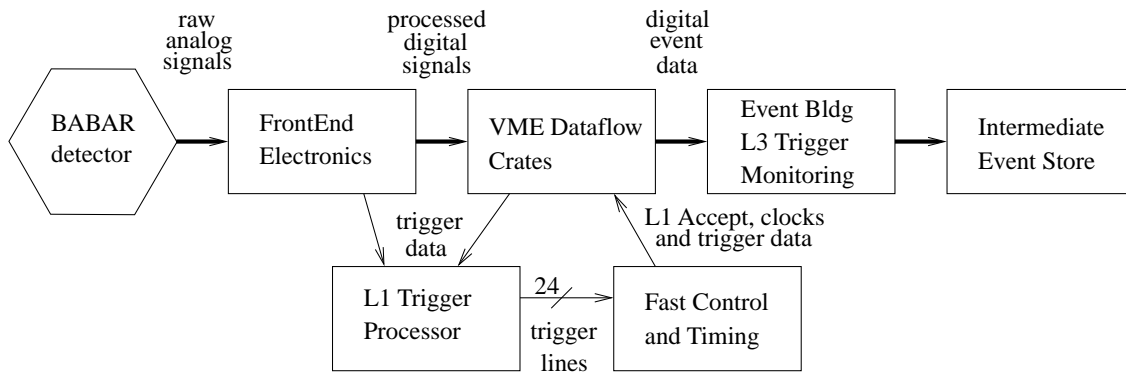


Figure 2.13: Schematic diagram of the data acquisition

Data are passed from the sub-detector front-end electronics (FEE) via optical fibres to the data flow readout modules (ROMs). The ROMs perform feature extraction to extract signals and minimise backgrounds and noise. If an L1 accept is received the data are passed on to the L3 trigger. If the L3 trigger criteria are passed the data are written to disk and enter the Online Prompt Reconstruction (OPR) system.

## 2.11 Online Prompt Reconstruction

Online Prompt Reconstruction (OPR) forms the link between the online and offline systems. The OPR system performs complete reconstruction on the stored data, creating all physics quantities necessary for analysis from the information provided by the sub-detectors. OPR also provides extensive information on important physics quantities that are used to monitor the data quality.

## 2.12 Monte Carlo Simulation

Monte Carlo simulated data are used for many purposes by the *BABAR* experiment. The simulation reproduces in detail the generation of the event at the interaction

point, the propagation of the resulting particles through the detector and the response of the detector to these particles. Detector response quantities are then used to construct candidate events which may be analysed as if they were real data.

There are two event generator programs used to create these MC events. **EvtGen** [39] is used for  $B$  decays and **JETSET** [40] is used for  $q\bar{q}$  events (where  $q = u, d, s, c$ ). The level of detail in the generators is high and allows effects such as polarisation, interference and  $CP$  violation to be included. The output of these generator programs is a set of four vectors and vertices for the decay products. The generator also simulates the spread in beam energies and positions allowed in the PEP-II beam collisions.

The next stage in the Monte Carlo production process is the detector simulation program which is based on **Geant4** [41]. This is designed to account for the passage of the particles through the material of the detector and subsequent interactions such as energy loss, production of secondaries and multiple scattering. As the particles pass through sensitive regions of the detector, information on energy, charge and angle is used to calculate positions and idealised energy deposits in the detector. Radiative Bhabha scattering events can be used to validate the electromagnetic processes used in this part of the simulation by examining the results for ionisation energy loss and calorimeter shower shapes, and looking for differences between real data and simulated data. Hadronic interactions are simulated using parameterisations and then validated using a variety of physics processes such as decays of  $\tau$  leptons and pions. The output at this stage includes generator level information as well as the individual signals the particles produce when traversing the detector. This allows “truth matching” to be performed as the signals have associated with them information about the particle that produced them.

The next step in producing Monte Carlo data is to take the idealised detector hits and transform them into realistic signals which mimic those collected from detector electronics. Real background events are stored in a database and are mixed with

simulated events in order to reproduce the data more closely. The output at this stage is an event containing raw subdetector information and hence is like that of the real data recorded by the *BABAR* detector.

The final stage in the Monte Carlo production process is to pass the simulated events through the same reconstruction procedure that is used for real data.

This analysis uses the  $B^+ \rightarrow \bar{D}^0 \pi^+$  decay as a calibration channel to identify any possible differences between data and MC events. This decay is chosen as it has a branching fraction in excess of the inclusive charmless  $B^+ \rightarrow K^+ \pi^+ \pi^-$  decay and can be easily isolated using invariant mass cuts.

# Chapter 3

## Data Reconstruction and Event Selection

### 3.1 Analysis Method

The aim of this analysis is to measure simultaneously the branching fractions of the resonant and non-resonant (NR) intermediate states of the  $B^\pm \rightarrow K^\pm \pi^\pm \pi^\mp$  decay. This is achieved in two stages. Firstly selection criteria are applied to the complete *BABAR* dataset to obtain a final data sample for the analysis, which consists of signal  $B^\pm \rightarrow K^\pm \pi^\pm \pi^\mp$  events and background events. The background events arise from two main sources. The first and dominant contribution to the background is from light quark and charm continuum production events where three random tracks from the jets happen to mimic the  $K^\pm \pi^\pm \pi^\mp$  final state and are reconstructed as signal. These events are labelled  $q\bar{q}$  background ( $q = u, d, s, c$ ). The second source of background is  $B$  decay to final states that are not  $K^\pm \pi^\pm \pi^\mp$  and these events are labelled  $B\bar{B}$  background. The selection procedure is described in detail in this chapter. A subsequent Dalitz-plot analysis is performed to study the different contributions to the  $B^\pm \rightarrow K^\pm \pi^\pm \pi^\mp$  decay. This procedure is described in Chapter 4.

## 3.2 Data Sample

The data used in this analysis were collected with the *BABAR* detector during its four data-taking runs between 1999 and 2004. The data taken at the  $\Upsilon(4S)$  resonance correspond to 231.8 million  $B\bar{B}$  pairs, which is equivalent to a total integrated luminosity of  $210.6 \text{ fb}^{-1}$ . This is termed on-resonance data. An additional integrated luminosity of  $21.6 \text{ fb}^{-1}$  was recorded at a centre of mass energy 40 MeV below the  $\Upsilon(4S)$  resonance, and is termed off-resonance data. This off-resonance data is used to study the  $q\bar{q}$  background.

## 3.3 Discriminating Variables

### 3.3.1 Kinematic Variables

The kinematics of the  $B$ -Factory operating at the  $\Upsilon(4S)$  resonance provide constraints that can be used to distinguish signal from background decays. The two kinematic constraints commonly used by the *BABAR* experiment [42] are:

$$\Delta E = E_B^* - E_{beam}^* \quad (3.1)$$

$$m_{ES} = \sqrt{E_{beam}^{*2} - p_B^{*2}} \quad (3.2)$$

where:

- $E_{beam}^* = \sqrt{s}/2$ , and  $s$  is the square of the energy in the centre of mass frame (CM) of the  $e^+e^-$  system,
- $E_B^*$  and  $p_B^*$  are the reconstructed energy and momentum of the  $B$  meson in the CM frame.

$m_{\text{ES}}$  can alternatively be written as:

$$m_{\text{ES}} = \sqrt{\left(\frac{\frac{1}{2}s + \mathbf{p}_i \cdot \mathbf{p}_B}{E_i}\right)^2 - \mathbf{p}_i^2} \quad (3.3)$$

where:

- $E_i$  and  $\mathbf{p}_i$  are the energy and momentum of the  $e^+e^-$  system measured in the laboratory frame,
- $\mathbf{p}_B$  is the momentum of the  $B$  meson measured in the laboratory frame.

For signal  $B$  decays  $\Delta E$  is peaked around zero and  $m_{\text{ES}}$  is peaked around the  $B$  mass of 5.279 GeV/ $c^2$ . As can be seen from Equation 3.2,  $m_{\text{ES}}$  cannot be greater than  $E_{\text{beam}}$  which has a value of 5.29 GeV/ $c^2$ .  $q\bar{q}$  background events populate the entire allowed  $m_{\text{ES}} - \Delta E$  region and they are the dominant contribution in the area where  $m_{\text{ES}}$  is much less than the  $B$  mass.  $B\bar{B}$  background events lie in different regions of the  $m_{\text{ES}} - \Delta E$  plane depending on their final states.  $B\bar{B}$  background decays to a two-body final state combined with a track from the rest of the event, tend to populate the region with positive  $\Delta E$  values.  $B\bar{B}$  background decays to four-body final states with one track missing populate the region with negative  $\Delta E$  values.  $B\bar{B}$  background events to a three-body final state will have a signal like  $m_{\text{ES}} - \Delta E$  distribution.

The kinematic variable  $m_{\text{ES}}$  is calculated using the  $B$ -meson momentum and the beam energy and momentum. The independence of  $m_{\text{ES}}$  from the  $B$ -meson energy leads to accurate calculations of this quantity and independence from the mass hypotheses used for the final state particles.  $\Delta E$  uses the  $B$ -meson energy so this quantity has a dependence on the final state mass assignments.

A signal strip, sideband and signal box are defined in Table 3.1 and illustrated in Figure 3.1. The value of  $\Delta E$  must be between  $-0.0349$  and  $0.0551$  GeV. These numbers derive from a selection of the magnitude of  $\Delta E$  to be less than 0.06 GeV,

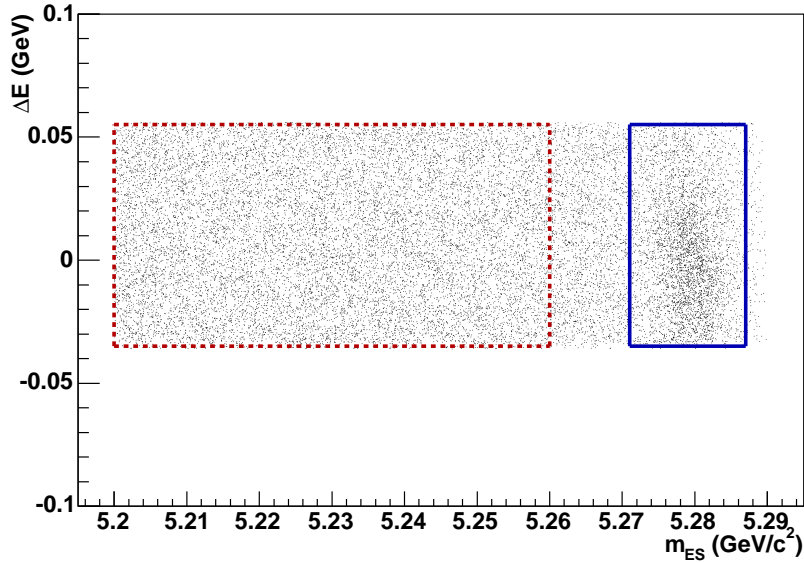


Figure 3.1:  $\Delta E$ - $m_{ES}$  plane, showing signal strip, sideband and signal box. The area populated by events (these are on-resonance data events) is the signal strip, the sideband is defined by the dashed, red lines, and the signal box by the solid, blue lines.

which is approximately  $3\sigma$  of the signal distribution, as determined from Monte Carlo events in a previous study of this decay [32, 33]. However, the mean of the signal  $\Delta E$  distribution in  $B^+ \rightarrow \bar{D}^0 \pi^+$  data is found to be shifted by  $-4.9$  MeV relative to zero, so the selection window is shifted by the same amount. Finally the lower edge of the  $\Delta E$  window is tightened by 30 MeV in order to reduce the amount of  $B\bar{B}$  background.

The signal strip is used to determine the fractions of  $q\bar{q}$  and  $B\bar{B}$  events in the signal box. The sideband is used to characterise the shape of the  $q\bar{q}$  background in the Dalitz plot. The signal box is used to select the events for which the Dalitz-plot fit is performed.

Table 3.1: Definitions of the signal strip, sideband and signal box, with  $-0.0349 < \Delta E < 0.0551$  GeV.

Region	$m_{\text{ES}}$ Selection Criteria ( GeV/ $c^2$ )
Signal Strip	$5.200 < m_{\text{ES}} < 5.290$
Signal Box	$5.271 < m_{\text{ES}} < 5.287$
Sideband	$5.200 < m_{\text{ES}} < 5.260$

### 3.3.2 Event Shape Variables

Signal and  $q\bar{q}$  background events have very different characteristic topologies. In a true signal event, the primary  $e^+e^-$  annihilation produces a  $B\bar{B}$  pair via the  $\Upsilon(4S)$  resonance. In the  $\Upsilon(4S)$  rest frame the  $B$  mesons have low momenta, and so the decay of each  $B$  meson is fairly isotropic. In contrast a  $q\bar{q}$  event has a pronounced two jet structure, and this results in a strongly preferred direction characterising the whole event. In a  $q\bar{q}$  event the three hadrons which form the  $B$  candidate are usually found to be in one or other of the two jets which are roughly back-to-back. The  $B$  candidates will therefore have non-isotropic decay shapes in the CM frame, and there will be correlations between the directions of the candidate decay products of the two  $B$  mesons.

The thrust axis of a collection of particles is the direction which maximises their longitudinal momenta. If the  $B$ -candidate decay products are excluded from the event data then the remaining particles are collectively labelled “rest of the event”. The event shape variable  $\cos\theta_T$  is defined as the cosine of the angle between the thrust axis of the  $B$  candidate and the thrust axis of the rest of the event. The distribution of  $\cos\theta_T$  is flat for signal events (as these  $B$  candidates are isotropic) and highly peaked at  $\pm 1$  for  $q\bar{q}$  events (as these  $B$  candidates lie in the jets which correspond to the thrust axes of the rest of the event). The  $|\cos\theta_T|$  distributions for

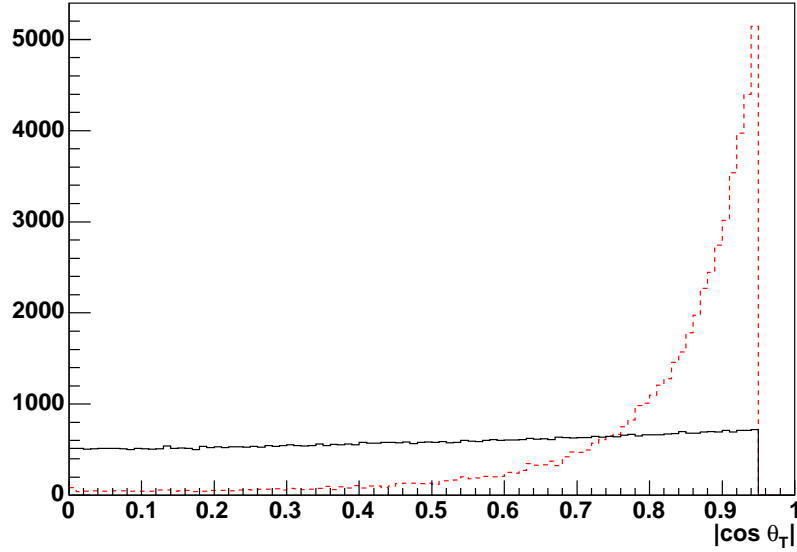


Figure 3.2:  $|\cos \theta_T|$  distributions for non-resonant  $B^\pm \rightarrow K^\pm \pi^\pm \pi^\mp$  MC events (solid black) and off-resonance events (dashed red). A cut of  $|\cos \theta_T| < 0.95$  is applied in the event pre-analysis described in Section 3.6.2.

non-resonant signal MC events and off-resonance events (which are  $q\bar{q}$  events) are shown in Figure 3.2.

In order to further reduce the background a Fisher discriminant [43] is constructed. The Fisher discriminant,  $\mathcal{F}$ , can be defined as:

$$\mathcal{F} = \sum a_i x_i = \vec{a}^T \vec{x}, \quad (3.4)$$

where  $x_i$  are some discriminating variables and  $a_i$  are chosen to maximise the separation of the signal and background distributions.  $\mathcal{F}$  is constructed using five variables:  $L_0$ ,  $L_2$ ,  $|\cos \theta_{Bmom}|$ ,  $|\cos \theta_{Bthr}|$  and  $|TFlv|$ :

- $L_0$  and  $L_2$  are defined as  $L_0 = \sum_i^{roe} p_i$  and  $L_2 = \sum_i^{roe} p_i \times \frac{1}{2} (3 \cos^2(\theta_i) - 1)$  where the sum is over tracks and clusters in the rest of the event (*roe*) and  $p_i$  and  $\theta_i$  are the momentum and polar angle respectively, of the track or cluster.

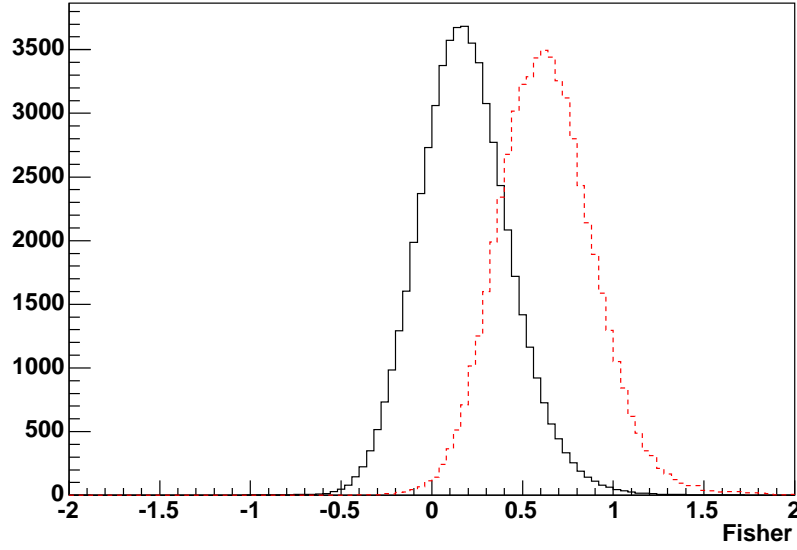


Figure 3.3:  $\mathcal{F}$  distributions for non-resonant  $B^\pm \rightarrow K^\pm \pi^\pm \pi^\mp$  MC events (solid black) and off-resonance events (dashed red).

- $\theta_{Bmom}$  is defined as the angle between the  $B$ -candidate momentum and the beam direction.
- $\theta_{Bthr}$  is the angle between the  $B$  candidate thrust axis and the beam direction.
- $TFlv$  is the tagging [44] variable used to distinguish  $B^0$  and  $\bar{B}^0$ . It uses information on high momentum leptons and kaons in the rest of the event. The output of  $TFlv$  is a number, with values towards 1 indicating that a good tag was obtained and values towards 0 indicating no tag was possible. Even though this analysis uses charged  $B$  mesons, this tagging algorithm output is useful in discriminating signal from background as continuum events do not contain the types of processes looked for by the algorithm and so will be more likely to return a value of 0 than  $B$  decays.

The  $\mathcal{F}$  distributions for non-resonant signal MC events and off-resonance events are shown in Figure 3.3.

## 3.4 Tracking

Track reconstruction [38] uses information from the SVT and DCH sub-detectors. Tracks are defined by five parameters that are measured at the point of closest approach to the  $z$ -axis;  $d_0$  is the distance from the origin in the  $x$ - $y$  plane,  $z_0$  is the distance along the  $z$ -axis,  $\phi_0$  is the azimuthal angle,  $\lambda$  is the dip angle and  $w$  is the track curvature with  $w = 1/p_t$  where  $p_t$  is the transverse momentum.

The offline charged particle track reconstruction builds on information available from the L3 trigger. A track is selected by performing a helix fit to the hits found by the L3 track finding algorithm, with a subsequent search being made for additional hits in the DCH that may belong to the track. Two more sophisticated tracking programs are applied which are designed to find tracks that either do not pass through the entire DCH or do not originate from the interaction point. The resulting tracks are then extrapolated into the SVT, and SVT track segments are added. Finally a SVT only track finder is run on the remaining SVT hits to identify low momentum tracks that did not reach the DCH.

This analysis uses tracks that satisfy the requirements of the `GoodTracksLoose` list:

- A minimum transverse momentum of 0.1 GeV/ $c$ ,
- A maximum momentum of 10.0 GeV/ $c$ ,
- At least 12 drift chamber hits,
- A maximum  $d_0$  of 1.5 cm,
- A maximum  $z_0$  of 10.0 cm.

The track reconstruction efficiency and  $p_T$  resolution are dominated by the DCH. The absolute DCH tracking efficiency is determined as the ratio of the number of reconstructed DCH tracks to the number of tracks detected in the SVT (that

fall within the acceptance of the DCH). The tracking efficiency of the DCH as a function of  $p_T$  and polar angle is shown in Figure 3.4. At the design voltage of

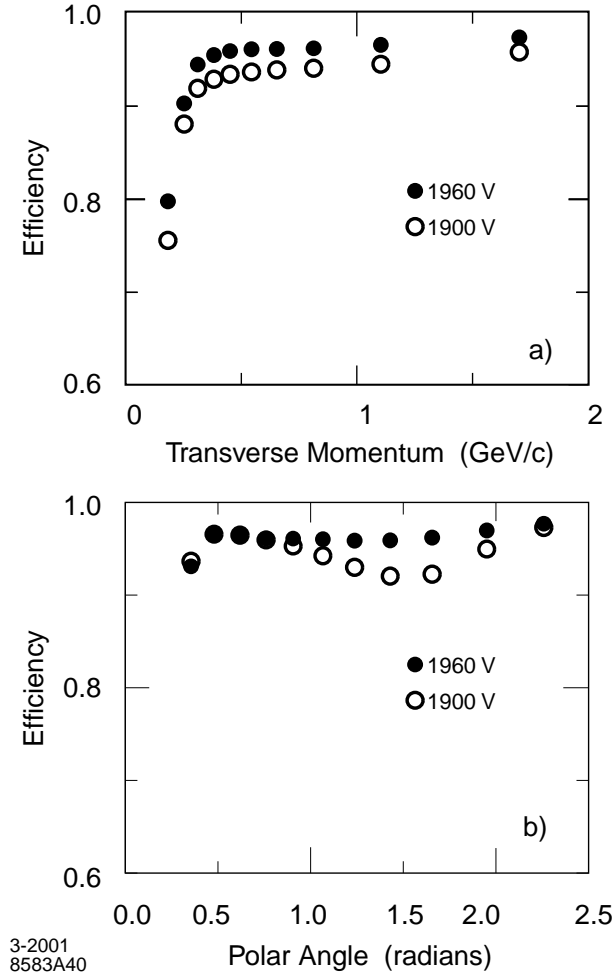


Figure 3.4: Track reconstruction efficiency as functions of  $p_T$  and polar angle for DCH operating voltages 1900V and 1960V

1960V, the tracking efficiency is  $98 \pm 1\%$  per track above  $200 \text{ MeV}/c$  and polar angle  $\theta$  greater than  $500 \text{ mrad}$ . The  $p_T$  resolution is obtained using cosmic ray events where the upper and lower halves of the tracks traversing the DCH and SVT are fitted separately. It is found to be:

$$\frac{\sigma_{p_T}}{p_T} = (0.13 \pm 0.01)\% p_T + (0.45 \pm 0.03)\% \quad (3.5)$$

where  $p_T$  is measured in  $\text{GeV}/c$ .

### 3.4.1 Tracking Efficiency Corrections

Discrepancies exist between the tracking efficiencies for data and MC events and therefore corrections must be applied to efficiencies measured using MC events. These corrections are calculated using a variety of methods [45, 46] and are stored in tables which are binned in momentum,  $\theta$  and  $\phi$ . The overall efficiency correction for an event is taken as the product of the efficiency corrections for the three tracks. The average tracking efficiency correction is found to be 0.984.

## 3.5 Particle Identification

After tracks have been reconstructed in the detector, particle identification (PID) selectors are run. Standard PID selectors have been developed by the *BABAR* collaboration and this analysis uses the kaon selector to discriminate between pions and kaons. The electron selector is also used to veto electrons in the final state.

### 3.5.1 Kaon Identification

The standard *BABAR* kaon selector is called `SMSKaonSelector` [47] and has 5 different modes (known as `very tight`, `tight`, `notApion`, `loose` and `very loose`) which vary in efficiency and purity.

The SVT and DCH provide ionization-energy loss,  $dE/dx$ , information which has a momentum dependence described by Bethe-Bloch functions [48]. The DCH  $dE/dx$  distributions for different particles are shown in Figure 3.5.

The parameterisations of these Bethe-Bloch functions are taken from calibration fits to data. Measurements of  $dE/dx$  are used only in momentum ranges where there is a  $2\sigma$  separation between kaons and pions. This corresponds to momenta below

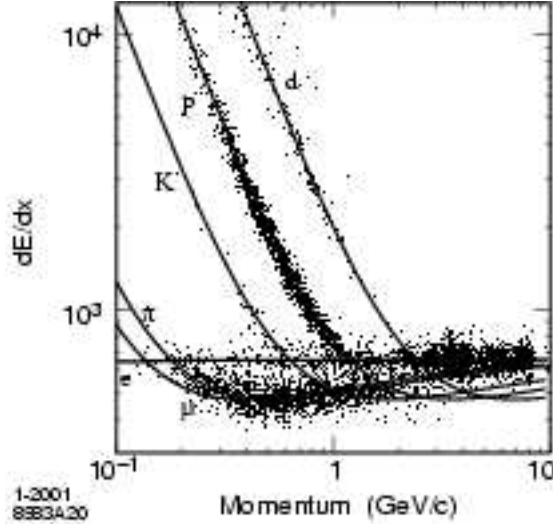


Figure 3.5: DCH  $dE/dx$  distributions for data as a function of momentum, showing the regions occupied by different charged particle types

0.6 GeV/c for the SVT and below 0.7 GeV/c for the DCH.  $2\sigma$  separation is also achieved in the DCH for momenta greater than 1.5 GeV/c (the relativistic rise part of the Bethe-Bloch function) but this region is used only in the `loose` and `very loose` modes of the selector.

The DIRC provides information on the Cerenkov angle and number of photons. Cerenkov photons are emitted by particles in the DIRC for momenta  $p$  above the threshold  $m/\sqrt{n^2 - 1}$  where  $m$  is the particle mass and  $n$  is the refractive index of the DIRC silica bars, which is 1.473. For kaons this threshold corresponds to approximately 0.45 GeV/c, so the DIRC information is used only in the momentum range  $> 0.6$  GeV/c for all modes of the selector. The central value of the Cerenkov emission angle,  $\theta_C$  with respect to the track is given by  $\cos \theta_C = E/pn$  where  $E$  is the particle energy. The number of photons produced for a fixed particle path in the silica follows Poissonian statistics with a central value dependent on the particle mass, charge, momentum, polar angle and bar number (position).

The `SMSKaonSelector` uses this information from the SVT, DCH and DIRC sub-

detectors to form three probability density functions (PDFs), the product of which is used to form a track likelihood for each particle type; kaon, pion and proton ( $l_K$ ,  $l_\pi$  and  $l_p$ ). In this analysis the `SMSKaonSelector` is used in `tight` mode. This requires that:

$$l_K > r_\pi l_\pi \quad \text{and} \quad l_K > l_p \quad (3.6)$$

where:

$$r_\pi = 15 \quad \text{for} \quad 0.5 < p < 0.7 \text{ GeV}/c \quad (3.7)$$

$$r_\pi = 1 \quad \text{for} \quad 0.7 < p < 2.7 \text{ GeV}/c \quad (3.8)$$

$$r_\pi = 80 \quad \text{for} \quad p > 2.7 \text{ GeV}/c \quad (3.9)$$

Particles are said to be kaons (pions) if they pass (fail) this `tight` selector.

There are a number of reasons why this kaon selection process is not 100% efficient or pure. There are instances where the DIRC information is not available due to the small number of photons produced or due to the kaons not reaching the DIRC, which has limited solid angle coverage. It is also possible that the kaons decayed or interacted with the material of the detector before reaching the DIRC. In these cases a single track often results that has very little deviation from that of the original kaon and hence can be misidentified as that of the original kaon. The resolution in track-momentum, direction and Cerenkov light measurement also lead to imperfect kaon identification.

The imperfect particle identification, where a  $K$  gets misidentified as a  $\pi$  and vice versa has been studied in the inclusive branching fraction analysis of the  $B^\pm \rightarrow K^\pm \pi^\pm \pi^\mp$  decay [33] using a  $D^{*\pm}$  control sample. The decay  $D^{*+} \rightarrow D^0 \pi^+$ ,  $D^0 \rightarrow K^- \pi^+$  gives a very pure sample of kaons and pions to find the PID efficiencies; the kaon (pion) has the opposite (same) charge as the  $D^{*\pm}$  meson. For the `SMSKaonSelector` operating in `tight` mode, the probability of correctly identifying a  $K$  is 80%, which includes the geometrical acceptance, and the corresponding rate

of mis-identification of a  $K$  as a  $\pi$  is 20%. For  $\pi$ 's the identification is 98% efficient with the corresponding probability of mis-identifying a  $\pi$  as a  $K$  being 2%.

### 3.5.2 Particle Identification Efficiency Corrections

The particle identification efficiencies and misidentification rates are different in MC and data. PID corrections [49] must therefore be applied to the MC. Data control samples are used to form tables of efficiencies,  $\epsilon_{data}$ , which can be compared to the efficiencies,  $\epsilon_{MC}$ , found when using MC events for the same decay modes. These efficiency tables are binned in momentum,  $\theta$  and  $\phi$ . This analysis uses a PID correction procedure which has two stages. The first stage ensures that a given track passes the PID selection criteria. The second stage rejects tracks with a probability  $1 - (\epsilon_{data}/\epsilon_{MC})$  if the requirement  $\epsilon_{MC} > \epsilon_{data}$  is satisfied. This reduces the MC efficiency to match that of the data whilst doing nothing in the limit  $\epsilon_{MC} = \epsilon_{data}$ . The effect of this PID correcting procedure can be quantified by looking at the number of non-resonant MC events obtained with and without this correction applied. This shows that the PID corrections reduce the data sample by a factor of 0.977.

### 3.5.3 Electron Identification

The standard *BABAR* electron selector [50] is also a likelihood based selector which combines information from the EMC, DIRC and DCH sub-detectors. Electrons entering the EMC produce an electromagnetic shower. The EMC provides information on the energy of this shower together with its lateral and longitudinal shape. The DIRC provides information on the Cerenkov angle but this information is used only for particle momenta  $< 1.5 \text{ GeV}/c$ . The DCH provides information on  $dE/dx$ .

## 3.6 Event Selection

### 3.6.1 Event Pre-Selection

The first level of selection on the full sample of events is a three-body filter that selects candidate  $B$  decays to final states that contain three “stable” charged particles. The three particles used must have passed the selection criteria for the `GoodTracksLoose` list. The  $B$  candidates are selected according to the following criteria:

- The total charge of the  $B$  is required to be  $\pm 1$ ,
- The total number of tracks in the event is required to be  $\geq 4$ ,
- The total energy of the event is required to be  $< 20$  GeV,
- $m_{\text{ES}}$  of the  $B$  candidate is required to be within  $0.1$  GeV/ $c^2$  of the beam energy,
- The final state tracks can be assigned as either pions or kaons. All possible combinations and assignments are tested and the event accepted if any combination passes the requirement that  $\Delta E$  has an absolute value less than  $0.45$  GeV.

### 3.6.2 Batch Level Pre-Analysis

The output from the preselection is further refined by applying additional selection criteria. The output is then stored in `Root` ntuples [51]. An initial vertex for the  $B$  candidate is found using both kinematic and geometric fits, which use an iterative  $\chi^2$  minimisation procedure [52]. The kinematic fit requires momentum conservation and the geometric fit requires the three tracks to originate from the same point in space. After the vertex is formed,  $m_{\text{ES}}$  and  $\Delta E$  are recalculated. Event shape variables

are also calculated and a cut  $|\cos\theta_T| < 0.95$  applied. At this stage PID selectors are run and all the results are stored in the ntuple. All possible combinations of pions and kaons in the final state are formed. The only effect of different final state mass hypotheses on the  $B$  candidate is to change its energy. A second vertexing of the  $B$  candidate is then performed but this time with the resultant  $B$ -candidate mass constrained to be the correct  $B$ -meson mass. The vertexing algorithm varies the tracks within their errors and the event is retained if a  $B$ -mass-constrained vertex is successfully obtained. The  $m_{\text{ES}}$  variable is recalculated and a further cut  $|\Delta E| < 0.35$  GeV is applied.

### 3.6.3 Final Selection

After the preselection and batch level selection further criteria are applied in order to isolate the  $B^\pm \rightarrow K^\pm \pi^\pm \pi^\mp$  final state and further suppress backgrounds. The cut optimisation procedure follows that detailed in the previous analysis of the  $B^\pm \rightarrow h^\pm h^\mp h^\pm$  modes [33] where  $h$  is a  $\pi$  or a  $K$ . The  $|\cos\theta_T|$  and Fisher cuts are chosen to give the best value for  $S/\sqrt{S+B}$  where  $S$  and  $B$  are the expected number of signal and background events respectively.

- Candidates must have a successful kinematic fit to the  $B$  vertex for the  $K^\pm \pi^\pm \pi^\mp$  final state,
- The kaon candidate track must pass the `SMSKaonSelector` in tight mode,
- Pion candidate tracks must fail the `SMSKaonSelector` in tight mode,
- All tracks must fail the electron selector,
- The two pion candidate tracks must have opposite charges,  $q_{\pi_1} \times q_{\pi_2} = -1$ ,
- $|\cos\theta_T| < 0.70$ ,
- The value of the Fisher discriminant must be  $< 0.21$ ,

- The  $m_{\text{ES}}$  and  $\Delta E$  signal strip cuts are applied:  $-0.0349 < \Delta E < 0.0551$  GeV and  $5.20 < m_{\text{ES}} < 5.29$  GeV/ $c^2$ ,
- Invariant mass vetoes are applied to eliminate decays containing charm quarks (see Section 4.4 for more details).
- The  $m_{\text{ES}}$  signal box and sideband cuts are applied:  $5.271 < m_{\text{ES}} < 5.287$  GeV/ $c^2$  and  $5.20 < m_{\text{ES}} < 5.26$  GeV/ $c^2$ ,

The requirement of a single candidate per event is then imposed. Multiple candidates occur in less than 3% of events, and in these cases the final candidate is chosen at random. The final output is stored in a `Root` ntuple with a much reduced number of events and only the necessary variables for the analysis retained. The efficiency for these cuts is calculated using a sample of  $1.299 \times 10^6$   $B^\pm \rightarrow K^\pm \pi^\pm \pi^\mp$  non-resonant MC events and can be seen in Table 3.2.

Table 3.2: Summary of average efficiencies in the analysis of  $B^\pm \rightarrow K^\pm \pi^\pm \pi^\mp$ . Each of the cut efficiencies is measured relative to the previous cut. Also shown is the total efficiency for the signal strip, signal box and sideband. These total efficiencies are the total number of events passing the selection criteria divided by the total number of input/generated events. The uncertainties shown are statistical only.

Cut	Efficiency for $B^\pm \rightarrow K^\pm \pi^\pm \pi^\mp$ non-resonant MC
Reconstruction and preselection	0.698
Valid $K^\pm \pi^\pm \pi^\mp$ vertex fit hypothesis	0.980
Kaon PID requirements	0.746
Electron veto	1.000
$q_{\pi_1} \times q_{\pi_2} = -1$	0.974
$ \cos \theta_T  < 0.70$	0.706
Fisher $< 0.21$	0.727
$5.20 < m_{\text{ES}} < 5.29 \text{ GeV}/c^2$	0.994
$-0.0349 < \Delta E < 0.0551 \text{ GeV}$	0.813
Veto $\bar{D}^0$ , $J/\psi$ and $\psi(2S)$	0.831
Signal Strip:	0.17137
$\pm$ uncertainty	$3.6 \times 10^{-4}$
Signal Box: $5.271 < m_{\text{ES}} < 5.287 \text{ GeV}/c^2$	0.16664
$\pm$ uncertainty	$3.6 \times 10^{-4}$
Sideband: $5.20 < m_{\text{ES}} < 5.26 \text{ GeV}/c^2$	$3.013 \times 10^{-3}$
$\pm$ uncertainty	$4.8 \times 10^{-5}$

# Chapter 4

## Dalitz-Plot Analysis

### 4.1 Introduction

In order to perform this Dalitz-plot fit, a C++ / Root based package called **Laura++** [53] was developed. **Laura++** is a maximum likelihood based fitting program designed specifically for the Dalitz-plot analysis of  $B$ -meson decays to three charmless hadronic particles.

Probability Density Functions (PDFs) are constructed to describe the signal and backgrounds in terms of the Dalitz-plot variables. These PDFs are then combined to form a per-event likelihood  $\mathcal{L}$ . The total likelihood for  $N_{Tot}$  events in the data sample is given by:

$$\mathcal{L}_{Tot} = \prod_{n=1}^{N_{Tot}} \mathcal{L}_n \quad (4.1)$$

The aim of the **Laura++** software in this analysis is to obtain the magnitudes and phases of the signal components contributing to the  $B^\pm \rightarrow K^\pm \pi^\pm \pi^\mp$  decay. This is achieved by floating certain parameters of the PDFs to maximise this total likelihood, or equivalently, minimise the negative natural logarithm of the total likelihood:

$$-\ln \mathcal{L}_{Tot} = -\ln \left( \prod_{n=1}^{N_{Tot}} \mathcal{L}_n \right) = -\sum_{n=1}^{N_{Tot}} \ln \mathcal{L}_n. \quad (4.2)$$

In this chapter a full description of the per-event likelihood is given. This is followed by an in-depth discussion of the Dalitz-plot modelling of the signal,  $q\bar{q}$  background and  $B\bar{B}$  background components. The chapter concludes with a discussion of efficiency considerations.

## 4.2 Dalitz Fitting

### 4.2.1 Per Event Likelihood

The Dalitz-plot fit uses the invariant mass-squared pairs  $m_{13}^2$  and  $m_{23}^2$  as input measurements. For the decay  $B^\pm \rightarrow K^\pm \pi^\pm \pi^\mp$  the  $K^\pm$ ,  $\pi^\pm$  and  $\pi^\mp$  are labelled as 1, 2 and 3 respectively.

The unbinned per event likelihood function used to fit the data in the signal box is shown in Equation 4.3:

$$\begin{aligned} \mathcal{L}(m_{13}^2, m_{23}^2) = & (1 - f_{q\bar{q}} - f_{B\bar{B}}) \frac{|\sum_{i=1}^N c_i e^{i\theta_i} F_i(m_{13}^2, m_{23}^2)|^2 \epsilon(m_{13}^2, m_{23}^2)}{\int \int_{DP} |\sum_{i=1}^N c_i e^{i\theta_i} F_i(m_{13}^2, m_{23}^2)|^2 \epsilon(m_{13}^2, m_{23}^2) dm_{13}^2 dm_{23}^2} \\ & + f_{q\bar{q}} \frac{Q(m_{13}^2, m_{23}^2)}{\int \int_{DP} Q(m_{13}^2, m_{23}^2) dm_{13}^2 dm_{23}^2} \\ & + f_{B\bar{B}} \frac{B(m_{13}^2, m_{23}^2)}{\int \int_{DP} B(m_{13}^2, m_{23}^2) dm_{13}^2 dm_{23}^2} \end{aligned} \quad (4.3)$$

where

- $N$  is the number of signal resonant and non-resonant contributions to the plot,
- $F_i$  is the dynamical part of the signal amplitude of the resonant or non-resonant contribution  $i$ ,
- $c_i e^{i\theta_i}$  are complex coefficients, where  $c_i$  are the signal magnitudes and  $\theta_i$  are the signal phases,

- $\epsilon(m_{13}^2, m_{23}^2)$  is the reconstruction efficiency, including vetoes, defined for all points in the Dalitz plot,
- $Q(m_{13}^2, m_{23}^2)$  is the distribution of  $q\bar{q}$  background,
- $B(m_{13}^2, m_{23}^2)$  is the distribution of  $B\bar{B}$  background,
- $f_{q\bar{q}}$  and  $f_{B\bar{B}}$  are the fractions of  $q\bar{q}$  and  $B\bar{B}$  background events, respectively.

The background fractions  $f_{q\bar{q}}$  and  $f_{B\bar{B}}$  are calculated (Section 4.6) and then fixed in the Dalitz-plot fit. All parameters of the  $Q(m_{13}^2, m_{23}^2)$  and  $B(m_{13}^2, m_{23}^2)$  distributions are also fixed in the Dalitz-plot fit. The only floating parameters are the complex coefficients  $c_i e^{i\theta_i}$  that describe the signal amplitudes. One amplitude is used as a reference, and has a fixed magnitude of 1.0 and a fixed phase of 0.0. All other components are defined relative to this. The overall phase measured will have contributions from all the possible tree and penguin decay amplitudes (as described in Section 1.6) and will be a combination of strong  $\delta_S$  and weak  $\phi_W$  phases. As such a measurement of this phase is difficult to interpret in terms of CKM matrix elements.

## 4.2.2 Normalisation

There are many normalisation quantities that need to be calculated for this analysis. The lineshapes  $F_i(m_{13}^2, m_{23}^2)$  are each normalised such that, over the whole Dalitz plot

$$\int \int_{DP} F_i(m_{13}^2, m_{23}^2) dm_{13}^2 dm_{23}^2 = 1. \quad (4.4)$$

There are also normalisation integrals that need to be calculated for the overall signal and background amplitudes. These can be seen as the denominators of the three terms in Equation 4.3. These integrals are calculated using numerical integration that follows a Gauss-Legendre method [54]. The accuracy of this integration method can be checked using other Monte Carlo integration methods.

### 4.2.3 Fit Fractions

The measured magnitudes depend critically on the normalisation convention used, which makes the results difficult to interpret. The results of this analysis will instead be given in terms of fit fractions. The fit fraction is a convention used to quantify the amount of a given resonant or non-resonant contribution to the Dalitz plot. It is defined as shown in Equation 4.5:

$$(\text{Fit Fraction})_i = \frac{\int |c_i e^{i\theta_i} F_i(m_{13}^2, m_{23}^2)|^2 dm_{13}^2 dm_{23}^2}{\int |\sum_j c_j e^{i\theta_j} F_j(m_{13}^2, m_{23}^2)|^2 dm_{13}^2 dm_{23}^2}. \quad (4.5)$$

The sum over the resonant and non-resonant fit fractions is not necessarily unity due to the potential presence of net constructive or destructive interference.

The error on the fit fraction of a particular component has two contributions. The first is related to the error on the magnitude of that component, and the second is related to the magnitudes and phases of all the components. In the Dalitz-plot fit the reference component has a fixed magnitude of 1.0. This will artificially lower the error on the fit fraction of that component. To correct for this the fit is repeated using a different fixed signal component to get the true error on the fit fraction of the original fixed component. The calculation of the fit fraction error will be discussed further in Section 6.8.3.

## 4.3 Signal Resonance Modelling

The amplitude for a given decay mode is:

$$A_i = c_i e^{i\theta_i} F_i(m_{13}^2, m_{23}^2) \quad (4.6)$$

where  $c_i$  and  $\theta_i$  are the unknown magnitude and phase of each partial decay mode, while  $F_i$  describes the dynamics of the amplitude. This  $F_i$  consists of a product of

the invariant mass and angular distribution probabilities:

$$F_i = R_i(m) \times T_i(\cos \theta_H) \quad (4.7)$$

where  $R_i(m)$  is the resonance mass distribution and  $T_i(\cos \theta_H)$  is the angular probability distribution, where  $\theta_H$  is the helicity angle. The angular distribution terms are just Legendre polynomials:

- Spin 0 particle:  $T_i(\cos \theta_H) = 1$
- Spin 1 particle:  $T_i(\cos \theta_H) = \cos \theta_H$
- Spin 2 particle:  $T_i(\cos \theta_H) = 3 \cos^2 \theta_H - 1$

The default resonance mass distribution used in **Laura++** is a Relativistic Breit-Wigner lineshape:

$$R_i(m) = \frac{(m_0^2 - m^2) + im_0\Gamma(m)}{(m_0^2 - m^2)^2 + m_0^2\Gamma^2(m)} \quad (4.8)$$

where  $m_0$  is the pole mass and  $\Gamma$  is the decay width of the resonance which depends on the invariant mass of the two-daughter combination:

$$\Gamma(m) = \Gamma_0 \left( \frac{q}{q_0} \right)^{2j+1} \left( \frac{m_0}{m} \right) \frac{W_j^2(q)}{W_j^2(q_0)}, \quad (4.9)$$

$\Gamma_0$  is the decay width when the invariant mass of the daughter combination is equal to  $m_0$  and  $q$  is the momentum of either daughter in the rest frame of the resonance:

$$q = \sqrt{[m^2 - (m_a + m_b)^2][m^2 - (m_a - m_b)^2]}/2m \quad (4.10)$$

where  $m_a$  and  $m_b$  are the masses of the two daughter particles, respectively.  $q_0$  denotes the value of  $q$  when  $m = m_0$ .  $W_j(q)$  represents the Blatt-Weisskopf barrier form factor [55], which depends on the momentum  $q$  and the spin of the resonance  $j$ :

$$W_0 = 1 \quad (4.11)$$

$$W_1 = \sqrt{1/(1 + z^2)} \quad (4.12)$$

$$W_2 = \sqrt{1/(z^4 + 3z^2 + 9)} \quad (4.13)$$

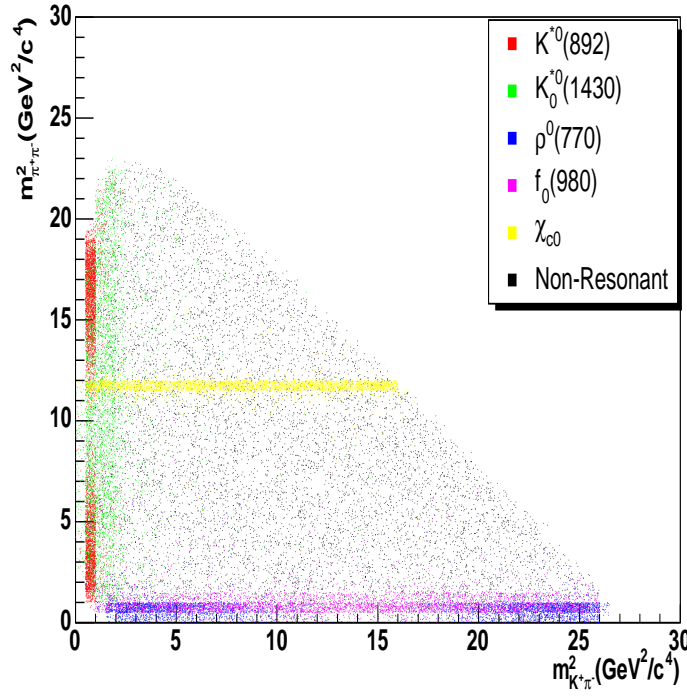


Figure 4.1: Simulated Dalitz plot for  $B^+ \rightarrow K^+ \pi^+ \pi^-$ . This plot is generated with six signal contributions  $K^{*0}(892)$ ,  $K_0^{*0}(1430)$ ,  $\rho^0(770)$ ,  $f_0(980)$ ,  $\chi_{c0}$  and non-resonant. Interference effects are not included.

where  $z = Rq$ , and  $R$  is the radius of the barrier, which is taken to be  $4.0 \text{ GeV}^{-1} \approx 0.8 \text{ fm}$ .

This Relativistic Breit-Wigner lineshape is used to describe all contributions to the Dalitz-plot except for the non-resonant amplitude which is generated flat in phase-space and the  $f_0(980)$  and  $K_0^{*0}(1430)$  components.

A simulated Dalitz plot for  $B^+ \rightarrow K^+ \pi^+ \pi^-$  containing six possible signal contributions is shown in Figure 4.1

### 4.3.1 $f_0(980)$ modelling

The  $f_0(980)$  component is modelled using a Flatté [56] lineshape which is a coupled-channel Breit-Wigner distribution. This is used for resonances that are above the  $KK$  threshold and hence can decay to both  $\pi\pi$  or  $KK$ .

$$R_i(m) = \frac{(m_0^2 - m^2) + im_0(\Gamma_{\pi\pi} + \Gamma_{KK})}{(m_0^2 - m^2)^2 + m_0^2(\Gamma_{\pi\pi} + \Gamma_{KK})^2} \quad (4.14)$$

The decay widths of the resonance in the  $\pi\pi$  and  $KK$  systems are given by:

$$\Gamma_{\pi\pi} = g_\pi \sqrt{(m^2 - 4m_\pi^2)}, \quad (4.15)$$

$$\Gamma_{KK} = g_K \sqrt{(m^2 - 4m_K^2)}, \quad (4.16)$$

where  $m_\pi$  and  $m_K$  are the masses of  $\pi$  and  $K$ , and  $g_\pi$  and  $g_K$  are coupling constants. To ensure continuity below the  $K$ - $K$  threshold, the width  $\Gamma_{KK}$  is set to be imaginary

$$\Gamma_{KK} = ig_K \sqrt{(4m_K^2 - m^2)} \quad (4.17)$$

when  $m < 2m_K$ . For the case when  $m < 2m_\pi$ , the widths for the  $\pi\pi$  and  $KK$  systems are both set to zero. There are three alternative sets of results for  $g_\pi$  and  $g_K$  to choose from:

- $g_\pi = 0.145$  and  $g_K/g_\pi = 4.35$  – BES experiment<sup>1</sup> [57]
- $g_\pi = 0.09 \pm 0.04 \pm 0.01$  and  $g_K = 0.02 \pm 0.01 \pm 0.03$  – E791 experiment [59]
- $g_\pi = 0.28 \pm 0.04$  and  $g_K = 0.56 \pm 0.18$  – WA76 experiment [60]

### 4.3.2 The $K\pi$ S-wave

Previous studies of the  $B^\pm \rightarrow K^\pm \pi^\pm \pi^\mp$  mode have suggested that there is a large contribution to the Dalitz-plot in the region around 1400 MeV/ $c^2$  in the  $K\pi$  spectrum. Experiments have disagreed on the details of the resonances involved, however

---

<sup>1</sup>These values were provided through private communication. A subsequent publication by the BES collaboration [58] uses values of  $g_\pi = 0.138 \pm 0.010$  and  $g_K/g_\pi = 4.45 \pm 0.25$

there is a consensus that resonant behaviour occurs at around  $1430 \text{ MeV}/c^2$  and this is labelled the  $K_0^{*0}(1430)$  resonance. The dynamics of the  $K\pi$  S-wave are not very well known. The LASS experiment studied  $K\pi$  scattering and produced a description of the S-wave that consists of a resonant part, the  $K_0^{*0}(1430)$ , and an effective range term [61,62]. The matrix element  $\mathcal{M}$ , modified for a production environment is shown in Equation 4.18,

$$\mathcal{M} = \frac{m_{K\pi}}{q \cot \delta_B - iq} + e^{2i\delta_B} \frac{m_0 \Gamma_0 \frac{m_0}{q_0}}{(m_0^2 - m_{K\pi}^2) - im_0 \Gamma_0 \frac{q}{m_{K\pi}} \frac{m_0}{q_0}} \quad (4.18)$$

where  $m_0$  and  $\Gamma_0$  are the mass and width of the  $K_0^{*0}(1430)$  resonance,  $q$  is defined in Equation 4.19,  $q_0$  is the value of  $q$  when  $m_{K\pi} = m_0$ , and  $\cot \delta_B$  is defined in Equation 4.20.

$$q = \sqrt{(m_{K\pi}^2 - (m_K + m_\pi)^2)(m_{K\pi}^2 - (m_K - m_\pi)^2)} / 2m_{K\pi} \quad (4.19)$$

$$\cot \delta_B = \frac{1}{aq} + \frac{1}{2}rq \quad (4.20)$$

where  $r$  is the effective range, and  $a$  is the scattering length. This amplitude is only tested up to around  $2 \text{ GeV}/c^2$ , and so the effective range term is cut off at the lower edge of the  $D^0$  veto.

### 4.3.3 Excited $\pi\pi$ resonances

There are many possibilities for resonances that may exist in the range  $1200\text{-}1600 \text{ MeV}/c^2$  in the  $\pi\pi$  spectrum. These higher resonances have many uncertainties associated with their properties. The  $f_0(1370)$  and  $\rho^0(1450)$  resonances have large errors on their masses and widths. All of the higher  $f$  resonances have possible decays to  $\pi\pi$  and  $KK$ , though the partial widths are poorly constrained. These excited  $\pi\pi$  resonances are implemented in `Laura++` as Relativistic Breit-Wigners with masses and widths as shown in Table 4.1.

Table 4.1: Possible resonances in the  $\pi\pi$  spectrum.

Resonance	Mass ( MeV/ $c^2$ )	Width ( MeV)
$f_2(1270)$	1275.4	185.1
$f_0(1370)$	1370	350
$\rho^0(1450)$	1465	310
$f_0(1500)$	1507	109
$f_2(1525)$	1525	76

## 4.4 $B\bar{B}$ Background Modelling

There is a significant source of background arising from  $B$ -meson decays to final states other than  $K^\pm\pi^\pm\pi^\mp$ . In order to identify the specific  $B\bar{B}$  background decays that contaminate the signal data, a high statistics MC sample of generic  $B^+B^-$  and  $B^0\bar{B}^0$  decays is studied. These generic events are subject to the same selection process as the on-resonance data and decays that pass the selection criteria are studied further and accounted for in the likelihood.

These  $B\bar{B}$  backgrounds can be characterised into four main categories. The first is pure combinatorics, where the  $B\bar{B}$  event contains three unrelated tracks which are subsequently reconstructed as signal. This combinatorial situation is the same as that of  $q\bar{q}$  backgrounds and hence these  $B\bar{B}$  events have a Dalitz-plot and  $m_{ES}$  distribution that looks almost identical to that for  $q\bar{q}$  decays. The second category is particle mis-identifications, where the  $B\bar{B}$  event is incorrectly identified due to a pion being reconstructed as a kaon or vice versa. The tight PID requirements reduce the feed-through from  $B^\pm \rightarrow \pi^\pm\pi^\pm\pi^\mp$  decays. The feed-through in the opposite direction from  $B^\pm \rightarrow K^\pm K^\mp\pi^\pm$  by misidentifying a kaon as a pion is very small due to the small branching fraction of this mode [32]. Alternatively there is the possibility of misidentifying a muon or electron as a pion. The largest sources of these backgrounds are from the modes  $B^\pm \rightarrow J/\psi K^\pm$ ,  $J/\psi \rightarrow \mu^+\mu^-$  and  $B^\pm \rightarrow \psi(2S)K^\pm$

,  $\psi(2S) \rightarrow \mu^+\mu^-$ . These modes are vetoed from the Dalitz-plot (see Section 4.4.1). The third category is specific  $B \rightarrow D$  decays. Due to the relative sizes of the CKM matrix elements  $B \rightarrow D$  decays have high branching fractions compared to the charmless decays. This means that decays with  $D$  mesons in the final state will be a significant contributor to the total  $B\bar{B}$  background. The majority of these decays are incorrectly reconstructed, with either misidentification of one of the final state particles or a low momentum  $\pi^0$  or  $\gamma$  being lost. This leads to the  $\Delta E$  distribution of these modes being peaked at negative values. Tightening the lower  $\Delta E$  edge of the signal box region (see Section 3.3.1) greatly reduces the presence of these background modes. The final category is 4-body charmless decays. Contributions exist from 4-body final states where one of the final state particles is lost. Modes with large contributions are  $B^\pm \rightarrow \eta' K^\pm$ ,  $\eta' \rightarrow \rho^0 \gamma$ ,  $\rho^0 \rightarrow \pi^+ \pi^-$  where the  $\gamma$  is not reconstructed and  $B^0 \rightarrow K^{*0} \bar{K}^{*0}$  with  $K^{*0} \rightarrow K^+ \pi^-$  and  $\bar{K}^{*0} \rightarrow K^- \pi^+$  where a kaon is lost.

Specific MC samples are made for any modes that are identified as contributing to the  $B\bar{B}$  background. These specific MC samples are used to determine the reconstruction efficiency which is combined with branching fraction information taken from the PDG [8] to calculate the number of expected events of the  $B\bar{B}$  background mode in the signal box. For those modes that are not yet measured, the branching fraction is taken to be half the measured upper limit, with an error that is also half the upper limit. A total of 73 modes are studied and 54 of these are found to be significant. The reconstruction efficiency and number of expected signal box events for all  $B\bar{B}$  backgrounds found to be significant can be seen in Table 4.2 and Table 4.3 for charged  $B$ -meson decays and Table 4.4 and Table 4.5 for neutral  $B$ -meson decays.

Table 4.2: Charm  $B^+B^-$  background modes. The table shows the branching fraction for each mode along with the reconstruction efficiency and number of events expected in the signal box.

Mode + Charge Conjugate	BF ( $10^{-6}$ )	Signal Box Efficiency			Number of Expected Events in Signal Box		
		All	$B^+$	$B^-$	All	$B^+$	$B^-$
$B^+ \rightarrow \bar{D}^0 K^+; \bar{D}^0 \rightarrow K^+ \pi^-$	$14.1 \pm 2.3$	$0.545 \pm 0.012$	$0.2762 \pm 0.0087$	$0.2691 \pm 0.0086$	$17.8 \pm 3.0$	$9.0 \pm 1.5$	$8.8 \pm 1.5$
$B^+ \rightarrow \bar{D}^0 K^+; \bar{D}^0 \rightarrow K^+ \pi^- \pi^0$	$48.1 \pm 8.3$	$0.0149 \pm 0.0033$	$0.0060 \pm 0.0021$	$0.0090 \pm 0.0026$	$1.66 \pm 0.47$	$0.66 \pm 0.26$	$1.00 \pm 0.34$
$B^+ \rightarrow \bar{D}^0 \pi^+; \bar{D}^0 \rightarrow K^+ K^-$	$19.4 \pm 1.3$	$0.530 \pm 0.051$	$0.260 \pm 0.036$	$0.270 \pm 0.037$	$23.8 \pm 2.8$	$11.7 \pm 1.8$	$12.1 \pm 1.9$
$B^+ \rightarrow \bar{D}^0 \pi^+; \bar{D}^0 \rightarrow K^+ \pi^-$	$189.2 \pm 11.9$	$0.238 \pm 0.010$	$0.1259 \pm 0.0076$	$0.1116 \pm 0.0072$	$104.2 \pm 8.1$	$55.2 \pm 4.9$	$48.9 \pm 4.4$
$B^+ \rightarrow \bar{D}^0 \pi^+; \bar{D}^0 \rightarrow K^+ \pi^- \pi^0$	$647.4 \pm 54.8$	$0.035 \pm 0.0037$	$0.0169 \pm 0.0026$	$0.0181 \pm 0.0027$	$52.4 \pm 7.2$	$25.3 \pm 4.5$	$27.1 \pm 4.7$
$B^+ \rightarrow \bar{D}^0 \rho^+; \bar{D}^0 \rightarrow K^+ \pi^-$	$509.2 \pm 69.5$	$0.0253 \pm 0.0025$	$0.0128 \pm 0.0018$	$0.0125 \pm 0.0017$	$29.9 \pm 5.0$	$15.1 \pm 2.9$	$14.8 \pm 2.9$
$B^+ \rightarrow \bar{D}^0 \rho^+; \bar{D}^0 \rightarrow K^+ \pi^- \pi^0$	$1742 \pm 257$	$0.0048 \pm 0.0013$	$0.00238 \pm 0.00090$	$0.00238 \pm 0.00090$	$19.2 \pm 5.9$	$9.6 \pm 3.9$	$9.6 \pm 3.9$
$B^+ \rightarrow \bar{D}^{*0} \pi^+; \bar{D}^{*0} \rightarrow \bar{D}^0 \gamma; \bar{D}^0 \rightarrow K^+ \pi^-$	$66.6 \pm 7.9$	$0.0913 \pm 0.0083$	$0.0377 \pm 0.0053$	$0.0536 \pm 0.0064$	$14.1 \pm 2.1$	$5.8 \pm 1.1$	$8.3 \pm 1.4$
$B^+ \rightarrow \bar{D}^{*0} \pi^+; \bar{D}^{*0} \rightarrow \bar{D}^0 \gamma; \bar{D}^0 \rightarrow K^+ \pi^- \pi^0$	$227.8 \pm 29.8$	$0.0076 \pm 0.0025$	$0.0059 \pm 0.0022$	$0.0017 \pm 0.0012$	$4.0 \pm 1.4$	$3.1 \pm 1.2$	$0.89 \pm 0.64$
$B^+ \rightarrow \bar{D}^{*0} \pi^+; \bar{D}^{*0} \rightarrow \bar{D}^0 \pi^0; \bar{D}^0 \rightarrow K^+ \pi^-$	$108.2 \pm 11.0$	$0.0785 \pm 0.0068$	$0.0471 \pm 0.0052$	$0.0314 \pm 0.0043$	$19.7 \pm 2.6$	$11.8 \pm 1.8$	$7.9 \pm 1.3$
$B^+ \rightarrow \bar{D}^{*0} \pi^+; \bar{D}^{*0} \rightarrow \bar{D}^0 \pi^0; \bar{D}^0 \rightarrow K^+ \pi^- \pi^0$	$370.2 \pm 43.1$	$0.0060 \pm 0.0016$	$0.0034 \pm 0.0012$	$0.0026 \pm 0.0011$	$5.2 \pm 1.5$	$3.0 \pm 1.1$	$2.22 \pm 0.94$
$B^+ \rightarrow \bar{D}^0 e^+ \nu_e; \bar{D}^0 \rightarrow K^+ \pi^-$	$817.0 \pm 85.8$	$0.00272 \pm 0.00096$	$0.00136 \pm 0.00068$	$0.00136 \pm 0.00068$	$5.2 \pm 1.9$	$2.6 \pm 1.3$	$2.6 \pm 1.3$
$B^+ \rightarrow \bar{D}^0 e^+ \nu_e; \bar{D}^0 \rightarrow K^+ \pi^- \pi^0$	$2795 \pm 334$	$0.00136 \pm 0.00068$	$0.00 \pm 0.00$	$0.00136 \pm 0.00068$	$8.8 \pm 4.5$	$0.0 \pm 0.0$	$8.8 \pm 4.5$
$B^+ \rightarrow \bar{D}^0 \mu^+ \nu_\mu; \bar{D}^0 \rightarrow K^+ \pi^-$	$817.0 \pm 85.8$	$0.0044 \pm 0.0012$	$0.00170 \pm 0.00076$	$0.00272 \pm 0.00096$	$8.4 \pm 2.5$	$3.2 \pm 1.5$	$5.2 \pm 1.9$
$B^+ \rightarrow \bar{D}^0 \mu^+ \nu_\mu; \bar{D}^0 \rightarrow K^+ \pi^- \pi^0$	$2795 \pm 334$	$0.00206 \pm 0.00084$	$0.00069 \pm 0.00048$	$0.00137 \pm 0.00069$	$13.3 \pm 5.7$	$4.4 \pm 3.2$	$8.9 \pm 4.6$
$B^+ \rightarrow \bar{D}^{*0} e^+ \nu_e; \bar{D}^{*0} \rightarrow \bar{D}^0 \gamma; \bar{D}^0 \rightarrow K^+ \pi^-$	$941.1 \pm 104.2$	$0.00138 \pm 0.00069$	$0.00138 \pm 0.00069$	$0.00 \pm 0.00$	$3.0 \pm 1.5$	$3.0 \pm 1.5$	$0.0 \pm 0.0$
$B^+ \rightarrow \bar{D}^{*0} e^+ \nu_e; \bar{D}^{*0} \rightarrow \bar{D}^0 \gamma; \bar{D}^0 \rightarrow K^+ \pi^- \pi^0$	$3219 \pm 401$	$0.00282 \pm 0.00010$	$0.00247 \pm 0.00094$	$0.00035 \pm 0.00035$	$21.1 \pm 7.9$	$18.4 \pm 7.3$	$2.6 \pm 2.7$
$B^+ \rightarrow \bar{D}^{*0} \mu^+ \nu_\mu; \bar{D}^{*0} \rightarrow \bar{D}^0 \gamma; \bar{D}^0 \rightarrow K^+ \pi^-$	$941.1 \pm 104.2$	$0.0031 \pm 0.0010$	$0.00139 \pm 0.00069$	$0.00174 \pm 0.00078$	$6.8 \pm 2.4$	$3.0 \pm 1.6$	$3.8 \pm 1.7$
$B^+ \rightarrow \bar{D}^{*0} \mu^+ \nu_\mu; \bar{D}^{*0} \rightarrow \bar{D}^0 \gamma; \bar{D}^0 \rightarrow K^+ \pi^- \pi^0$	$3219 \pm 401$	$0.00068 \pm 0.00048$	$0.00 \pm 0.00$	$0.00068 \pm 0.00048$	$5.1 \pm 3.6$	$0.0 \pm 0.0$	$5.1 \pm 3.6$
$B^+ \rightarrow \bar{D}^{*0} e^+ \nu_e; \bar{D}^{*0} \rightarrow \bar{D}^0 \pi^0; \bar{D}^0 \rightarrow K^+ \pi^-$	$1529 \pm 142$	$0.00102 \pm 0.00059$	$0.00068 \pm 0.00048$	$0.00034 \pm 0.00034$	$3.6 \pm 2.1$	$2.4 \pm 1.7$	$1.2 \pm 1.2$
$B^+ \rightarrow \bar{D}^{*0} e^+ \nu_e; \bar{D}^{*0} \rightarrow \bar{D}^0 \pi^0; \bar{D}^0 \rightarrow K^+ \pi^- \pi^0$	$5231 \pm 571$	$0.00206 \pm 0.00084$	$0.00103 \pm 0.00059$	$0.00103 \pm 0.00059$	$24.9 \pm 10.5$	$12.5 \pm 7.3$	$12.5 \pm 7.3$
$B^+ \rightarrow \bar{D}^{*0} \mu^+ \nu_\mu; \bar{D}^{*0} \rightarrow \bar{D}^0 \pi^0; \bar{D}^0 \rightarrow K^+ \pi^-$	$1529 \pm 142$	$0.00204 \pm 0.00083$	$0.00034 \pm 0.00034$	$0.00170 \pm 0.00076$	$7.2 \pm 3.0$	$1.2 \pm 1.2$	$6.0 \pm 2.8$
$B^+ \rightarrow \bar{D}^{*0} \mu^+ \nu_\mu; \bar{D}^{*0} \rightarrow \bar{D}^0 \pi^0; \bar{D}^0 \rightarrow K^+ \pi^- \pi^0$	$5231 \pm 571$	$0.00068 \pm 0.00048$	$0.00034 \pm 0.00034$	$0.00034 \pm 0.00034$	$8.3 \pm 5.9$	$4.1 \pm 4.1$	$4.1 \pm 4.1$
Total Charm Charged $B$ backgrounds					$407 \pm 23$	$205 \pm 15$	$202 \pm 15$

Table 4.3: Charmless  $B^+B^-$  background modes. The table shows the branching fraction for each mode along with the reconstruction efficiency and number of events expected in the signal box.

Mode + Charge Conjugate	BF ( $10^{-6}$ )	Signal Box Efficiency			Number of Expected Events in Signal Box		
		All	$B^+$	$B^-$	All	$B^+$	$B^-$
$B^+ \rightarrow K^+K^-K^+$	$30.1 \pm 1.9$	$0.0339 \pm 0.0016$	$0.0177 \pm 0.0012$	$0.0162 \pm 0.0011$	$2.36 \pm 0.19$	$1.23 \pm 0.11$	$1.13 \pm 0.11$
$B^+ \rightarrow K^+K^-\pi^+$	$< 6.3$	$0.7813 \pm 0.0077$	$0.3880 \pm 0.0055$	$0.3834 \pm 0.0054$	$5.7 \pm 5.7$	$2.9 \pm 2.9$	$2.8 \pm 2.8$
$B^+ \rightarrow \pi^+\pi^-\pi^+$	$16.2 \pm 2.5$	$0.4859 \pm 0.0047$	$0.2437 \pm 0.0033$	$0.2422 \pm 0.0033$	$18.2 \pm 2.8$	$9.2 \pm 1.2$	$9.1 \pm 1.4$
$B^+ \rightarrow K^{*+}\gamma$	$40.3 \pm 2.6$	$0.00275 \pm 0.00080$	$0.00115 \pm 0.00051$	$0.00161 \pm 0.00061$	$0.257 \pm 0.076$	$0.107 \pm 0.048$	$0.150 \pm 0.058$
$B^+ \rightarrow K^{*+}K^{*0}; K^{*+} \rightarrow K^0\pi^+; K^{*0} \rightarrow K^+\pi^-$ - Long <sup>a</sup>	$< 15.8$	$0.0172 \pm 0.0038$	$0.0090 \pm 0.0027$	$0.0082 \pm 0.0026$	$0.31 \pm 0.32$	$0.16 \pm 0.17$	$0.15 \pm 0.15$
$B^+ \rightarrow K^{*+}K^{*0}; K^{*+} \rightarrow K^+\pi^0; K^{*0} \rightarrow K^+\pi^-$ - Long	$< 7.9$	$0.0397 \pm 0.0056$	$0.0206 \pm 0.0040$	$0.0290 \pm 0.0039$	$0.36 \pm 0.37$	$0.19 \pm 0.19$	$0.17 \pm 0.18$
$B^+ \rightarrow \rho^+K^{*0}; K^{*0} \rightarrow K^+\pi^-$ - Long	$3.07 \pm 0.67$	$0.0905 \pm 0.0034$	$0.0458 \pm 0.0024$	$0.0448 \pm 0.0024$	$0.64 \pm 0.14$	$0.325 \pm 0.073$	$0.318 \pm 0.071$
$B^+ \rightarrow \rho^0K^{*+}; K^{*+} \rightarrow K^+\pi^0$ - Long	$1.8 \pm 0.6$	$0.1811 \pm 0.0095$	$0.0856 \pm 0.0065$	$0.0955 \pm 0.0069$	$0.74 \pm 0.26$	$0.35 \pm 0.12$	$0.39 \pm 0.14$
$B^+ \rightarrow \rho^+\rho^0$	$26.4 \pm 6.2$	$0.0588 \pm 0.0041$	$0.0341 \pm 0.0031$	$0.0247 \pm 0.0026$	$3.60 \pm 0.88$	$2.09 \pm 0.53$	$1.51 \pm 0.39$
$B^+ \rightarrow \eta'K^+; \eta' \rightarrow \pi^+\pi^-\gamma$	$22.9 \pm 1.6$	$0.710 \pm 0.022$	$0.371 \pm 0.016$	$0.339 \pm 0.015$	$37.7 \pm 2.9$	$19.7 \pm 1.6$	$18.0 \pm 1.5$
$B^+ \rightarrow \eta'\pi^+; \eta' \rightarrow \pi^+\pi^-\gamma$	$1.24 \pm 0.33$	$0.1158 \pm 0.0089$	$0.0603 \pm 0.0064$	$0.0555 \pm 0.0062$	$0.332 \pm 0.092$	$0.173 \pm 0.049$	$0.159 \pm 0.046$
$B^+ \rightarrow K_s^0K^+;$	$0.14 \pm 0.14$	$6.175 \pm 0.0056$	$3.134 \pm 0.0041$	$3.141 \pm 0.0040$	$5.9 \pm 5.9$	$3.0 \pm 3.0$	$2.9 \pm 2.9$
$B^+ \rightarrow K_s^0\pi^+;$	$8.31 \pm 0.45$	$0.228 \pm 0.010$	$0.1160 \pm 0.0072$	$0.1132 \pm 0.0072$	$4.40 \pm 0.31$	$2.23 \pm 0.19$	$2.16 \pm 0.18$
Total Charmless Charged $B$ backgrounds					$81 \pm 9$	$42 \pm 5$	$39 \pm 5$

<sup>a</sup>Long refers to the longitudinal part of the vector-vector decay

Table 4.4: Charm  $B^0\bar{B}^0$  background modes. The table shows the branching fraction for each mode along with the reconstruction efficiency and number of events expected in the signal box.

Mode + Charge Conjugate	BF ( $10^{-6}$ )	Signal Box Efficiency (%)			Number of Expected Events in Signal Box		
		All	$B^+$	$B^-$	All	$B^+$	$B^-$
$B^0 \rightarrow D^- K^+; D^- \rightarrow \pi^- \pi^0$	$0.52 \pm 0.21$	$0.1417 \pm 0.0069$	$0.0664 \pm 0.0047$	$0.0753 \pm 0.0050$	$0.171 \pm 0.069$	$0.080 \pm 0.033$	$0.091 \pm 0.038$
$B^0 \rightarrow \bar{D}^0 \rho^0; \bar{D}^0 \rightarrow K^+ \pi^-$	$11.0 \pm 4.2$	$0.0300 \pm 0.0065$	$0.0214 \pm 0.0055$	$0.0086 \pm 0.0035$	$0.77 \pm 0.34$	$0.55 \pm 0.25$	$0.22 \pm 0.12$
$B^0 \rightarrow D^{*-} \pi^+; D^{*-} \rightarrow \bar{D}^0 \pi^-; \bar{D}^0 \rightarrow X$	$1870 \pm 143$	$0.00431 \pm 0.00032$	$0.00232 \pm 0.00023$	$0.00199 \pm 0.00022$	$18.7 \pm 2.0$	$10.0 \pm 1.3$	$8.6 \pm 1.2$
$B^0 \rightarrow D^{*-} \rho^+; D^{*-} \rightarrow \bar{D}^0 \pi^-; \bar{D}^0 \rightarrow X$	$4600 \pm 610$	$0.00019 \pm 0.00013$	$0.00 \pm 0.00$	$0.00019 \pm 0.00013$	$2.0 \pm 1.5$	$0.00 \pm 0.00$	$2.0 \pm 1.5$
$B^0 \rightarrow \bar{D}^{*0} \rho^0; \bar{D}^{*0} \rightarrow \bar{D}^0 \gamma \text{ or } \bar{D}^0 \pi^0; \bar{D}^0 \rightarrow K^+ \pi^-$	$9.69 \pm 9.69$	$0.0021 \pm 0.0012$	$0.00 \pm 0.00$	$0.0021 \pm 0.0012$	$0.048 \pm 0.056$	$0.00 \pm 0.00$	$0.048 \pm 0.056$
Total Charm Neutral $B$ backgrounds					$22 \pm 2$	$11 \pm 1$	$11 \pm 2$

Table 4.5: Charmless  $B^0\bar{B}^0$  background modes. The table shows the branching fraction for each mode along with the reconstruction efficiency and number of events expected in the signal box.

Mode + Charge Conjugate	BF ( $10^{-6}$ )	Signal Box Efficiency (%)			Number of Expected Events in Signal Box		
		All	$B^+$	$B^-$	All	$B^+$	$B^-$
$B^0 \rightarrow K^+K^-\pi^0$	< 19	$0.0373 \pm 0.0054$	$0.0222 \pm 0.0042$	$0.0151 \pm 0.0035$	$0.82 \pm 0.83$	$0.49 \pm 0.49$	$0.33 \pm 0.34$
$B^0 \rightarrow K^+\pi^-\pi^0$	$35.6 \pm 3.4$	$0.0905 \pm 0.0020$	$0.0446 \pm 0.0014$	$0.0459 \pm 0.0014$	$7.47 \pm 0.74$	$3.68 \pm 0.37$	$3.79 \pm 0.38$
$B^0 \rightarrow \pi^+\pi^-\pi^0$	< 72	$0.0261 \pm 0.0011$	$0.01324 \pm 0.00079$	$0.01282 \pm 0.00078$	$2.2 \pm 2.2$	$1.1 \pm 1.1$	$1.1 \pm 1.1$
$B^0 \rightarrow K_2^{*0}(1430)\gamma$	$12.4 \pm 2.4$	$0.0092 \pm 0.0022$	$0.0049 \pm 0.0016$	$0.0044 \pm 0.0015$	$0.266 \pm 0.083$	$0.141 \pm 0.054$	$0.125 \pm 0.050$
$B^0 \rightarrow K^{*0}(1410)\gamma$	< 130	$0.00208 \pm 0.00085$	$0.00139 \pm 0.00069$	$0.00069 \pm 0.00049$	$0.32 \pm 0.34$	$0.21 \pm 0.23$	$0.10 \pm 0.13$
$B^0 \rightarrow K^{*0}\gamma$	$40.1 \pm 2.1$	$0.0099 \pm 0.0016$	$0.0059 \pm 0.0012$	$0.0041 \pm 0.0010$	$0.92 \pm 0.16$	$0.55 \pm 0.12$	$0.379 \pm 0.097$
$B^0 \rightarrow K^{*0}\bar{K}^{*0}; K^{*0} \rightarrow K^+\pi^-; \bar{K}^{*0} \rightarrow K^-\pi^+ - \text{Long}^a$	< 4.9	$0.0475 \pm 0.0062$	$0.0189 \pm 0.0039$	$0.0287 \pm 0.0048$	$0.27 \pm 0.27$	$0.11 \pm 0.11$	$0.16 \pm 0.16$
$B^0 \rightarrow K^+\pi^-$	$18.2 \pm 0.8$	$0.0646 \pm 0.0019$	$0.0335 \pm 0.0013$	$0.0311 \pm 0.0013$	$2.72 \pm 0.15$	$1.414 \pm 0.085$	$1.311 \pm 0.081$
$B^0 \rightarrow \rho^+K^-$	$9.9 \pm 1.6$	$0.766 \pm 0.011$	$0.3978 \pm 0.0078$	$0.3686 \pm 0.0075$	$17.6 \pm 2.9$	$9.1 \pm 1.5$	$8.5 \pm 1.4$
$B^0 \rightarrow \rho^+K^{*-}; K^{*+} \rightarrow K^+\pi^0 - \text{Long}$	< 8	$0.125 \pm 0.032$	$0.083 \pm 0.026$	$0.042 \pm 0.019$	$1.2 \pm 1.2$	$0.77 \pm 0.81$	$0.39 \pm 0.42$
$B^0 \rightarrow \rho^0K^{*0}; K^{*0} \rightarrow K^+\pi^- - \text{Long}$	< 0.86	$0.1708 \pm 0.0092$	$0.0842 \pm 0.0065$	$0.0866 \pm 0.0065$	$0.17 \pm 0.17$	$0.085 \pm 0.085$	$0.087 \pm 0.087$
$B^0 \rightarrow \rho^+\rho^-$	$30.0 \pm 6.0$	$0.0486 \pm 0.0010$	$0.02553 \pm 0.00076$	$0.02307 \pm 0.00073$	$3.38 \pm 0.68$	$1.78 \pm 0.36$	$1.60 \pm 0.33$
$B^0 \rightarrow \rho^0\rho^0$	< 1.1	$0.0970 \pm 0.0069$	$0.0434 \pm 0.0046$	$0.0537 \pm 0.0051$	$0.12 \pm 0.12$	$0.055 \pm 0.056$	$0.069 \pm 0.069$
Total Charmless Neutral $B$ backgrounds					$37 \pm 4$	$19 \pm 2$	$18 \pm 2$

<sup>a</sup>Long refers to the longitudinal part of the vector-vector decay

The  $B\bar{B}$  background Dalitz plot shape is modelled using a 2-dimensional histogram. For a given contributing mode, the available MC events are plotted on the Dalitz-plot and then scaled to the calculated expected number of events. A comparison of the  $B^-$  and  $B^+$  invariant mass distributions is shown in Figure 4.2. The statistics used

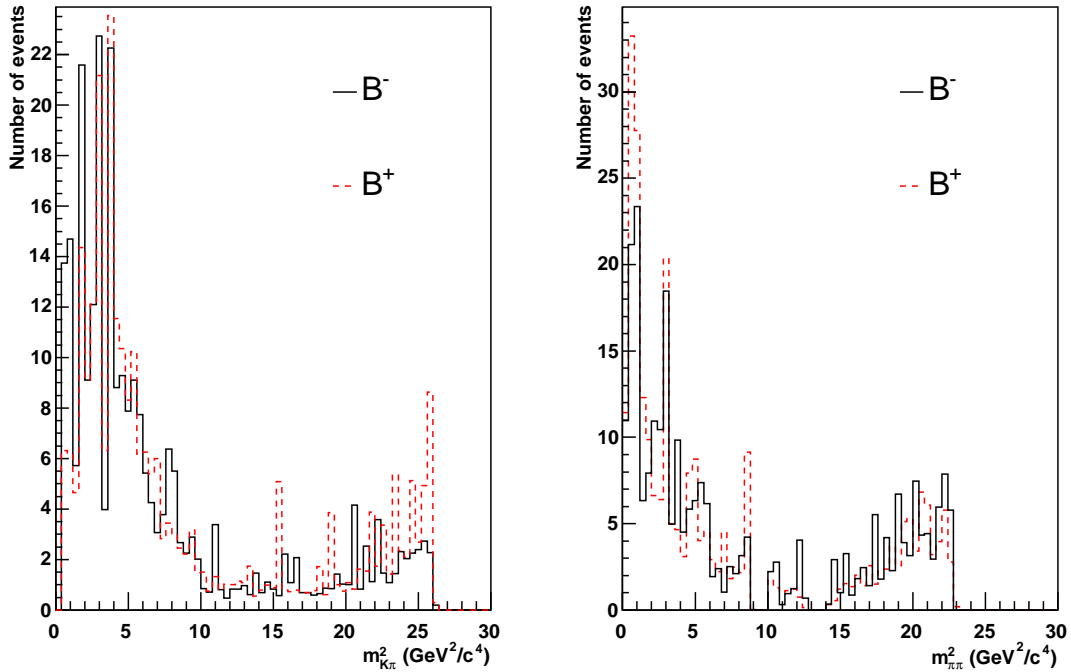


Figure 4.2:  $B\bar{B}$  background invariant mass squared distributions for  $B^-$  and  $B^+$ . The left histogram is for the  $K\pi$  pair and the right histogram is for the  $\pi\pi$  pair.

to construct these distributions are quite low but it is possible that differences exist between the  $B^-$  and  $B^+$  samples. Therefore separate  $B\bar{B}$  background histograms are constructed for  $B^-$  and  $B^+$  decays. These  $B\bar{B}$  histograms can be seen in Figure 4.3. In order to reduce the effect of statistical fluctuations linear interpolation is applied between the histogram bins.

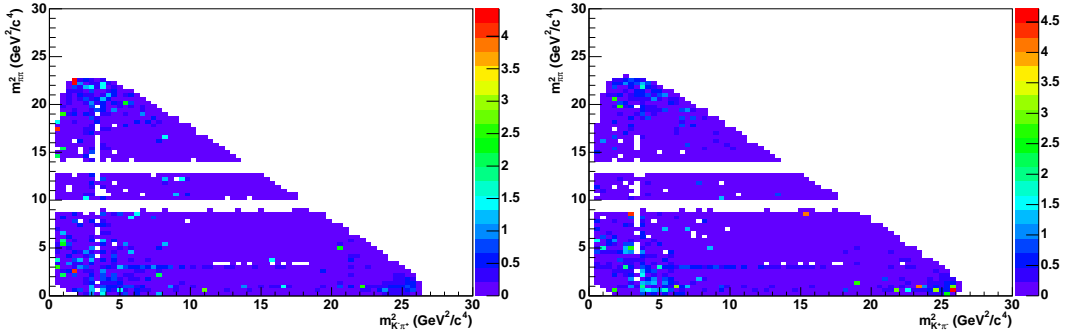


Figure 4.3:  $B\bar{B}$  background histograms constructed using MC events. The left plot is for  $B^-$  events and the right plot is for  $B^+$  events.

#### 4.4.1 Charm Vetoes

Decays containing  $D$  mesons have large branching fractions compared to the charmless decays.  $D$  mesons are extremely narrow and subsequently do not interfere with the charmless contributions to the Dalitz plot. These decays are removed from the Dalitz plot by applying the invariant mass vetoes shown in Table 4.6. Charmonium states such as  $J/\psi$  and  $\psi(2S)$  can also have large contributions to the Dalitz plot due to the mis-reconstruction of their lepton decay products as pions. These states are also vetoed.

Table 4.6: The invariant mass veto ranges (in  $\text{GeV}/c^2$ ) for intermediate resonances for  $K^\pm\pi^\pm\pi^\mp$ . The leptons,  $l$ , in the  $J/\psi$  and  $\psi(2S)$  decays are misidentified as pions.

Resonance	Veto Region $\text{GeV}/c^2$
$\bar{D}^0 \rightarrow K^\pm\pi^\mp$	$1.80 < m_{K\pi} < 1.90$
$\bar{D}^0 \rightarrow \pi^\pm\pi^\mp$	$1.80 < m_{\pi\pi} < 1.90$
$J/\psi \rightarrow l^+l^-$	$2.97 < m_{\pi\pi} < 3.17$
$\psi(2S) \rightarrow l^+l^-$	$3.56 < m_{\pi\pi} < 3.76$

### 4.4.2 $\chi_{c0}$

The  $\chi_{c0}$  is a charmonium state with  $J^{PC} = 0^{++}$ . It has a mass of 3.415 GeV/ $c^2$  and a width of 14.9 MeV [8]. It can interfere with the charmless resonant and non-resonant decay amplitudes. It is therefore included in the Dalitz Plot analysis.

## 4.5 Continuum Background Modelling

The distribution of  $q\bar{q}$  background events in the Dalitz plot is determined using a sample of data events from an  $m_{ES}$  sideband. This region is illustrated in Figure 3.1 in Section 3.3.1.

The possibility of correlations between  $m_{ES}$  and Dalitz distribution variables has been studied and found to be negligible. This can be seen in Figure 4.4 where the invariant mass  $m_{K\pi}$  and  $m_{\pi\pi}$  distributions are shown for two different  $m_{ES}$  regions. No significant differences in shape are observed and so it is safe to take the  $q\bar{q}$  background Dalitz-plot distribution from this sideband.

### 4.5.1 Analytical Model

An analytical model for describing the  $q\bar{q}$  background Dalitz-plot distribution was developed for `Laura++`. This model uses a parameterisation which is the sum of three functions of the form:

$$B(m_{ij}, \cos\theta_{H_{ij}}) = A \left( m_{ij} - m_{ij}^0 \right)^{b/c} e^{-(m_{ij} - m_{ij}^0)/c} \times (1 + d_k \cos\theta_{H_{ij}} + e_k \cos^2\theta_{H_{ij}}), \quad (4.21)$$

where  $B$  is the intensity of the background for a side in the Dalitz plot,  $m_{ij}$  is the invariant mass combination of the two daughters  $i$  and  $j$ ,  $m_{ij}^0$  is the kinematic threshold for  $m_{ij}$ ,  $A$  is the normalisation factor,  $b$  is the position of the peak with

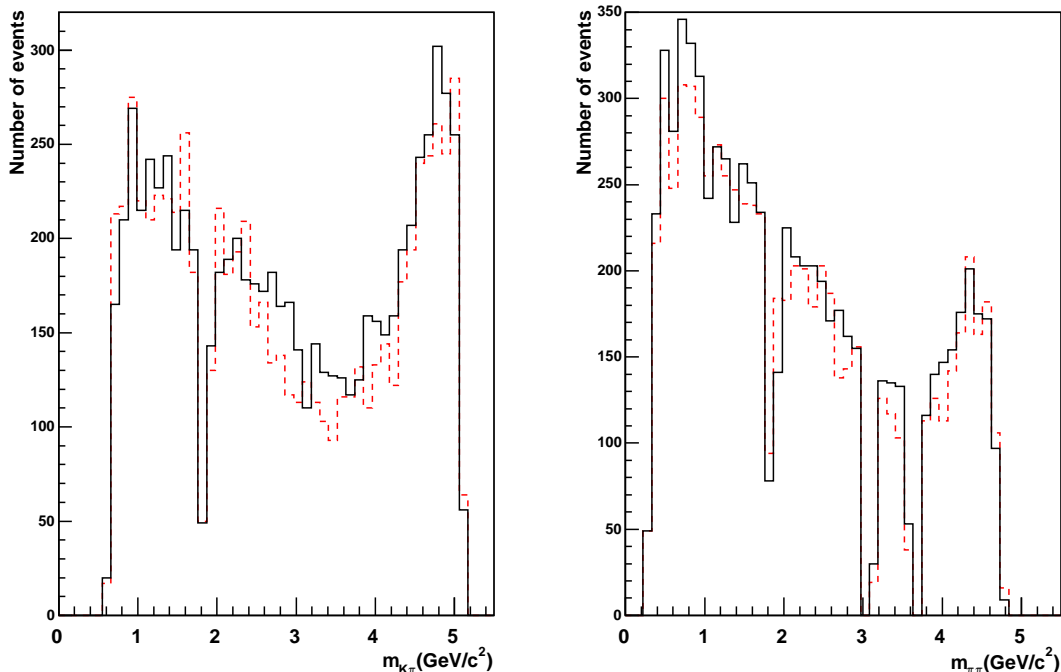


Figure 4.4: Invariant mass distributions for on-resonance events in different sideband  $m_{ES}$  regions. The solid black histogram corresponds to  $5.20 < m_{ES} < 5.23 \text{ GeV}/c^2$  and the dashed red histogram corresponds to  $5.23 < m_{ES} < 5.26 \text{ GeV}/c^2$ .

respect to  $m_{ij}^0$  and  $c$  is the decay scale. This equation also assumes a possible quadratic dependence on the cosine of the helicity angle,  $\cos\theta_{H_{ij}}$ , where  $d_k$  and  $e_k$  are coefficients for the linear and quadratic terms, however in the current analysis the helicity angle dependence is not used and  $d_k = e_k = 0$ .

The background is parameterised in  $m_{ij} - \cos\theta_{H_{ij}}$  space as shown in Equation 4.21, rather than  $m_{ij}^2 - m_{ik}^2$ . Hence the  $B$  term must be divided by the appropriate Jacobean ( $J$ ) in order to get the background term  $Q$  in Equation 4.3:

$$Q(m_{13}^2, m_{23}^2) = \sum_1^3 B(m_{ij}, \cos\theta_{H_{ij}})/J \quad (4.22)$$

where the sum is over the three possible invariant mass pairs. This background

function has an analytical integral (ignoring the cosine helicity terms):

$$\int_0^\infty (m_{ij} - m_{ij}^0)^{b/c} e^{-(m_{ij}-m_{ij}^0)/c} dm_{ij} = \Gamma(1 + b/c)c^{1+b/c} \quad (4.23)$$

where  $\Gamma$  is the mathematical Gamma function<sup>2</sup>. A slight numerical correction is made to the integral (using Simpson's rule) to account for the fact that the function does not extend to infinity, nor is it zero at  $m_{ij} \approx 5.279 \text{ GeV}/c^2$ , the mass of the  $B$  meson. A small quantity  $I_\delta$  is therefore subtracted from the integral where  $I_\delta$  is the area under the  $B(m_{ij})$  function for  $m_{ij}$  between the maximum kinematic limit and 20 GeV where the function has dropped to zero. The normalisation integral is also modified by a weighting technique to account for the regions of the Dalitz plot that are vetoed.

There is also the possibility of resonance peaks in the continuum background. These are modelled by adding terms representing appropriate non-relativistic Breit-Wigner amplitudes to  $Q(m_{13}^2, m_{23}^2)$ . These resonances take into account the efficiency variation across the Dalitz plot. It is assumed that different background resonances will not interfere with each other.

The result of fitting this analytical model plus  $K^{*0}(892)$  and  $\rho^0(770)$  resonances to sideband data is shown in Figure 4.5. This shows that the analytical function does not provide a satisfactory description of the  $q\bar{q}$  background.

## 4.5.2 Histogram Model

An alternative to the analytical model for the  $q\bar{q}$  background is to use a 2-dimensional histogram. There is some contamination of the sideband from  $B\bar{B}$  background decays. The level of this contamination is studied using the MC samples described in Section 4.4. It is found that 1554  $B\bar{B}$  events (758 for  $B^-$  and 796 for  $B^+$ ) are expected to pollute the on-resonance sideband, which is 10.7% of the reconstructed

---

<sup>2</sup>The  $\Gamma$  function is defined for  $x > 0$  as  $\Gamma(x) = \int_0^\infty t^{x-1}e^{-t} dt$

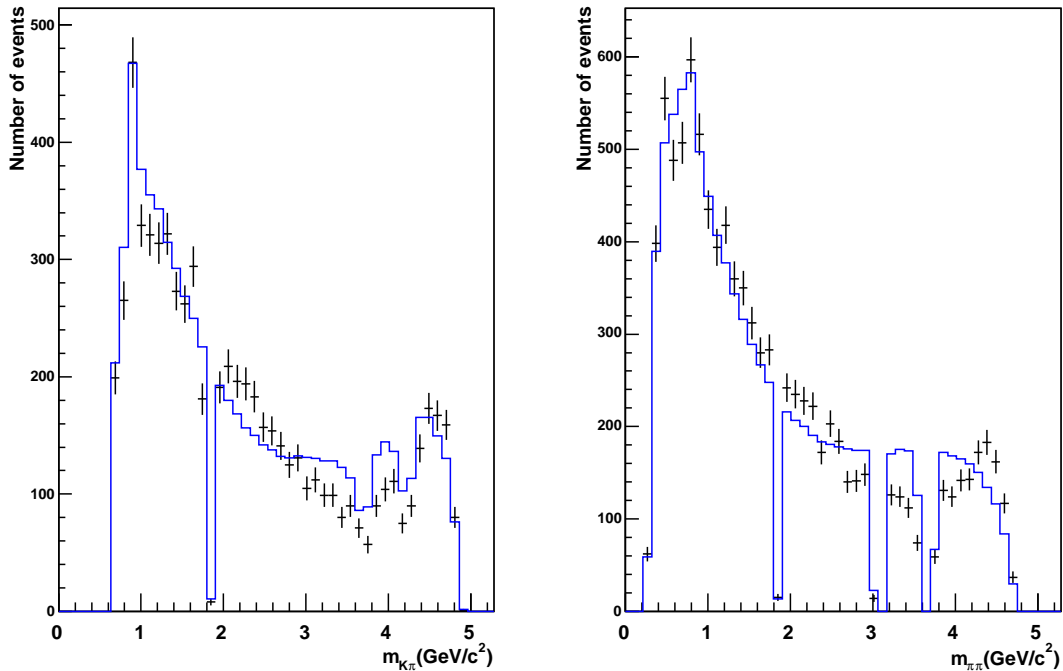


Figure 4.5: Plot showing the invariant mass spectra of on-resonance sideband events for  $B^-$  and  $B^+$  (black points) and the results of the best fit to this data using the analytical continuum model (blue histogram). The left histogram is for the  $K\pi$  pair and the right histogram is for the  $\pi\pi$  pair. A cut of  $> 2 \text{ GeV}/c^2$  on the other mass pair is applied.

sideband events. The  $B\bar{B}$  background contamination is histogrammed and a bin-by-bin subtraction from the  $q\bar{q}$  background histogram is then performed.

It is possible to increase the number of events available for modelling the  $q\bar{q}$  background by using off-resonance data events from across the whole available  $m_{\text{ES}} - \Delta E$  plane. There are 1646 off-resonance events in this sample (818 for  $B^-$  and 828 for  $B^+$ ). The invariant mass squared distributions for this sample of events can be seen in Figure 4.6 together with the original distribution of sideband on-resonance events (with  $B\bar{B}$  background subtracted) for comparison. The two distributions are consistent so the higher statistics combined sample of off-resonance and on-resonance

sideband events is used in the construction of the  $q\bar{q}$  histogram.

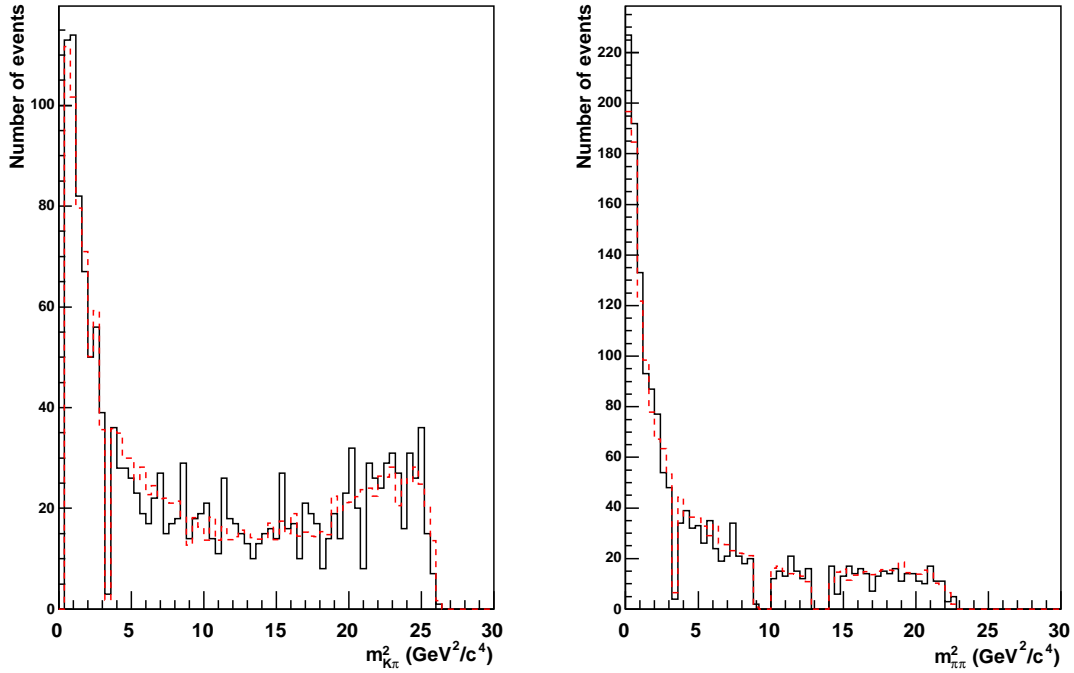


Figure 4.6:  $q\bar{q}$  background invariant mass squared distributions. The left plot shows the  $K\pi$  pair and the right plot is for the  $\pi\pi$  pair. The solid black histogram is for off-resonance events. The dashed red histogram is for sideband on-resonance events.

A comparison of the  $B^-$  and  $B^+$  invariant mass squared distributions is shown in Figure 4.7. The distributions are consistent which allows the combined sample of  $B^-$  and  $B^+$  decays to be used in the construction of the  $q\bar{q}$  histogram. The resulting histogram for the combined  $B^-$  and  $B^+$  sample can be seen in Figure 4.8. This histogram shows regions of high population near the edges of the Dalitz plot which coincide with the regions containing signal resonances. It is therefore essential to model the  $q\bar{q}$  background events in these regions accurately. The histogram also shows a region of negligible population in the centre of the Dalitz plot. A fine binning for the  $q\bar{q}$  histogram is chosen because the accurate modelling of the populated regions is found to be more important than the effect of statistical fluctuations in

the central region induced by this fine binning.

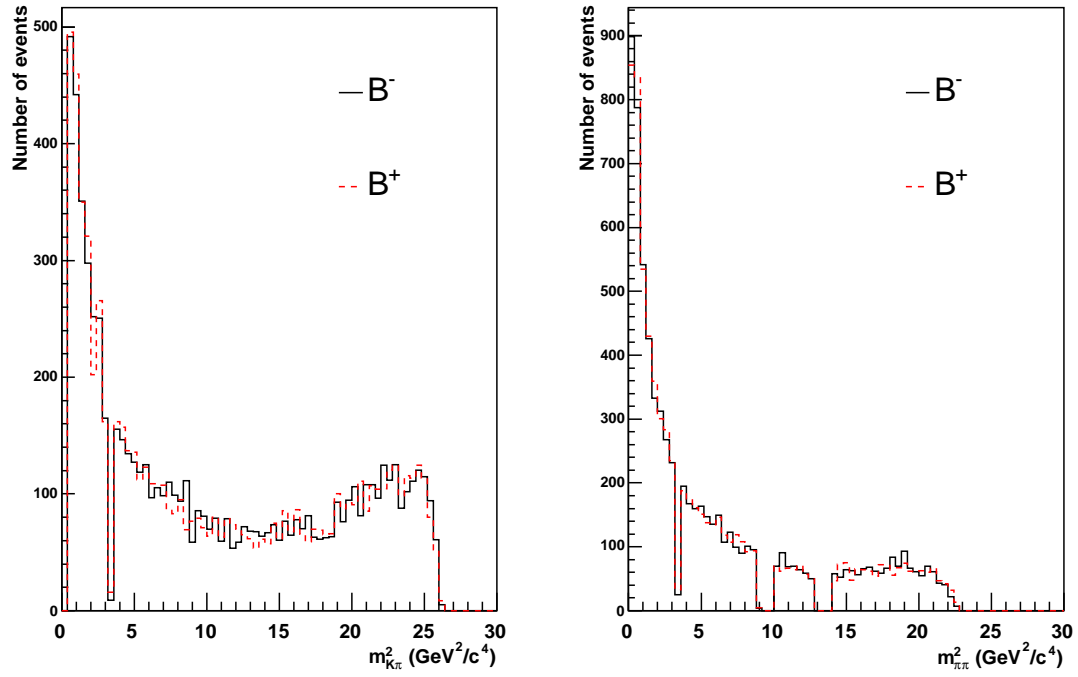


Figure 4.7:  $q\bar{q}$  background invariant mass squared distributions for  $B^-$  and  $B^+$ . The left histogram is for the  $K\pi$  pair and the right histogram is for the  $\pi\pi$  pair.

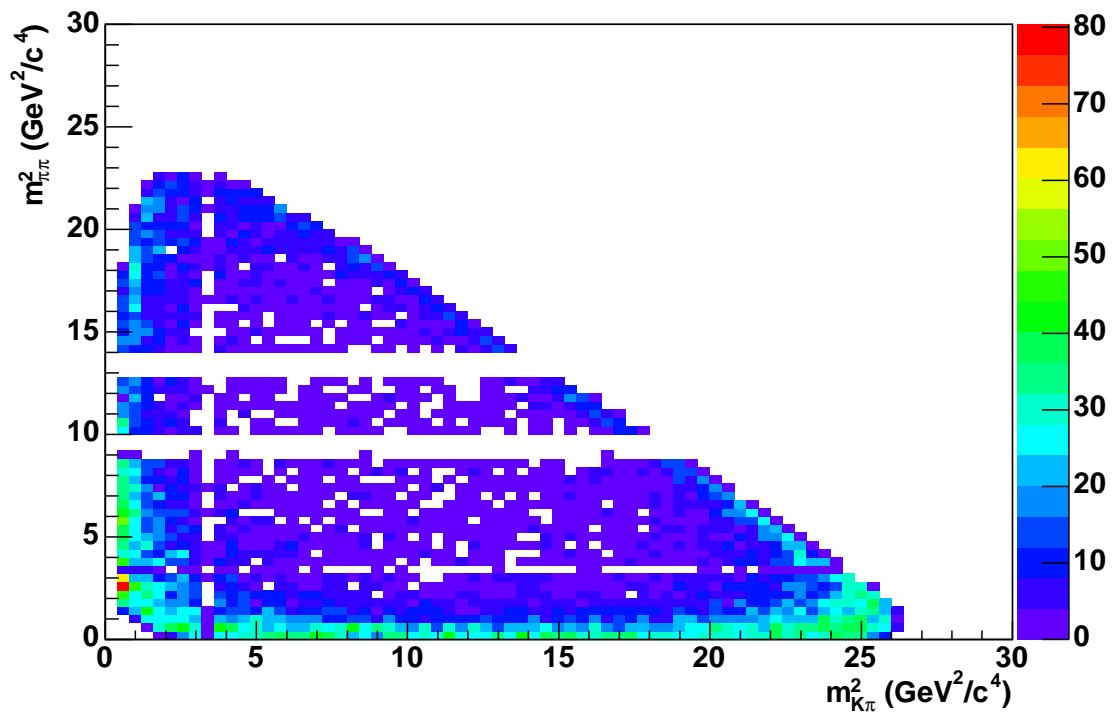


Figure 4.8:  $q\bar{q}$  background Dalitz-plot distribution.

## 4.6 Background Normalisations

The reconstructed data sample consists of signal  $B^\pm \rightarrow K^\pm \pi^\pm \pi^\mp$  decays together with backgrounds from  $q\bar{q}$  events and other non-signal  $B\bar{B}$  decays. The total number of expected  $B\bar{B}$  background events is calculated using MC reconstruction efficiencies and PDG [8] branching fractions for the specific decays listed in Section 4.4. The  $q\bar{q}$  background fraction however remains to be calculated. This is achieved by performing an extended maximum likelihood fit [63] to the kinematical variable  $m_{\text{ES}}$  in the signal strip (see Section 3.3.1).

The signal  $m_{\text{ES}}$  distribution is modelled using a Double Gaussian function. The parameters of this function are obtained by fitting a sample of “truth matched” (see Section 4.7)  $B^\pm \rightarrow K^\pm \pi^\pm \pi^\mp$  non-resonant MC events. These parameters are then fixed in the  $m_{\text{ES}}$  fit apart from the mean of the core Gaussian which is allowed to float. The  $q\bar{q}$   $m_{\text{ES}}$  distribution is modelled using the experimentally motivated Argus function [64]. The endpoint for this Argus function is fixed to the beam energy but the parameter describing the shape is left floating. The  $B\bar{B}$  background  $m_{\text{ES}}$  distribution is modelled as an Argus + Gaussian function. The parameters of the Argus shape and the Gaussian are obtained from the  $B\bar{B}$  MC samples and are fixed in the fit.

The fractions of signal and  $q\bar{q}$  events are allowed to float whereas the fraction of  $B\bar{B}$  events is fixed. The result of the fit is illustrated in Figure 4.9 for  $B^-$  events and Figure 4.10 for  $B^+$  events.

The fitted Argus function shape is used to evaluate the number of  $q\bar{q}$  events expected in the signal box region. The number of  $B\bar{B}$  events in this region is known, as is the total number of events reconstructed. This allows the calculation of the number of signal events expected in the signal box. These expected fractions are shown in Table 4.7.

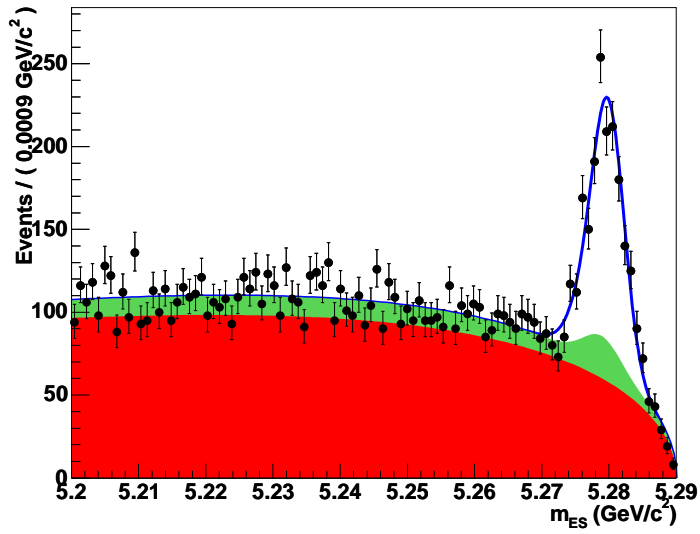


Figure 4.9: The  $m_{ES}$  fit to  $B^-$  data events. The black points are data, the solid blue curve is the total model, the red histogram is continuum, and the green histogram is the total background

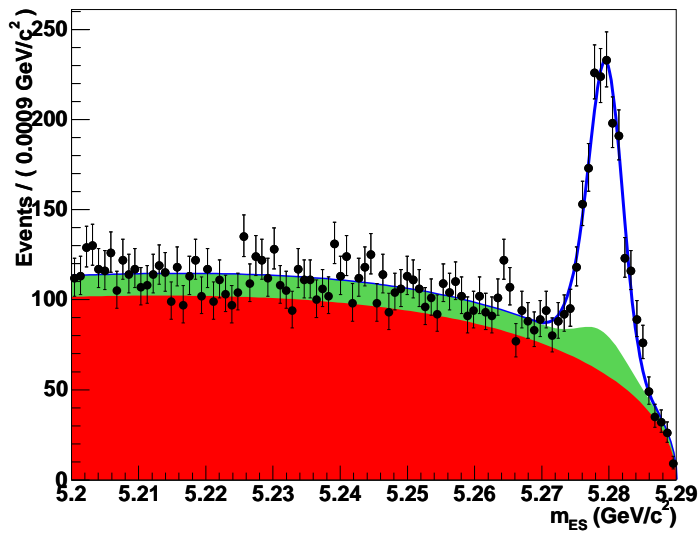


Figure 4.10: The  $m_{ES}$  fit to  $B^+$  data events. The black points are data, the solid blue curve is the total model, the red histogram is continuum, and the green histogram is the total background

Table 4.7: The event yields from the fit to  $m_{\text{ES}}$ . The statistical errors are from the fit for signal and  $q\bar{q}$  background, whilst the statistical error for  $B\bar{B}$  background is from the uncertainty on the various branching fractions and efficiencies.

Hypothesis	Fraction of Events in Signal Box
Both Charges	
Signal	$0.446 \pm 0.011$
$q\bar{q}$ background	$0.438 \pm 0.010$
$B\bar{B}$ background	$0.116 \pm 0.006$
$B^-$ Events	
Signal	$0.445 \pm 0.016$
$q\bar{q}$ background	$0.440 \pm 0.014$
$B\bar{B}$ background	$0.115 \pm 0.007$
$B^+$ Events	
Signal	$0.447 \pm 0.016$
$q\bar{q}$ background	$0.435 \pm 0.014$
$B\bar{B}$ background	$0.117 \pm 0.007$

## 4.7 Efficiency Modelling

Only a fraction of  $B^\pm \rightarrow K^\pm \pi^\pm \pi^\mp$  signal events in the full  $210.6 \text{ fb}^{-1}$  data sample will be reconstructed and pass the selection criteria. This fraction is known as the reconstruction efficiency. The average reconstruction efficiency for  $B^\pm \rightarrow K^\pm \pi^\pm \pi^\mp$  events is shown in Table 3.2. This reconstruction efficiency has a dependency on the final state daughter particle momenta as well as their angular distribution in the detector. Hence the efficiency will vary across the Dalitz Plot. This is included in the likelihood in order to ensure the correct modelling of signal events.

This variation of efficiency across the Dalitz Plot is studied using a sample of  $1.299 \times 10^6$   $B^\pm \rightarrow K^\pm \pi^\pm \pi^\mp$  non-resonant MC events. These events are reconstructed and all selection criteria are applied except for those corresponding to the Charm Vetoes (to ensure that the whole Dalitz plot is populated). This reduces the non-resonant MC sample to 267991 events. A further selection is then applied to select only true  $B^\pm \rightarrow K^\pm \pi^\pm \pi^\mp$  decays, i.e. the three daughters must originate from the same  $B$  meson and be the only daughters of that  $B$ . These events are labelled “truth matched events”. There are 258945 truth matched decays. A 2-dimensional efficiency histogram is constructed according to the following procedure. Firstly a denominator histogram is constructed showing the true Dalitz-plot distribution of the MC events as determined from the MC truth information. The event reconstruction process shifts these events away from their true positions and a numerator histogram is constructed by binning the reconstructed MC events. This numerator histogram also has efficiency corrections for PID and tracking applied. The quotient of these two histograms is the 2-dimensional efficiency histogram used in the Dalitz-plot likelihood.

A comparison of the  $B^-$  and  $B^+$  reconstruction efficiency Dalitz-plot distributions is shown in Figure 4.11. The Dalitz-plot distributions for the  $B^+$  and  $B^-$  decays are consistent and so the two samples are combined and a single efficiency histogram is

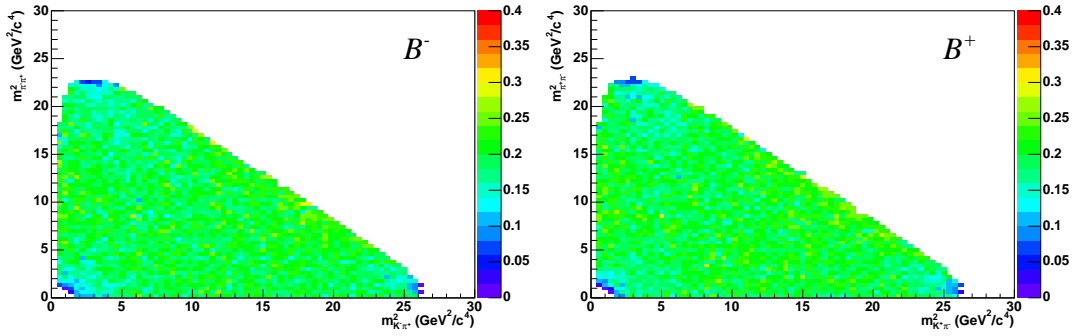


Figure 4.11: Reconstruction efficiency Dalitz plot histograms. The left plot is for  $B^-$  events and the right plot is for  $B^+$  events.

produced for use in the Dalitz-plot fit. This histogram is shown in Figure 4.12. The

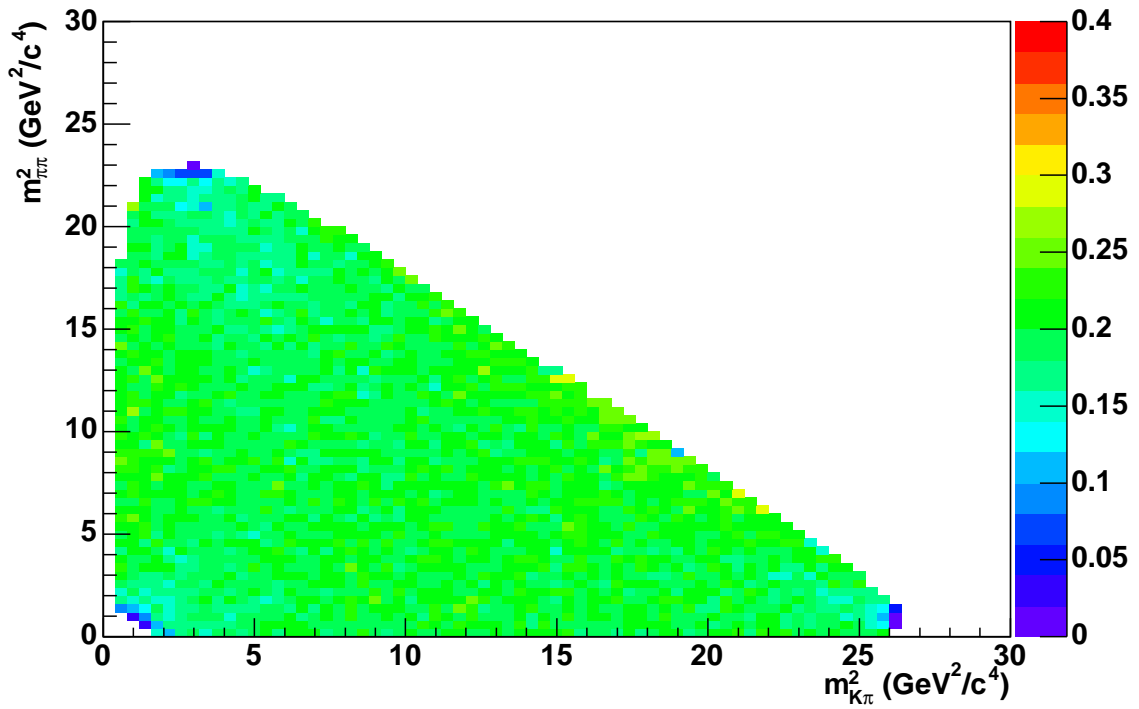


Figure 4.12: Efficiency variation across the Dalitz plot.

efficiency shows very little variation across the majority of the Dalitz plot but there are decreases towards the corners. The corner regions of the Dalitz plot contain

events that have one very low energy particle. There are also some edge effects present which are caused by bins that have very low content in both the numerator and denominator histograms and hence give a large statistical error on that bin. This effect is corrected for by merging low content bins with a neighbouring bin for both the numerator and denominator histogram and recalculating the efficiency for this larger sized bin. Linear interpolation is again applied to smooth out any statistical fluctuations.

### 4.7.1 Self Cross Feed Decays

Self Cross Feed (SCF) decays occur when the signal events have been misreconstructed by switching one or more particles from the decay of the signal  $B$  meson with particles from the other  $B$  meson in the event. After reconstruction there are 9046 SCF decays in the MC sample (the remaining events correspond to the truth matched MC sample). For the signal strip the SCF fraction is 3.4% and for the signal box it is 1.3%. A comparison of the  $B^-$  and  $B^+$  invariant mass distributions of SCF shows that they are the same. The SCF Dalitz-plot distribution for the combined  $B^-$  and  $B^+$  sample can be seen in Figure 4.13. The SCF fraction is very small with the largest values (greater than 0.05) occurring in the extreme corners of the Dalitz plot. This effect is neglected and no additional term is implemented in the fit for these decays.

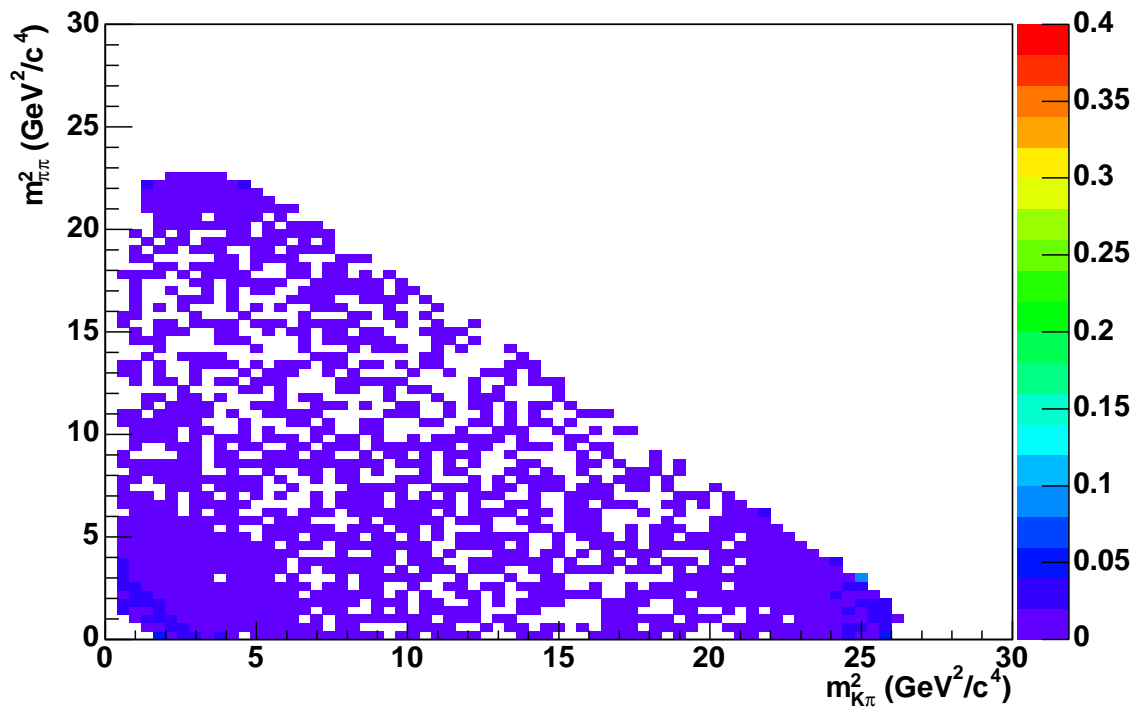


Figure 4.13: SCF variation across the Dalitz plot

# Chapter 5

## Fitting Procedures

### 5.1 Introduction

In this chapter the technicalities of the fitting programs are discussed. Some of the problems encountered using the `Laura++` fitting routine are described together with possible improvements. Validation tests of the `Laura++` fitting procedure are shown using both MC and toy MC events. The chapter concludes with a discussion of an alternative fitting procedure which uses a Genetic Algorithm.

### 5.2 Multiple Solutions

It is found that there is no single unique solution for the Dalitz-plot likelihood fit. The `Laura++` package uses `Minuit` [65, 66] to perform the likelihood fit. `Minuit` is a function minimization and error analysis package written at CERN, which takes the Dalitz-plot likelihood, shown in Equation 4.3, and returns the values of its parameters (the signal magnitudes and phases) which correspond to the minimum negative log likelihood (NLL), shown in Equation 4.1. The solution found by `Laura++` de-

depends critically on the initial values of the floating parameters provided to `Minuit`. This problem is known as *multiple solutions* or *local minima in the likelihood*. To study the fitting performance toy Monte Carlo events are used. Toy MC events are those that have been generated from the `Laura++` PDF using an accept-reject algorithm [67]. The invariant mass-squared variables are generated randomly and the total signal likelihood at that point is calculated. A likelihood value is then generated randomly between zero and the maximum possible signal likelihood. If this random likelihood is less than the signal likelihood at that point then the invariant mass variables are accepted into the toy MC dataset. Toy MC tests are useful as the generated parameters are known.

A toy MC dataset consisting of 2350 signal and background events is generated. This dataset consists of six signal components that are expected to contribute to the  $B^- \rightarrow K^- \pi^- \pi^+$  Dalitz plot. The background fractions are fixed in the fits to the values shown in Table 4.7 and the signal magnitudes and phases allowed to float (except for the  $K^{*0}(892)$  resonance which is used as the reference signal component). 500 fits are performed, with `Minuit` being initialised using random values for the magnitudes (between 0 and 2) and phases (between  $-\pi$  and  $\pi$ ). The resulting distribution of NLL's can be seen in Figure 5.1.

This NLL distribution shows two clear peaks, separated by 10 units. The fitted values for the signal magnitudes and phases of the two solutions are shown in Table 5.1. The greatest difference occurs for the  $\chi_{c0}$  component, which shows two distinct values for the phase.

This multiple solution behaviour can depend on many features of the Dalitz-plot fit. Higher background levels, greater numbers of signal resonances included in the fit and lower total statistics can all lead to a more complicated NLL distribution. At current statistics the multiple-solution behaviour can also depend on the exact sample of toy MC events generated. This effect is illustrated in Figure 5.2. Five additional toy MC samples are generated with the same magnitudes and phases as

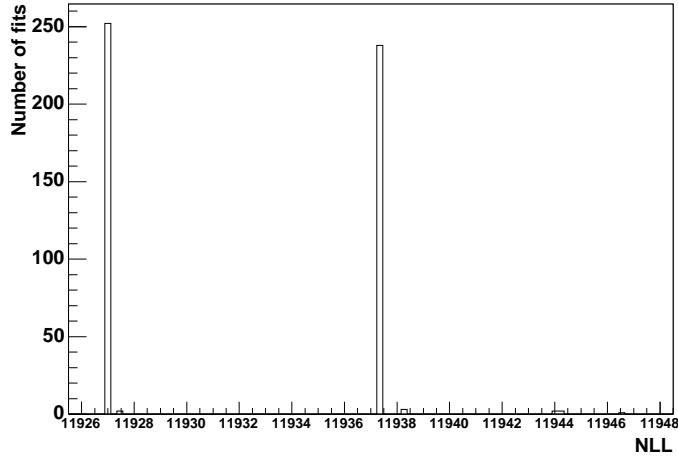


Figure 5.1: Negative log likelihood distributions for the toy MC experiment. 500 fits are performed using different randomised starting values for the floating parameters.

the original sample. The exact value of the NLL varies with the sample, but it is the distributions of the fitted NLL values that are of interest. Figure 5.2 shows the

Table 5.1: Fitted parameters of the two solutions in the negative log-likelihood distribution.

Component	Generated Value	Fitted Values of Solution 1	Fitted Values of Solution 2
NLL	—	11927.0	11937.3
$K_0^{*0}$ (1430) Magnitude	1.950	$2.326 \pm 0.200$	$2.269 \pm 0.197$
$K_0^{*0}$ (1430) Phase	2.860	$2.845 \pm 0.137$	$2.857 \pm 0.143$
$\rho^0$ (770) Magnitude	0.790	$1.046 \pm 0.119$	$1.038 \pm 0.119$
$\rho^0$ (770) Phase	0.210	$0.228 \pm 0.378$	$0.278 \pm 0.396$
$f_0$ (980) Magnitude	1.110	$1.324 \pm 0.127$	$1.316 \pm 0.127$
$f_0$ (980) Phase	-0.920	$-0.936 \pm 0.367$	$-0.887 \pm 0.382$
$\chi_{e0}$ Magnitude	0.316	$0.378 \pm 0.067$	$0.542 \pm 0.071$
$\chi_{e0}$ Phase	-0.450	$-0.385 \pm 0.374$	$2.531 \pm 0.462$
NR Magnitude	0.690	$0.747 \pm 0.137$	$0.770 \pm 0.144$
NR Phase	0.280	$0.792 \pm 0.347$	$0.766 \pm 0.402$

multiple solution behaviour of the six toy MC samples to be very different.

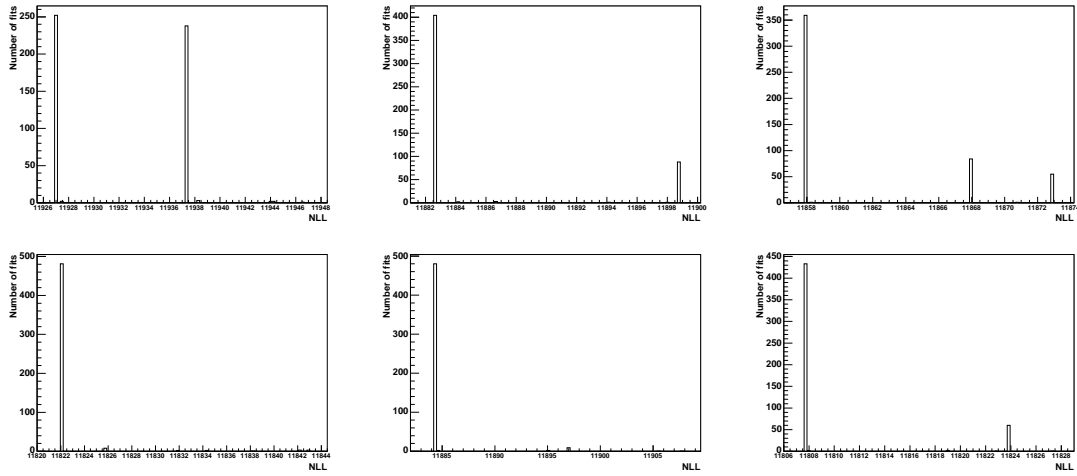


Figure 5.2: Negative log-likelihood distributions for different toy MC samples generated with identical values for the signal magnitudes and phases.

### 5.3 Minuit

`Minuit` uses the `MIGRAD` routine to find the parameters (signal magnitudes and phases) that correspond to the minimum negative log likelihood and then subsequently uses the `HESSE` routine to calculate the errors on those parameters.

In order to solve the multiple solution problem, two possibilities for improving the `Minuit` fitting procedure are considered. The first involves changing the initial step size of the floating parameters. This step size corresponds to the expected uncertainty on that parameter. The default step size in `Laura++` is 0.01, but values of 0.1 and 0.001 are also tested. The resultant NLL distributions of 500 fits to the original data sample discussed in Section 5.2 are shown in Figure 5.3. No improvement in the multiple solution behaviour is seen when using a different initial step size. The second possibility for improving the performance of `Minuit` comes from the compromise to be made in the fitting procedure between accuracy and

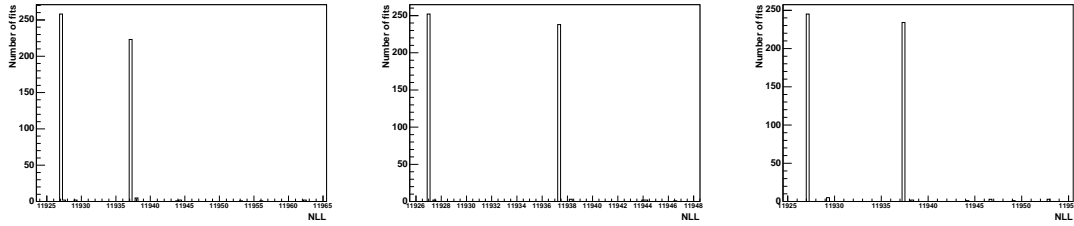


Figure 5.3: Negative log likelihood distributions for the toy MC experiment using different initial step sizes. 500 fits are performed using different randomised starting values for the floating parameters. The left distribution corresponds to a step size of 0.001, the middle distribution corresponds to a step size of 0.01 and the right distribution corresponds to a step size 0.1.

computational speed. `Minuit` has a strategy parameter (0, 1, or 2) that can be set by the user (the default value is 1). A strategy of 0 indicates that `Minuit` should use the fewest possible number of function calls, and is used in the case where the parameter errors do not have to be precise or where the function to be minimised is difficult to calculate. A strategy of 2 indicates that `Minuit` is allowed to make numerous function calls in order ensure precise values, and is used when accurate parameter errors are required or where the function is easily calculated. The results of using these different strategies can be seen in Figure 5.4. Using a strategy of 0 or 2 gives a significantly worse performance as there are only 381 and 169 successful fits out of 500 respectively. No improvement on the multiple solution behaviour is seen either. As can be seen from the above tests, `Minuit` is performing optimally, and the multiple solution behaviour cannot be solved in this way.

## 5.4 Toy MC Tests

The problem of multiple solutions cannot be solved by improvements to the fitting routine and so it is necessary to determine what useful information can be extracted

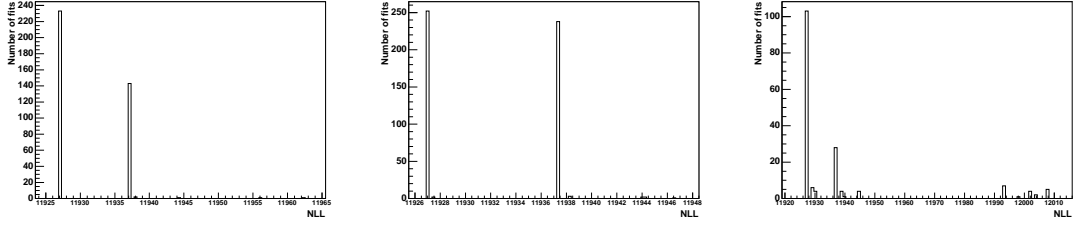


Figure 5.4: Negative log likelihood distributions for the toy MC experiment using different `Minuit` strategies. 500 fits are performed using different randomised starting values for the floating parameters. The left distribution corresponds to a strategy of 0, the middle distribution corresponds to a strategy 1 and the right distribution corresponds to a strategy of 2.

in the presence of these multiple minima. To study this problem 500 toy MC datasets are created using the same resonance composition and parameters as those in Section 5.2. Each of these datasets is then fitted 500 times with `Minuit` initialised each time with random values for the magnitudes and phases. As a measure of how well the fit results correspond to the generated parameters the pull on each parameter is calculated as:

$$\text{pull} = \frac{(\text{fitted value} - \text{generated value})}{\text{error on fitted value}} \quad (5.1)$$

If the fit is performing well then a histogram of these pulls for a set of toy experiments should be a Gaussian distribution with a mean of zero and a width ( $\sigma$ ) of one.

For each toy experiment the solution with the lowest NLL out of the 500 fits is extracted. These best solutions are then histogrammed for the 500 toy MC samples. The pull plots for the magnitudes and phases can be seen in Figure 5.5 and Figure 5.6. The mean and width for each of these plots are tabulated in Table 5.2. The Table shows that the fitting routine is working well and is capable of recovering the true signal magnitudes and phases. A systematic error will be calculated to account for any small biases introduced in those cases where the magnitude or phase pull plot has a mean that deviates from zero. The procedure of running multiple `Minuit`

fits with randomised starting points and choosing the solution with the lowest NLL is adopted in this analysis as the standard method for the Dalitz-plot fit.

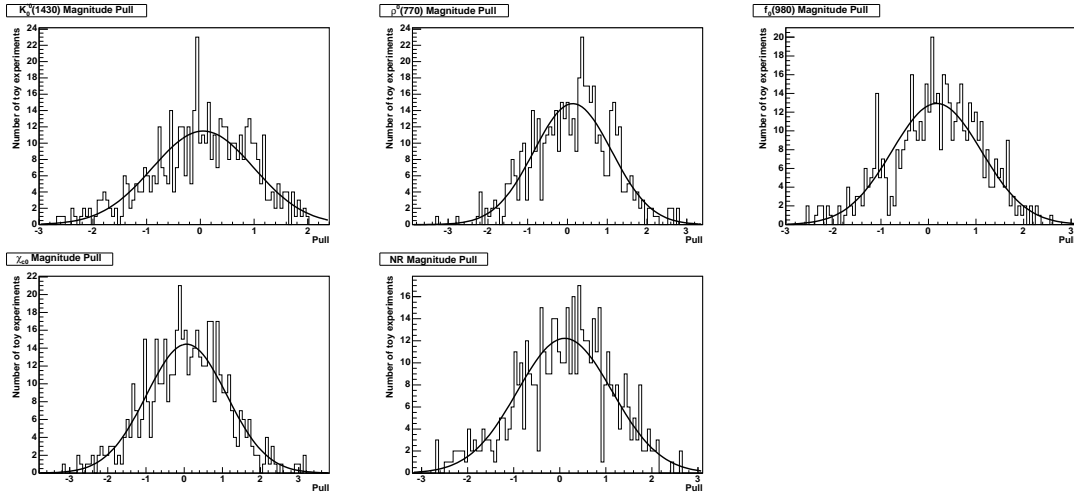


Figure 5.5: Magnitude pull distributions for the 500 toy MC samples. Top left shows the  $K_0^{*0}(1430)$ , top middle the  $\rho^0(770)$ , top right the  $f_0(980)$ , bottom left the  $\chi_{c0}$  and bottom middle the non-resonant.

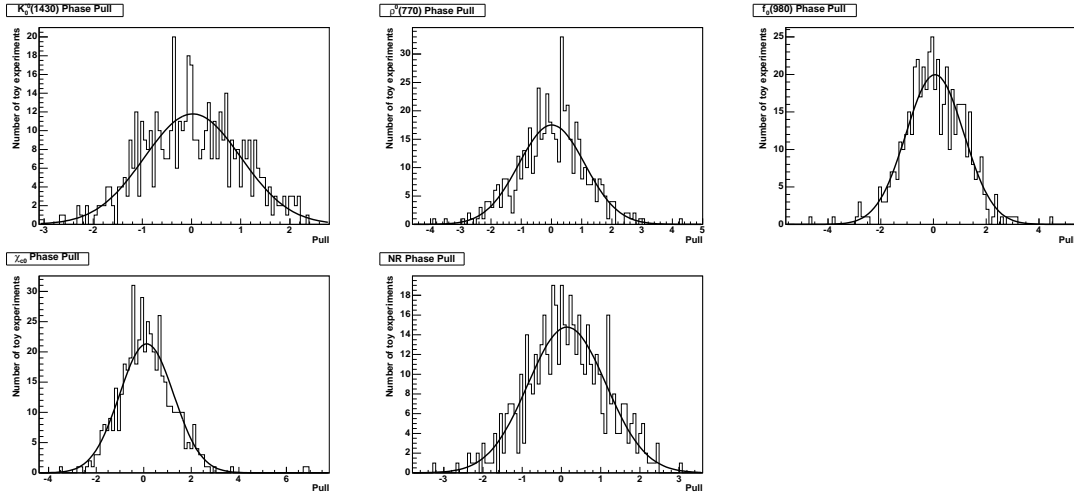


Figure 5.6: Phase pull distributions for the 500 toy MC samples. Top left shows the  $K_0^{*0}(1430)$ , top middle the  $\rho^0(770)$ , top right the  $f_0(980)$ , bottom left the  $\chi_{c0}$  and bottom middle the non-resonant.

Table 5.2: Magnitude and phase pulls in fit with 6 components. The lowest solution of the 500 fits is extracted for each of the 500 toy MC samples.

	Pull Mean	Pull Width
$K_0^{*0}(1430)$ Magnitude	$0.053 \pm 0.044$	$0.945 \pm 0.034$
$K_0^{*0}(1430)$ Phase	$0.023 \pm 0.045$	$0.981 \pm 0.034$
$\rho^0(770)$ Magnitude	$0.135 \pm 0.044$	$0.981 \pm 0.032$
$\rho^0(770)$ Phase	$0.012 \pm 0.049$	$1.093 \pm 0.035$
$f_0(980)$ Magnitude	$0.173 \pm 0.042$	$0.942 \pm 0.031$
$f_0(980)$ Phase	$0.057 \pm 0.049$	$1.098 \pm 0.035$
$\chi_{c0}$ Magnitude	$0.063 \pm 0.047$	$1.049 \pm 0.034$
$\chi_{c0}$ Phase	$0.121 \pm 0.051$	$1.140 \pm 0.036$
NR Magnitude	$0.107 \pm 0.047$	$1.031 \pm 0.035$
NR Phase	$0.142 \pm 0.045$	$0.999 \pm 0.032$

## 5.5 Full MC Tests

In this case MC events are used for the signal sample instead of toy MC events.  $B^\pm \rightarrow K^\pm \pi^\pm \pi^\mp$  non-resonant MC events are reweighted using the `Laura++` amplitude model in order to correctly account for interference effects. The reweighting procedure begins by examining the “truth information” for a given MC event. The  $m_{13}^2$  and  $m_{23}^2$  values are found and the total signal amplitude at this point is calculated. A random number is then generated and the event is accepted into the reweighted sample if this random number is less than the total signal amplitude. A further check is applied to ensure that this event also appears in the final MC sample which has undergone detector simulation and reconstruction.

The same signal parameters given in Section 5.2 are used to generate a reweighted MC dataset. Toy MC events are then added for  $q\bar{q}$  and  $B\bar{B}$  background events. This sample is fitted 500 times using `Minuit` initialised with random magnitudes and phases. The lowest NLL is chosen as the best solution. The results can be seen in Table 5.3. These results are another validation of the fitting routine, in addition to the toy MC tests, as they show that the fitting program can correctly recover the signal magnitudes and phases from MC events that have been through the reconstruction process. The success of the reweighting test shows that neglecting the small SCF term is acceptable as the fit is still able to recover the correct magnitudes and phases.

Table 5.3: Magnitude and phase results of fit to reweighted MC dataset with six signal components.

	Generated	Fitted
$K_0^{*0}(1430)$ Magnitude	1.950	$2.027 \pm 0.147$
$K_0^{*0}(1430)$ Phase	2.860	$2.771 \pm 0.128$
$\rho^0(770)$ Magnitude	0.790	$0.946 \pm 0.095$
$\rho^0(770)$ Phase	0.210	$0.232 \pm 0.440$
$f_0(980)$ Magnitude	1.110	$1.224 \pm 0.102$
$f_0(980)$ Phase	-0.920	$-1.064 \pm 0.455$
$\chi_{c0}$ Magnitude	0.316	$0.350 \pm 0.055$
$\chi_{c0}$ Phase	-0.450	$-0.313 \pm 0.325$
NR Magnitude	0.690	$0.477 \pm 0.121$
NR Phase	0.280	$0.732 \pm 0.434$

## 5.6 Genetic Algorithms

A possible alternative to the `Minuit` fitting routine is to use a Genetic Algorithm (GA) [68,69]. The GA is based on a Darwinian process of selection of the fittest in a population. The GA differs from the `Minuit` fitting routine in that it does not require initial starting values for the parameters of the likelihood.

The first step in the Genetic Algorithm is the creation of an initial *population*, which consists of a number of *individuals*. Each individual has a number of *phenotypes* which correspond to the unknown signal magnitudes or phases. The initial population's phenotypes are created using random numbers, hence a wide range of points on the likelihood space is used rather than the single initial point provided to `Minuit`. A random number seed can be specified to the GA so that different initial populations can be created. The magnitudes and phases are transformed in order to ensure that the phenotypes can only have values between 0 and 1. Each of the digits after the decimal place in the phenotype is called a *genotype*. The number of digits used in each phenotype and hence the overall number of genotypes can be chosen.

The NLL is used as a measure of each individual's *fitness*. The population is ranked according to this fitness such that the individual with the lowest NLL is considered the fittest. The population then "breeds" to make a new population. Two individuals are crossed to make two new *daughter* individuals. The *parent* individuals can be selected at random or those with a greater fitness can be preferentially selected, using the *fitness differential* parameter.

Breeding occurs as follows. There is a probability for successful breeding, known as the *crossover probability*, that can be set. If the breeding is successful then a random number is generated which is used as the cutting point. This number varies between one and the total number of genotypes in the individual. All the genotypes that appear after the chosen cutting point are swapped between the two parents to

produce the daughters - in this way the daughters retain some of the characteristics of their parents.

Consider a daughter that has six phenotypes, three magnitudes (M) and three phases (P). Each phenotype is encoded with three genotypes:

	M1	P1	M2	P2	M3	P3
parent 1	0.567	0.890	0.974	0.945	0.337	0.112
parent 2	0.102	0.578	0.394	0.682	0.559	0.888

If the cutting point is chosen to be say eleven then the resultant daughters would be:

	M1	P1	M2	P2	M3	P3
daughter 1	0.567	0.890	0.974	0.982	0.559	0.888
daughter 2	0.102	0.578	0.394	0.645	0.337	0.112

There are then two possible methods for inserting the daughters into the population. The first method is to replace the entire parent population with the daughters. This is known as *full generational replacement*. The second method is to insert the daughters into the parent population if their fitness is greater than the least fit member of the parent generation. This is known as *steady state reproduction*. The parent to be replaced can either be chosen at random or chosen to be the least fit parent of the population. The GA can retain information about the fittest individuals throughout the generations by always retaining the most fit individual. This is achieved by setting the *elitism* flag to one.

In order to allow the phenotypes to have more variability and to avoid the population becoming too homogeneous then it is also possible for *mutation* to occur. The

probability for mutation to occur can be set and is known as the *global mutation rate*. There are two types of mutation. In the case of *one point mutation* the genotype is changed to be a random integer between 0 and 9. In the case of *creep mutation* the value of the genotype is incremented or decremented by one. The mutation rate can be further altered in two ways. The first is such that the mutation rate depends on the fitness of the individual. The second is such that the mutation rate is based on the numerical differences between the phenotypes of the individual concerned and the phenotypes of the fittest individual.

The GA continues to evolve and produce new generations of individuals. Evolution continues until a chosen number of generations have been produced where no daughter is fitter than the current fittest individual, or until a maximum number of generations has been reached. The GA cannot be used as a standalone fitting procedure as it has no error analysis capability. It can however be used to provide the correct initial starting point for a `Minuit` fit.

### 5.6.1 Default Genetic Algorithm Setup

The default internal parameters for the Genetic Algorithm (as taken from [69]) are as follows:

- 100 individuals are used in every generation
- A maximum of 200 generations is produced
- The GA stops if the best solution doesn't change in 10 generations
- The phenotypes are coded to 5 decimal places
- The probability of a successful breeding occurring is 0.85
- The mutation rate is chosen to vary according to the individual's fitness with a minimum rate of 0.05 and a maximum rate of 0.55

- The fitness differential parameter is set to 1.0 so that the fittest individuals breed with the greatest probability
- The parent population is replaced by the daughter population
- The elitism flag is set so that the fittest individual of each generation is retained

Five initial populations are created to fit to the same original toy dataset used in Section 5.2 of this chapter. The NLL results can be seen in Table 5.4. This table shows a large difference between the best NLL value obtained by the GA and the output of the subsequent `Minuit` fit. This suggests that the GA is not performing optimally.

Table 5.4: Fitted parameters of the solutions found by five GA fits with the default setup.

Component	Output of GA	Output of subsequent <code>Minuit</code> fit
GA Fit 1	11968.1	11927.0
GA Fit 2	11970.0	11927.0
GA Fit 3	11982.6	11927.0
GA Fit 4	11969.0	11927.0
GA Fit 5	11981.4	11927.0

## 5.6.2 Initial Optimisation

An initial optimisation is performed. The first GA parameter that is altered is the fitness differential. In the default setup this parameter is set to 1.0 which means that the parents with the best NLL values are more likely to breed. In the initial population this best NLL value may not correspond well to the true best NLL value and there may be a danger of focusing on a local minimum solution by using this

preferential breeding. The fitness differential is changed to 0.0 and all parents in the population breed with equal probability. The fits described in Section 5.6.1 are repeated and the results are shown in Table 5.5. Changing the fitness differential has no effect on the performance of the GA and hence this parameter is set to be 0.0.

Table 5.5: Fitted parameters of the solutions found by the five GA fits after initial optimisation.

Component	Output of GA	Output of subsequent Minuit fit
GA Fit 1	11980.4	11927.0
GA Fit 2	11968.1	11927.0
GA Fit 3	11963.4	11927.0
GA Fit 4	11981.3	11927.0
GA Fit 5	11989.5	11927.0

### 5.6.3 Steady State Reproduction

One of the most influential choices in the performance of the GA is the method for inserting the daughters into the population. The default is to use full generational replacement which means that the daughter population replaces the entire parent population (except for the fittest parent if the elitism flag is set). This has the advantage of scanning a wide range of parameter space, as a large number of different combinations of magnitudes and phases are used. It also has the advantage of keeping the population varied. However it may not be the smartest way of using the GA. The GA is designed to mimic the biological process of natural selection. Instead it may be better to use steady state reproduction where the daughter only enters the population if it has a better NLL value than the least fit parent. In this way the GA evolves in a more intelligent way, selecting daughters that are better

than their parents.

Three possible reproduction plans are tested. The first is full generational replacement with the elitism flag set so the fittest parent is always retained. The second is to use steady state reproduction with the elitism flag set where the daughters replace parents at random (except the fittest parent which is again retained). The third possibility is to use steady state reproduction in the mode where the daughters replace the least fit of the parent generation. The results are shown in Table 5.6 which clearly indicates that using steady state reproduction with the daughters replacing the least fit parent consistently gives the best results for the output of the GA.

Table 5.6: Fitted parameters of the solutions found by the five GA fits using different reproduction plans.

Component	Reproduction Plan 1		Reproduction Plan 2		Reproduction Plan 3	
	Output of GA	Final output	Output of GA	Final output	Output of GA	Final output
GA Fit 1	11980.4	11927.0	11994.1	11937.3	11965.8	11937.3
GA Fit 2	11968.1	11927.0	11986.9	11937.3	11963.7	11927.0
GA Fit 3	11963.4	11927.0	11990.0	11927.0	11968.2	11927.0
GA Fit 4	11981.3	11927.0	12000.4	11927.0	11957.8	11927.0
GA Fit 5	11989.5	11927.0	11991.9	11927.0	11972.3	11927.0

At this point it is also possible to set a few of the remaining parameters of the GA. The crossover probability is now set to 1.0 so that breeding is always successful and daughters are always produced. There is no need for unsuccessful breeding in order to retain parents in the steady state reproduction case, as daughters only replace unfit parents and some parents will therefore survive between generations. The number of possible generations is kept at 200 (in the present configuration the GA does not evolve for anywhere near this amount) but the number of generations checked for a new best solution is raised to 20. The results for five GA fits with these changes can be seen in Table 5.7 which shows that altering these parameters

has no detrimental effects on the performance of the GA.

Table 5.7: Fitted parameters of the solutions found by five GA fits with the new reproduction plan and subsequent settings.

Component	Output of GA	Output of subsequent Minuit fit
GA Fit 1	11953.1	11937.3
GA Fit 2	11964.6	11937.3
GA Fit 3	11964.0	11927.0
GA Fit 4	11958.4	11927.0
GA Fit 5	11961.9	11927.0

#### 5.6.4 Mutation Rate

In its current form the GA does not evolve for many generations. This suggests that there is not enough variability in the daughters, as very few new best solutions are being found. Changing the way mutation occurs in the GA may solve this problem. In the default setup the mutation rate is chosen to vary depending on an individual's fitness. It may be more correct to mutate all individuals at the same rate. The default setup for mutation changes the genotype being mutated to a random integer between 0 and 1. A more intelligent form of mutation is additionally to use creep mutation which increments or decrements the genotype. This type of mutation may be more successful at finding new best solutions. The results for using a constant mutation plus creep mutation strategy can be seen in Table 5.8 for three different mutation rates. Table 5.8 shows that using this new mutation strategy leads to a greatly improved performance for the GA, with the best results corresponding to a mutation rate of 0.05.

Table 5.8: Fitted parameters of the solutions found by five GA fits with a new mutation plan and three different mutation rates.

Component	Mutation Rate 0.01		Mutation Rate 0.05		Mutation Rate 0.10	
	Output of GA	Final output	Output of GA	Final output	Output of GA	Final output
GA Fit 1	11932.2	11927.0	11931.6	11927.0	11929.0	11927.0
GA Fit 2	11943.6	11927.0	11929.2	11927.0	11932.3	11927.0
GA Fit 3	11956.7	11937.3	11930.0	11927.0	11942.8	11927.0
GA Fit 4	11929.8	11927.0	11928.8	11927.0	11928.9	11927.0
GA Fit 5	11929.2	11927.0	11930.2	11927.0	11933.4	11927.0

### 5.6.5 Final Optimisation

There are two remaining internal GA parameters that can be optimised. The first is the number of individuals in a generation and the second is the number of digits used to encode the phenotypes (magnitudes and phases). The results from varying the number of individuals is shown in Table 5.9 which indicates that increasing this number generally improves the performance of the GA. Increasing the number of individuals used decreases the computational speed of the GA so a compromise of 140 individuals is chosen. The default set-up is to use 5 decimal places to encode the phenotypes. The errors on the magnitudes and phases are large and so this level of accuracy may not be required. Using a large number of decimal places can also reduce the speed of the algorithm as small changes in these parameters will lead to small changes in the NLL value which will keep the algorithm evolving. The results for using different numbers of digits in the phenotype encoding are shown in Table 5.10. This shows that lowering the number of digits leads to an observable decrease in the performance of the GA and so this parameter is left unchanged.

The number of generations can now be optimised. To aid in this procedure it is instructive to look at the evolution of the algorithm in more detail. To do this the details of the population are recorded every 10 generations. This allows the

magnitudes and phases of the individuals making up the population to be studied. An example evolution plot corresponding to the first column of Table 5.10 can be seen in Figure 5.7. This shows that the population becomes homogenous after a very small number of generations. This allows the total number of generations produced to be reduced to 120 which will speed up the GA.

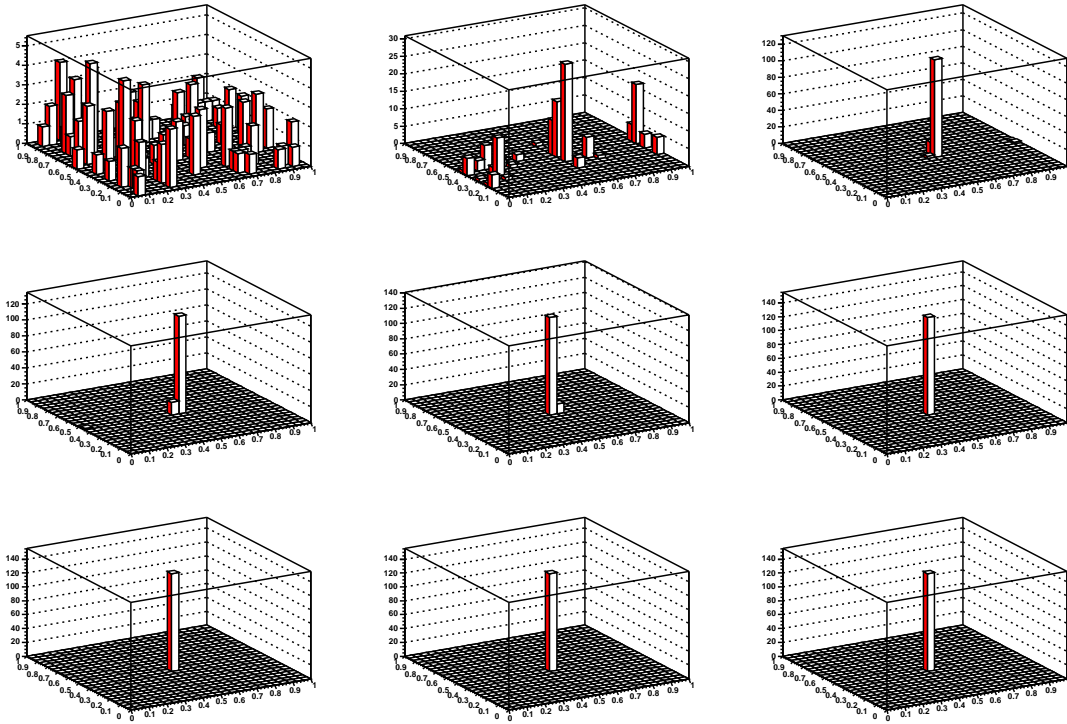


Figure 5.7: Evolution of the GA for the  $\rho^0(770)$  component The histograms show the distribution of the  $\rho^0(770)$  magnitude against the  $\rho^0(770)$  phase for the individuals in the population every 10 generations.

The corresponding histograms for the other parameters in this test can be seen in Appendix A

### 5.6.6 Results

The final internal parameters for the Genetic Algorithm are as follows:

- 140 individuals are used in every generation
- A maximum of 120 generations is produced
- The GA stops if the best solution does not change in 20 generations
- The phenotypes are coded to 5 decimal places
- The probability of a successful breeding occurring is 1.00
- The mutation strategy is chosen to be a constant mutation rate plus creep mutation at the same rate. The mutation rate is 0.05
- The fitness differential parameter is set to 0.0 so that all individuals breed with equal probability
- If the daughter is fitter than the least fit member of the parent population then the daughter replaces the least fit parent

The same toy distributions described in Section 5.2 are fitted using the GA with 25 different initial populations. The output is shown in Figure 5.8 and can be compared to Figure 5.2. Figure 5.8 shows that the multiple solution problem still remains although the proportion of solutions in the lowest peak has increased.

### 5.6.7 Conclusion

The GA is a powerful technique that can be used to provide correct starting values for the `Minuit` Dalitz-plot fit. However it is a time-consuming process and the multiple solution issue is not solved completely. The GA has many internal parameters that can be optimised for different situations. For instance, increasing the number of individuals and mutation rate while lowering the number of digits can lead to an algorithm that can scan a very large region of likelihood space. This may be helpful in situations where the multiple solution phenomenon is problematic. In the current

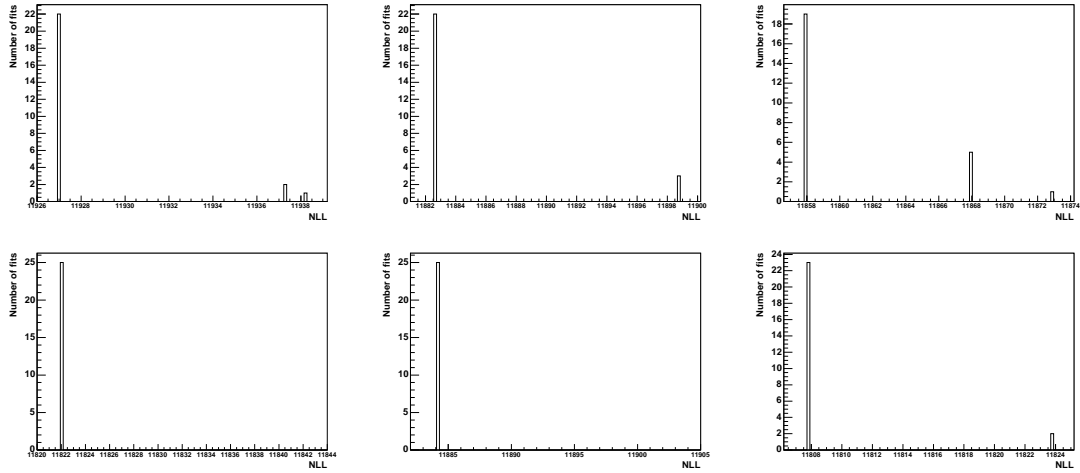


Figure 5.8: Negative log-likelihood distributions for different toy MC samples generated with identical values for the signal magnitudes and phases and fitted with the GA.

$B^\pm \rightarrow K^\pm \pi^\pm \pi^\mp$  analysis it may not be optimal to use the GA as there are very few multiple minima and the toy experiments described in Section 5.4 show that running multiple `Minuit` fits with random starting points, and then selecting the lowest NLL value, can recover the true values. The GA may be more useful in other Dalitz-plot analyses where the multiple minima are worse, perhaps in the case of lower statistics or higher backgrounds.

Table 5.9: Fitted parameters of the solutions found by five GA fits with different numbers of individuals.

Component	80 Individuals		100 Individuals		120 Individuals		140 Individuals		160 Individuals		180 Individuals	
	GA	Final	GA	Final	GA	Final	GA	Final	GA	Final	GA	Final
GA Fit 1	11938.8	11927.0	11931.6	11927.0	11929.6	11927.0	11928.8	11927.0	11929.2	11927.0	11929.7	11927.0
GA Fit 2	11929.3	11927.0	11929.2	11927.0	11928.8	11927.0	11929.9	11927.0	11929.5	11927.0	11929.3	11927.0
GA Fit 3	11930.1	11927.0	11930.0	11927.0	11956.3	11937.3	11929.2	11927.0	11956.3	11937.3	11928.8	11927.0
GA Fit 4	11929.9	11927.0	11928.8	11927.0	11929.5	11927.0	11929.8	11927.0	11929.2	11927.0	11929.1	11927.0
GA Fit 5	11929.3	11927.0	11930.2	11927.0	11929.0	11927.0	11929.3	11927.0	11931.6	11927.0	11931.6	11927.0

Table 5.10: Fitted parameters of the solutions found by five GA fits with different numbers of digits encoding the phenotypes.

Component	5 Digits		4 Digits		3 Digits		2 Digits	
	GA	Final	GA	Final	GA	Final	GA	Final
GA Fit 1	11928.8	11927.0	11929.3	11927.0	11932.4	11927.0	11931.9	11927.0
GA Fit 2	11929.9	11927.0	11932.1	11927.0	11929.4	11927.0	11941.4	11927.0
GA Fit 3	11929.2	11927.0	11929.0	11927.0	11931.7	11927.0	11934.5	11927.0
GA Fit 4	11929.8	11927.0	11928.8	11927.0	11929.2	11927.0	11936.6	11927.0
GA Fit 5	11929.3	11927.0	11929.3	11927.0	11930.3	11937.3	11957.3	11937.3

# Chapter 6

## $B^\pm \rightarrow K^\pm \pi^\pm \pi^\mp$ Dalitz Analysis - Final Results

### 6.1 Introduction

In this chapter the results of the Dalitz-plot fits to the  $B^-$  and  $B^+$  data samples are presented. Lineshape issues are discussed followed by a detailed investigation of the composition of the signal model. Results are given for fit fractions and phases of the components that provide the major contributions to the Dalitz plot, with a subsequent description of the systematic errors associated with these measurements. Upper limits are then calculated for those components in the Dalitz plot that are found to be small. This chapter concludes with a description of the inclusive  $B^\pm \rightarrow K^\pm \pi^\pm \pi^\mp$  rate measurement and its associated systematic errors.

## 6.2 Data Projection Plots

After the selection cuts (Section 3.6) have been applied there are 2344  $B^-$  and 2360  $B^+$  events in the signal box. The fractions quoted in Table 4.7 can be used to determine the expected numbers of signal and background events. The 2344 event  $B^-$  sample consists of  $1043 \pm 57$  signal events,  $1031 \pm 25$   $q\bar{q}$  background events and  $270 \pm 16$   $B\bar{B}$  background events. The 2360 event  $B^+$  sample consists of  $1056 \pm 57$  signal events,  $1027 \pm 25$   $q\bar{q}$  background events and  $277 \pm 16$   $B\bar{B}$  background events. The resultant Dalitz plots can be seen in Figure 6.1. Invariant mass projection plots for the  $B^-$  data sample can be seen in Figure 6.2 and for the  $B^+$  data sample in Figure 6.3.

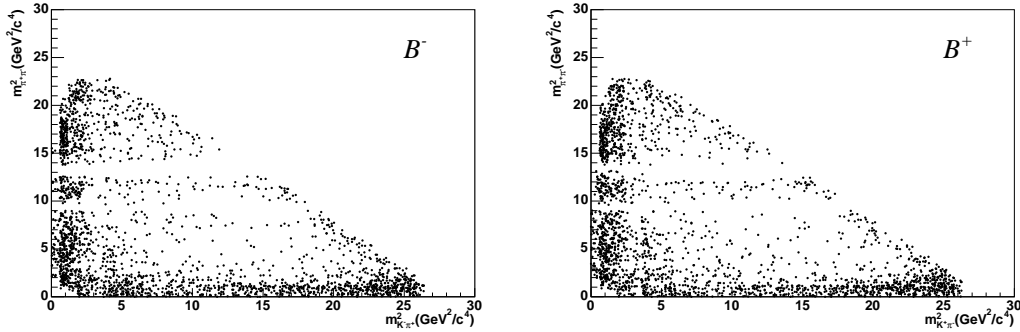


Figure 6.1: Data Dalitz plots. The left plot is for  $B^-$  data and the right plot is for  $B^+$  data.

A bin-by-bin subtraction can be performed on these projection plots to isolate the signal invariant mass distributions. The resultant Dalitz plots can be seen in Figure 6.4. The background-subtracted invariant mass distributions are compared for  $B^-$  and  $B^+$  in Figure 6.5. The same distributions can be seen in Figure 6.6 where the invariant mass distribution is plotted only for events that have a value greater than  $2 \text{ GeV}/c^2$  in the other invariant mass pair. In the high mass range of each mass pair there are substantial contributions from resonances in the other mass pair. Applying the  $2 \text{ GeV}/c^2$  cut is therefore a useful tool in order to illustrate the resonant

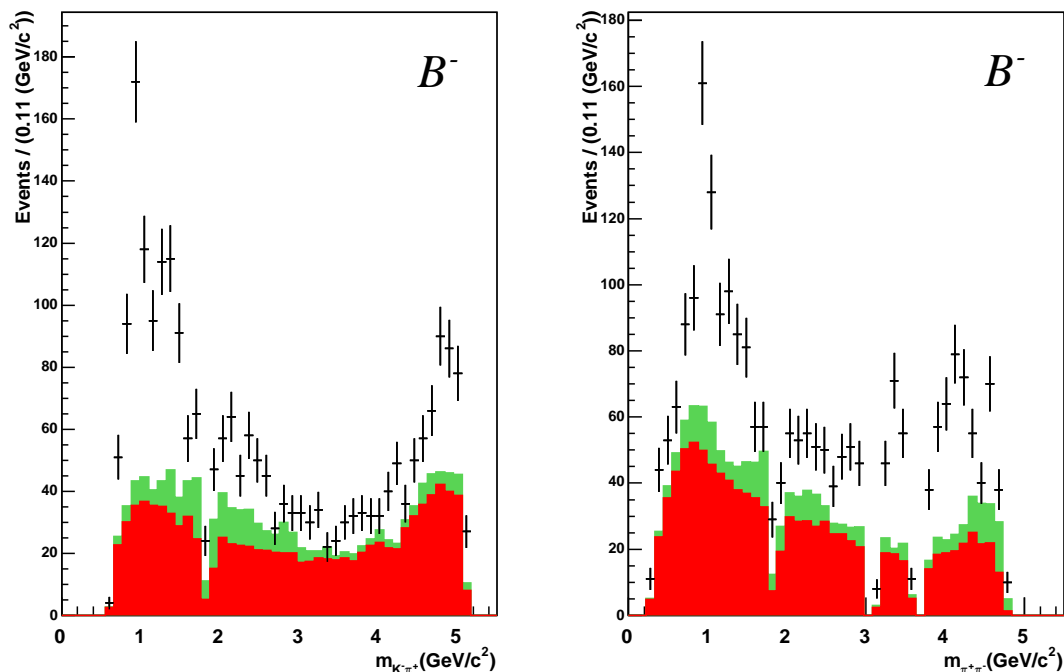


Figure 6.2: The left histogram is for the  $K^-\pi^+$  invariant mass pair and the right histogram is for the  $\pi^+\pi^-$  invariant mass pair. The black points are for the data events in the signal box. The bottom red histogram shows the expected distribution of  $q\bar{q}$  background events and the middle green histogram shows the expected distribution of  $B\bar{B}$  background events.

contributions to a particular mass pair spectrum. The  $K\pi$  projections for both  $B^-$  and  $B^+$  data show evidence for the  $K^{*0}(892)$  resonance and an excited resonance which from previous measurements is known to be  $K_0^{*0}(1430)$ . The  $\pi\pi$  projections for  $B^-$  and  $B^+$  data show evidence of the  $f_0(980)$  and  $\chi_{c0}$  resonances. There is little sign of the expected  $\rho^0(770)$  resonance below the  $f_0(980)$  but the region above the  $f_0(980)$  shows structure which could arise from many possible resonances as listed in Table 4.1 in Section 4.3.

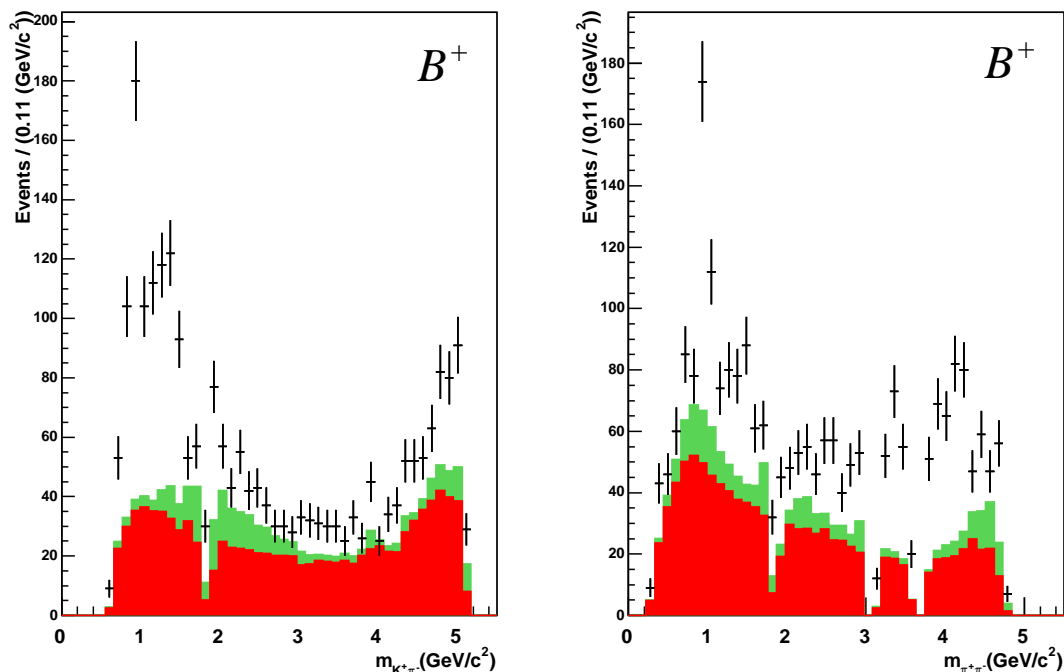


Figure 6.3: The left histogram is for the  $K^+\pi^-$  invariant mass pair and the right histogram is for the  $\pi^+\pi^-$  invariant mass pair. The black points are for the data events in the signal box. The bottom red histogram shows the expected distribution of  $q\bar{q}$  background events and the middle green histogram shows the expected distribution of  $B\bar{B}$  background events.

### 6.2.1 Nominal Model

The fitting routine needs a model for which resonances to try to fit, but the resonance composition of the Dalitz plot is unknown. Information from previous studies of the  $B^\pm \rightarrow K^\pm \pi^\pm \pi^\mp$  decay and the projection plots of the data samples shown in Figure 6.2 and Figure 6.3 can be used to decide which resonances are likely to provide the dominant contributions. A six component model is chosen to be the nominal model and consists of components for  $K^{*0}(892)$ ,  $K_0^{*0}(1430)$ ,  $\rho^0(770)$ ,  $f_0(980)$ ,  $\chi_{c0}$  and non-resonant components.

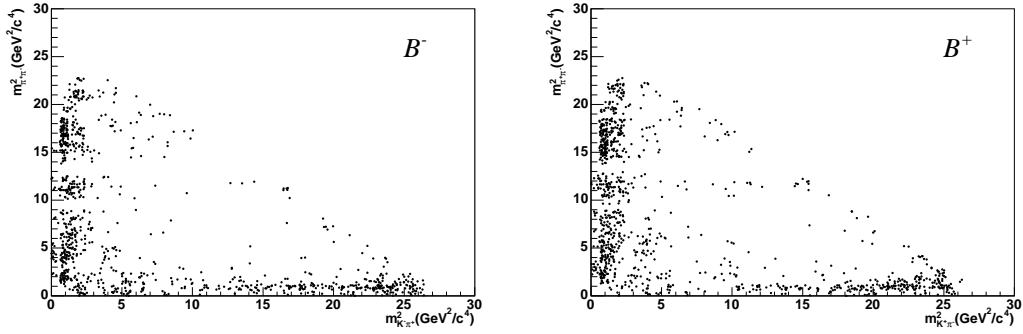


Figure 6.4: Background subtracted data Dalitz plots. The left plot is for  $B^-$  data and the right plot is for  $B^+$  data.

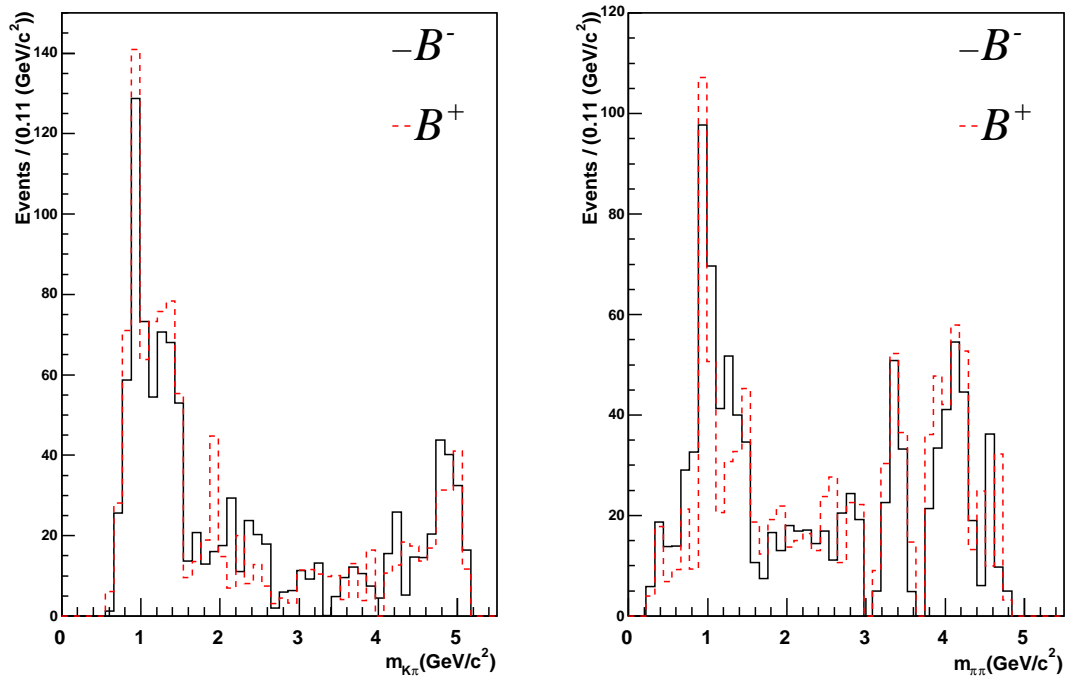


Figure 6.5: Background subtracted invariant mass projections for data. The left histogram is for the  $K\pi$  pair and the right histogram is for the  $\pi\pi$  pair.

### 6.3 Lineshapes

There are several possible lineshapes that can be used to model the resonant components. Relativistic Breit-Wigner lineshapes are chosen for all components apart

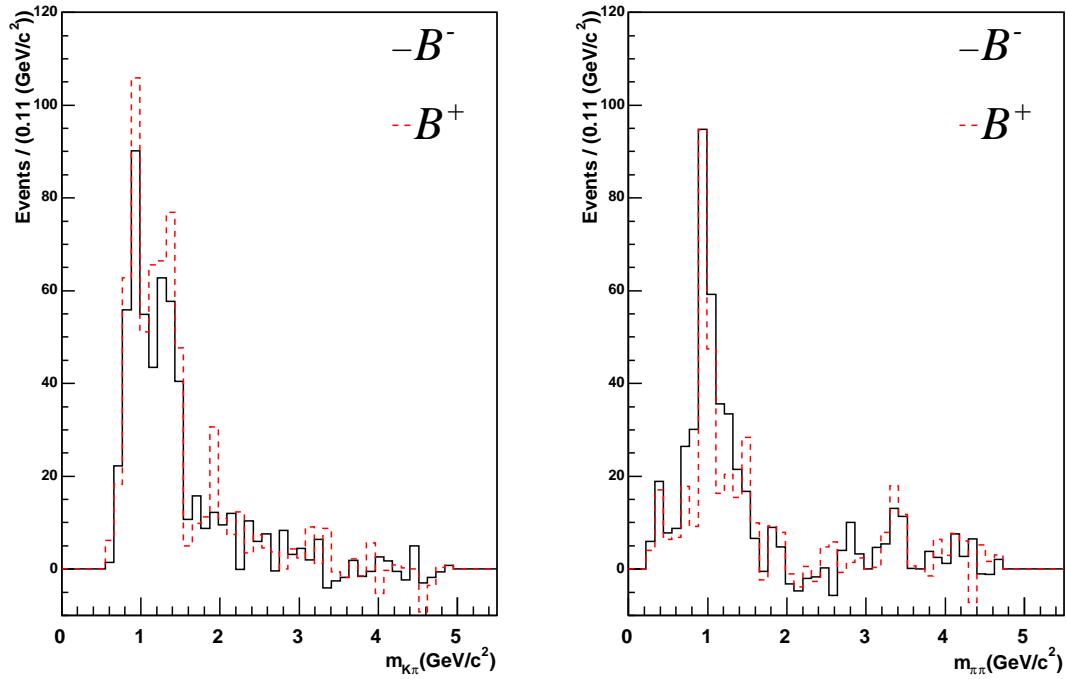


Figure 6.6: Background subtracted invariant mass projections for data with a  $2 \text{ GeV}/c^2$  cut on the other mass pair applied. The left histogram is for the  $K\pi$  pair and the right histogram is for the  $\pi\pi$  pair.

from the  $f_0(980)$  resonance and the  $K_0^{*0}(1430)$  resonance. The alternative lineshapes used for these two components have a number of parameters which have not been studied extensively and hence are not known with confidence. A study of these parameters is presented in this section. The aim of this study is to provide working models of the  $f_0(980)$  and  $K_0^{*0}(1430)$  resonances that enable a reasonable fit to the data to be obtained. The resultant values for the LASS parameters  $a$ ,  $r$  and the Flatté parameters  $g_\pi$ ,  $g_K$  and mass, are not to be taken as accurate measurements of these quantities.

### 6.3.1 $f_0(980)$

The Flatté lineshape has two parameters  $g_\pi$  and  $g_K$  for which there are different experimental measurements as shown in Section 4.3.1. These three sets of values produce different lineshapes as shown in Figure 6.7. Changing the mass of the

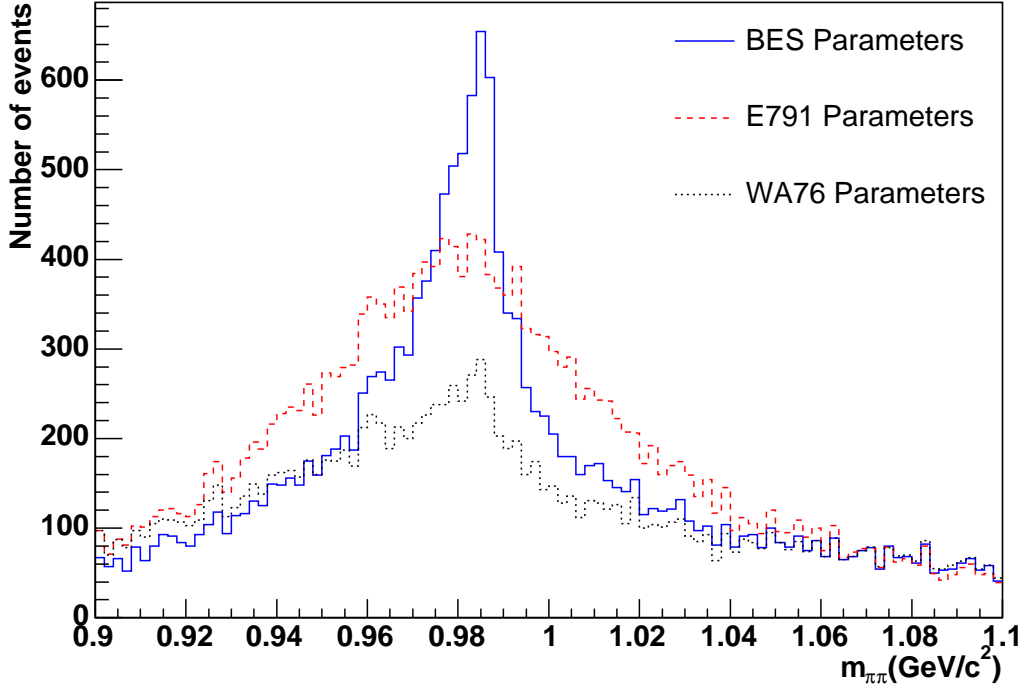


Figure 6.7: Toy MC events showing the Flatté lineshape for the  $f_0(980)$  resonance with different values for the parameters  $g_\pi$  and  $g_K$ .

$f_0(980)$  resonance also has an effect on this lineshape. This is illustrated in Figure 6.8 where the Flatté lineshape for the  $f_0(980)$  resonance is shown with the parameters  $g_\pi$  and  $g_K$  fixed to BES values but with different values of the mass. The six component fit to the  $B^-$  data sample is run with the three sets of values for the parameters  $g_\pi$  and  $g_K$ . The BES values are found to give the best negative log likelihood (NLL) but the  $\pi^+\pi^-$  invariant mass projection, shown in Figure 6.9, indicates that the fit is a poor representation of the data.

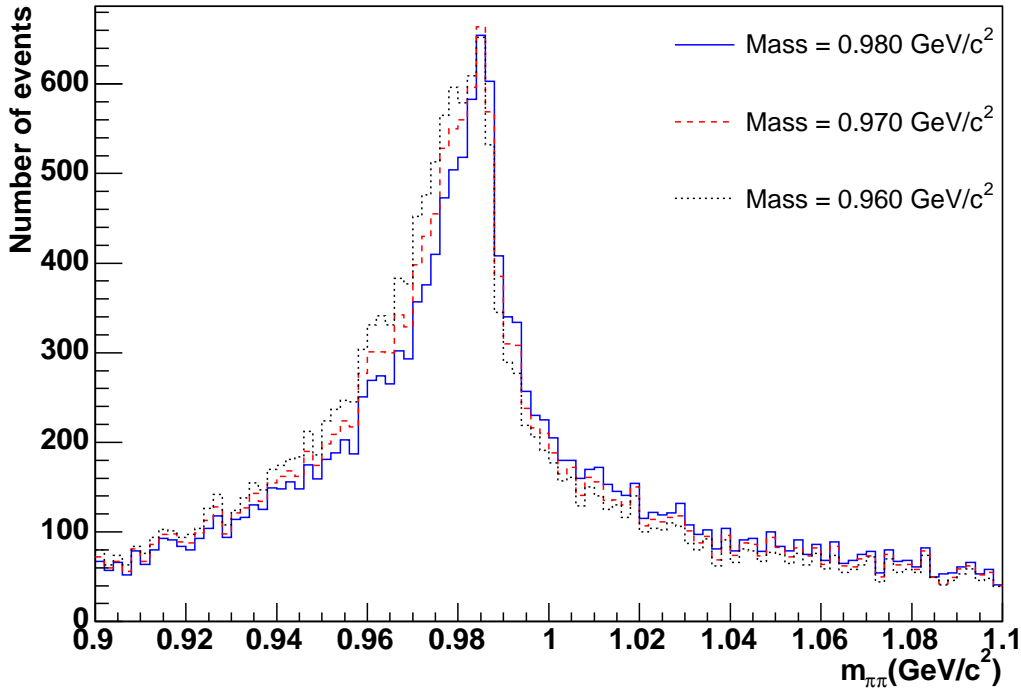


Figure 6.8: Toy MC events showing the Flatté lineshape for the  $f_0(980)$  resonance: the parameters  $g_\pi$  and  $g_K$  are fixed to the BES values but with different values for the mass.

A range of values for the parameters  $g_\pi$  and  $g_K$  are then tested. The exact values used can be seen in Figure 6.10. This shows that there are two possibilities for the minimum NLL value. These correspond to the situations with  $g_\pi = 0.12$ ,  $g_K = 0.41$  and  $g_\pi = 0.11$ ,  $g_K = 0.36$ . A range of masses between 0.960 and 0.980  $\text{GeV}/c^2$  are then tested for these cases. The results are shown in Figure 6.11. This shows that the best NLL occurs for  $g_\pi = 0.11$ ,  $g_K = 0.36$  and a mass of 0.965  $\text{GeV}/c^2$ . An estimate of the errors on these parameters can be obtained by calculating the difference between the best parameter value and the parameter value that results in an increase in NLL of  $\frac{1}{2}$  a unit. This gives errors of 0.02 for  $g_\pi$ , 0.10 for  $g_K$  and 10.0  $\text{MeV}/c^2$  for the mass. The fit now shows better agreement with the data as illustrated in Figure 6.12. The improved Flatté lineshape is also used in a six

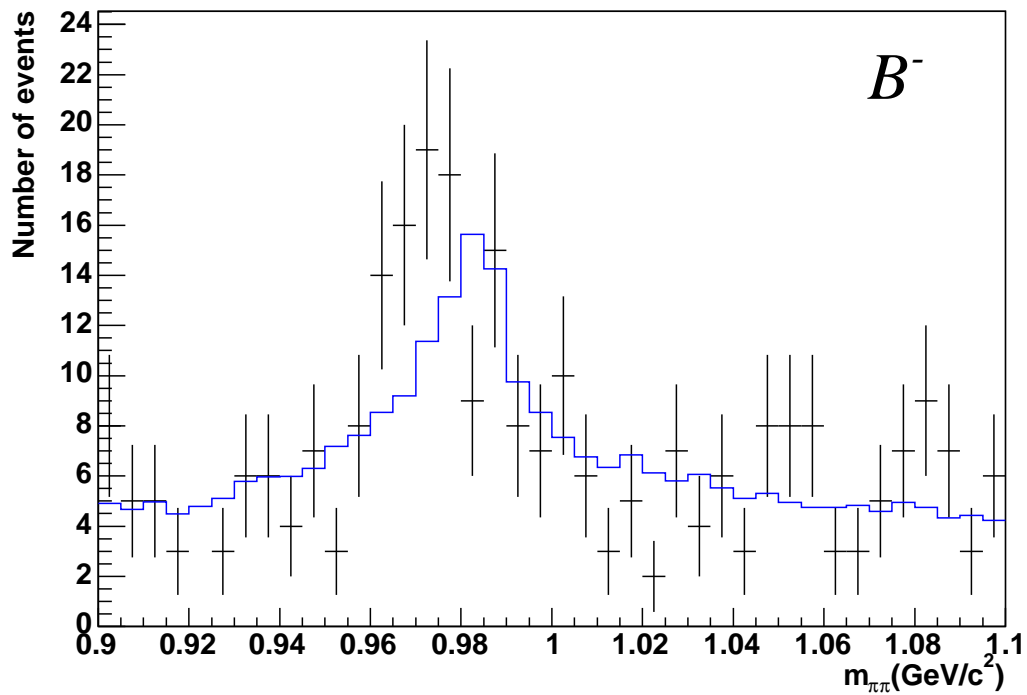


Figure 6.9: Invariant mass projection for the  $B^-$  data in the  $f_0(980)$  region. The black points are the data events in the signal box. The blue histogram is the fit result.

component fit to the  $B^+$  data, and the resulting  $\pi^+\pi^-$  invariant mass spectrum is shown in Figure 6.12. This new Flatté lineshape is found to be in good agreement with the  $B^+$  data.

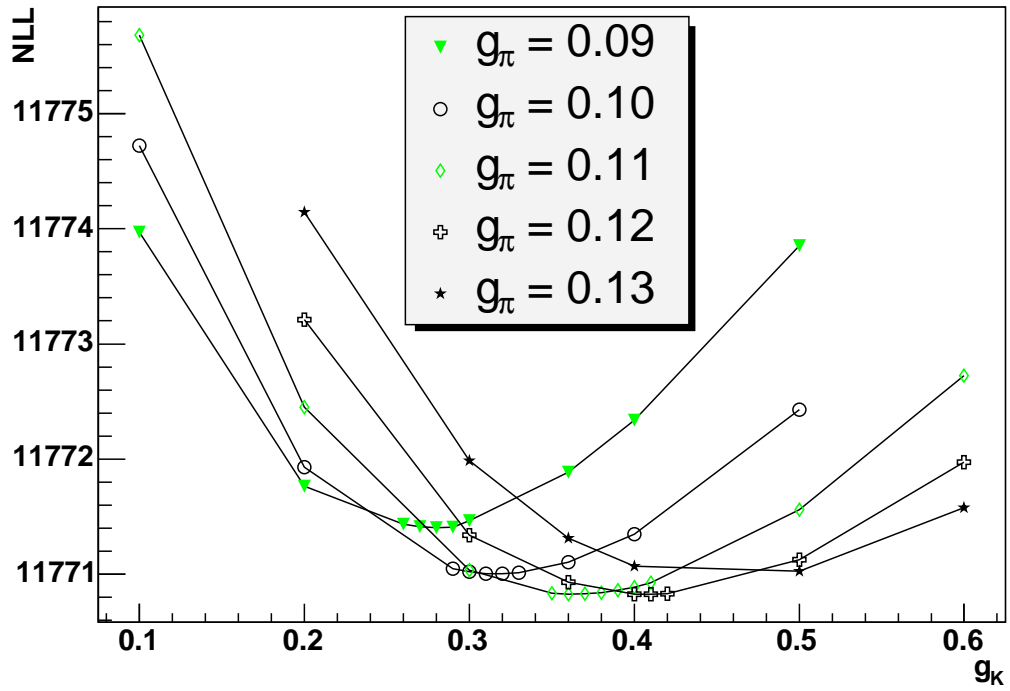
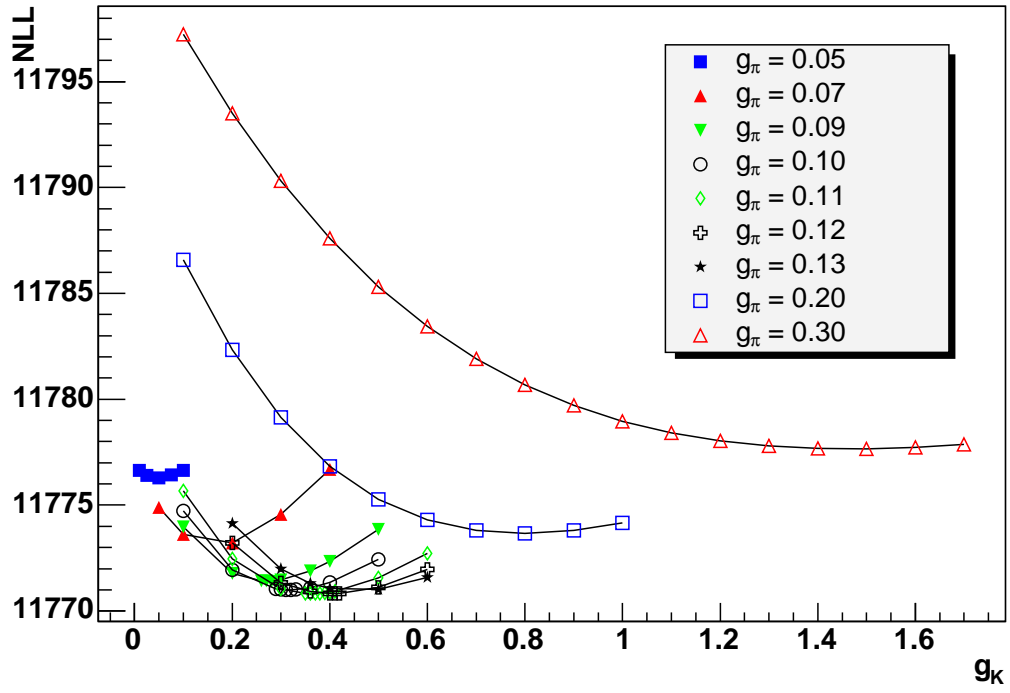


Figure 6.10: Negative log-likelihood results for fits using different Flatté lineshapes. The  $g_\pi$  values tested are shown in the legend. The mass is fixed to be  $0.980 \text{ GeV}/c^2$ . The bottom plot is an enlargement of the region around the minimum.

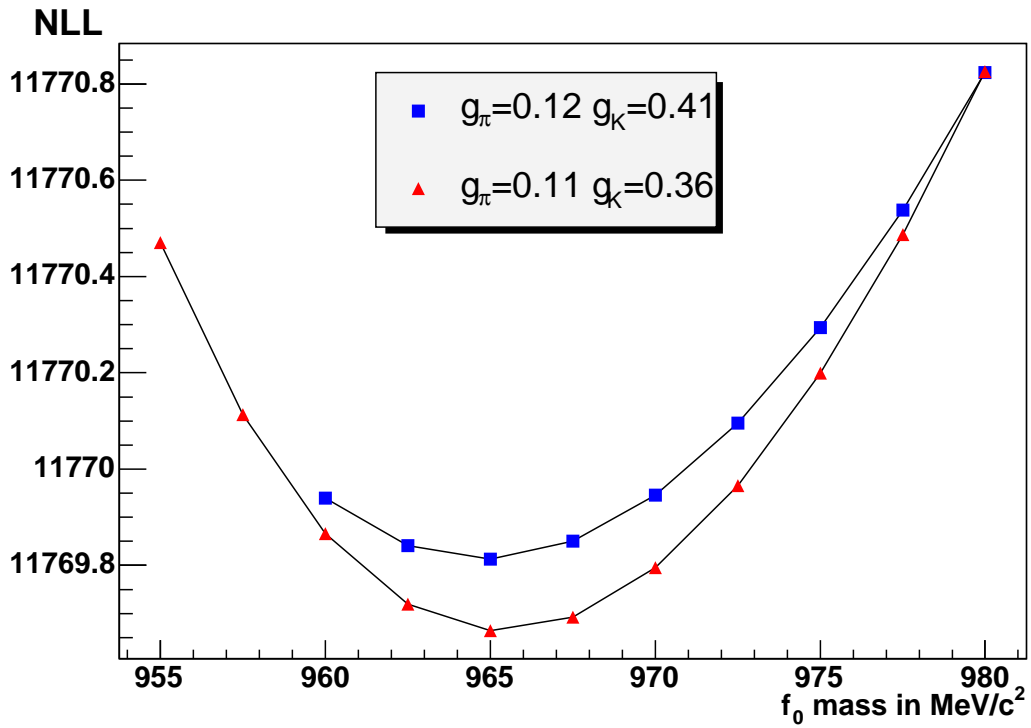


Figure 6.11: Negative log-likelihood results for fits using different values for the  $f_0(980)$  mass. The  $g_\pi$  and  $g_K$  values tested are shown in the legend.

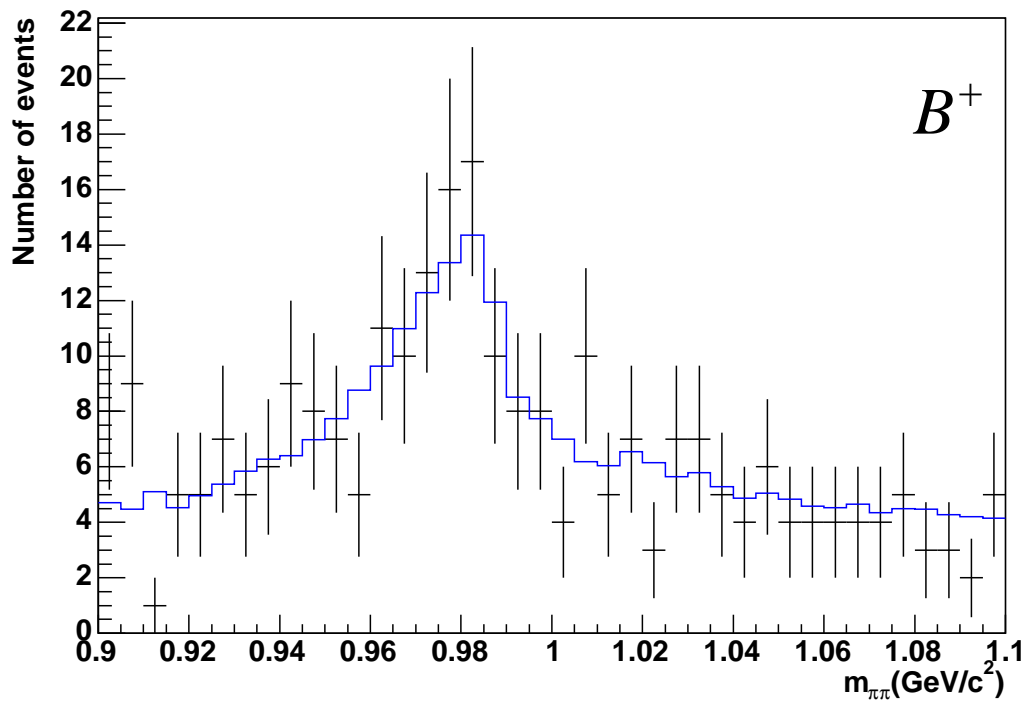
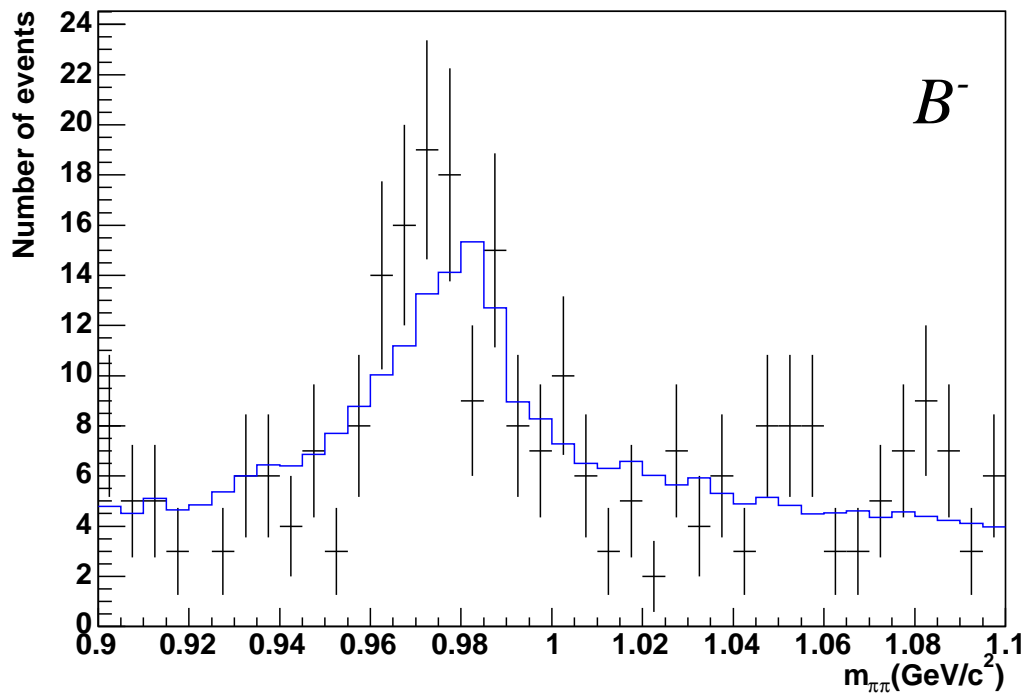


Figure 6.12: Invariant mass projection for the  $B^-$  and  $B^+$  data in the  $f_0(980)$  region with an improved Flatté lineshape. The black points are the data events in the signal box. The blue histogram is the fit result.

### 6.3.2 $K\pi$ S Wave

Section 4.3.2 gives details of the lineshape that can be used for the  $K_0^{*0}(1430)$  resonance. The initial six component fit is run on the  $B^-$  data sample using the LASS lineshape with the parameters  $a$  and  $r$  set to  $2.0 \text{ (GeV}/c)^{-1}$  and  $1.5 \text{ (GeV}/c)^{-1}$  respectively, which are the values used in the preliminary version of this analysis documented in [36]. These can be compared to the values obtained from the LASS data of  $a = 2.07 \pm 0.10 \text{ (GeV}/c)^{-1}$  and  $r = 3.32 \pm 0.34 \text{ (GeV}/c)^{-1}$  [62]. The resulting  $K^-\pi^+$  invariant mass spectrum for the fit is shown together with the data in Figure 6.13. The projection shows that the modelling of the  $K_0^{*0}(1430)$  resonance could

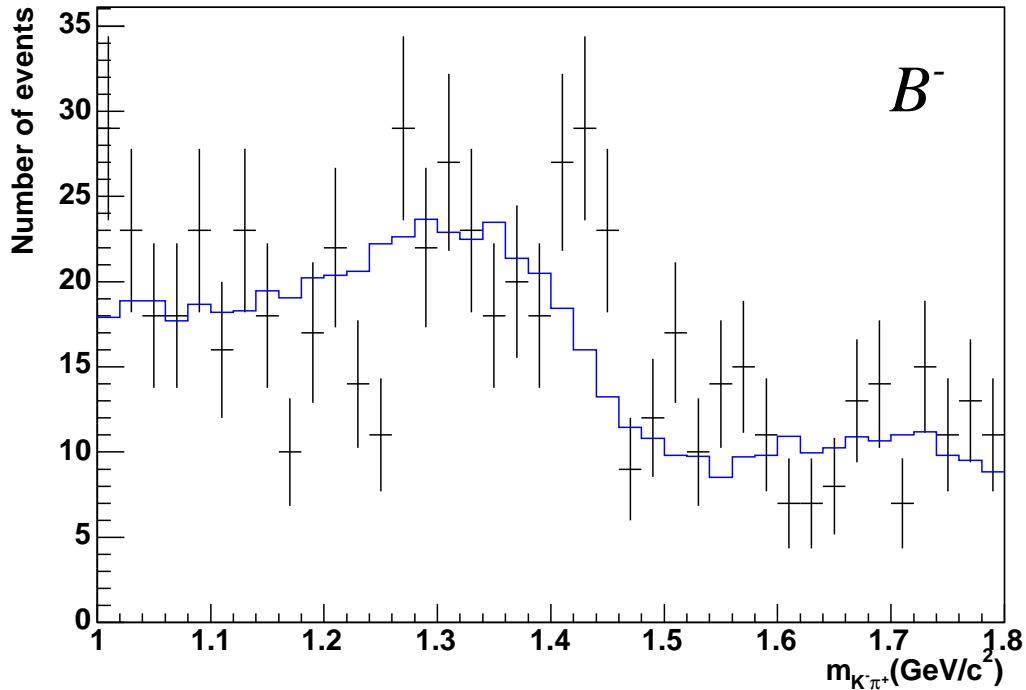


Figure 6.13: Invariant mass projection for the  $B^-$  data in the  $K_0^{*0}(1430)$  region. The black points are the data events in the signal box. The blue histogram is the fit result.

be improved. A wide range of values for the  $a$  and  $r$  parameters are studied and the

minimum is found to occur for  $a = 2.5 \text{ (GeV}/c)^{-1}$  and  $r = 5.25 \text{ (GeV}/c)^{-1}$ . The estimated errors on these parameters are calculated in the same way as described in Section 6.3.1, and are found to be  $0.3 \text{ (GeV}/c)^{-1}$  for  $a$  and  $0.95 \text{ (GeV}/c)^{-1}$  for  $r$ . The fit result shown in Figure 6.14 is now in better agreement with the data. The improved LASS lineshape is also used in a six component fit to the  $B^+$  data, and the resulting  $K^+\pi^-$  invariant mass spectrum is shown in Figure 6.14. This new LASS parameterisation is found to agree well with the  $B^+$  data.

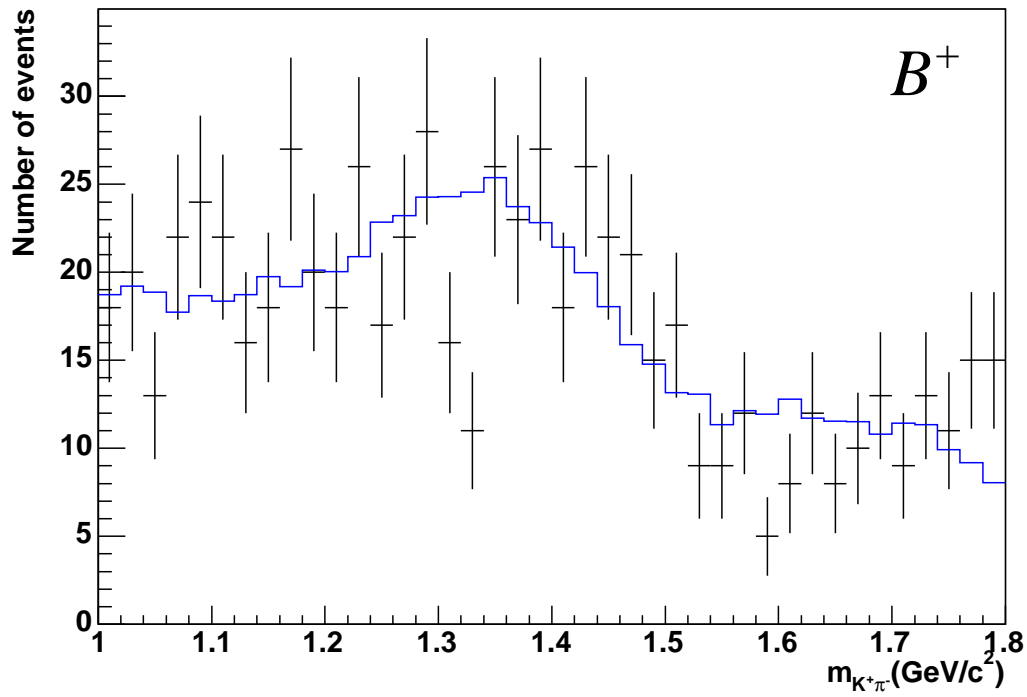
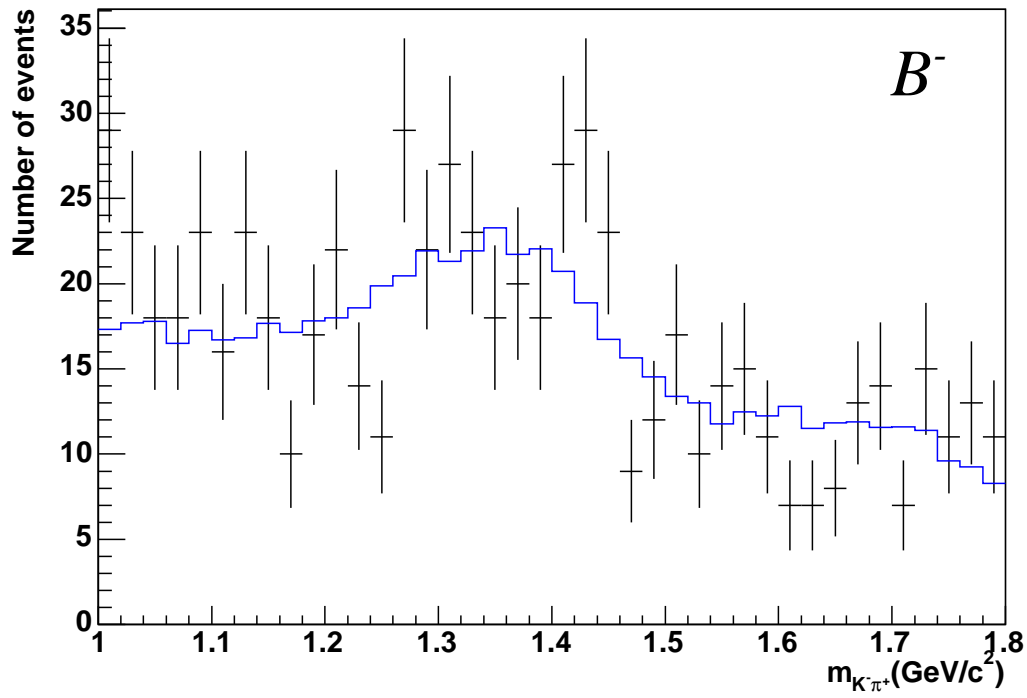


Figure 6.14: Invariant mass projection for the  $B^-$  and  $B^+$  data in the  $K_0^{*0}(1430)$  region with an improved LASS lineshape. The black points are the data events in the signal box. The blue histogram is the fit result.

## 6.4 Results - Six Component Nominal Model

The results of the fit using the nominal six component model are shown in Table 6.1 separately for  $B^-$  and  $B^+$  data. The  $\rho^0(770)$  resonance shows the greatest difference in fit fractions between the two samples. The full projection plots can be seen in Figure 6.15. These projection plots show that the fit is a good representation of the data in all regions apart from the 1.2 - 1.6 GeV/ $c^2$  region of the  $\pi\pi$  spectrum. This is easily explained as the nominal model does not contain a resonant contribution in that area. The same projections can be seen in Figure 6.16 where the invariant mass distribution is plotted only for events that have a value greater than 2 GeV/ $c^2$  in the other invariant mass pair. These plots show a much better agreement between the fit result and data in the very high  $K\pi$  mass region. This result is not surprising as the high  $K\pi$  mass region is populated almost entirely by events in the low  $\pi\pi$  mass region due to the shape of the Dalitz plot, and applying the 2 GeV/ $c^2$  cut will therefore dramatically depopulate the high  $K\pi$  mass region.

As an indication of goodness of fit, and to aid comparisons between fits that use different models, a  $\chi^2$  value is calculated as:

$$\chi^2 = \sum_{i=1}^{N_{Bins}} \frac{[y_i - f(x_i)]^2}{f(x_i)} \quad (6.1)$$

where  $y_i$  is the number of events found in bin  $i$  and  $f(x_i)$  is the number of events in that bin as predicted by the fit results. The associated number of degrees of freedom ( $ndof$ ) is calculated as  $N_{Bins} - k - 1$ , where  $k$  is the number of free parameters in the Dalitz-plot fit. A minimum of 10 entries in each bin is required; if this requirement is not met then neighbouring bins are combined. These  $\chi^2/ndof$  values are shown in Table 6.1.

Table 6.1: Results of fits to  $B^-$  and  $B^+$  data with nominal 6 component model

Component	$B^-$ Fit	$B^+$ Fit
Dalitz-plot $\chi^2/ndof$	205/121	193/117
$m_{K\pi}$ projection $\chi^2/ndof$	57/30	66/30
$m_{\pi\pi}$ projection $\chi^2/ndof$	86/27	73/27
$K^{*0}(892)$ Mag	1.0 = FIXED	1.0 = FIXED
$K^{*0}(892)$ Fraction (%)	$14.0 \pm 2.1$	$12.5 \pm 2.3$
$K^{*0}(892)$ Phase	0.0 = FIXED	0.0 = FIXED
$K_0^{*0}(1430)$ Mag	$1.90 \pm 0.13$	$2.14 \pm 0.16$
$K_0^{*0}(1430)$ Fraction (%)	$50.4 \pm 4.0$	$57.4 \pm 4.4$
$K_0^{*0}(1430)$ Phase	$2.73 \pm 0.13$	$3.08 \pm 0.12$
$\rho^0(770)$ Mag	$0.870 \pm 0.083$	$0.663 \pm 0.094$
$\rho^0(770)$ Fraction (%)	$10.6 \pm 2.0$	$5.5 \pm 1.6$
$\rho^0(770)$ Phase	$-0.49 \pm 0.36$	$1.12 \pm 0.49$
$f_0(980)$ Mag	$1.064 \pm 0.083$	$1.027 \pm 0.092$
$f_0(980)$ Fraction (%)	$15.9 \pm 2.4$	$13.2 \pm 2.4$
$f_0(980)$ Phase	$-1.90 \pm 0.35$	$-0.87 \pm 0.45$
$\chi_{c0}$ Mag	$0.254 \pm 0.050$	$0.321 \pm 0.054$
$\chi_{c0}$ Fraction (%)	$0.90 \pm 0.36$	$1.29 \pm 0.44$
$\chi_{c0}$ Phase	$-0.81 \pm 0.39$	$0.45 \pm 0.37$
NR Mag	$0.501 \pm 0.079$	$0.56 \pm 0.10$
NR Fraction (%)	$3.5 \pm 1.1$	$4.0 \pm 1.4$
NR Phase	$0.87 \pm 0.38$	$1.33 \pm 0.32$

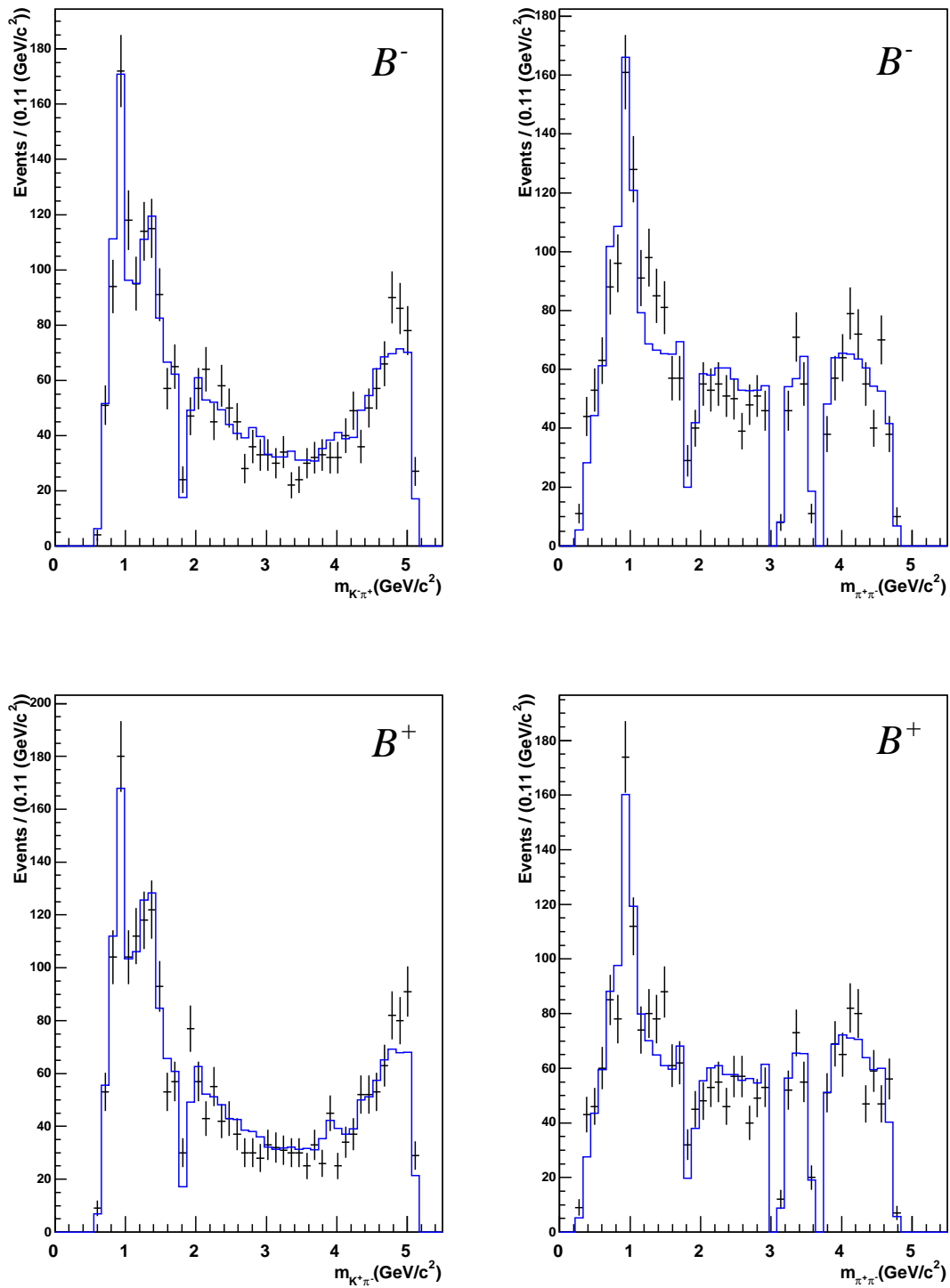


Figure 6.15: Invariant mass projections for the data. The left histograms are for the  $K\pi$  pair and the right histograms are for the  $\pi\pi$  pair. The black points are the data events in the signal box. The blue histogram is the fit result.

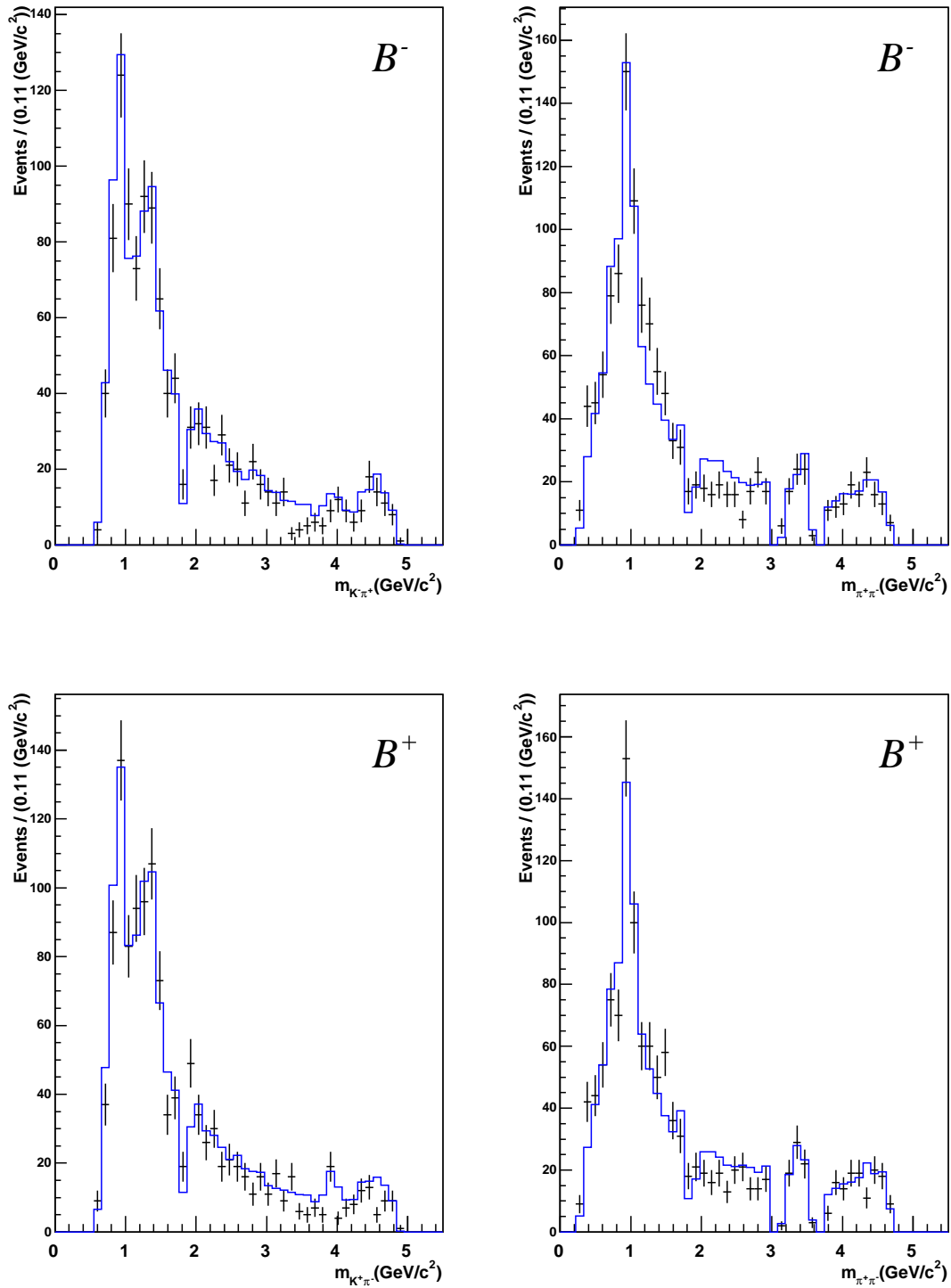


Figure 6.16: Invariant mass projections for the data with a  $2 \text{ GeV}/c^2$  cut on the other mass pair applied. The left histograms are for the  $K\pi$  pair and the right histograms are for the  $\pi\pi$  pair. The black points are the data events in the signal box. The blue histogram is the fit result.

## 6.5 Omission Tests

The actual resonance composition of the Dalitz plot is unknown. The fit may be looking for a component that is not present or incorrectly modelled. The Dalitz-plot fit is repeated omitting each of the six components in turn. A comparison of the NLL values,  $\chi^2$  values, fit fractions and phases are shown in Table 6.2 for  $B^-$  data and Table 6.3 for  $B^+$  data. As can be seen from these tables, omitting any component results in a significantly worse NLL value. The fitted fractions and phases of the remaining components vary wildly from their nominal fit values. This leads to the conclusion that all six nominal components are present in the Dalitz plot and must be included in the fit.

Table 6.2: Results of fit to  $B^-$  data with a different component omitted in turn from the nominal fit.

	Nominal	No $K^{*0}$ (892)	No $K_0^{*0}$ (1430)	No $\rho^0$ (770)	No $f_0$ (980)	No $\chi_{c0}$	No non-resonant
(NLL) – (NLL(nominal))	—	130.1	185.2	45.0	134.5	16.4	22.5
Dalitz-plot $\chi^2/ndof$	205/121	255/123	444/123	297/123	328/123	208/123	225/123
$m_{K-\pi^+}$ projection $\chi^2/ndof$	57/30	100/32	298/32	109/32	69/32	57/32	61/32
$m_{\pi^+\pi^-}$ projection $\chi^2/ndof$	86/27	111/29	100/29	105/29	255/29	88/29	99/29
$K^{*0}$ (892) Fraction (%)	$14.0 \pm 2.1$	—	$24.6 \pm 2.7$	$14.8 \pm 2.2$	$15.2 \pm 1.9$	$13.8 \pm 2.2$	$14.5 \pm 2.0$
$K^{*0}$ (892) Phase	0.0 FIXED	—	0.0 FIXED	0.0 FIXED	0.0 FIXED	0.0 FIXED	0.0 FIXED
$K_0^{*0}$ (1430) Fraction (%)	$50.4 \pm 4.0$	$64.2 \pm 3.5$	—	$55.0 \pm 4.2$	$53.5 \pm 4.1$	$50.6 \pm 4.0$	$53.3 \pm 3.2$
$K_0^{*0}$ (1430) Phase	$2.73 \pm 0.13$	$2.25 \pm 0.27$	—	$2.73 \pm 0.13$	$2.76 \pm 0.15$	$2.74 \pm 0.13$	$2.66 \pm 0.12$
$\rho^0$ (770) Fraction (%)	$10.6 \pm 2.0$	$11.0 \pm 1.6$	$15.7 \pm 2.4$	—	$15.7 \pm 2.5$	$10.5 \pm 2.0$	$11.5 \pm 2.2$
$\rho^0$ (770) Phase	$-0.49 \pm 0.36$	$-0.45 \pm 0.20$	$1.32 \pm 0.25$	—	$0.93 \pm 0.89$	$-0.37 \pm 0.36$	$-0.96 \pm 0.33$
$f_0$ (980) Fraction (%)	$15.9 \pm 2.4$	$15.9 \pm 1.7$	$24.5 \pm 2.7$	$17.3 \pm 2.5$	—	$15.6 \pm 2.4$	$19.2 \pm 2.6$
$f_0$ (980) Phase	$-1.90 \pm 0.35$	-1.90 FIXED	$0.21 \pm 0.22$	$-0.92 \pm 0.37$	—	$-1.80 \pm 0.35$	$-2.28 \pm 0.29$
$\chi_{c0}$ Fraction (%)	$0.90 \pm 0.36$	$0.87 \pm 0.35$	$0.98 \pm 0.39$	$0.87 \pm 0.36$	$0.72 \pm 0.33$	—	$1.51 \pm 0.46$
$\chi_{c0}$ Phase	$-0.81 \pm 0.39$	$-0.96 \pm 0.47$	$2.86 \pm 0.42$	$-0.72 \pm 0.40$	$-0.67 \pm 0.46$	—	$-1.04 \pm 0.34$
Non Resonant Fraction (%)	$3.5 \pm 1.1$	$5.8 \pm 1.7$	$32.6 \pm 3.2$	$6.0 \pm 1.6$	$10.1 \pm 2.1$	$4.8 \pm 1.3$	—
Non Resonant Phase	$0.87 \pm 0.38$	$1.23 \pm 0.33$	$-2.27 \pm 0.19$	$0.83 \pm 0.35$	$0.74 \pm 0.55$	$1.01 \pm 0.35$	—

Table 6.3: Results of fit to  $B^+$  data with a different component omitted in turn from the nominal fit.

	Nominal	No $K^{*0}$ (892)	No $K_0^{*0}$ (1430)	No $\rho^0$ (770)	No $f_0$ (980)	No $\chi_{c0}$	No non-resonant
(NLL) – (NLL(nominal))	—	101.2	250.4	19.7	106.3	21.9	20.3
Dalitz-plot $\chi^2/ndof$	193/117	226/119	495/119	234/119	275/119	197/119	216/119
$m_{K^+\pi^-}$ projection $\chi^2/ndof$	66/30	122/32	399/32	100/32	75/32	66/32	73/32
$m_{\pi^+\pi^-}$ projection $\chi^2/ndof$	73/27	102/29	101/29	76/29	225/29	75/29	82/29
$K^{*0}$ (892) Fraction (%)	$12.5 \pm 2.3$	—	$26.3 \pm 2.7$	$12.8 \pm 2.2$	$13.4 \pm 1.7$	$12.6 \pm 2.3$	$12.7 \pm 1.9$
$K^{*0}$ (892) Phase	0.0 FIXED	—	0.0 FIXED	0.0 FIXED	0.0 FIXED	0.0 FIXED	0.0 FIXED
$K_0^{*0}$ (1430) Fraction (%)	$57.4 \pm 4.4$	$71.1 \pm 12.6$	—	$61.1 \pm 4.4$	$63.8 \pm 4.0$	$57.5 \pm 4.3$	$59.8 \pm 3.1$
$K_0^{*0}$ (1430) Phase	$3.08 \pm 0.12$	$2.78 \pm 0.39$	—	$3.08 \pm 0.13$	$-3.12 \pm 0.12$	$3.12 \pm 0.12$	$2.98 \pm 0.12$
$\rho^0$ (770) Fraction (%)	$5.5 \pm 1.6$	$5.7 \pm 1.4$	$9.0 \pm 2.0$	—	$10.2 \pm 2.2$	$5.3 \pm 1.5$	$6.4 \pm 1.6$
$\rho^0$ (770) Phase	$1.12 \pm 0.49$	$1.01 \pm 0.23$	$1.71 \pm 0.24$	—	$2.73 \pm 0.36$	$1.38 \pm 0.46$	$0.04 \pm 0.37$
$f_0$ (980) Fraction (%)	$13.2 \pm 2.4$	$13.1 \pm 1.6$	$27.3 \pm 3.0$	$14.0 \pm 2.4$	—	$12.3 \pm 2.2$	$17.8 \pm 2.7$
$f_0$ (980) Phase	$-0.87 \pm 0.45$	-0.87 FIXED	$0.01 \pm 0.19$	$-0.36 \pm 0.38$	—	$-0.61 \pm 0.42$	$-1.85 \pm 0.31$
$\chi_{c0}$ Fraction (%)	$1.29 \pm 0.44$	$1.28 \pm 0.40$	$1.30 \pm 0.46$	$1.30 \pm 0.45$	$1.07 \pm 0.41$	—	$2.01 \pm 0.54$
$\chi_{c0}$ Phase	$0.45 \pm 0.37$	$0.44 \pm 0.50$	$-2.67 \pm 0.35$	$0.51 \pm 0.38$	$0.90 \pm 0.40$	—	$0.20 \pm 0.34$
Non Resonant Fraction (%)	$4.0 \pm 1.4$	$5.2 \pm 1.6$	$44.4 \pm 3.7$	$5.5 \pm 1.7$	$12.8 \pm 2.8$	$6.0 \pm 1.7$	—
Non Resonant Phase	$1.33 \pm 0.32$	$1.69 \pm 0.47$	$-1.82 \pm 0.15$	$1.35 \pm 0.30$	$1.92 \pm 0.23$	$1.40 \pm 0.29$	—

## 6.6 Addition Tests

It is also possible that the fit is neglecting to look for a component that contributes to the Dalitz plot. In the  $\pi\pi$  spectrum there are possible higher resonances including  $f_2(1270)$ ,  $f_0(1370)$ ,  $\rho^0(1450)$ ,  $f_0(1500)$  and  $f_2(1525)$ . In the  $K\pi$  spectrum there are possible  $K_2^{*0}(1430)$  and  $K^{*0}(1680)$  resonances. Each of these resonances is added in turn to the signal model and the Dalitz-plot fit is repeated. A comparison of the NLL values,  $\chi^2$  values, fit fractions and phases are shown in Table 6.4 for  $B^-$  data and Table 6.5 for  $B^+$  data.

Generally, adding another component does not significantly affect the measured fit fractions and phases of the six nominal components. For  $B^-$  data, the  $f_2(1270)$  and  $f_0(1370)$  components cause the greatest change in NLL. The  $f_2(1270)$  has a significant fit fraction of  $8.3 \pm 2.3$ . For  $B^+$  data the  $\rho^0(1450)$  and  $f_2(1270)$  cause the greatest change in NLL. The  $f_2(1270)$  fit fraction is  $4.8 \pm 1.7$  which is smaller than that measured for  $B^-$  data. The  $\rho^0(1450)$  component has a large fit fraction of  $10.1 \pm 2.5$ , which is very different to that measured in  $B^-$  data, and the addition of this resonance leads to a large change in value for the  $f_0(980)$  phase.

The possible additional contributions to the  $\pi\pi$  spectrum, and the differences between  $B^-$  and  $B^+$  data, are investigated further in the next section.

Table 6.4: Results of fit to  $B^-$  data with a different resonance added in turn to the nominal fit

	Nominal	With $f_2(1270)$	With $f_0(1370)$	With $\rho^0(1450)$	With $f_0(1500)$	With $f_2(1525)$	With $K_2^{*0}(1430)$	With $K^{*0}(1680)$
(NLL) – (NLL(nominal))	—	–7.935	–7.865	–2.486	–4.658	–0.363	–4.891	–0.997
Dalitz-plot $\chi^2/ndof$	205/121	204/119	202/119	203/119	203/119	205/119	200/119	206/119
$m_{K-\pi^+}$ projection $\chi^2/ndof$	57/30	43/28	58/28	54/28	58/28	56/28	58/28	56/28
$m_{\pi^+\pi^-}$ projection $\chi^2/ndof$	86/27	63/25	64/25	82/25	70/25	86/25	82/25	86/25
$K^{*0}(892)$ Fraction (%)	$14.0 \pm 2.1$	$12.7 \pm 2.1$	$13.8 \pm 2.8$	$13.6 \pm 2.1$	$14.0 \pm 2.3$	$14.0 \pm 2.2$	$13.6 \pm 2.1$	$14.3 \pm 2.3$
$K_0^{*0}(1430)$ Fraction (%)	$50.4 \pm 4.0$	$47.8 \pm 4.2$	$48.9 \pm 4.2$	$48.7 \pm 4.2$	$49.6 \pm 4.0$	$50.6 \pm 4.0$	$47.3 \pm 4.1$	$50.4 \pm 4.1$
$K_0^{*0}(1430)$ Phase	$2.73 \pm 0.13$	$2.83 \pm 0.13$	$2.73 \pm 0.13$	$2.76 \pm 0.13$	$2.73 \pm 0.13$	$2.73 \pm 0.13$	$2.77 \pm 0.13$	$2.78 \pm 0.13$
$\rho^0(770)$ Fraction (%)	$10.6 \pm 2.0$	$8.0 \pm 1.8$	$10.6 \pm 2.0$	$9.5 \pm 1.9$	$10.8 \pm 2.0$	$10.6 \pm 2.0$	$10.5 \pm 2.0$	$10.4 \pm 2.0$
$\rho^0(770)$ Phase	$-0.49 \pm 0.36$	$0.09 \pm 0.37$	$-0.45 \pm 0.38$	$0.63 \pm 0.41$	$-0.48 \pm 0.36$	$-0.49 \pm 0.37$	$-0.45 \pm 0.31$	$-0.45 \pm 0.36$
$f_0(980)$ Fraction (%)	$15.9 \pm 2.4$	$14.6 \pm 2.3$	$13.9 \pm 2.6$	$16.0 \pm 2.5$	$15.5 \pm 2.5$	$15.8 \pm 2.4$	$16.0 \pm 2.4$	$15.7 \pm 2.4$
$f_0(980)$ Phase	$-1.90 \pm 0.35$	$-1.21 \pm 0.35$	$-2.04 \pm 0.40$	$-2.15 \pm 0.38$	$-1.95 \pm 0.35$	$-1.90 \pm 0.35$	$-1.91 \pm 0.33$	$-1.94 \pm 0.35$
$\chi_{c0}$ Fraction (%)	$0.90 \pm 0.36$	$0.94 \pm 0.37$	$0.96 \pm 0.37$	$0.94 \pm 0.37$	$0.92 \pm 0.36$	$0.90 \pm 0.36$	$0.89 \pm 0.36$	$0.93 \pm 0.36$
$\chi_{c0}$ Phase	$-0.81 \pm 0.39$	$-0.79 \pm 0.38$	$-0.85 \pm 0.38$	$-0.82 \pm 0.38$	$-0.82 \pm 0.39$	$-0.81 \pm 0.39$	$-0.56 \pm 0.41$	$-0.81 \pm 0.39$
Non-resonant Fraction (%)	$3.5 \pm 1.1$	$3.2 \pm 1.1$	$3.6 \pm 1.2$	$3.0 \pm 1.0$	$3.8 \pm 1.1$	$3.5 \pm 1.1$	$4.0 \pm 1.4$	$3.4 \pm 1.1$
Non-resonant Phase	$0.87 \pm 0.38$	$0.79 \pm 0.39$	$0.63 \pm 0.40$	$0.87 \pm 0.39$	$0.79 \pm 0.39$	$0.87 \pm 0.39$	$1.25 \pm 0.38$	$0.82 \pm 0.40$
Additional Fraction(%)	—	$8.3 \pm 2.3$	$2.3 \pm 1.2$	$1.6 \pm 1.2$	$1.7 \pm 1.7$	$0.12 \pm 0.29$	$4.9 \pm 2.0$	$0.52 \pm 0.77$
Additional Phase	—	$-0.68 \pm 0.28$	$0.22 \pm 0.41$	$0.57 \pm 0.44$	$1.11 \pm 0.63$	$-1.7 \pm 1.2$	$2.63 \pm 0.17$	$-2.22 \pm 0.62$

Table 6.5: Results of fit to  $B^+$  data with a different resonance added in turn to the nominal fit

	Nominal	With $f_2(1270)$	With $f_0(1370)$	With $\rho^0(1450)$	With $f_0(1500)$	With $f_2(1525)$	With $K_2^{*0}(1430)$	With $K^{*0}(1680)$
(NLL) – (NLL(nominal))	—	–14.9721	–4.209	–18.219	–4.943	–3.947	–1.83	–0.487
Dalitz-plot $\chi^2/ndof$	193/117	168/115	188/115	181/115	190/115	180/115	193/115	195/115
$m_{K^+\pi^-}$ projection $\chi^2/ndof$	66/30	49/28	67/28	58/28	67/28	57/28	65/28	66/28
$m_{\pi^+\pi^-}$ projection $\chi^2/ndof$	73/27	67/25	62/25	60/25	61/25	67/25	74/25	74/25
$K^{*0}(892)$ Fraction (%)	$12.5 \pm 2.3$	$11.5 \pm 2.1$	$12.3 \pm 2.5$	$11.4 \pm 2.0$	$12.5 \pm 2.3$	$11.9 \pm 2.1$	$13.0 \pm 2.3$	$12.8 \pm 2.4$
$K_0^{*0}(1430)$ Fraction (%)	$57.4 \pm 4.4$	$55.4 \pm 4.5$	$56.6 \pm 4.8$	$56.3 \pm 4.4$	$56.6 \pm 4.5$	$56.4 \pm 4.4$	$54.8 \pm 4.6$	$57.6 \pm 4.4$
$K_0^{*0}(1430)$ Phase	$3.08 \pm 0.12$	$3.11 \pm 0.12$	$3.07 \pm 0.12$	$3.12 \pm 0.13$	$3.10 \pm 0.13$	$3.10 \pm 0.13$	$3.09 \pm 0.12$	$3.10 \pm 0.13$
$\rho^0(770)$ Fraction (%)	$5.5 \pm 1.6$	$4.3 \pm 1.4$	$4.8 \pm 1.5$	$5.5 \pm 1.9$	$5.2 \pm 1.5$	$5.1 \pm 1.5$	$5.3 \pm 1.5$	$5.5 \pm 1.5$
$\rho^0(770)$ Phase	$1.12 \pm 0.49$	$1.17 \pm 0.41$	$1.29 \pm 0.43$	$1.94 \pm 0.38$	$1.34 \pm 0.45$	$1.36 \pm 0.46$	$1.70 \pm 0.50$	$1.22 \pm 0.46$
$f_0(980)$ Fraction (%)	$13.2 \pm 2.4$	$13.4 \pm 2.4$	$10.7 \pm 2.1$	$11.8 \pm 2.1$	$11.5 \pm 2.1$	$12.9 \pm 2.3$	$12.6 \pm 2.2$	$12.8 \pm 2.4$
$f_0(980)$ Phase	$-0.87 \pm 0.45$	$-0.77 \pm 0.37$	$-0.53 \pm 0.41$	$0.47 \pm 0.37$	$-0.60 \pm 0.43$	$-0.58 \pm 0.44$	$-0.36 \pm 0.46$	$-0.78 \pm 0.42$
$\chi_{c0}$ Fraction (%)	$1.29 \pm 0.44$	$1.27 \pm 0.44$	$1.35 \pm 0.46$	$1.28 \pm 0.44$	$1.31 \pm 0.45$	$1.29 \pm 0.44$	$1.25 \pm 0.43$	$1.29 \pm 0.44$
$\chi_{c0}$ Phase	$0.45 \pm 0.37$	$0.41 \pm 0.37$	$0.40 \pm 0.37$	$0.53 \pm 0.39$	$0.44 \pm 0.37$	$0.47 \pm 0.38$	$0.52 \pm 0.38$	$0.43 \pm 0.37$
Non-resonant Fraction (%)	$4.0 \pm 1.4$	$3.7 \pm 1.2$	$3.6 \pm 1.4$	$5.0 \pm 1.7$	$4.4 \pm 1.5$	$3.9 \pm 1.4$	$5.4 \pm 1.8$	$4.1 \pm 1.4$
Non-resonant Phase	$1.33 \pm 0.32$	$1.25 \pm 0.32$	$1.14 \pm 0.33$	$1.53 \pm 0.29$	$1.21 \pm 0.32$	$1.39 \pm 0.32$	$1.57 \pm 0.31$	$1.30 \pm 0.31$
Additional Fraction (%)	—	$4.8 \pm 1.7$	$1.18 \pm 0.77$	$10.1 \pm 2.5$	$0.97 \pm 0.59$	$2.8 \pm 1.1$	$2.3 \pm 1.6$	$0.27 \pm 0.54$
Additional Phase	—	$-0.11 \pm 0.26$	$-0.25 \pm 0.50$	$-0.32 \pm 0.29$	$0.83 \pm 0.50$	$0.19 \pm 0.38$	$-0.20 \pm 0.21$	$-1.11 \pm 0.80$

## 6.7 Results - Seven Component Model

### 6.7.1 Projection Plots

In order to try to define the resonance composition and to get an accurate idea of how well the Dalitz-plot fit is performing in the 1.2 - 1.8 GeV/ $c^2$  region of the  $\pi\pi$  spectrum the signal parts of the data and fit result are compared. For the data a bin-by-bin subtraction is performed to get background-subtracted data plots. For the fit result, a toy MC sample is generated using the fitted parameters, and the signal part of this sample is extracted. This comparison can be seen in Figure 6.17 for  $B^-$  events. The top left plot of this figure is the background-subtracted data, and its shape can be compared to the other five plots in the figure, which represent the results of fits using different additional components. The same plots can be seen in Figure 6.18 for  $B^+$  events.

Figure 6.17 shows that the  $f_2(1270)$  resonance or  $f_0(1370)$  resonance appear to improve the model's description of the  $B^-$  data. Figure 6.18 shows that the  $B^+$  signal distribution in this region has a different shape to  $B^-$ , and can best be described by the  $\rho^0(1450)$  resonance although the  $f_2(1270)$  resonance is also a reasonable model. Both of these plots show that the signal distribution in this region is affected by low statistics. As the  $f_2(1270)$  resonance is a possible component for both  $B^-$  and  $B^+$ , the results of fits including the  $f_2(1270)$  are used to make full projection plots which are shown in Figure 6.19 for  $B^-$  and  $B^+$ . The projections are an improvement on the nominal model in the 1.2 - 1.8 GeV/ $c^2$  region of the  $\pi\pi$  spectrum (see Figure 6.15), however the plots suggest that there may be more than one resonance contribution in this area.

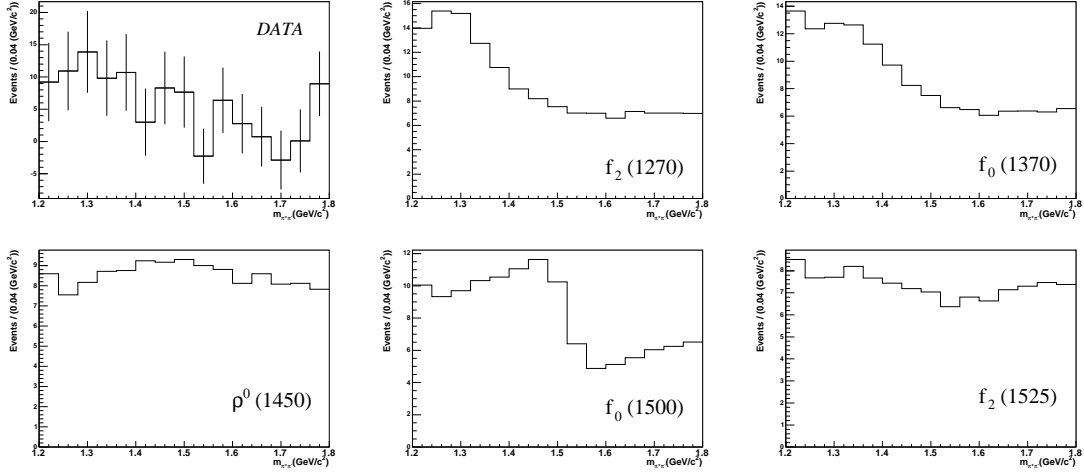


Figure 6.17: Signal data and fit results in the 1.2 - 1.8  $\text{GeV}/c^2$  region of the  $m_{\pi\pi}$  spectrum for  $B^-$ . The top left plot shows the background subtracted data. The top middle plot shows the fit results with the  $f_2(1270)$  resonance included, the top right plot includes the  $f_0(1370)$  resonance, the bottom left plot includes the  $\rho^0(1450)$  resonance, the bottom middle plot the  $f_0(1500)$  resonance and the bottom right plot the  $f_2(1525)$  resonance.

### 6.7.2 Addition Tests

The hypothesis of the presence of the  $f_2(1270)$  resonance is tested by further fitting experiments, where an additional resonance is added in turn to the 7 component nominal+ $f_2(1270)$  model. These results can be seen in Table 6.6 for  $B^-$  and Table 6.7 for  $B^+$ . Table 6.6 shows that the  $f_2(1270)$  fit fraction is not stable for  $B^-$  data, and can decrease significantly when another resonance is present in the same invariant mass region. Table 6.7 shows that the  $\rho^0(1450)$  fit fraction for  $B^+$  data has decreased from its value in the nominal+ $\rho^0(1450)$  model (see Table 6.5) and the  $f_2(1270)$  fit fraction is generally stable when another resonance is added in this invariant mass region.

Given the low statistics, the high level of uncertainty about the precise nature of the resonant contribution to the 1.2 - 1.8  $\text{GeV}/c^2$  region of the  $\pi\pi$  spectrum, and

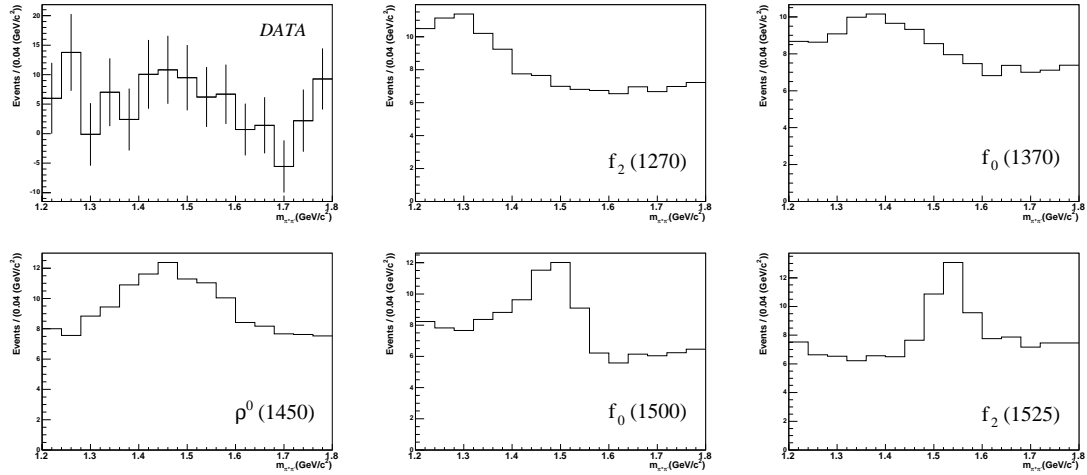


Figure 6.18: Signal data and fit results in the 1.2 - 1.8  $\text{GeV}/c^2$  region of the  $m_{\pi\pi}$  spectrum for  $B^+$ . The top left plot shows the background subtracted data. The top middle plot shows the fit results with the  $f_2(1270)$  resonance included, the top right plot includes the  $f_0(1370)$  resonance, the bottom left plot includes the  $\rho^0(1450)$  resonance, the bottom middle plot the  $f_0(1500)$  resonance and the bottom right plot the  $f_2(1525)$  resonance.

possible differences between  $B^-$  and  $B^+$  data, this analysis will use the nominal model (which has no resonance model for this region) to make measurements of the fit fractions and phases of the six nominal fit components. Upper limits for the fit fractions of possible higher resonances will be calculated separately.

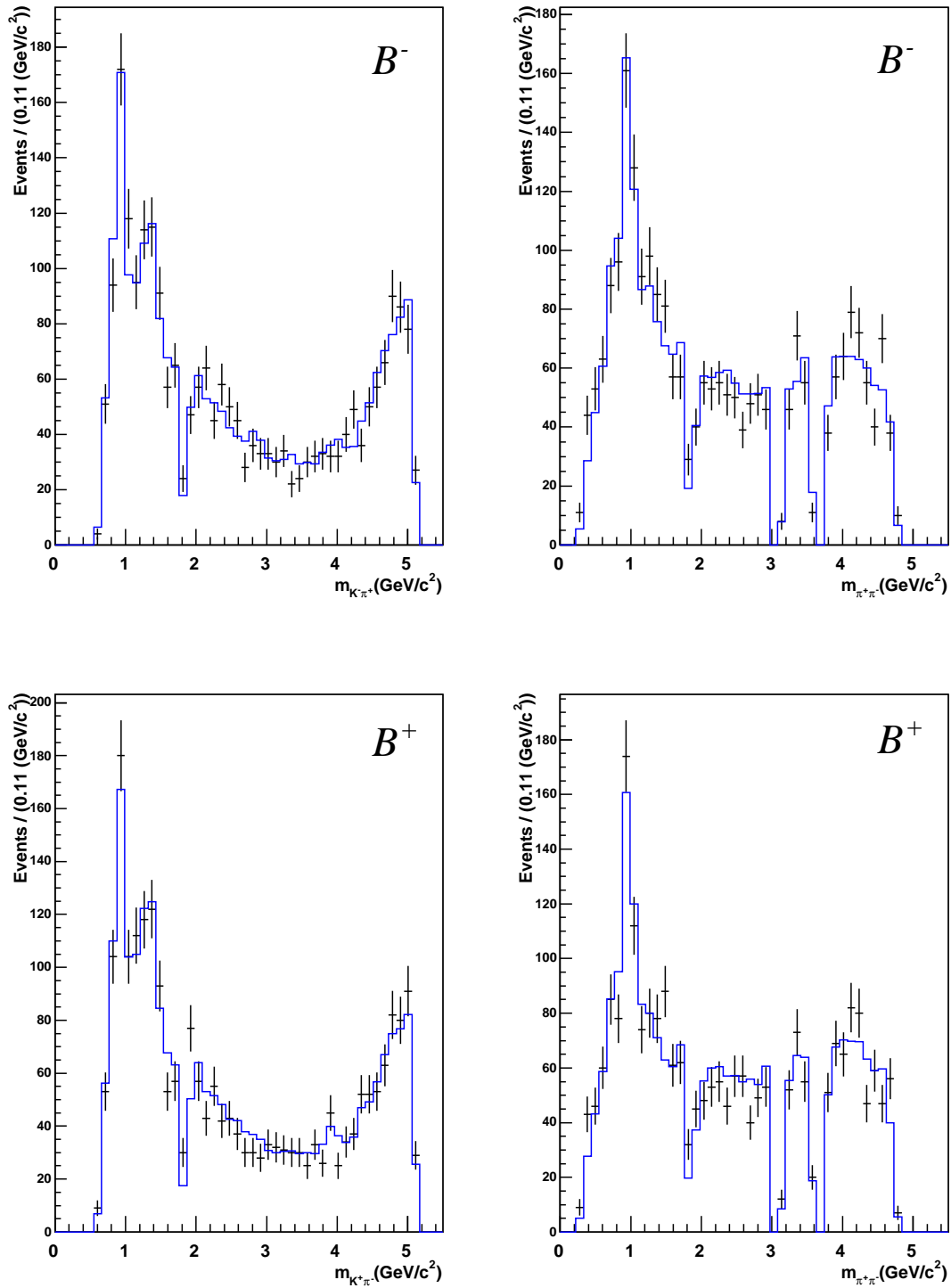


Figure 6.19: Invariant mass projections for the data. The left histograms are for the  $K\pi$  pair and the right histograms are for the  $\pi\pi$  pair. The black points are the data events in the signal box. The blue histogram is the fit result using the seven component model, including an additional  $f_2(1270)$  component.

Table 6.6: Results of fit to  $B^-$  data with a different resonance added in turn to the nominal +  $f_2(1270)$  fit

	Nominal + $f_2(1270)$	With $f_0(1370)$	With $\rho^0(1450)$	With $f_0(1500)$	With $f_2(1525)$
(NLL) – (NLL(nominal + $f_2(1270)$ ))	—	–6.091	–0.827	–2.857	–1.313
Dalitz-plot $\chi^2/ndof$	204/119	196/117	202/117	198/117	201/117
$m_{K^-\pi^+}$ projection $\chi^2/ndof$	43/28	46/26	43/26	46/26	43/26
$m_{\pi^+\pi^-}$ projection $\chi^2/ndof$	63/25	60/23	62/23	63/23	63/23
$K^{*0}(892)$ Fraction (%)	$12.7 \pm 2.1$	$13.1 \pm 3.0$	$12.5 \pm 2.1$	$13.4 \pm 2.3$	$12.8 \pm 2.1$
$K_0^{*0}(1430)$ Fraction (%)	$47.8 \pm 4.2$	$47.4 \pm 4.5$	$47.0 \pm 4.2$	$48.9 \pm 4.2$	$48.5 \pm 4.3$
$K_0^{*0}(1430)$ Phase	$2.83 \pm 0.13$	$2.79 \pm 0.13$	$2.86 \pm 0.13$	$2.77 \pm 0.13$	$2.81 \pm 0.133$
$\rho^0(770)$ Fraction (%)	$8.0 \pm 1.8$	$9.4 \pm 2.0$	$8.0 \pm 1.8$	$9.7 \pm 1.9$	$8.0 \pm 1.8$
$\rho^0(770)$ Phase	$0.09 \pm 0.37$	$-0.28 \pm 0.42$	$0.23 \pm 0.38$	$-0.22 \pm 0.36$	$0.04 \pm 0.37$
$f_0(980)$ Fraction (%)	$14.6 \pm 2.3$	$13.5 \pm 2.9$	$14.6 \pm 2.3$	$15.6 \pm 2.6$	$14.5 \pm 2.4$
$f_0(980)$ Phase	$-1.21 \pm 0.35$	$-1.87 \pm 0.44$	$-1.19 \pm 0.36$	$-1.64 \pm 0.36$	$-1.25 \pm 0.36$
$\chi_{c0}$ Fraction (%)	$0.94 \pm 0.37$	$0.95 \pm 0.37$	$0.94 \pm 0.37$	$0.92 \pm 0.37$	$0.94 \pm 0.37$
$\chi_{c0}$ Phase	$-0.79 \pm 0.38$	$-0.81 \pm 0.38$	$-0.77 \pm 0.38$	$-0.80 \pm 0.39$	$-0.81 \pm 0.38$
Non-resonant Fraction (%)	$3.2 \pm 1.1$	$3.7 \pm 1.2$	$3.2 \pm 1.1$	$3.6 \pm 1.2$	$3.2 \pm 1.1$
Non-resonant Phase	$0.79 \pm 0.39$	$0.68 \pm 0.41$	$0.82 \pm 0.37$	$0.92 \pm 0.38$	$0.78 \pm 0.40$
$f_2(1270)$ Fraction(%)	$8.3 \pm 2.3$	$1.40 \pm 0.82$	$8.5 \pm 2.4$	$3.6 \pm 2.1$	$9.3 \pm 2.6$
$f_2(1270)$ Phase	$-0.68 \pm 0.28$	$-0.60 \pm 0.53$	$-0.67 \pm 0.29$	$-1.13 \pm 0.34$	$-0.69 \pm 0.31$
$f_0(1370)$ Fraction(%)	—	$3.6 \pm 1.6$	—	—	—
$f_0(1370)$ Phase	—	$0.25 \pm 0.35$	—	—	—
$\rho^0(1450)$ Fraction(%)	—	—	$0.34 \pm 0.52$	—	—
$\rho^0(1450)$ Phase	—	—	$0.13 \pm 0.95$	—	—
$f_0(1500)$ Fraction(%)	—	—	—	$3.7 \pm 1.6$	—
$f_0(1500)$ Phase	—	—	—	$1.73 \pm 0.42$	—
$f_2(1525)$ Fraction(%)	—	—	—	—	$0.57 \pm 0.71$
$f_2(1525)$ Phase	—	—	—	—	$-2.69 \pm 0.70$

Table 6.7: Results of fit to  $B^+$  data with a different resonance added in turn to the nominal +  $f_2(1270)$  fit

	Nominal + $f_2(1270)$	With $f_0(1370)$	With $\rho^0(1450)$	With $f_0(1500)$	With $f_2(1525)$
(NLL) – (NLL(nominal + $f_2(1270)$ ))	—	–5.241	–9.859	–6.241	–0.349
Dalitz-plot $\chi^2/ndof$	168/115	164/113	168/113	163/113	169/113
$m_{K^+\pi^-}$ projection $\chi^2/ndof$	49/28	50/26	51/26	50/26	50/26
$m_{\pi^+\pi^-}$ projection $\chi^2/ndof$	67/25	60/23	59/23	57/23	65/23
$K^{*0}(892)$ Fraction (%)	$11.5 \pm 2.1$	$11.3 \pm 2.4$	$11.4 \pm 2.0$	$11.4 \pm 2.2$	$11.6 \pm 2.1$
$K_0^{*0}(1430)$ Fraction (%)	$55.4 \pm 4.5$	$54.6 \pm 4.9$	$55.8 \pm 4.6$	$54.6 \pm 4.6$	$55.5 \pm 4.5$
$K_0^{*0}(1430)$ Phase	$3.11 \pm 0.12$	$3.11 \pm 0.13$	$3.09 \pm 0.13$	$3.13 \pm 0.13$	$3.11 \pm 0.13$
$\rho^0(770)$ Fraction (%)	$4.3 \pm 1.4$	$3.6 \pm 1.3$	$4.2 \pm 1.7$	$4.0 \pm 1.4$	$4.4 \pm 1.4$
$\rho^0(770)$ Phase	$1.17 \pm 0.41$	$1.28 \pm 0.38$	$1.58 \pm 0.41$	$1.30 \pm 0.39$	$1.16 \pm 0.44$
$f_0(980)$ Fraction (%)	$13.4 \pm 2.4$	$10.6 \pm 2.2$	$12.5 \pm 2.2$	$11.6 \pm 2.2$	$13.3 \pm 2.4$
$f_0(980)$ Phase	$-0.77 \pm 0.37$	$-0.40 \pm 0.37$	$0.16 \pm 0.41$	$-0.54 \pm 0.38$	$-0.77 \pm 0.40$
$\chi_{c0}$ Fraction (%)	$1.27 \pm 0.44$	$1.32 \pm 0.45$	$1.31 \pm 0.45$	$1.29 \pm 0.45$	$1.29 \pm 0.44$
$\chi_{c0}$ Phase	$0.41 \pm 0.37$	$0.39 \pm 0.36$	$0.40 \pm 0.38$	$0.42 \pm 0.36$	$0.41 \pm 0.37$
Non-resonant Fraction (%)	$3.7 \pm 1.2$	$3.5 \pm 1.3$	$4.2 \pm 1.4$	$4.2 \pm 1.4$	$3.6 \pm 1.3$
Non-resonant Phase	$1.25 \pm 0.32$	$1.10 \pm 0.32$	$1.28 \pm 0.32$	$1.16 \pm 0.31$	$1.23 \pm 0.32$
$f_2(1270)$ Fraction(%)	$4.8 \pm 1.7$	$3.8 \pm 1.5$	$2.9 \pm 1.6$	$4.1 \pm 1.6$	$5.0 \pm 1.8$
$f_2(1270)$ Phase	$-0.11 \pm 0.26$	$-0.20 \pm 0.28$	$0.55 \pm 0.37$	$-0.15 \pm 0.27$	$-0.19 \pm 0.28$
$f_0(1370)$ Fraction(%)	—	$2.0 \pm 1.1$	—	—	—
$f_0(1370)$ Phase	—	$-0.23 \pm 0.41$	—	—	—
$\rho^0(1450)$ Fraction(%)	—	—	$6.9 \pm 2.6$	—	—
$\rho^0(1450)$ Phase	—	—	$-0.81 \pm 0.38$	—	—
$f_0(1500)$ Fraction(%)	—	—	—	$1.38 \pm 0.74$	—
$f_0(1500)$ Phase	—	—	—	$0.73 \pm 0.44$	—
$f_2(1525)$ Fraction(%)	—	—	—	—	$0.16 \pm 0.41$
$f_2(1525)$ Phase	—	—	—	—	$2.9 \pm 2.1$

## 6.8 Systematic Errors on Fit Fractions and Phases

The systematic errors that affect the measurement of the fit fractions and phases are evaluated separately for  $B^-$  and  $B^+$ . There are six contributions that are added to give the final systematic error. Three of these contributions arise from uncertainties of the histogram shapes used to model  $q\bar{q}$  background,  $B\bar{B}$  background and efficiency in this analysis. Two of the contributions arise from the uncertainty in the  $q\bar{q}$  and  $B\bar{B}$  background fractions. The final contribution to the systematic error accounts for any possible fit bias.

### 6.8.1 Histogram Fluctuations

Each bin of the efficiency histogram has an associated error. To estimate the overall systematic error, the contents of the bins are fluctuated independently in accordance with their errors, so that 300 new histograms are made that differ slightly in shape from the original histogram. The nominal fit is then repeated, the fit fraction and phase results for the 300 different histograms are plotted and the root-mean-square (RMS) of the distribution is taken as the absolute systematic error. This procedure is then repeated for the  $q\bar{q}$  and  $B\bar{B}$  background histograms. The resultant RMS values can be seen in Table 6.8 for the efficiency histogram, Table 6.9 for the  $q\bar{q}$  background histogram and Table 6.10 for the  $B\bar{B}$  background histogram.

### 6.8.2 Background Fraction Fluctuations

The background fractions have associated uncertainties arising from the  $m_{\text{ES}}$  fit in the case of  $q\bar{q}$  background and the MC study in the case of the  $B\bar{B}$  background. To estimate the uncertainty, the  $q\bar{q}$  background fraction is fluctuated according to its error so that 300 experiments are produced with different values for this background fraction. The nominal fit is then repeated, the fit fraction and phase results for the

Table 6.8: Absolute systematic errors on the fit fractions and phases of the  $B^- \rightarrow K^- \pi^- \pi^+$  and  $B^+ \rightarrow K^+ \pi^+ \pi^-$  nominal six component models, due to the efficiency histogram fluctuation.

Component	$B^- \rightarrow K^- \pi^- \pi^+$	$B^+ \rightarrow K^+ \pi^+ \pi^-$
$K^{*0}(892)$ Fraction (%) RMS	0.305	0.357
$K^{*0}(892)$ Phase RMS	0.0 = FIXED	0.0 = FIXED
$K_0^{*0}(1430)$ Fraction (%) RMS	0.276	0.333
$K_0^{*0}(1430)$ Phase RMS	0.017	0.018
$\rho^0(770)$ Fraction (%) RMS	0.180	0.117
$\rho^0(770)$ Phase RMS	0.028	0.040
$f_0(980)$ Fraction (%) RMS	0.165	0.157
$f_0(980)$ Phase RMS	0.027	0.035
$\chi_{c0}$ Fraction (%) RMS	0.017	0.020
$\chi_{c0}$ Phase RMS	0.027	0.026
NR Fraction (%) RMS	0.054	0.080
NR Phase RMS	0.030	0.024

300 different histograms are plotted and the RMS of the distribution is taken as the absolute systematic error. This procedure is repeated for the  $B\bar{B}$  background. The resultant RMS values can be seen in Table 6.11 for the  $q\bar{q}$  background fraction and Table 6.12 for the  $B\bar{B}$  background fraction.

Table 6.9: Absolute systematic errors on the fit fractions and phases of the  $B^- \rightarrow K^- \pi^- \pi^+$  and  $B^+ \rightarrow K^+ \pi^+ \pi^-$  nominal six component models, due to the  $q\bar{q}$  background histogram fluctuation.

Component	$B^- \rightarrow K^- \pi^- \pi^+$	$B^+ \rightarrow K^+ \pi^+ \pi^-$
$K^{*0}(892)$ Fraction (%) RMS	0.122	0.116
$K^{*0}(892)$ Phase RMS	0.0 = FIXED	0.0 = FIXED
$K_0^{*0}(1430)$ Fraction (%) RMS	0.370	0.348
$K_0^{*0}(1430)$ Phase RMS	0.021	0.016
$\rho^0(770)$ Fraction (%) RMS	0.258	0.227
$\rho^0(770)$ Phase RMS	0.055	0.065
$f_0(980)$ Fraction (%) RMS	0.244	0.259
$f_0(980)$ Phase RMS	0.049	0.065
$\chi_{c0}$ Fraction (%) RMS	0.029	0.051
$\chi_{c0}$ Phase RMS	0.062	0.050
NR Fraction (%) RMS	0.210	0.286
NR Phase RMS	0.058	0.041

Table 6.10: Absolute systematic errors on the fit fractions and phases of the  $B^- \rightarrow K^- \pi^- \pi^+$  and  $B^+ \rightarrow K^+ \pi^+ \pi^-$  nominal six component models, due to the  $B\bar{B}$  background histogram fluctuation.

Component	$B^- \rightarrow K^- \pi^- \pi^+$	$B^+ \rightarrow K^+ \pi^+ \pi^-$
$K^{*0}(892)$ Fraction (%) RMS	0.143	0.068
$K^{*0}(892)$ Phase RMS	0.0 = FIXED	0.0 = FIXED
$K_0^{*0}(1430)$ Fraction (%) RMS	0.280	0.328
$K_0^{*0}(1430)$ Phase RMS	0.020	0.011
$\rho^0(770)$ Fraction (%) RMS	0.168	0.320
$\rho^0(770)$ Phase RMS	0.035	0.089
$f_0(980)$ Fraction (%) RMS	0.175	0.212
$f_0(980)$ Phase RMS	0.035	0.061
$\chi_{c0}$ Fraction (%) RMS	0.013	0.021
$\chi_{c0}$ Phase RMS	0.032	0.028
NR Fraction (%) RMS	0.140	0.186
NR Phase RMS	0.050	0.039

Table 6.11: Absolute systematic errors on the fit fractions and phases of the  $B^- \rightarrow K^- \pi^- \pi^+$  and  $B^+ \rightarrow K^+ \pi^+ \pi^-$  nominal six component models, due to the  $q\bar{q}$  background fraction fluctuation.

Component	$B^- \rightarrow K^- \pi^- \pi^+$	$B^+ \rightarrow K^+ \pi^+ \pi^-$
$K^{*0}(892)$ Fraction RMS (%)	0.361	0.295
$K^{*0}(892)$ Phase RMS	0.0 = FIXED	0.0 = FIXED
$K_0^{*0}(1430)$ Fraction RMS (%)	0.022	0.197
$K_0^{*0}(1430)$ Phase RMS	0.000	0.001
$\rho^0(770)$ Fraction RMS (%)	0.184	0.234
$\rho^0(770)$ Phase RMS	0.030	0.045
$f_0(980)$ Fraction RMS (%)	0.118	0.120
$f_0(980)$ Phase RMS	0.014	0.027
$\chi_{c0}$ Fraction RMS (%)	0.041	0.045
$\chi_{c0}$ Phase RMS	0.016	0.015
NR Fraction RMS (%)	0.235	0.303
NR Phase RMS	0.017	0.012

Table 6.12: Absolute systematic errors on the fit fractions and phases of the  $B^- \rightarrow K^- \pi^- \pi^+$  and  $B^+ \rightarrow K^+ \pi^+ \pi^-$  nominal six component models, due to the  $B\bar{B}$  background fraction fluctuation.

Component	$B^- \rightarrow K^- \pi^- \pi^+$	$B^+ \rightarrow K^+ \pi^+ \pi^-$
$K^{*0}(892)$ Fraction RMS (%)	0.188	0.168
$K^{*0}(892)$ Phase RMS	0.0 = FIXED	0.0 = FIXED
$K_0^{*0}(1430)$ Fraction RMS (%)	0.032	0.101
$K_0^{*0}(1430)$ Phase RMS	0.000	0.001
$\rho^0(770)$ Fraction RMS (%)	0.069	0.096
$\rho^0(770)$ Phase RMS	0.001	0.012
$f_0(980)$ Fraction RMS (%)	0.047	0.046
$f_0(980)$ Phase RMS	0.003	0.007
$\chi_{c0}$ Fraction RMS (%)	0.025	0.029
$\chi_{c0}$ Phase RMS	0.010	0.005
NR Fraction RMS (%)	0.159	0.175
NR Phase RMS	0.020	0.007

### 6.8.3 Fit Bias Tests

To search for possible biases in the fitting procedure, toy MC tests as described in Section 5.4 are run. 500 toy MC samples are generated for  $B^-$  and  $B^+$  using the nominal magnitudes and phases shown in Table 6.1. Each of these toy MC samples is then fitted 200 times using randomised initial starting points. The fit with the lowest NLL solution is extracted and used to make pull plots. The magnitude, fit fraction and phase pull plots can be seen in Appendix B in Figure B.1, Figure B.2 and Figure B.3 respectively, for  $B^-$ , and in Figure B.4, Figure B.5 and Figure B.6 respectively, for  $B^+$ . The means and widths for each of these plots are tabulated in Table 6.13. The pull means are used to give an indication of possible fit biases but are not subsequently used to evaluate the associated systematic error.

Table 6.13 shows that the widths of the fit fraction pull plots have significant deviations from a value of one, for all components excluding the  $\chi_{c0}$ . This indicates that there is a problem with the calculation of the fit fraction statistical error using Equation 4.5 in Section 4.2.3. A pull plot with a width less than one implies that the statistical error on this fit fraction is being over-estimated. The problem with the statistical error is probably due to the fact that possible correlations between the fitted parameters are neglected. The calculation of the true statistical error would involve utilising the full error matrix reported by `Minuit`. For this analysis the statistical error can be found by looking at the widths of the fit fraction distributions in the toy experiments (this is also the procedure used by the Belle collaboration in [35]). These distributions can be seen in Figure 6.20 for  $B^-$  events and Figure 6.21 for  $B^+$  events. The means and widths for these distributions are shown in Table 6.14. The new statistical errors on the fit fractions are the widths shown in Table 6.14 and they can be compared to the old statistical errors shown in Table 6.1. The greatest change occurs for the  $K_0^{*0}(1430)$  component.

The systematic error on the components that show a possible bias are calculated as the difference between the mean fit fraction shown in Table 6.14 and the nominal

Table 6.13: Magnitude, fit fraction and phase pulls in toy MC tests using the nominal fit results.

	$B^-$		$B^+$	
	Pull Mean	Pull Width	Pull Mean	Pull Width
$K_0^{*0}(1430)$ Magnitude	$-0.015 \pm 0.044$	$0.985 \pm 0.032$	$0.051 \pm 0.045$	$0.985 \pm 0.034$
$K_0^{*0}(1430)$ Fit Fraction	$-0.139 \pm 0.026$	$0.579 \pm 0.018$	$-0.125 \pm 0.025$	$0.551 \pm 0.018$
$K_0^{*0}(1430)$ Phase	$-0.054 \pm 0.047$	$1.052 \pm 0.034$	$0.021 \pm 0.048$	$1.076 \pm 0.034$
$\rho^0(770)$ Fit Magnitude	$0.091 \pm 0.043$	$0.963 \pm 0.031$	$0.215 \pm 0.041$	$0.921 \pm 0.030$
$\rho^0(770)$ Fit Fraction	$-0.007 \pm 0.036$	$0.810 \pm 0.026$	$0.081 \pm 0.039$	$0.854 \pm 0.028$
$\rho^0(770)$ Phase	$0.012 \pm 0.049$	$1.104 \pm 0.035$	$-0.070 \pm 0.053$	$1.189 \pm 0.037$
$f_0(980)$ Magnitude	$0.069 \pm 0.046$	$1.035 \pm 0.033$	$0.183 \pm 0.043$	$0.956 \pm 0.032$
$f_0(980)$ Fit Fraction	$-0.025 \pm 0.038$	$0.838 \pm 0.027$	$0.044 \pm 0.031$	$0.739 \pm 0.024$
$f_0(980)$ Phase	$0.042 \pm 0.053$	$1.177 \pm 0.039$	$0.001 \pm 0.0057$	$1.281 \pm 0.041$
$\chi_{c0}$ Magnitude	$0.148 \pm 0.048$	$1.069 \pm 0.034$	$0.183 \pm 0.049$	$1.096 \pm 0.035$
$\chi_{c0}$ Fit Fraction	$-0.021 \pm 0.049$	$1.098 \pm 0.035$	$0.016 \pm 0.049$	$1.077 \pm 0.036$
$\chi_{c0}$ Phase	$0.224 \pm 0.072$	$1.607 \pm 0.052$	$0.219 \pm 0.052$	$1.160 \pm 0.038$
NR Magnitude	$0.524 \pm 0.042$	$0.930 \pm 0.031$	$0.407 \pm 0.042$	$0.931 \pm 0.030$
NR Fit Fraction	$0.432 \pm 0.038$	$0.837 \pm 0.029$	$0.292 \pm 0.039$	$0.868 \pm 0.028$
NR Phase	$0.131 \pm 0.052$	$1.154 \pm 0.037$	$0.153 \pm 0.055$	$1.221 \pm 0.039$

measured fit fraction in Table 6.1. The means of the phase distributions are tabulated in Table 6.15. The systematic error is again taken as the difference between the mean in toy MC samples and the value measured in the nominal fit.

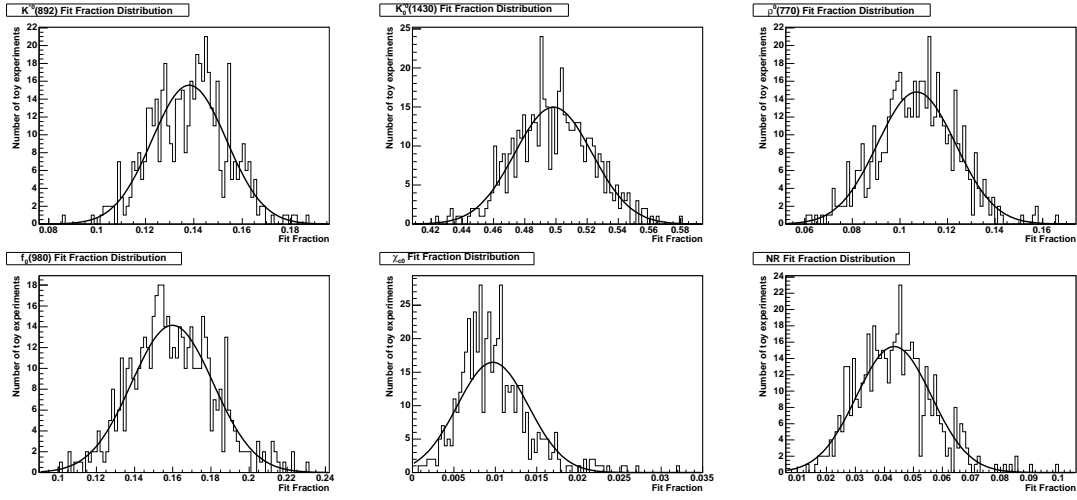


Figure 6.20: Fit fraction distributions for the 500  $B^-$  toy MC samples. Top left shows the  $K^{*0}(892)$ , top middle the  $K_0^{*0}(1430)$ , top right the  $\rho^0(770)$ , bottom left the  $f_0(980)$ , bottom middle the  $\chi_{c0}$  and bottom right the non-resonant.

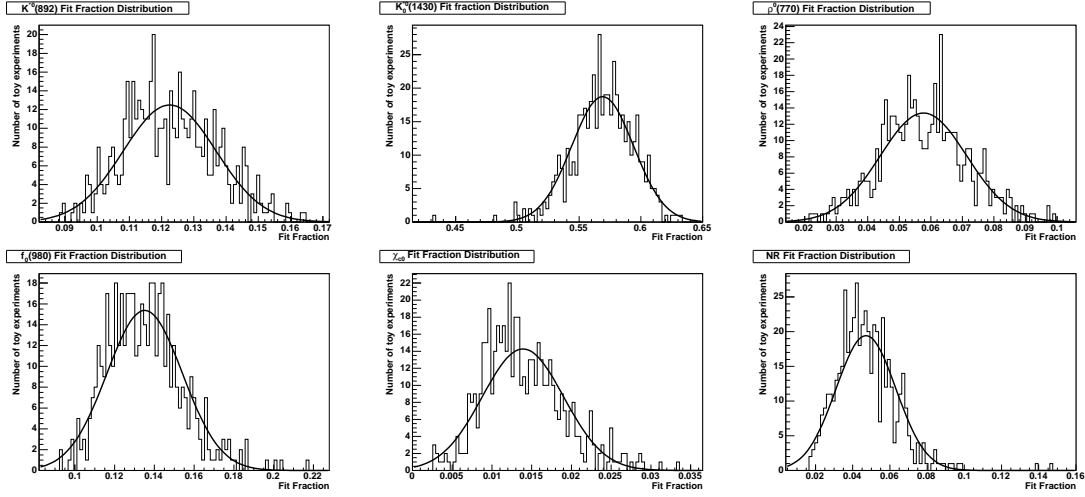


Figure 6.21: Fit fraction distributions for the 500  $B^+$  toy MC samples. Top left shows the  $K^{*0}(892)$ , top middle the  $K_0^{*0}(1430)$ , top right the  $\rho^0(770)$ , bottom left the  $f_0(980)$ , bottom middle the  $\chi_{c0}$  and bottom right the non-resonant.

Table 6.14: Fit fraction distribution means and widths from toy MC samples using the nominal fit results.

	$B^-$		$B^+$	
	Mean	Width	Mean	Width
$K^{*0}(892)$ Fit Fraction (%)	$13.810 \pm 0.069$	$1.538 \pm 0.049$	$12.250 \pm 0.065$	$1.441 \pm 0.049$
$K_0^{*0}(1430)$ Fit Fraction (%)	$49.84 \pm 0.11$	$2.480 \pm 0.079$	$56.90 \pm 0.11$	$2.504 \pm 0.081$
$\rho^0(770)$ Fit Fraction (%)	$10.699 \pm 0.074$	$1.644 \pm 0.053$	$5.767 \pm 0.062$	$1.373 \pm 0.045$
$f_0(980)$ Fit Fraction (%)	$15.982 \pm 0.096$	$2.145 \pm 0.069$	$13.513 \pm 0.086$	$1.899 \pm 0.063$
$\chi_{c0}$ Fit Fraction (%)	$0.970 \pm 0.020$	$0.429 \pm 0.016$	$1.390 \pm 0.023$	$0.512 \pm 0.017$
NR Fit Fraction (%)	$4.332 \pm 0.058$	$1.292 \pm 0.043$	$4.713 \pm 0.073$	$1.607 \pm 0.054$

Table 6.15: Phase distribution means from toy MC samples using the nominal fit results.

	$B^-$ Mean	$B^+$ Mean
$K_0^{*0}(1430)$ Phase	$2.732 \pm 0.006$	$3.081 \pm 0.006$
$\rho^0(770)$ Phase	$-0.475 \pm 0.021$	$1.070 \pm 0.026$
$f_0(980)$ Phase	$-1.876 \pm 0.020$	$-0.871 \pm 0.025$
$\chi_{c0}$ Phase	$-0.732 \pm 0.028$	$0.534 \pm 0.020$
NR Phase	$0.879 \pm 0.021$	$1.340 \pm 0.022$

#### 6.8.4 Conclusions

A summary of all the systematic errors affecting the fit fractions and phases is shown in Table 6.16 for the fit fractions and Table 6.17 for the phases. Table 6.16 shows that one of the largest systematic errors for the  $K^{*0}(892)$  fit fraction arises from the efficiency histogram fluctuation tests, which is to be expected as the greatest variations in this histogram occur in the far corners of the Dalitz-plot. The  $K_0^{*0}(1430)$  and  $f_0(980)$  fit fraction and phase total systematic errors have large contributions from the background histogram fluctuations. The  $\rho^0(770)$  fit fraction and phase total systematic errors have significant contributions from all of the possible sources. For the  $\chi_{c0}$  and non-resonant fit fractions, the fit bias provides the dominant contribution to the total systematic error. The  $\chi_{c0}$  phase also has the fit bias as the greatest contribution to the systematic error whilst the non-resonant phase is most affected by the background histogram variation.

Table 6.16: Percentage systematic errors on the fit fractions of the nominal six component model

Component	$B\bar{B}$ Fraction	$B\bar{B}$ Hist	$q\bar{q}$ Fraction	$q\bar{q}$ Hist	Efficiency Hist	Fit Bias	Total Error
$B^-$							
$K^{*0}(892)$ Fraction	1.34	1.02	2.58	0.87	2.18	1.43	4.13
$K_0^{*0}(1430)$ Fraction	0.06	0.56	0.04	0.73	0.55	1.19	1.60
$\rho^0(770)$ Fraction	0.65	1.57	1.74	2.43	1.70	0.94	3.95
$f_0(980)$ Fraction	0.30	1.10	0.74	1.54	1.04	0.63	2.39
$\chi_{c0}$ Fraction	2.78	1.44	4.56	3.22	1.89	7.78	10.25
Non-resonant Fraction	4.52	3.98	6.68	5.97	1.53	22.86	22.33
$B^+$							
$K^{*0}(892)$ Fraction	1.34	0.54	2.35	0.93	2.85	1.60	4.38
$K_0^{*0}(1430)$ Fraction	0.18	0.57	0.34	0.61	0.58	0.87	1.39
$\rho^0(770)$ Fraction	1.74	5.81	4.25	4.12	2.12	5.45	10.30
$f_0(980)$ Fraction	0.35	1.60	0.91	1.96	1.19	2.27	3.73
$\chi_{c0}$ Fraction	2.25	1.63	3.49	3.95	1.55	7.75	9.90
Non-resonant Fraction	4.41	4.69	7.63	7.20	2.02	17.50	21.49

Table 6.17: Absolute systematic errors on the phases of the nominal six component model

Component	$B\bar{B}$ Fraction	$B\bar{B}$ Hist	$q\bar{q}$ Fraction	$q\bar{q}$ Hist	Efficiency Hist	Fit Bias	Total Error
$B^-$							
$K_0^{*0}(1430)$ Phase	0.000	0.020	0.000	0.021	0.017	0.005	0.034
$\rho^0(770)$ Phase	0.001	0.035	0.030	0.055	0.028	0.011	0.079
$f_0(980)$ Phase	0.003	0.035	0.014	0.049	0.027	0.022	0.072
$\chi_{c0}$ Phase	0.010	0.032	0.016	0.062	0.027	0.075	0.110
Non-resonant Phase	0.020	0.050	0.017	0.058	0.030	0.012	0.087
$B^+$							
$K_0^{*0}(1430)$ Phase	0.001	0.011	0.001	0.016	0.018	0.001	0.027
$\rho^0(770)$ Phase	0.012	0.089	0.045	0.065	0.040	0.047	0.136
$f_0(980)$ Phase	0.007	0.061	0.027	0.065	0.035	0.005	0.100
$\chi_{c0}$ Phase	0.005	0.028	0.015	0.050	0.026	0.086	0.106
Non-resonant Phase	0.007	0.039	0.012	0.041	0.024	0.011	0.064

## 6.9 Model Dependence

The systematic errors described in the previous section all relate to the specific model chosen in terms of the components included in the fits and the lineshapes used. Variation of this model could lead to different results being obtained for the nominal fit fractions and phases. To account for this a third “model-dependent” error is calculated. There are three contributions to this error:

- There is a possibility of additional resonances being present in the Dalitz plot. This error is calculated using Table 6.4 and Table 6.5 in Section 6.6. The change that occurs in the value for a measured nominal fit fraction and phase in the presence of each additional resonance is examined and the maximum deviation in each direction is taken as the error.
- The modelling of the  $f_0(980)$  component has an associated error due to the uncertainty in its lineshape parameters. This error is quantified as the difference between the nominal fit fractions and phases shown in Table 6.1 in Section 6.4 and those obtained in a fit using the BES parameters for the Flatté lineshape as given in Section 4.3.1. The results for the fit using the BES parameters are shown in Table 6.18.
- The modelling of the  $K_0^{*0}(1430)$  component also has an associated error with its lineshape parameters. This error is taken as the difference between the nominal fit fractions and phases shown in Table 6.1 in Section 6.4 and those obtained using the parameters obtained from LASS data as given in Section 6.3.2. The results for the fit using the LASS parameters are shown in Table 6.18.

These three sources of error are then added in quadrature.

Table 6.18: Results of fits to  $B^-$  and  $B^+$  data with different lineshape models

Component	$B^-$ Fit			$B^+$ Fit		
	Nominal	BES $f_0(980)$	LASS $K_0^{*0}(1430)$	Nominal	BES $f_0(980)$	LASS $K_0^{*0}(1430)$
$K^{*0}(892)$ Fraction(%)	14.003	14.039	14.424	12.537	12.490	12.902
$K_0^{*0}(1430)$ Fraction(%)	50.411	49.904	50.011	57.449	56.996	56.854
$K_0^{*0}(1430)$ Phase	2.727	2.705	2.738	3.080	3.072	3.096
$\rho^0(770)$ Fraction (%)	10.596	10.011	10.936	5.509	4.867	5.403
$\rho^0(770)$ Phase	-0.486	-0.426	-0.616	1.117	1.317	1.095
$f_0(980)$ Fraction (%)	15.861	16.982	15.933	13.226	13.744	13.218
$f_0(980)$ Phase	-1.898	-1.618	-1.953	-0.866	-0.410	-0.886
$\chi_{c0}$ Fraction (%)	0.904	0.968	0.905	1.289	1.320	1.273
$\chi_{c0}$ Phase	-0.807	-0.872	-0.817	0.448	0.411	0.447
NR Fraction (%)	3.521	2.395	4.064	3.970	3.862	4.410
NR Phase	0.867	0.717	0.749	1.329	1.156	1.206

## 6.10 Final Results for the Six Component Nominal Model

The final results for the fit fractions and phases of the six components that are included in the nominal model with full statistical, systematic and model dependent errors, can be seen in Table 6.19. Since the LASS amplitude contains both a resonant and non-resonant part, the results for the  $K_0^{*0}(1430)$  are not purely due to this resonance but to the  $K\pi$  S-wave as a whole. The results for the non-resonant component refer to the uniform part of this amplitude.

Table 6.19: Final results of fits with statistical, systematic and model dependent errors, to  $B^-$  and  $B^+$  data with 6 component model.

Component	$B^-$ Fit	$B^+$ Fit
$K^{*0}(892)$ Fraction (%)	$14.0 \pm 1.5 \pm 0.6 \begin{smallmatrix} +0.5 \\ -1.4 \end{smallmatrix}$	$12.5 \pm 1.4 \pm 0.6 \begin{smallmatrix} +0.6 \\ -1.2 \end{smallmatrix}$
$K_0^{*0}(1430)$ Fraction (%)	$50.4 \pm 2.5 \pm 0.8 \begin{smallmatrix} +0.7 \\ -3.2 \end{smallmatrix}$	$57.5 \pm 2.5 \pm 0.8 \begin{smallmatrix} +0.8 \\ -2.8 \end{smallmatrix}$
$K_0^{*0}(1430)$ Phase	$2.73 \pm 0.13 \pm 0.03 \begin{smallmatrix} +0.11 \\ -0.02 \end{smallmatrix}$	$3.08 \pm 0.12 \pm 0.03 \begin{smallmatrix} +0.04 \\ -0.02 \end{smallmatrix}$
$\rho^0(770)$ Fraction (%)	$10.6 \pm 1.6 \pm 0.4 \begin{smallmatrix} +0.7 \\ -2.7 \end{smallmatrix}$	$5.5 \pm 1.4 \pm 0.6 \begin{smallmatrix} +0.7 \\ -1.4 \end{smallmatrix}$
$\rho^0(770)$ Phase	$-0.49 \pm 0.36 \pm 0.08 \begin{smallmatrix} +1.13 \\ -0.14 \end{smallmatrix}$	$1.12 \pm 0.49 \pm 0.14 \begin{smallmatrix} +0.85 \\ -0.20 \end{smallmatrix}$
$f_0(980)$ Fraction (%)	$15.9 \pm 2.1 \pm 0.4 \begin{smallmatrix} +1.1 \\ -2.3 \end{smallmatrix}$	$13.2 \pm 1.9 \pm 0.5 \begin{smallmatrix} +0.6 \\ -2.6 \end{smallmatrix}$
$f_0(980)$ Phase	$-1.90 \pm 0.35 \pm 0.07 \begin{smallmatrix} +0.74 \\ -0.38 \end{smallmatrix}$	$-0.87 \pm 0.45 \pm 0.10 \begin{smallmatrix} +1.41 \\ -0.46 \end{smallmatrix}$
$\chi_{c0}$ Fraction (%)	$0.90 \pm 0.43 \pm 0.09 \begin{smallmatrix} +0.09 \\ -0.07 \end{smallmatrix}$	$1.29 \pm 0.51 \pm 0.13 \begin{smallmatrix} +0.07 \\ -0.05 \end{smallmatrix}$
$\chi_{c0}$ Phase	$-0.81 \pm 0.39 \pm 0.11 \begin{smallmatrix} +0.26 \\ -0.08 \end{smallmatrix}$	$0.45 \pm 0.37 \pm 0.11 \begin{smallmatrix} +0.09 \\ -0.06 \end{smallmatrix}$
Non-resonant Fraction (%)	$3.5 \pm 1.3 \pm 0.9 \begin{smallmatrix} +1.3 \\ -1.4 \end{smallmatrix}$	$4.0 \pm 1.6 \pm 0.9 \begin{smallmatrix} +1.5 \\ -0.6 \end{smallmatrix}$
Non-resonant Phase	$0.87 \pm 0.38 \pm 0.09 \begin{smallmatrix} +0.43 \\ -0.30 \end{smallmatrix}$	$1.33 \pm 0.32 \pm 0.06 \begin{smallmatrix} +0.32 \\ -0.28 \end{smallmatrix}$

## 6.11 Upper Limits

For those components that do not have a significant fit fraction a 90% confidence level upper limit (UL) is calculated using:

$$\frac{\int_0^{x_{max}} \mathcal{L} dx}{\int_0^{\infty} \mathcal{L} dx} = 0.90 \quad (6.2)$$

where  $\mathcal{L}$  is the likelihood and  $x_{max}$  is the maximum magnitude for the component, such that the integral of the total likelihood function  $\mathcal{L}$  is 90% of the total area. For this maximum magnitude  $x_{max}$ , Equation 4.5 in Section 4.2 is used to calculate the upper limit on the fit fraction (all other magnitudes and phases are fixed to the results from the nominal six component fit). The results for the statistical 90% confidence level upper limits can be seen in Table 6.20.

The calculated upper limits do not incorporate the uncertainties due to the background fractions and histogram shapes. To account for this systematic uncertainty, 150 fits are run where the  $q\bar{q}$  background fraction,  $B\bar{B}$  background fraction, efficiency histogram shape,  $q\bar{q}$  histogram shape and  $B\bar{B}$  histogram shape are fluctuated simultaneously. This will give a range of measured upper limits. Table 6.16 in Section 6.8 shows that the  $\chi_{c0}$  and non-resonant fit fractions have large fit bias systematic errors. The toy tests show that these components have a tendency to be over-fitted, hence no additional error is incorporated into the upper limit to account for fit bias.

Table 6.20: Upper limits for the  $\chi_{c0}$  and non-resonant components.

Upper Limit (%)	$B^-$			$B^+$		
	90% CL UL	Systematic Mean	Systematic RMS	90% CL UL	Systematic Mean	Systematic RMS
$\chi_{c0}$ Fit Fraction	2.8	2.8	0.1	3.2	3.1	0.1
NR Fit Fraction	8.5	10.6	1.0	7.9	9.9	0.9

The same procedure is then applied to the resonances that are used in the addition tests. Each upper limit is calculated in turn using the appropriate values from Table 6.4 and Table 6.5 for the other components. The results for the upper limits can be seen in Table 6.21.

Table 6.21: Upper limits for the components used in the addition tests.

Upper Limit (%)	$B^-$			$B^+$		
	90% CL UL	Systematic Mean	Systematic RMS	90% CL UL	Systematic Mean	Systematic RMS
$K_2^{*0}(1430)$ Fit Fraction	7.1	7.0	0.7	3.9	3.8	0.5
$K^{*0}(1680)$ Fit Fraction	1.6	1.4	0.5	1.3	1.1	0.4
$f_2(1270)$ Fit Fraction	10.4	10.0	0.7	6.7	6.7	0.5
$f_0(1370)$ Fit Fraction	8.5	7.0	2.4	2.0	3.0	0.4
$\rho^0(1450)$ Fit Fraction	3.1	2.9	0.5	10.8	10.6	0.3
$f_0(1500)$ Fit Fraction	6.3	6.5	0.5	6.0	5.9	0.8
$f_2(1525)$ Fit Fraction	0.9	0.9	0.2	4.0	4.0	0.4

The final statistical 90% confidence level upper limits is chosen conservatively to be the largest out of that found for  $B^-$  and  $B^+$ . A table of the final results for upper

limits can be found in the conclusion of this thesis.

## 6.12 Total Rate Measurement

In order to convert the fit fractions for the resonant and non-resonant components into branching fractions a measurement of the inclusive  $B^\pm \rightarrow K^\pm \pi^\pm \pi^\mp$  branching fraction is needed. The branching fraction can be calculated using:

$$\text{Branching Fraction} = \frac{N_{\text{Signal}}}{N_{B\bar{B}} \times \text{Efficiency}} \quad (6.3)$$

where  $N_{\text{Signal}}$  is the number of signal events observed and  $N_{B\bar{B}}$  is the number of  $B\bar{B}$  pairs<sup>1</sup>. The efficiency is the average reconstruction efficiency for the  $B^\pm \rightarrow K^\pm \pi^\pm \pi^\mp$  decay.

The efficiency in the Dalitz-plot is weighted by the  $|\text{signal amplitude}|^2$  at that point and the average efficiency is calculated from:

$$\frac{\int \int_{DP} |\text{Total Signal Amplitude}|^2 \times \text{Efficiency} \, dm_{13}^2 dm_{23}^2}{\int \int_{DP} |\text{Total Signal Amplitude}|^2 \, dm_{13}^2 dm_{23}^2}$$

The average efficiency is found to be 15.92% for  $B^-$  and 15.96% for  $B^+$ . This average efficiency needs to be corrected to account for differences between data and MC in the selection procedure. The  $|\cos \theta_T|$ , Fisher,  $m_{\text{ES}}$  and  $\Delta E$  cuts are studied using  $B^+ \rightarrow \bar{D}^0 \pi^+$  (+ C.C) data and MC. The efficiency of each cut can be determined for MC and for data can be calculated using repeated  $m_{\text{ES}}$  fits (as described in Section 4.6) to determine the number of signal events in data before and after each cut is applied. The correction factor applied is:

$$\text{Correction Factor} = \frac{\text{Efficiency for data}}{\text{Efficiency for MC}} \quad (6.4)$$

These correction factors for the  $|\cos \theta_T|$ , Fisher,  $m_{\text{ES}}$  and  $\Delta E$  cuts are shown in Table 6.22.

---

<sup>1</sup>The  $\Upsilon(4S) \rightarrow B\bar{B}$  decay produces two  $B$  mesons and it is assumed that 50% of these will be  $B^+B^-$ .

Table 6.22: Efficiency correction factors.

Cut	Correction Factor
$ \cos \theta_T $	0.979
Fisher	0.988
$m_{\text{ES}}$	0.996
$\Delta E$	0.916
Total	0.882

The inclusive branching fractions are measured to be  $(64.1 \pm 3.5) \times 10^{-6}$  for  $B^- \rightarrow K^- \pi^- \pi^+$  and  $(64.7 \pm 3.5) \times 10^{-6}$  for  $B^+ \rightarrow K^+ \pi^+ \pi^-$ , where the errors shown are statistical only.

### 6.12.1 Systematics on Total Rate Measurement

There are several contributions to the systematic uncertainty on the inclusive branching fraction measurement.

- There is an uncertainty on the number of  $B\bar{B}$  background events used in the  $m_{\text{ES}}$  fit described in Section 4.6. This number is varied by the value of its error to calculate the change in the number of signal events measured. This feeds through to be a systematic uncertainty of 0.4% for  $B^- \rightarrow K^- \pi^- \pi^+$  and  $B^+ \rightarrow K^+ \pi^+ \pi^-$ .
- The statistical errors on the average efficiencies are calculated by looking at the width of the efficiency distributions in the toy MC experiments described in Section 6.8.3. These distributions are shown in Figure 6.22, and the absolute statistical errors are calculated to be 0.06% for  $B^-$  and 0.05% for  $B^+$ . There is also a systematic uncertainty associated with this average efficiency which

is due to the uncertainty in the signal model. The histogram and fraction fluctuation tests described in Section 6.8 are used to evaluate this error, which is found to be 0.08% (absolute) for both  $B^-$  and  $B^+$ . The corresponding percentage statistical and systematic uncertainties are 0.38% and 0.50% respectively for  $B^- \rightarrow K^- \pi^- \pi^+$  and 0.31% and 0.50% respectively for  $B^+ \rightarrow K^+ \pi^+ \pi^-$ .

- There is an error associated with the measured number of  $B\bar{B}$  pairs that enter into the denominator of Equation 6.3. This uncertainty is measured from  $B$ -counting studies [70] and is found to be 1.1%.
- There is a systematic uncertainty associated with the tracking efficiency correction described in Section 3.4. This is evaluated to be 0.8% per track giving a total systematic error of 2.4%.
- There is also a systematic uncertainty associated with the PID corrections. This has been studied in the previous analysis of the  $B^\pm \rightarrow K^\pm \pi^\pm \pi^\mp$  inclusive branching fraction [33] and is found to be 1.0% per track per selector (kaon and electron). This gives a total per track error of 1.4% and a total systematic error of 4.2%.

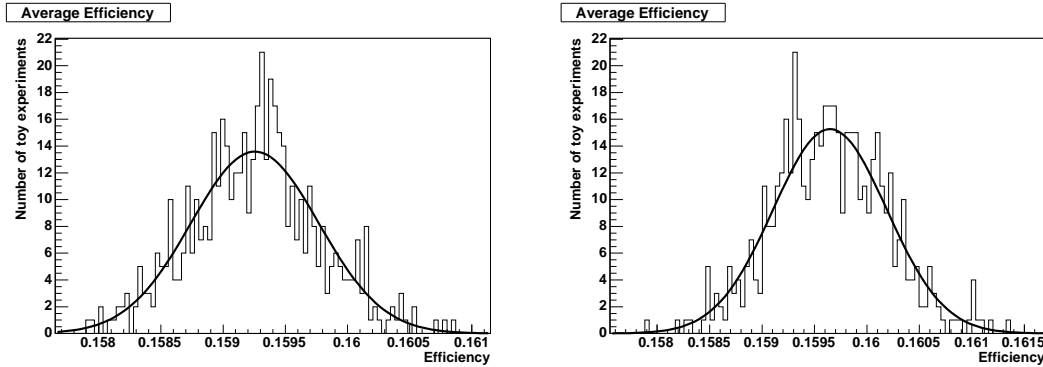


Figure 6.22: Average efficiency distributions for the 500 toy MC samples, with  $B^-$  on the left and  $B^+$  on the right.

There are also systematic errors arising from the efficiency corrections that need to be made to account for differences between data and MC. These uncertainties are

found to be:

- Systematic error due to  $|\cos\theta_T|$  cut efficiency correction is 2.7%
- Systematic error due to Fisher cut efficiency correction is 3.0%
- Systematic error due to  $m_{ES}$  cut efficiency correction is 1.6%
- Systematic error due to  $\Delta E$  cut efficiency correction is 2.5%

All of these sources of systematic error are added in quadrature to give the total systematic on the inclusive branching fraction measurement. The final measurement of the inclusive branching fraction for  $B^- \rightarrow K^- \pi^- \pi^+$  is  $(64.1 \pm 3.5 \pm 4.5) \times 10^{-6}$  and for  $B^+ \rightarrow K^+ \pi^+ \pi^-$  is  $(64.7 \pm 3.5 \pm 4.6) \times 10^{-6}$ .

# Chapter 7

## Conclusion and Discussion

The final measurements of the fit fractions and phases of the nominal components, with full statistical and systematic errors, are shown in Table 6.19 in Section 6.10. The fit fraction measurements can be converted into branching fractions by multiplying them by the appropriate inclusive branching fraction. These results can be seen in Table 7.1. These measurements all refer to the  $B^\pm \rightarrow K^\pm \pi^\pm \pi^\mp$  Dalitz-plot and so include the subsequent decay of the resonance to  $K^\pm \pi^\mp$  or  $\pi^\pm \pi^\mp$ . The measurement of the  $K^{*0}(892)$  branching fraction can be compared to previous experimental measurements and theoretical predictions from factorisation. The theoretical predictions are for the final state  $K^{*0}(892)\pi$  with no information on the  $K^{*0}(892)$  decay, and so the measured branching fraction is multiplied by the isospin factor  $\frac{3}{2}$  in order to make direct comparisons. This yields a measurement of  $B^- \rightarrow \bar{K}^{*0}(892)\pi^- = (13.5 \pm 1.7 \pm 1.1 \begin{smallmatrix} +0.5 \\ -1.4 \end{smallmatrix}) \times 10^{-6}$  and  $B^+ \rightarrow K^{*0}(892)\pi^+ = (12.2 \pm 1.5 \pm 1.1 \begin{smallmatrix} +0.6 \\ -1.2 \end{smallmatrix}) \times 10^{-6}$ . These measurements are higher than the majority of the theoretical predictions detailed in Section 1.6.4.

These measurements all correspond to a particular model of the components included, the lineshapes used to describe them and the resonance parameters (masses and widths). Changes to this model would lead to different results. An investigation

Table 7.1: Final branching fraction results with statistical and systematic errors.

Branching Fraction $\times 10^{-6}$	$B^-$	$B^+$
$B^\pm \rightarrow K^{*0}(892)\pi^\pm, K^{*0}(892) \rightarrow K^\pm\pi^\mp$	$9.0 \pm 1.1 \pm 0.7 \begin{smallmatrix} +0.3 \\ -0.9 \end{smallmatrix}$	$8.1 \pm 1.0 \pm 0.7 \begin{smallmatrix} +0.4 \\ -0.8 \end{smallmatrix}$
$B^\pm \rightarrow K_0^{*0}(1430)\pi^\pm, K_0^{*0}(1430) \rightarrow K^\pm\pi^\mp$	$32.3 \pm 2.4 \pm 2.3 \begin{smallmatrix} +0.4 \\ -2.1 \end{smallmatrix}$	$37.1 \pm 2.6 \pm 2.7 \begin{smallmatrix} +0.5 \\ -1.8 \end{smallmatrix}$
$B^\pm \rightarrow \rho^0(770)K^\pm, \rho^0(770) \rightarrow \pi^+\pi^-$	$6.8 \pm 1.1 \pm 0.5 \begin{smallmatrix} +0.4 \\ -1.7 \end{smallmatrix}$	$3.56 \pm 0.93 \pm 0.45 \begin{smallmatrix} +0.45 \\ -1.68 \end{smallmatrix}$
$B^\pm \rightarrow f_0(980)K^\pm, f_0(980) \rightarrow \pi^+\pi^-$	$10.2 \pm 1.5 \pm 0.8 \begin{smallmatrix} +0.7 \\ -1.5 \end{smallmatrix}$	$8.5 \pm 1.3 \pm 0.7 \begin{smallmatrix} +0.4 \\ -1.7 \end{smallmatrix}$

into the model composition is described in Sections 6.6 and 6.7. With the present statistics it is not possible to identify the precise resonance contributions in the 1.2 - 1.8 GeV/ $c^2$  region of the  $\pi\pi$  spectrum. The PDG values for the masses and widths of some of the possible resonances in this region have large uncertainties. In the future, with a greater number of events it may be possible to analyse helicity angle distributions in order to identify the spin of the resonant contributions to this region. A scan of possible masses and widths for the resonances could then be performed. A preliminary investigation of lineshapes is described in Section 6.3, with new lineshape parameters describing the  $f_0(980)$  and  $K_0^{*0}(1430)$  components being found. Higher statistics would allow further study of these lineshapes and also of the non-resonant component, which has attracted recent interest [35, 71]. Future versions of this analysis should be able to provide a quantitative measure of this model dependence, which could then be reported as a third error on the fit fractions and phases.

Upper limits are calculated for resonances that are not found to be statistically significant. The final upper limits can be seen in Table 7.2. These values can be compared to previous results which are summarised in [72]. The upper limits for the  $f_2(1270)$ ,  $f_2(1525)$  and  $K_2^{*0}(1430)$  components are all slightly larger than those presented by the BELLE collaboration. There are no previous upper limits for the  $f_0(1500)$ ,  $\rho^0(1450)$  and  $f_0(1370)$  components.

Table 7.2: Final upper limits.

	Branching Fraction 90% Statistical UL	Systematic RMS
$\chi_{c0}$	$2.1 \times 10^{-6}$	$0.1 \times 10^{-6}$
NR	$5.5 \times 10^{-6}$	$0.6 \times 10^{-6}$
$K_2^{*0}(1430)$	$4.6 \times 10^{-6}$	$0.5 \times 10^{-6}$
$K^{*0}(1680)$	$1.0 \times 10^{-6}$	$0.3 \times 10^{-6}$
$f_2(1270)$	$6.7 \times 10^{-6}$	$0.5 \times 10^{-6}$
$f_0(1370)$	$5.5 \times 10^{-6}$	$1.6 \times 10^{-6}$
$\rho^0(1450)$	$7.0 \times 10^{-6}$	$0.2 \times 10^{-6}$
$f_0(1500)$	$4.1 \times 10^{-6}$	$0.3 \times 10^{-6}$
$f_2(1525)$	$2.6 \times 10^{-6}$	$0.3 \times 10^{-6}$

The final measurement of the inclusive branching fraction for  $B^- \rightarrow K^- \pi^- \pi^+$  is  $(64.1 \pm 3.5 \pm 4.5) \times 10^{-6}$  and for  $B^+ \rightarrow K^+ \pi^+ \pi^-$  is found to be  $(64.7 \pm 3.5 \pm 4.6) \times 10^{-6}$ . These measurements are consistent with the previous experimental measurements discussed in Section 1.6.5.

A further iteration of this analysis would involve changes to the `Laura++` code so that the  $B^-$  and  $B^+$  data samples could be fitted simultaneously. This would allow the calculation of interesting  $CP$  quantities [73] and also the possible extraction of the strong and weak phases for the various amplitudes.

The Dalitz-plot analysis of  $B$ -meson decay is a relatively new area of study. As such there are many possible three-body decays for which the Dalitz plot has never been studied in great detail. Many of these modes will require more data than are currently available, particularly in the case of neutral  $B$  decays where the identity of the decaying meson has to be determined through flavour-tagging of the other  $B$  in the event. The *BABAR* experiment and the PEP-II  $B$  Factory have provided excellent conditions for the study of  $B$  physics, and are expected to continue to do

so for a number of years to come. With improvements to accelerator luminosity, this should provide a larger sample of  $B\bar{B}$  pairs which will greatly aid in the further study of charmless three-body  $B$ -meson decays.

# Appendix A

## GA Evolution Histograms

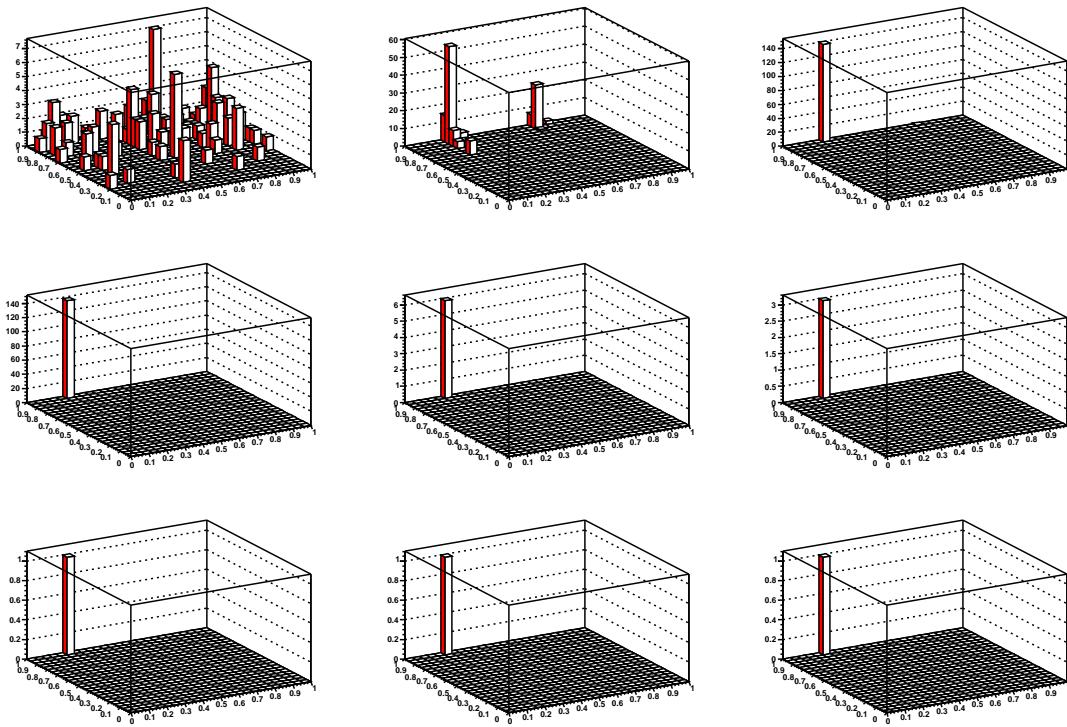


Figure A.1: Evolution of the GA. The histograms show the distribution of the  $K_0^{*0}(1430)$  magnitude against the  $K_0^{*0}(1430)$  phase for the individuals in the population every 10 generations.

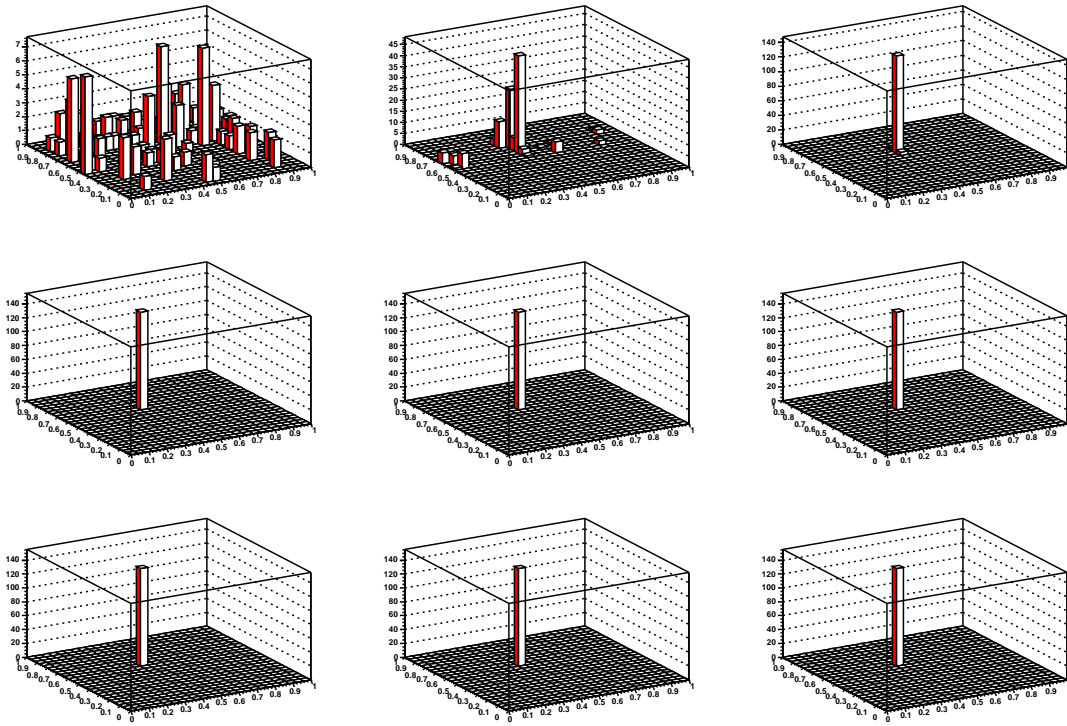


Figure A.2: Evolution of the GA. The histograms show the distribution of the  $f_0(980)$  magnitude against the  $f_0(980)$  phase for the individuals in the population every 10 generations.

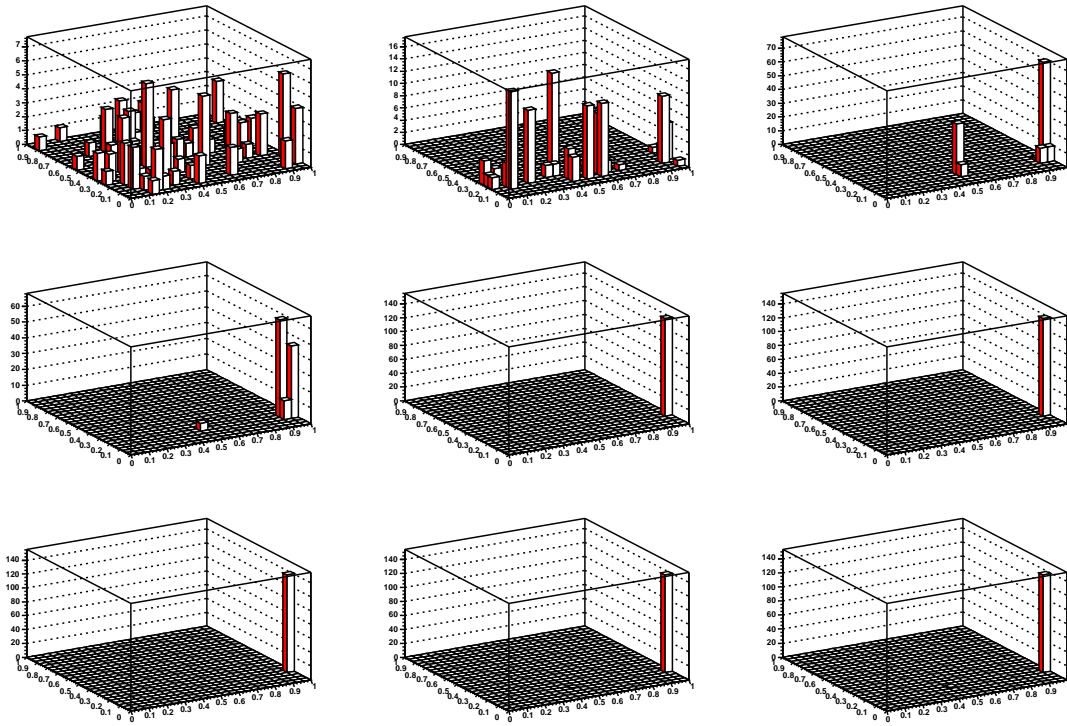


Figure A.3: Evolution of the GA. The histograms show the distribution of the  $\chi_{c0}$  magnitude against the  $\chi_{c0}$  phase for the individuals in the population every 10 generations.

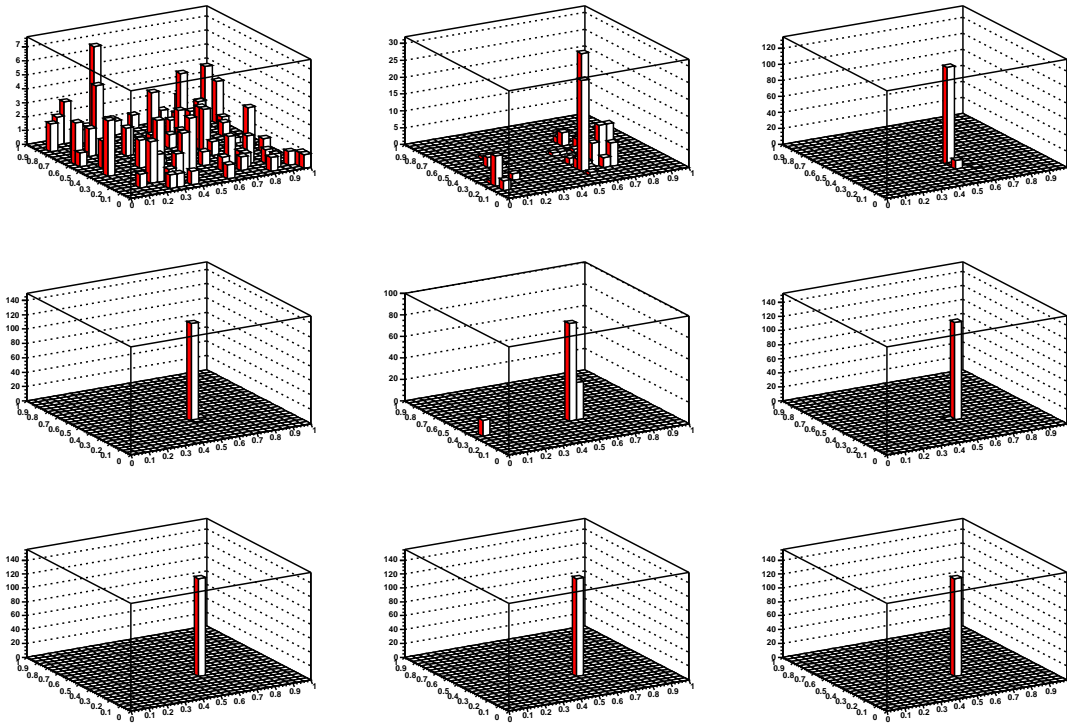


Figure A.4: Evolution of the GA. The histograms show the distribution of the NR magnitude against the NR phase for the individuals in the population every 10 generations.

# Appendix B

## Pull Plots

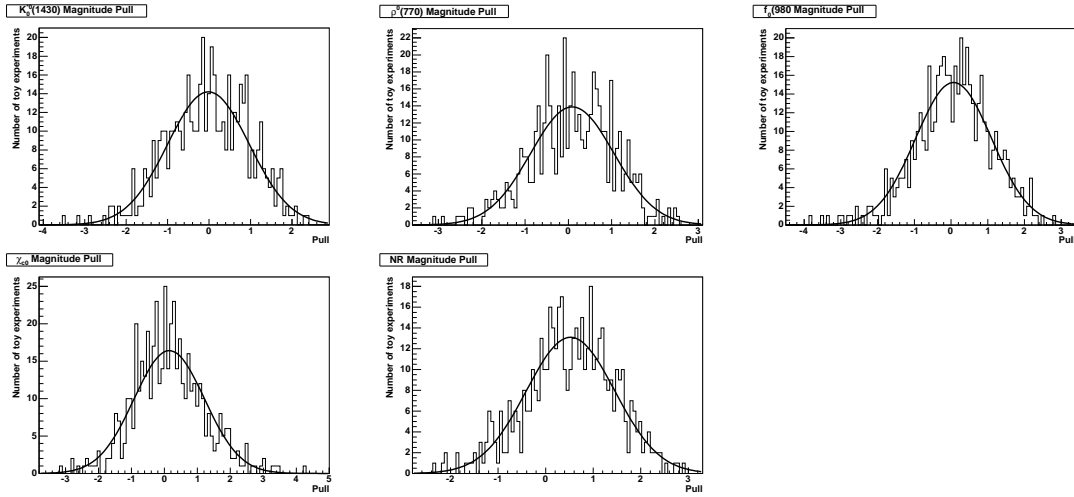


Figure B.1: Magnitude pull distributions for the 500  $B^-$  toy MC samples. Top left shows the  $K_0^{*0}(1430)$ , top middle the  $\rho^0(770)$ , top right the  $f_0(980)$ , bottom left the  $\chi_{c0}$  and bottom middle the non-resonant.

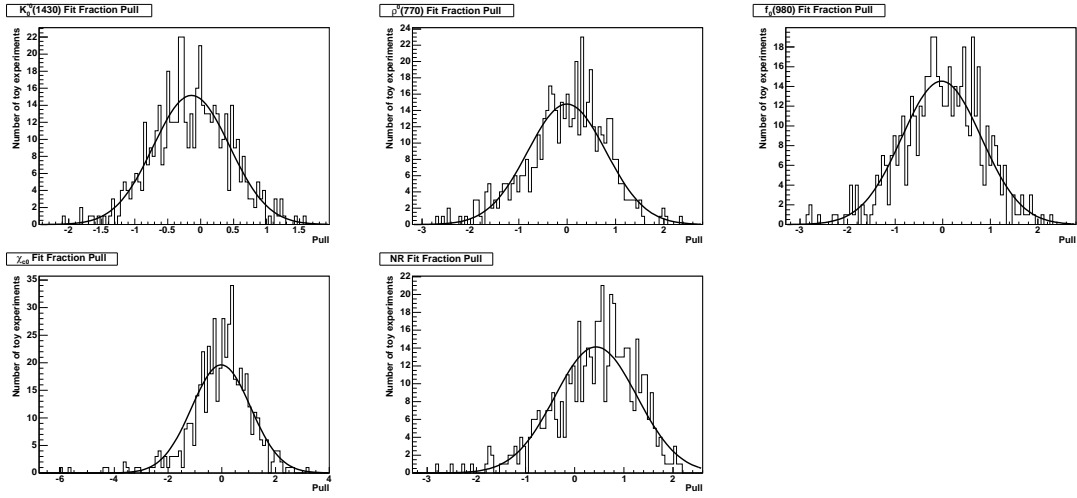


Figure B.2: Fit fraction pull distributions for the 500  $B^-$  toy MC samples. Top left shows the  $K_0^{*0}(1430)$ , top middle the  $\rho^0(770)$ , top right the  $f_0(980)$ , bottom left the  $\chi_{c0}$  and bottom middle the non-resonant.

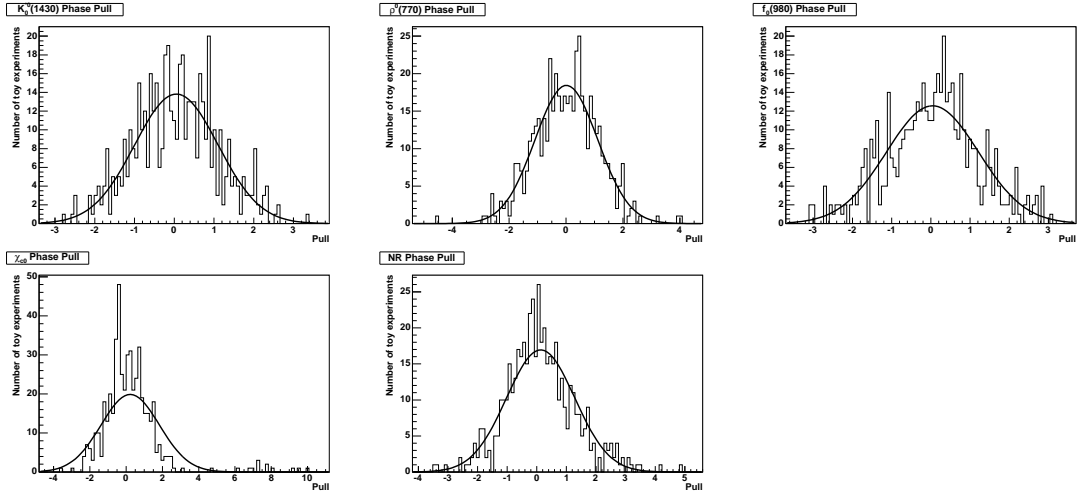


Figure B.3: Phase pull distributions for the 500  $B^-$  toy MC samples. Top left shows the  $K_0^{*0}(1430)$ , top middle the  $\rho^0(770)$ , top right the  $f_0(980)$ , bottom left the  $\chi_{c0}$  and bottom middle the non-resonant.

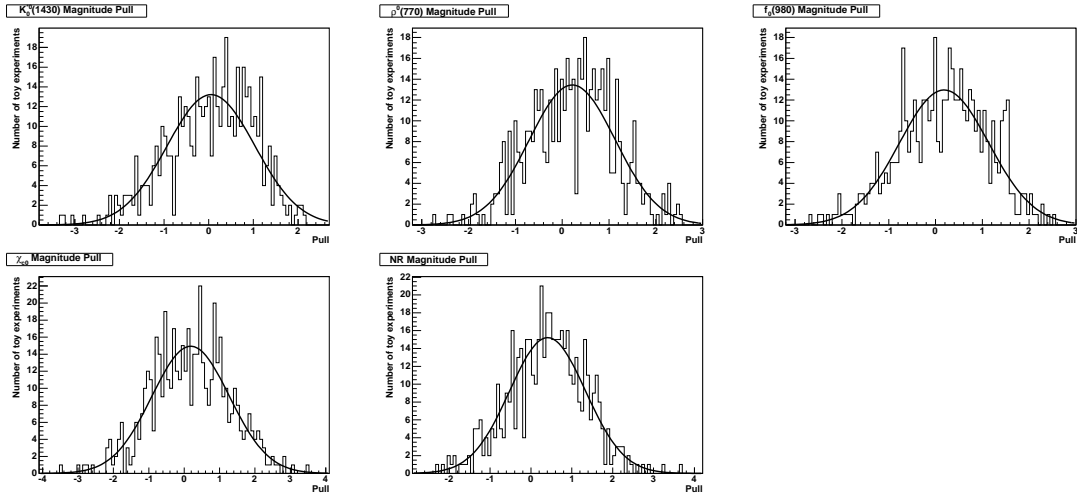


Figure B.4: Magnitude pull distributions for the 500  $B^+$  toy MC samples. Top left shows the  $K_0^{*0}(1430)$ , top middle the  $\rho^0(770)$ , top right the  $f_0(980)$ , bottom left the  $\chi_{c0}$  and bottom middle the non-resonant.

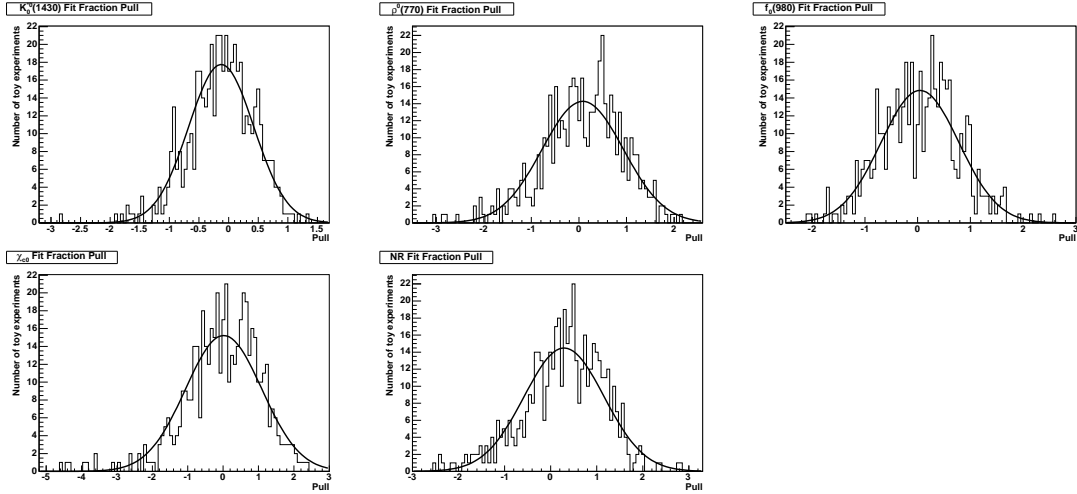


Figure B.5: Fit fraction pull distributions for the 500  $B^+$  toy MC samples. Top left shows the  $K_0^{*0}(1430)$ , top middle the  $\rho^0(770)$ , top right the  $f_0(980)$ , bottom left the  $\chi_{c0}$  and bottom middle the non-resonant.

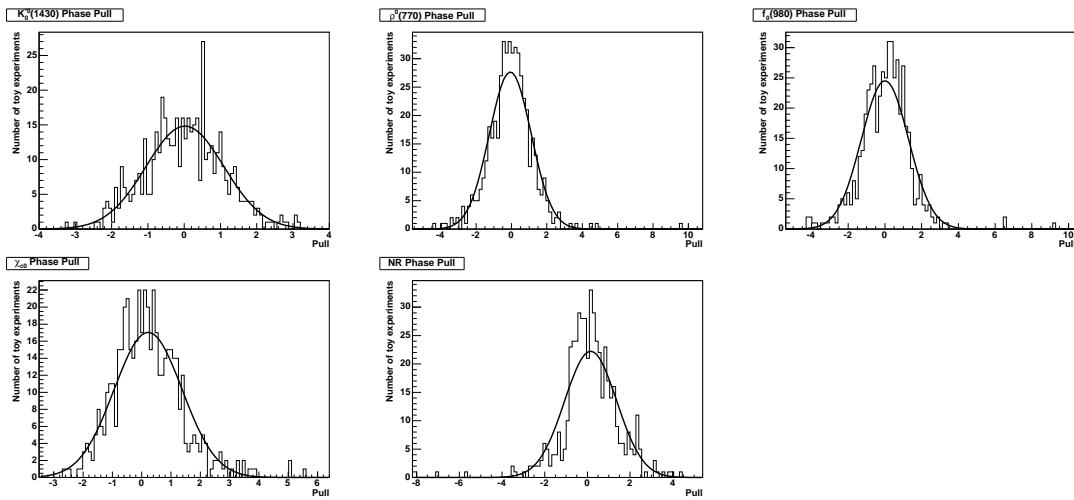


Figure B.6: Phase pull distributions for the 500  $B^+$  toy MC samples. Top left shows the  $K_0^{*0}(1430)$ , top middle the  $\rho^0(770)$ , top right the  $f_0(980)$ , bottom left the  $\chi_{c0}$  and bottom middle the non-resonant.

# Bibliography

- [1] C. S. Wu, E. Ambler, R. W. Hayward, D. D. Hoppes and R. P. Hudson, Phys. Rev. **105** (1957) 1413.
- [2] J. H. Christenson, J. W. Cronin, V. L. Fitch and R. Turlay, Phys. Rev. Lett. **13** (1964) 138.
- [3] B. Aubert *et al.* [BABAR Collaboration], Phys. Rev. Lett. **87** (2001) 091801 [arXiv:hep-ex/0107013].
- [4] K. Abe *et al.* [Belle Collaboration], Phys. Rev. Lett. **87** (2001) 091802 [arXiv:hep-ex/0107061].
- [5] N. Cabibbo, Phys. Rev. Lett. **10** (1963) 531.
- [6] M. Kobayashi and T. Maskawa, Prog. Theor. Phys. **49** (1973) 652.
- [7] S. W. Herb *et al.*, Phys. Rev. Lett. **39** (1977) 252.
- [8] S. Eidelman *et al.* [Particle Data Group Collaboration], Phys. Lett. B **592** (2004) 1.
- [9] L. Wolfenstein, Phys. Rev. Lett. **51** (1983) 1945.
- [10] The *BABAR* Collaboration edited by P. F. Harrison and H. R. Quinn, “The *BABAR* Physics Book”, SLAC-R-504, 1998.
- [11] [http://www.slac.stanford.edu/xorg/ckmfitter/ckm\\_results\\_ichep04.html](http://www.slac.stanford.edu/xorg/ckmfitter/ckm_results_ichep04.html)

- [12] J. Charles *et al.* [CKMfitter Group Collaboration], arXiv:hep-ph/0406184.
- [13] B. Aubert [BABAR Collaboration], arXiv:hep-ex/0408127.
- [14] K. Abe *et al.* [BELLE Collaboration], arXiv:hep-ex/0408111.
- [15] L. Roos [BABAR Collaboration], arXiv:hep-ex/0407051.
- [16] B. Aubert [BABAR Collaboration], arXiv:hep-ex/0408038.
- [17] B. Aubert *et al.* [BaBar Collaboration], arXiv:hep-ex/0407057.
- [18] Y. Chao [the Belle Collaboration], arXiv:hep-ex/0408100.
- [19] B. Aubert *et al.* [BABAR Collaboration], Phys. Rev. Lett. **92** (2004) 181801 [arXiv:hep-ex/0311037].
- [20] M. Verderi [BABAR Collaboration], arXiv:hep-ex/0406082.
- [21] G. Buchalla, A. J. Buras and M. E. Lautenbacher, Rev. Mod. Phys. **68** (1996) 1125 [arXiv:hep-ph/9512380].
- [22] M. Beneke, G. Buchalla, M. Neubert and C. T. Sachrajda, Phys. Rev. Lett. **83** (1999) 1914 [arXiv:hep-ph/9905312].
- [23] M. Beneke, G. Buchalla, M. Neubert and C. T. Sachrajda, Nucl. Phys. B **591** (2000) 313 [arXiv:hep-ph/0006124].
- [24] R. Aleksan, P. F. Giraud, V. Morenas, O. Pene and A. S. Safir, Phys. Rev. D **67** (2003) 094019 [arXiv:hep-ph/0301165].
- [25] M. Ciuchini, E. Franco, G. Martinelli, M. Pierini and L. Silvestrini, Phys. Lett. B **515** (2001) 33 [arXiv:hep-ph/0104126].
- [26] M. Beneke and M. Neubert, Nucl. Phys. B **675** (2003) 333 [arXiv:hep-ph/0308039].

- [27] W. N. Cottingham, H. Mehrban and I. B. Whittingham, J. Phys. G **28** (2002) 2843 [arXiv:hep-ph/0102012].
- [28] N. de Groot, W. N. Cottingham and I. B. Whittingham, Phys. Rev. D **68** (2003) 113005 [arXiv:hep-ph/0308269].
- [29] D. S. Du, H. J. Gong, J. F. Sun, D. S. Yang and G. H. Zhu, Phys. Rev. D **65** (2002) 094025 [Erratum-ibid. D **66** (2002) 079904] [arXiv:hep-ph/0201253].
- [30] C. P. Jessop *et al.* [CLEO Collaboration], Phys. Rev. Lett. **85** (2000) 2881 [arXiv:hep-ex/0006008].
- [31] K. Abe *et al.* [Belle Collaboration], Phys. Rev. D **65** (2002) 092005 [arXiv:hep-ex/0201007].
- [32] B. Aubert *et al.* [BABAR Collaboration], Phys. Rev. Lett. **91** (2003) 051801 [arXiv:hep-ex/0304006].
- [33] J. Back, *BABAR* Analysis Document #505.
- [34] B. Aubert *et al.* [BABAR Collaboration], Phys. Rev. D **70** (2004) 092001 [arXiv:hep-ex/0308065].
- [35] A. Garmash *et al.* [BELLE Collaboration], arXiv:hep-ex/0412066.
- [36] B. Aubert *et al.* [BABAR Collaboration], arXiv:hep-ex/0408032.
- [37] R.H. Dalitz, Phil. Mag. **44** (1953) 1068.
- [38] B. Aubert *et al.* [BABAR Collaboration], Nucl. Instrum. Meth. A **479** (2002) 1 [arXiv:hep-ex/0105044].
- [39] <http://www.slac.stanford.edu/BFROOT/www/Physics/Tools/generators/EvtGen/Evt.ps>
- [40] T. Sjostrand, Comput. Phys. Commun. **82** (1994) 74.

- [41] S. Agostinelli *et al.* [GEANT4 Collaboration], Nucl. Instrum. Meth. A **506** (2003) 250.
- [42] W.T. Ford, *BABAR* Analysis Document #53.
- [43] R.A. Fisher, Ann. Eugenics **7**, 179 (1936);  
G. Cowan, *Statistical Data Analysis*, (Oxford University Press, 1998), p51.
- [44] J. Beringer, *BABAR* Analysis Document #317.
- [45] T. Allmendinger *et al.*, *BABAR* Analysis Document #867.
- [46] <http://www.slac.stanford.edu/BFROOT/www/Physics/TrackEfficTaskForce/TrackingTaskForce-2004.html>
- [47] S. Spanier and G. Mancinelli, *BABAR* Analysis Document #116.
- [48] S. Eidelman *et al.* [Particle Data Group Collaboration], Phys. Lett. B **592** (2004) 1, p242.
- [49] <http://www.slac.stanford.edu/BFROOT/www/Physics/Tools/Pid/PidOnMc/pidonmc.html>
- [50] T. Brandt, *BABAR* Analysis Document #396.
- [51] <http://root.cern.ch/>
- [52] Vertexing and Composition Tools Group, *BABAR* Analysis Document #102.
- [53] J. Back, *Laura++* Manual - Likelihood Analysis Unbinned Reconstruction of Amplitudes, *BABAR* Analysis Document #806.
- [54] <http://www.library.cornell.edu/nr/cbookcpdf.html>
- [55] J. Blatt and V. Weisskopf, "Theoretical Nuclear Physics", John Wiley & Sons, New York, 1956.
- [56] S. M. Flatte, Phys. Lett. B **63** (1976) 224.

- [57] D. Bugg, Private communication.
- [58] M. Ablikim *et al.* [BES Collaboration], Phys. Lett. B **598** (2004) 149 [arXiv:hep-ex/0406038].
- [59] E. M. Aitala *et al.* [E791 Collaboration], Phys. Rev. Lett. **86** (2001) 765 [arXiv:hep-ex/0007027].
- [60] T. A. Armstrong *et al.* [WA76 Collaboration], Z. Phys. C **51** (1991) 351.
- [61] D. Aston *et al.*, Nucl. Phys. B **296** (1988) 493.
- [62] W.M. Dunwoodie, Fits to K pi I=1/2 S-wave Amplitude and Phase Data:  
[http://www.slac.stanford.edu/~wmd/kpi\\_swave/kpi\\_swave\\_fit.note](http://www.slac.stanford.edu/~wmd/kpi_swave/kpi_swave_fit.note)
- [63] R. Barlow, “Statistics”, John Wiley & Sons, 1989.
- [64] H. Albrecht *et al.* [ARGUS Collaboration], Z. Phys. C **48** (1990) 543.
- [65] F. James and M. Roos, Comput. Phys. Commun. **10** (1975) 343.
- [66] F. James, “Minuit Reference Manual (Version 94.1)”, Program Library Long Writeup D506, CERN, Geneva, August 1998.
- [67] G. Cowan, “Statistical Data Analysis”, Oxford University Press, Oxford, 1998.
- [68] P. Charbonneau and B. Knapp, “A Guide to PIKAIA 1.0”, NCAR/TN-418+IA (1995); <http://www.hao.ucar.edu/public/research/si/pikaia/pikaia.html>
- [69] A. Hoecker and M. Laget, *BABAR* Analysis Document #672.
- [70] C. Hearty, *BABAR* Analysis Document #134.
- [71] B. Bajc, S. Fajfer, R. J. Oakes, T. N. Pham and S. Prelovsek, Phys. Lett. B **447** (1999) 313 [arXiv:hep-ph/9809262].
- [72] <http://www.slac.stanford.edu/xorg/hfag/rare/ichep04/charmless/OUTPUT/TABLES/charmless.pdf>

- [73] D. M. Asner *et al.* [CLEO Collaboration], Phys. Rev. D **70** (2004) 091101  
[arXiv:hep-ex/0311033].